Dissertation zur Erlangung des Doktorgrades
der Fakultät Chemie und Pharmazie
der Ludwig–Maximilians–Universität München

Development of
Efficient Electronic-Structure Methods
Based on
the Adiabatic-Connection
Fluctuation-Dissipation Theorem
and
Møller–Plesset Perturbation Theory

Daniel Graf

aus

Göppingen, Deutschland

2021

Erklärung

Diese Dissertation wurde im Sinne von §7 der Promotionsordnung vom 28. November 2011 von Herrn Prof. Dr. Christian Ochsenfeld betreut.

Eidesstattliche Versicherung

Diese Dissertation wurde eigenständig und ohne unerlaubte Hilfsmittel erarbeitet.

München, 07.04.2021   . . . .

                                     (Daniel Graf)

Dissertation eingereicht am:	16.02.2021
Erstgutachter:	Prof. Dr. Christian Ochsenfeld
Zweitgutachterin:	Prof. Dr. Regina de Vivie-Riedle
Mündliche Prüfung am:	26.03.2021

Danksagung

An erster Stelle gilt mein Dank Prof. Dr. Christian Ochsenfeld für die Möglichkeit, diese Dissertation in seinem Arbeitskreis und unter seiner Anleitung anzufertigen, sowie für die Unterstützung im Laufe der Jahre.

Außerdem bedanke ich mich bei Prof. Dr. Regina de Vivie-Riedle für das Anfertigen des Zweitgutachtens.

Des Weiteren danke ich dem ganzen Arbeitskreis Ochsenfeld für das nette Miteinander sowie für das positive und motivierende Arbeitsklima. Ganz besonderer Dank gebührt an dieser Stelle Dr. Matthias Beuerle, Henryk Laqua, Dr. Arne Lünser, Dr. Henry Schurkus, Michael Glasbrenner, Viktoria Drontschenko, Gökçen Savaşçı und Dr. Jörg Kussmann für die hervorragende Zusammenarbeit und die gemeinsame Zeit, die ich stets in bester Erinnerung behalten werde.

Zuletzt danke ich meinen Eltern und Großeltern, meinem Bruder, meinen Freunden und Charlotte Fischer für die fortwährende Unterstützung, die unzähligen heiteren Momente und das ehrliche Vertrauen in mich.

Summary

One of the major goals of quantum chemistry is to develop electronic-structure methods, which are not only highly accurate in the evaluation of electronic ground-state properties, but also computationally tractable and versatile in their application. A theory with great potential in this respect, however, without being free from shortcomings is the random phase approximation (RPA).

In this work, developments are presented, which address the most important of these shortcomings subject to the constraint to obtain low- and linear-scaling electronic-structure methods. A scheme combining an elegant way to introduce local orbitals and multi-node parallelism is put forward, which not only allows to evaluate the RPA correlation energy in a fraction of the time of former theories, but also enables a scalable decrease of the high memory requirements. Furthermore, a quadratic-scaling self-consistent minimization of the total RPA energy with respect to the one-particle density matrix in the atomic-orbital space is introduced, making the RPA energy variationally stable and independent of the quality of the reference calculation. To address the slow convergence with respect to the size of the basis set and the self-correlation inherent in the RPA functional, range-separation of the electron-electron interaction is exploited for atomic-orbital RPA, yielding a linear-scaling range-separated RPA method with consistent performance over a broad range of chemical problems. As a natural extension, the concepts including local orbitals, self-consistency, and range-separation are further combined in a RPA-based generalized Kohn–Sham method, which not only shows a balanced performance in general main group thermochemistry, kinetics, and noncovalent interactions, but also yields accurate ionization potentials and fundamental gaps.

The origin of the self-correlation error within RPA lies in the neglect of exchange-effects in the calculation of the interacting density-density response functions. While range-separation is a reasonable approach to counteract this shortcoming — since self-correlation is pronounced at short interelectronic distances — a more rigorous but computationally sophisticated approach is to introduce the missing exchange-effects,

at least to some extent. To make RPA with exchange methods applicable to systems containing hundreds of atoms and hence a suitable choice for practical applications, a framework is developed, which allows to devise highly efficient low- and linear-scaling RPA with exchange methods.

The developments presented in this work, however, are not only limited to RPA and beyond-RPA methods. The connection between RPA and many-body perturbation theory is further used to present a second-order Møller–Plesset perturbation theory method, which combines the tools to obtain low- and linear-scaling RPA and beyond-RPA methods with efficient linear-algebra routines, making it highly efficient and applicable to large molecular systems comprising several thousand of basis functions.

List of Publications

This is a cumulative dissertation, comprising six articles published in peer-reviewed journals. In the following, all articles are stated together with the author's contribution to each of them.

I **D. Graf**, M. Beuerle, H. F. Schurkus, A. Luenser, G. Savasci, C. Ochsenfeld
"Accurate and Efficient Parallel Implementation of an Effective Linear-Scaling Direct Random Phase Approximation Method"
J. Chem. Theory Comput. **14**, 2505 (2018).
Contributions by the Author: *Conjoint development of the theory with M. Beuerle, H. F. Schurkus, and A. Luenser. All of the implementation, calculations, and writing.*

II **D. Graf**, M. Beuerle, C. Ochsenfeld
"Low-Scaling Self-Consistent Minimization of a Density Matrix Based Random Phase Approximation Method in the Atomic Orbital Space"
J. Chem. Theory Comput. **15**, 4468 (2019).
Contributions by the Author: *Most of the theory and most of the implementation. All calculations and writing.*

III A. Kreppel, **D. Graf**, H. Laqua, C. Ochsenfeld
"Range-Separated Density-Functional Theory in Combination with the Random Phase Approximation: An Accuracy Benchmark"
J. Chem. Theory Comput. **16**, 2985 (2020).
Contributions by the Author: *Parts of the theory. All of the RPA implementation. Contributions to the manuscript.*

IV **D. Graf**, C. Ochsenfeld

"A range-separated generalized Kohn–Sham method including a long-range nonlocal random phase approximation correlation potential"

J. Chem. Phys. **153**, 244118 (2020).

Contributions by the Author: *All of the theory, all of the implementation, all of the calculations and writing.*

V M. Beuerle, **D. Graf**, H. F. Schurkus, C. Ochsenfeld

"Efficient calculation of beyond RPA correlation energies in the dielectric matrix formalism"

J. Chem. Phys. **148**, 204104 (2018).

Contributions by the Author: *Parts of the theory and implementation.*

VI M. Glasbrenner, **D. Graf**, C. Ochsenfeld

"Efficient Reduced-Scaling Second-Order Møller–Plesset Perturbation Theory with Cholesky-Decomposed Densities and an Attenuated Coulomb Metric"

J. Chem. Theory Comput. **16**, 6856 (2020).

Contributions by the Author: *Conjoint development of the theory with M. Glasbrenner. Parts of the implementation and writing.*

Contents

1

Introduction

The central equation in quantum chemistry is the Schrödinger equation,[1] which exactly describes the correlated movement of particles in a non-relativistic physical system. However, even the time-independent Schrödinger equation in the Born–Oppenheimer approximation[2] will probably never be solved analytically for molecular systems containing more than one electron due to the complexity of the interactions between electrons. Therefore, one needs to rely on further approximations and numerical schemes to approach the solution of the electronic Schrödinger equation for systems of relevant size.

Two main directions evolved over the years after the publication of the Schrödinger equation in 1926 pursuing this goal: wave-function-based methods (e.g., Ref. [3]) and Kohn–Sham[4] (KS) density functional theory (DFT). The beauty of wave-function-based methods lies in the fact that they are systematically improvable and hence can be ranked in a strong hierarchy of accuracy which indeed goes up to the exact numerical solution of the electronic Schrödinger equation. However, in case of wave-function-based methods, high accuracy is often coupled to high computational cost, which makes highly accurate wave-function methods only applicable to molecular systems on the few atoms scale and hence unsuitable for most problems of practical relevance.

Density functional theory on the other hand follows a more pragmatic path, which lacks a strict hierarchy, but yields useful accuracy at an affordable cost, making it the most popular approach to describe the electronic structure in most areas of quantum chemistry. However, since the pioneering work of Kohn and Sham[4] hundreds of different density functional approximations (DFAs)[5] have been developed,[6] which is sometimes referred to as functional inflation.[7] One reason for this still increasing number is that a functional might perform very well for certain types of compounds and properties, but fail for others. Furthermore, it should be noted that there are well-known

deficiencies of standard density functional approximations such as the incomplete correction of the unphysical Coulomb self-interaction[8–17] and the missing description of nonlocal phenomena like long-range dispersion interactions.[18] This, of course, makes the selection of a suitable functional for a specific problem challenging and underlines the necessity to develop methods which are broadly applicable and come with a tractable computational cost.

An electron-correlation method, which places itself on the border of wave-function-based methods and density functional theory, is the random phase approximation (RPA). The roots of RPA lie in a series of three papers by Bohm and Pines published between 1951 and 1953,[19–21] in which they attempted to solve the many-electron problem of the homogeneous electron gas. In the high-density limit the electrons are so close to each other that the movement of one electron will also effect all other electrons. This strong coupling of the motions of the electrons leads to wave-like density fluctuations called plasmon oscillations.[22] In order to describe the collective motion of the electrons, Bohm and Pines made use of a coupled harmonic oscillator Hamiltonian and corrected it with a short-range term, accounting for the random thermal motion of the electrons, which also appears in the noninteracting system. The description of the collective motion was further separated into in-phase oscillations and coupled out-of-phase oscillations. Bohm and Pines[20] showed that the out-of-phase terms can be neglected and called this approximation the *random phase approximation*. In 1957, Gell-Mann and Brueckner[23] showed for the first time that the RPA ground-state correlation energy of the homogeneous electron gas can equivalently be obtained by summing over all ring-diagrams in a many-body perturbation theory expansion, which is the reason why RPA is sometimes also referred to as 'ring-approximation'. However, the most accepted definition of the random phase approximation to date is that of Langreth and Perdew,[24,25] who combined the concept of an adiabatic-connection between the interacting and the noninteracting system within DFT with the fluctuation-dissipation theorem[26] and showed that RPA arises as a zeroth-order approximation within this framework. They termed this formalism the *adiabatic-connection fluctuation-dissipation theorem* (ACFDT).[24,25]

With the initial work of Furche in 2001,[27] RPA as a post-KS method found its way into quantum chemistry and became increasingly popular in the last years.[7,27–51] However, this first implementation of 2001, which was based on molecular orbitals (MOs), showed a prohibitive $O(M^6)$ scaling with the molecular size M, making the method only applicable to systems of few atoms. Introduction of the resolution of

the identity (RI) in combination with a numerical integration scheme by Furche and co-workers[34] in 2010 allowed for a $O(M^4)$ scaling formulation, opening the door for calculations on systems comprising around 100 atoms. In 2016, a formulation of RPA in the local atomic-orbital (AO) basis by Schurkus and Ochsenfeld[50] decreased the scaling behavior with the molecular size further to linear, however, at the cost of increased scaling with the size of the basis set. Luenser *et al.*[51] remedied the above-mentioned drawback by introducing local Cholesky orbitals, making AO-RPA competitive with MO-RPA also for small systems without locality in the electronic structure.

In **Publication I**, the central transformation, allowing for a pure AO formulation of RPA, is shown to be equivalent to a Fourier transform of the noninteracting density-density response function connecting the imaginary-time and imaginary-frequency representation thereof. This allows for the use of improved integration schemes, which not only increase the accuracy of the method with respect to MO-RPA by orders of magnitudes, but also decrease its computational cost by a factor of four. Furthermore, a new scheme to introduce local Cholesky orbitals is presented that only makes use of the one-particle density matrix, significantly reducing the memory requirements of the method on a single node. Finally, a multi-node parallel algorithm of the new method is brought forward, which decreases the computation time and additionally leads to a scalable decrease of the memory requirements. All together, the new method allows for RPA correlation energy calculations on systems far out of reach before.

Besides a few exceptions,[37,52–56] RPA is routinely performed in a post-KS fashion. Since the RPA functional is a functional of the fifth rung on Jacob's Ladder,[57] this means that orbitals and the respective orbital energies are used that stem from a preceding, in general semi-local, DFT calculation. This, of course, is accompanied by some drawbacks, the most obvious being that the total RPA energy is not variationally minimized. Furthermore, as mentioned above, DFAs can give accurate energies for some compounds, but fail for others. This, of course, is not only true for the energy itself, but also for the orbitals and the respective orbital energies, especially if one bares in mind that most DFAs are constructed to yield accurate energies and not necessarily good orbitals/orbital energies. It goes without saying that such orbitals/orbital energies can lead to significant errors when they are used in a subsequent RPA calculation. In **Publication II**, a method is presented, which minimizes the total RPA energy with respect to the one-particle density matrix in the atomic-orbital space. It is shown that this method yields lower errors in the description of noncovalent interactions

and removes errors, stemming from low-quality references as demonstrated on the dissociation of the helium dimer. Furthermore, a scheme is presented, which allows for an asymptotically quadratic-scaling implementation by applying Cholesky-factorized projectors on the RPA correlation potential, making this method applicable to systems comprising hundreds of atoms.

Within the ACFDT framework, the central quantities are the density-density response functions for different interaction-strengths between the electrons along the adiabatic-connection path. While the response function for the noninteracting system — the KS response function — is well-known, the response functions for all other interaction-strengths are unknown and need to be approximated. To be more specific, the quantity which needs to be approximated is the frequency-dependent exchange-correlation kernel. Within the random phase approximation, the exchange-correlation kernel is neglected completely, which is the reason why it is sometimes called the Hartree approximation within time-dependent density functional theory[58] (TDDFT).[7,59] As a result, there is no Pauli repulsion between same-spin particle-hole pairs, leading to a too deep on-top correlation hole and hence over-correlation, especially for short interelectronic distances.[7,60–63] Another problem is the slow convergence of the energy with respect to the basis-set size.[27,64] The reason for this observation is the fact that the electron-electron cusp[65] needs to be modeled explicitly, which requires a lot of basis functions with high angular momentum. Both self-correlation and the slow basis-set convergence can be tackled with a range-separation ansatz, using a standard density functional for the short-range part and RPA for the long-range part.[64,66–79] In **Publication III**, a range-separated RPA method is presented, which is based on the method introduced in **Publication I**. Compared to the $O(M^6)$ scaling of existing range-separated RPA methods,[64,66–79] the new method shows asymptotically linear scaling with the system size. The efficiency of the method allows for a detailed benchmark of range-separated RPA, which, first, confirms the faster convergence with respect to the basis-set size and the tremendously improved performance on self-interaction related problems, and, second, demonstrates that range-separated RPA performs more stably over a broad range of different chemical problems than standard RPA.

The range-separated RPA method of **Publication III** evaluates the long-range RPA correlation energy using orbitals and orbital energies obtained with the range-separated hybrid PBE (RSHPBE) functional,[80] which lacks a long-range correlation potential. However, it is known that the reference has a significant impact on the correlation energy obtained with the RPA functional.[53,76,81–83] In **Publication IV**, the RSHPBE

functional is extended by a long-range RPA correlation potential, making the new method a full-featured variational generalized Kohn–Sham (GKS) functional, combining all advantages of the methods presented in **Publications I-III**. The new method is, on average, more accurate than all other tested methods including PBE,[84,85] RSHPBE, RPA, range-separated RPA, and self-consistent RPA on test sets covering general main group thermochemistry, kinetics, and noncovalent interactions. Furthermore, it outperforms the popular G_0W_0 method in approximating ionization potentials and fundamental gaps using the quasi-particle spectra obtained from the GKS Hamiltonian, demonstrating the high quality of the underlying potential.

Another way of tackling self-correlation within RPA — besides the above-mentioned range-separation approach — is to explicitly include exchange-effects, cancelling this spurious self-interaction. Since there are several ways to include exchange-effects into RPA, a number of different RPA with exchange methods exist to date.[35,40,48,64,70,86–92] However, they all have one thing in common, which is their steep computational cost, limiting their applicability to small systems. In **Publication V**, methodologies combining the insights of **Publication I** with novel integral estimates for integral screening are presented, which allow for the derivation of low- and linear-scaling RPA with exchange methods of all different kinds. The new methodologies are demonstrated on the example of RPA with second-order screened-exchange (RPA-SOSEX),[87,90] allowing for calculations on systems comprising up to 500 atoms, which is far beyond what was possible before.

As mentioned above, RPA can also be derived in the framework of many-body perturbation theory (MBPT) as an infinite sum of ring-diagrams. In case of RPA with exchange methods, further diagrams accounting for exchange-effects occur in the series expansion. In fact, the well-known second-order Møller–Plesset perturbation theory[93] (MP2) energy expression (in terms of KS orbitals) is a second-order approximation to RPA-SOSEX and all the other beyond-RPA methods presented in **Publication V**. In **Publication VI**, the ideas to devise low- and linear-scaling beyond-RPA methods are transferred to MP2 and combined with a modified version of the natural blocking approach of Head-Gordon and co-workers,[94] yielding a MP2 method much more efficient than the methods presented before.

In the following, Chapter 2 briefly outlines the theoretical foundations of this work. Chapter 3 constitutes the main part of this cumulative dissertation and reproduces **Publications I-VI** in their entirety. Finally, a conclusion is given in Chapter 4.

2

Theoretical Background

This Chapter is intended to set the theoretical foundations of the work presented in Chapter 3. In Sections 2.1 to 2.4 some basic aspects of quantum chemistry, including the time-independent electronic Schrödinger equation (Section 2.1), second quantization (Section 2.2), the Hartree–Fock approximation (Section 2.3), and Kohn–Sham density functional theory (Section 2.4) are briefly outlined. Section 2.5 describes the adiabatic-connection within density functional theory. This concept is then combined with the fluctuation-dissipation theorem in Section 2.6 to form the adiabatic-connection fluctuation-dissipation framework. Section 2.7 gives a short introduction to density-density linear response functions obtained from time-dependent linear response theory and establishes the random phase approximation in the context of the adiabatic-connection fluctuation-dissipation theorem. Finally, in Sections 2.8 and 2.9 the RPA, beyond-RPA, and perturbation theory methods are derived, which form the basis of Chapter 3.

2.1 The Time-Independent Electronic Schrödinger Equation

The time-independent electronic Schrödinger equation[1] in the Born–Oppenheimer approximation[2] is given by

$$\hat{H}\Psi = E\Psi, \tag{2.1}$$

where $\hat{H}$ denotes the electronic Hamilton operator in atomic units

$$\hat{H} = -\sum_{i}^{N_{\text{el}}} \frac{1}{2}\nabla_i^2 - \sum_{i}^{N_{\text{el}}} \sum_{A}^{N_{\text{atoms}}} \frac{Z_A}{r_{iA}} + \sum_{i}^{N_{\text{el}}} \sum_{j>i}^{N_{\text{el}}} \frac{1}{r_{ij}} \tag{2.2}$$

of a system consisting of N_{el} electrons and N_{atoms} atoms with r_{iA} denoting the distance between electron i and nucleus A, r_{ij} denoting the distance between electrons i and j, and Z_A denoting the charge of nucleus A. Ψ is the molecular wave function, which can be expanded in terms of antisymmetrized products of a complete set of one-electron functions $\{\varphi_p\}$. The antisymmetry of fermionic wave functions[95,96] is a generalization of the Pauli exclusion principle,[97,98] stating that two electrons cannot have identical values for all four quantum numbers. One elegant way to account for the antisymmetry of the wave function is to employ so-called Slater determinants[99] defined as

$$\Phi_0(\mathbf{x}_1, \mathbf{x}_2, \ldots, \mathbf{x}_{N_{\text{el}}}) = \frac{1}{\sqrt{N_{\text{el}}!}} \begin{vmatrix} \varphi_1(\mathbf{x}_1) & \varphi_2(\mathbf{x}_1) & \ldots & \varphi_{N_{\text{el}}}(\mathbf{x}_1) \\ \varphi_1(\mathbf{x}_2) & \varphi_2(\mathbf{x}_2) & \ldots & \varphi_{N_{\text{el}}}(\mathbf{x}_2) \\ \vdots & \vdots & \ddots & \vdots \\ \varphi_1(\mathbf{x}_{N_{\text{el}}}) & \varphi_2(\mathbf{x}_{N_{\text{el}}}) & \ldots & \varphi_{N_{\text{el}}}(\mathbf{x}_{N_{\text{el}}}) \end{vmatrix} \qquad \text{2.3a}$$

$$= \left| \Phi_0 \right\rangle . \qquad \text{2.3b}$$

It can be shown that any antisymmetric function with N variables can be exactly expanded in terms of all unique N-variable Slater determinants formed from a complete set of one-variable functions and hence the same holds true for the exact wave function, which can, therefore, be expressed as

$$\left| \Psi \right\rangle = \sum_i c_i \left| \Phi_i \right\rangle . \qquad \text{2.4}$$

Since each of the different Slater determinants $\left| \Phi_i \right\rangle$ is formed from a specific set of one-particle functions — also called configuration — this approach is known as *configuration interaction* (CI) or *full configuration interaction* (FCI; cf. Ref. [100]) in case of the complete expansion.

Another very convenient way to account for the antisymmetry of the wave function lies in the concept called *second quantization*, which will be discussed in more detail in the next section.

2.2 Second Quantization

The formalism of second quantization[101–103] is another elegant way to account for the antisymmetry property of the electronic wave function. It should be noted that within this formalism, the electronic Schrödinger equation is merely rewritten, it does not introduce any new physics.

In second quantization, the state of the system is described in the basis of abstract state-vectors

$$|n_1 n_2 \ldots n_N\rangle, \qquad 2.5$$

where the one-particle states are ordered according to their quantum numbers and n_1, n_2, ..., n_N denote their occupation numbers. Just like the basis of Slater determinants, this state-vector basis is required to be orthogonal and complete. To account for the statistics of fermions, the creation $\hat{a}_p^\dagger$ and annihilation $\hat{a}_p$ operators, which raise and lower the respective occupation number by one, are introduced in the abstract occupation-number space, satisfying the following anticommutation rules:[104]

$$\left\{\hat{a}_p, \hat{a}_q^\dagger\right\} = \hat{a}_p \hat{a}_q^\dagger + \hat{a}_q^\dagger \hat{a}_p = \delta_{pq} \qquad 2.6$$

$$\left\{\hat{a}_p, \hat{a}_q\right\} = \left\{\hat{a}_p^\dagger, \hat{a}_q^\dagger\right\} = 0, \qquad 2.7$$

with δ_{pq} denoting the Kronecker delta. Using the anticommutation rules and introducing the vacuum state $|\mathrm{vac}\rangle$, it can be trivially shown that

$$|n_i n_j\rangle = \hat{a}_i^\dagger \hat{a}_j^\dagger |\mathrm{vac}\rangle = -\hat{a}_j^\dagger \hat{a}_i^\dagger |\mathrm{vac}\rangle = -|n_j n_i\rangle \qquad 2.8$$

and hence the antisymmetry property of the wave function has been transferred to the algebraic properties of the creation and annihilation operators.

Another appealing feature of the second quantization formalism is the simple description of operators. One-particle operators, e.g., take the form[104]

$$\hat{O}_1 = \sum_{pq} \langle p|\hat{O}_1|q\rangle \, \hat{a}_p^\dagger \hat{a}_q, \qquad 2.9$$

where p and q run over all one-particle states and

$$\langle p|\hat{O}_1|q\rangle = \int \mathrm{d}\mathbf{x} \, \varphi_p^*(\mathbf{x})\hat{O}_1(\mathbf{x})\varphi_q(\mathbf{x}), \qquad 2.10$$

with **x** denoting a combined spin- and space-index. Analogously, two-particle operators are defined according to

$$\hat{O}_2 = \frac{1}{2} \sum_{pqrs} \langle pq|\hat{O}_2|rs \rangle \, \hat{a}_p^\dagger \hat{a}_q^\dagger \hat{a}_s \hat{a}_r, \qquad 2.11$$

where

$$\langle pq|\hat{O}_2|rs \rangle = (pr|\hat{O}_2|qs) = \iint d\mathbf{x}_1 \, d\mathbf{x}_2 \, \varphi_p^*(\mathbf{x}_1)\varphi_r(\mathbf{x}_1)\hat{O}_2(\mathbf{x}_1, \mathbf{x}_2)\varphi_q^*(\mathbf{x}_2)\varphi_s(\mathbf{x}_2). \quad 2.12$$

The expressions can be further simplified by introducing so-called field operators[104]

$$\hat{\Psi}(\mathbf{x}) = \sum_p \varphi_p(\mathbf{x}) \, \hat{a}_p \qquad 2.13$$

$$\hat{\Psi}^\dagger(\mathbf{x}) = \sum_p \varphi_p^*(\mathbf{x}) \, \hat{a}_p^\dagger, \qquad 2.14$$

which linearly combine the creation and annihilation operators using the one-particle states as coefficients and satisfy the following anticommutation relations:[104]

$$\left\{ \hat{\Psi}(\mathbf{x}_1), \hat{\Psi}^\dagger(\mathbf{x}_2) \right\} = \hat{\Psi}(\mathbf{x}_1)\hat{\Psi}^\dagger(\mathbf{x}_2) + \hat{\Psi}^\dagger(\mathbf{x}_2)\hat{\Psi}(\mathbf{x}_1) = \delta(\mathbf{x}_1 - \mathbf{x}_2) \qquad 2.15$$

$$\left\{ \hat{\Psi}(\mathbf{x}_1), \hat{\Psi}(\mathbf{x}_2) \right\} = \left\{ \hat{\Psi}^\dagger(\mathbf{x}_1), \hat{\Psi}^\dagger(\mathbf{x}_2) \right\} = 0, \qquad 2.16$$

where $\delta(\mathbf{x}_1 - \mathbf{x}_2)$ is the Dirac delta function. The one- and two-particle operators are then given by[104]

$$\hat{O}_1 = \int d\mathbf{x} \, \hat{\Psi}^\dagger(\mathbf{x})\hat{O}_1(\mathbf{x})\hat{\Psi}(\mathbf{x}) \qquad 2.17$$

$$\hat{O}_2 = \frac{1}{2} \iint d\mathbf{x}_1 \, d\mathbf{x}_2 \, \hat{\Psi}^\dagger(\mathbf{x}_1)\hat{\Psi}^\dagger(\mathbf{x}_2)\hat{O}_2(\mathbf{x}_1, \mathbf{x}_2)\hat{\Psi}(\mathbf{x}_2)\hat{\Psi}(\mathbf{x}_1). \qquad 2.18$$

The form of the operators in Equations 2.17 and 2.18 appears to be very similar to the expressions for taking their expectation values with respect to $|\Psi\rangle$. However, as mentioned above, $\hat{\Psi}$ and $\hat{\Psi}^\dagger$ are operators not wave functions. Further, it is to be noted that in second quantization the operators of first quantization are just coefficients and the fields are the operators. Hence the name *second quantization*.

2.3 The Hartree–Fock Approximation

As mentioned in Chapter 1, there are two main avenues to approach the numerical solution of the time-independent Schrödinger equation: wave-function-based methods and density functional theory. The simplest wave-function method used to date is the Hartree–Fock (HF) method,[105–107] which also forms the basis of more sophisticated wave-function methods. The HF method uses the exact Hamiltonian $\hat{H}$, but approximates the wave function as a single Slater determinant.

In second quantization, the energy expression — given by the expectation value of the Hamiltonian — is obtained according to

$$\langle \Phi_0|\hat{H}|\Phi_0\rangle = \sum_{pq} \langle p|\hat{h}|q\rangle \langle \Phi_0|\hat{a}_p^\dagger \hat{a}_q|\Phi_0\rangle + \frac{1}{2}\sum_{pqrs} \langle pq|rs\rangle \langle \Phi_0|\hat{a}_p^\dagger \hat{a}_q^\dagger \hat{a}_s \hat{a}_r|\Phi_0\rangle \quad 2.19$$

$$= \sum_i^{N_{occ}} \langle i|\hat{h}|i\rangle + \frac{1}{2}\sum_{ij}^{N_{occ}} \langle ij||ij\rangle = \sum_i^{N_{occ}} (i|\hat{h}|i) + \frac{1}{2}\sum_{ij}^{N_{occ}} (ii||jj), \quad 2.20$$

where N_{occ} denotes the number of occupied orbitals and

$$\hat{h} = -\frac{1}{2}\nabla_1^2 - \sum_A^{N_{atoms}} \frac{Z_A}{r_{1A}} \quad 2.21$$

$$\langle ij|ij\rangle = (ii|jj) = \iint d\mathbf{x}_1 d\mathbf{x}_2 \ \varphi_i^*(\mathbf{x}_1)\varphi_i(\mathbf{x}_1)\frac{1}{r_{12}}\varphi_j^*(\mathbf{x}_2)\varphi_j(\mathbf{x}_2) \quad 2.22$$

$$\langle ij||ij\rangle = \langle ij|ij\rangle - \langle ij|ji\rangle. \quad 2.23$$

Minimization with respect to the one-particle functions φ_i under the orthonormality-constraint yields, after unitary transformation, the well-known canonical HF equations[108]

$$\hat{F}\varphi_i(\mathbf{x}_1) = \varepsilon_i\varphi_i(\mathbf{x}_1), \quad 2.24$$

with the Fock operator

$$\hat{F} = \hat{h} + \sum_j^{N_{occ}} \left[\hat{J}_j - \hat{K}_j\right], \quad 2.25$$

where the Coulomb operator $\hat{J}$ and the exchange operator $\hat{K}$ are defined as

$$\hat{J}_j\varphi_i(\mathbf{x}_1) = \int d\mathbf{x}_2 \ \varphi_i(\mathbf{x}_1)\frac{1}{r_{12}}\varphi_j^*(\mathbf{x}_2)\varphi_j(\mathbf{x}_2) \quad 2.26$$

$$\hat{K}_j \varphi_i(\mathbf{x}_1) = \int \mathrm{d}\mathbf{x}_2 \, \varphi_j(\mathbf{x}_1) \frac{1}{r_{12}} \varphi_j^*(\mathbf{x}_2) \varphi_i(\mathbf{x}_2). \qquad 2.27$$

Introduction of (atomic) basis functions leads to the Roothaan–Hall[109,110] equation

$$\mathbf{FC} = \mathbf{SC}\varepsilon, \qquad 2.28$$

which can be solved by orthogonalization of the basis functions followed by a diagonalization.

Although same-spin electrons are correlated to some extent in this simple method, due to the effect of the exchange operator and the resulting exchange-hole around each electron, there are still important correlation-effects missing in the description. In the next sections, approaches are presented, which try to go beyond that and account for correlation effects of all kinds.

2.4 Kohn–Sham Density Functional Theory

A more pragmatic way to approximate the solution of the Schrödinger equation, which goes beyond the HF approximation, is density functional theory. As the name suggests, the central quantity in DFT is the (electron) density

$$\rho(\mathbf{r}) = N_{el} \int\!\!\int \dots \int \mathrm{d}\sigma_1 \mathrm{d}\mathbf{x}_2 \dots \mathrm{d}\mathbf{x}_{N_{el}} \Psi^*(\mathbf{x}_1, \mathbf{x}_2, \dots, \mathbf{x}_{N_{el}}) \Psi(\mathbf{x}_1, \mathbf{x}_2, \dots, \mathbf{x}_{N_{el}}), \qquad 2.29$$

which is used to describe the probability of finding one of the N_{el} electrons in a volume element $\mathrm{d}\mathbf{r}$ at $\mathbf{r}$ according to $\rho(\mathbf{r})\mathrm{d}\mathbf{r}$. The legitimation for the use of the density as the central quantity is given by the first Hohenberg–Kohn theorem,[111] which states that there is a one-to-one mapping between the external potential $v_{ext}(\mathbf{r})$ — typically given by the electrostatic potentials of the nuclei — and the ground-state density. Since the external potential of a non-degenerate ground-state (together with the number of electrons) uniquely determines the ground-state wave function, the ground-state wave function is a unique functional of the ground-state density

$$\Psi_0(\mathbf{x}_1, \mathbf{x}_2, \dots, \mathbf{x}_{N_{el}}) = \Psi[\rho_0]. \qquad 2.30$$

Therefore, the ground-state expectation value of *any* observable is also a functional of the density[112]

$$O[\rho_0] = \langle \Psi[\rho_0] || \hat{O} | \Psi[\rho_0] \rangle, \qquad 2.31$$

with the ground-state energy being the most important one:

$$E[\rho_0] = \langle \Psi[\rho_0] || \hat{H} | \Psi[\rho_0] \rangle . \qquad 2.32$$

Equation 2.32 further implies that the variational principle is valid

$$E[\rho_0] = \langle \Psi[\rho_0] || \hat{H} | \Psi[\rho_0] \rangle \leqslant \langle \Psi[\rho'] || \hat{H} | \Psi[\rho'] \rangle = E[\rho'], \qquad 2.33$$

where ρ' denotes a trial density, and is known as the second Hohenberg–Kohn theorem.

While it is very appealing to replace the highly complicated $4N_{el}$-dimensional wave function by the 3-dimensional electron density, the exact density functional is unknown and accurately approximating it has shown to be extremely challenging. The general energy expression in terms of the density is given by

$$E[\rho] = T[\rho] + V_{ee}[\rho] + E_{ext}[\rho], \qquad 2.34$$

where $T[\rho]$ denotes the (correlated) kinetic energy, $V_{ee}[\rho]$ denotes the electron-electron interaction energy, and $E_{ext}[\rho]$ denotes the potential energy. In fact, even expressing the kinetic energy only in terms of the density showed to be problematic. In their groundbreaking work, Kohn and Sham[4] circumvented that problem by introducing single-particle functions $\phi_i(\mathbf{r})$ — the Kohn–Sham orbitals — stemming from a noninteracting local and multiplicative potential $v_{KS}(\mathbf{r})$ — the Kohn–Sham potential — to DFT, which yield the exact ground-state density according to

$$\rho_0(\mathbf{r}) = \sum_i^{N_{occ}} \phi_i^*(\mathbf{r}) \phi_i(\mathbf{r}). \qquad 2.35$$

That has the important advantage that the total kinetic energy of a noninteracting system is known exactly (as the sum of the individual kinetic energies of the particles):

$$T_s[\rho] = -\frac{1}{2} \sum_i^{N_{occ}} \int d\mathbf{r}\, \phi_i^*(\mathbf{r}) \nabla_1^2 \phi_i(\mathbf{r}). \qquad 2.36$$

The total energy of the Kohn–Sham approach is then given by

$$E[\rho] = T_s[\rho] + E_{ext}[\rho] + E_H[\rho] + E_{xc}[\rho], \qquad 2.37$$

with

$$E_{ext}[\rho] = \int d\mathbf{r} \, \rho(\mathbf{r}) v_{ext}(\mathbf{r}) \qquad 2.38$$

$$E_H[\rho] = \frac{1}{2} \iint d\mathbf{r}_1 \, d\mathbf{r}_2 \, \frac{\rho(\mathbf{r}_1)\rho(\mathbf{r}_2)}{r_{12}} \qquad 2.39$$

$$E_{xc}[\rho] = T[\rho] - T_s[\rho] + V_{ee}[\rho] - E_H[\rho], \qquad 2.40$$

where $E_H[\rho]$ denotes the Hartree (or classical Coulomb) energy and $E_{xc}[\rho]$ denotes the exchange-correlation energy, which contains all unknown terms and hence constitutes the target of most modern density functional approximations. Minimization of Equation 2.37 with respect to the KS orbitals yields the well-known KS equations[4]

$$\hat{F}_{KS}\phi_i(\mathbf{r}) = \varepsilon_i \phi_i(\mathbf{r}), \qquad 2.41$$

with

$$\hat{F}_{KS} = \hat{T} + v_{KS}(\mathbf{r}) \qquad 2.42$$

$$\hat{T} = -\frac{1}{2}\nabla_1^2 \qquad 2.43$$

$$v_{KS}(\mathbf{r}) = v_H(\mathbf{r}) + v_{xc}(\mathbf{r}) + v_{ext}(\mathbf{r}) \qquad 2.44$$

$$v_H(\mathbf{r}) = \frac{dE_H[\rho]}{d\rho(\mathbf{r})} = \int d\mathbf{r}_2 \, \frac{\rho(\mathbf{r}_2)}{r_{12}} \qquad 2.45$$

$$v_{xc}(\mathbf{r}) = \frac{dE_{xc}[\rho]}{d\rho(\mathbf{r})}, \qquad 2.46$$

where $v_H(\mathbf{r})$ denotes the Hartree potential and $v_{xc}(\mathbf{r})$ denotes the unknown exchange-correlation potential. One way to find an exact expression for the exchange-correlation functional is described by the adiabatic-connection formalism, which will be discussed in the next section.

2.5 The Adiabatic-Connection Formalism

The adiabatic-connection approach introduced by Langreth and Perdew[24,25] is a way to obtain an exact expression for the unknown exchange-correlation energy in DFT. The central idea is to scale the interaction-strength between the electrons by a single parameter α to smoothly interpolate between the interacting system

$$\hat{H} = -\sum_i^{N_{el}} \frac{1}{2}\nabla_i^2 + \int d\mathbf{r}\, \hat{\rho}(\mathbf{r})v_{ext}(\mathbf{r}) + \hat{V}_{ee} \qquad \hat{H}\Psi = E\Psi \qquad\qquad 2.47$$

and the noninteracting system, which is chosen to be the Kohn–Sham system

$$\hat{H}_{KS} = -\sum_i^{N_{el}} \frac{1}{2}\nabla_i^2 + \int d\mathbf{r}\, \hat{\rho}(\mathbf{r})v_{KS}(\mathbf{r}) \qquad \hat{H}_{KS}\Phi_{KS} = E_{KS}\Phi_{KS}, \qquad 2.48$$

where

$$\hat{\rho}(\mathbf{r}) = \hat{\Psi}^\dagger(\mathbf{r})\hat{\Psi}(\mathbf{r}) \qquad\qquad 2.49$$

denotes the one-particle density operator. The Hamiltonian of the system with scaled electron-electron interactions is then given by[33]

$$\hat{H}_\alpha = -\sum_i^{N_{el}} \frac{1}{2}\nabla_i^2 + \int d\mathbf{r}\, \hat{\rho}(\mathbf{r})v_\alpha(\mathbf{r}) + \alpha\hat{V}_{ee}, \qquad\qquad 2.50$$

with eigenfunctions Ψ_α. In Equation 2.50, $v_\alpha(\mathbf{r})$ is a local multiplicative potential, which equals the external potential $v_{ext}(\mathbf{r})$ and the KS potential $v_{KS}(\mathbf{r})$ for $\alpha = 1$ and $\alpha = 0$, respectively, and is further constrained to keep the electron-density fixed for all values of α.

To obtain an expression for the exchange-correlation energy, the difference between the ground-state energy of the interacting and the noninteracting system is expressed in terms of an integral along the adiabatic-connection path according to[113]

$$E_0^{\alpha=1} - E_0^{\alpha=0} = \int_0^1 d\alpha\, \frac{\partial E_0(\alpha)}{\partial\alpha} = \int_0^1 d\alpha\, \frac{\partial\langle\Psi_0^\alpha|\hat{H}_\alpha|\Psi_0^\alpha\rangle}{\partial\alpha}. \qquad\qquad 2.51$$

Using the Hellmann–Feynman theorem[114]

$$\frac{\partial \langle \Psi_0^\alpha | \hat{H}_\alpha | \Psi_0^\alpha \rangle}{\partial \alpha} = \langle \Psi_0^\alpha | \frac{\partial \hat{H}_\alpha}{\partial \alpha} | \Psi_0^\alpha \rangle \qquad 2.52$$

yields

$$E_0^{\alpha=1} - E_0^{\alpha=0} = \int_0^1 d\alpha \ \langle \Psi_0^\alpha | \hat{V}_{ee} + \int d\mathbf{r} \ \hat{\rho}(\mathbf{r}) \frac{\partial v_\alpha(\mathbf{r})}{\partial \alpha} | \Psi_0^\alpha \rangle . \qquad 2.53$$

Since $v_\alpha(\mathbf{r})$ is local and multiplicative and the density is kept fixed along the adiabatic-connection path, it follows that

$$E_0^{\alpha=1} - E_0^{\alpha=0} = \int_0^1 d\alpha \ \langle \Psi_0^\alpha | \hat{V}_{ee} | \Psi_0^\alpha \rangle + \int d\mathbf{r} \ \rho(\mathbf{r}) v_{ext}(\mathbf{r}) - \int d\mathbf{r} \ \rho(\mathbf{r}) v_{KS}(\mathbf{r}). \qquad 2.54$$

Using Equation 2.38 for the potential energy and

$$E_0^{\alpha=0} - \int d\mathbf{r} \ \rho(\mathbf{r}) v_{KS}(\mathbf{r}) = T_s[\rho] \qquad 2.55$$

yields

$$E_0^{\alpha=1} = T_s[\rho] + E_{ext}[\rho] + \int_0^1 d\alpha \ \langle \Psi_0^\alpha | \hat{V}_{ee} | \Psi_0^\alpha \rangle . \qquad 2.56$$

Comparing this result with Equation 2.37 reveals that

$$\int_0^1 d\alpha \ \langle \Psi_0^\alpha | \hat{V}_{ee} | \Psi_0^\alpha \rangle = E_{xc}[\rho] + E_H[\rho] \qquad 2.57$$

and hence

$$E_{xc}[\rho] = \int_0^1 d\alpha \ \langle \Psi_0^\alpha | \hat{V}_{ee} | \Psi_0^\alpha \rangle - E_H[\rho]. \qquad 2.58$$

Since the expression for the exchange energy E_x is known exactly in terms of non-interacting single-particle functions from Hartree–Fock theory — as is the Hartree energy E_H — it can be subtracted from Equation 2.58 to yield the remaining correlation energy[33]

$$E_c[\rho] = \int_0^1 d\alpha \ \langle \Psi_0^\alpha | \hat{V}_{ee} | \Psi_0^\alpha \rangle - E_H[\rho] - E_x[\rho] \qquad 2.59$$

$$= \int_0^1 d\alpha \ \langle \Psi_0^\alpha | \hat{V}_{ee} | \Psi_0^\alpha \rangle - \langle \Phi_0^{KS} | \hat{V}_{ee} | \Phi_0^{KS} \rangle . \qquad 2.60$$

Although the derivation of an exact expression for the correlation energy is a great achievement, Equation 2.60 is of no practical use. In the next section, the adiabatic-connection fluctuation-dissipation framework is established, which allows to reformulate Equation 2.60 in terms of density-density linear response functions known from TDDFT and hence constitutes a further step towards the efficient evaluation of the electron-correlation energy.

2.6 The Adiabatic-Connection Fluctuation-Dissipation Theorem

The adiabatic-connection fluctuation-dissipation theorem (ACFDT)[24,25] provides a way to use time-dependent DFT[58] — a successful tool to describe excited state properties — in the description of the ground state. To establish the connection to TDDFT, the electron-electron interaction operator $\hat{V}_{ee}$ is expressed in second quantization (cf. Equation 2.18) as

$$\hat{V}_{ee} = \frac{1}{2} \iint d\mathbf{x}_1 d\mathbf{x}_2 \; \frac{\hat{\Psi}^\dagger(\mathbf{x}_1)\hat{\Psi}^\dagger(\mathbf{x}_2)\hat{\Psi}(\mathbf{x}_2)\hat{\Psi}(\mathbf{x}_1)}{r_{12}} \qquad 2.61$$

$$= \iint d\mathbf{x}_1 d\mathbf{x}_2 \; \frac{\hat{P}(\mathbf{x}_1, \mathbf{x}_2)}{r_{12}}, \qquad 2.62$$

where $\hat{P}(\mathbf{x}_1, \mathbf{x}_2) = \frac{1}{2}\hat{\Psi}^\dagger(\mathbf{x}_1)\hat{\Psi}^\dagger(\mathbf{x}_2)\hat{\Psi}(\mathbf{x}_2)\hat{\Psi}(\mathbf{x}_1)$ is the two-particle density operator. Using the anticommutation rules of the field operators, the two-particle density operator can be rewritten according to[33]

$$\hat{P}(\mathbf{x}_1, \mathbf{x}_2) = \frac{1}{2}(\hat{\rho}(\mathbf{x}_1)\hat{\rho}(\mathbf{x}_2) - \delta(\mathbf{x}_1 - \mathbf{x}_2)\hat{\rho}(\mathbf{x}_1)). \qquad 2.63$$

In the next step, the density-fluctuation operator[33]

$$\Delta\hat{\rho}(\mathbf{x}) = \hat{\rho}(\mathbf{x}) - \rho(\mathbf{x}) \qquad 2.64$$

is introduced, yielding

$$\hat{P}(\mathbf{x}_1, \mathbf{x}_2) = \frac{1}{2}(\Delta\hat{\rho}(\mathbf{x}_1)\Delta\hat{\rho}(\mathbf{x}_2) + \Delta\hat{\rho}(\mathbf{x}_1)\rho(\mathbf{x}_2) + \rho(\mathbf{x}_1)\Delta\hat{\rho}(\mathbf{x}_2) + \rho(\mathbf{x}_1)\rho(\mathbf{x}_2)$$
$$- \delta(\mathbf{x}_1 - \mathbf{x}_2)\hat{\rho}(\mathbf{x}_1)). \qquad 2.65$$

Using Equation 2.65 in the expression for the electron-electron interaction operator (Equation 2.62) and subsequently inserting it into the electron-correlation functional (Equation 2.60) yields[33]

$$E_c = \frac{1}{2}\int_0^1 d\alpha \iint d\mathbf{x}_1 d\mathbf{x}_2 \frac{\langle\Psi_0^\alpha|\Delta\hat{\rho}(\mathbf{x}_1)\Delta\hat{\rho}(\mathbf{x}_2)|\Psi_0^\alpha\rangle - \langle\Phi_0^{KS}|\Delta\hat{\rho}(\mathbf{x}_1)\Delta\hat{\rho}(\mathbf{x}_2)|\Phi_0^{KS}\rangle}{r_{12}}$$
$$2.66$$

since all one-electrons terms cancel due to the constancy of the density along the adiabatic-connection path. It is worthwhile to note that — as can be seen in Equation 2.65 — the difference between the Hartree approximation to the two-particle density and the exact two-particle density solely amounts to the correction of the self-interaction (last term in Equation 2.65) and quantum fluctuations about the expectation value of the density. Therefore, quantum fluctuations give rise to quantum correlations between interacting particles, which rationalizes the result of Equation 2.66.

Now that the correlation energy is expressed solely in terms of density fluctuations, the connection to time-dependent linear response theory can be established. To that end, the expectation value of the product of density-fluctuation operators is transformed into a sum of products of density-fluctuation operator expectation values using the completeness of the space spanned by the states $|\Psi_n^\alpha\rangle$

$$\sum_n |\Psi_n^\alpha\rangle\langle\Psi_n^\alpha| = \hat{1} \qquad 2.67$$

according to[33]

$$\langle\Psi_0^\alpha|\Delta\hat{\rho}(\mathbf{x}_1)\Delta\hat{\rho}(\mathbf{x}_2)|\Psi_0^\alpha\rangle = \sum_n \langle\Psi_0^\alpha|\Delta\hat{\rho}(\mathbf{x}_1)|\Psi_n^\alpha\rangle\langle\Psi_n^\alpha|\Delta\hat{\rho}(\mathbf{x}_2)|\Psi_0^\alpha\rangle. \qquad 2.68$$

Using that the ground-state expectation value of the density-fluctuation operator is zero

$$\langle\Psi_0^\alpha|\Delta\hat{\rho}(\mathbf{x}_1)|\Psi_0^\alpha\rangle = 0 \qquad 2.69$$

and introducing the transition densities[33]

$$\rho_{0n}^{\alpha}(\mathbf{x}) = \langle \Psi_0^{\alpha} | \Delta \hat{\rho}(\mathbf{x}) | \Psi_n^{\alpha} \rangle = \langle \Psi_0^{\alpha} | \hat{\rho}(\mathbf{x}) | \Psi_n^{\alpha} \rangle \qquad 2.70$$

yields

$$\langle \Psi_0^{\alpha} | \Delta \hat{\rho}(\mathbf{x}_1) \Delta \hat{\rho}(\mathbf{x}_2) | \Psi_0^{\alpha} \rangle = \sum_{n \neq 0} \rho_{0n}^{\alpha}(\mathbf{x}_1) \rho_{n0}^{\alpha}(\mathbf{x}_2). \qquad 2.71$$

Next, the Lehmann representation[115] of the (density-density linear) response function known from TDDFT is considered:[116]

$$\chi_{\alpha}(\mathbf{x}_1, \mathbf{x}_2, \omega) = \lim_{\eta \to 0^+} \sum_{n \neq 0} \left[\frac{\rho_{0n}^{\alpha}(\mathbf{x}_1) \rho_{n0}^{\alpha}(\mathbf{x}_2)}{\omega - \Omega_{0n}^{\alpha} + \mathrm{i}\eta} - \frac{\rho_{0n}^{\alpha}(\mathbf{x}_2) \rho_{n0}^{\alpha}(\mathbf{x}_1)}{\omega + \Omega_{0n}^{\alpha} + \mathrm{i}\eta} \right], \qquad 2.72$$

where ω is the frequency of the perturbing potential, $\Omega_{0n}^{\alpha} = E_n^{\alpha} - E_0^{\alpha}$ are the excitation energies, and η shifts the poles occurring at $\omega = \pm \Omega_{0n}^{\alpha}$ away from the real axis. Since for real wave functions

$$\rho_{0n}^{\alpha}(\mathbf{x}) = \rho_{n0}^{\alpha}(\mathbf{x}) \qquad 2.73$$

holds true, the two terms in Equation 2.72 can be combined to yield

$$\chi_{\alpha}(\mathbf{x}_1, \mathbf{x}_2, \omega) = \sum_{n \neq 0} \frac{2\Omega_{0n}^{\alpha}}{\omega^2 - (\Omega_{0n}^{\alpha})^2} \rho_{0n}^{\alpha}(\mathbf{x}_1) \rho_{0n}^{\alpha}(\mathbf{x}_2) \qquad 2.74$$

after setting η to zero. To avoid the poles, a switch from real to imaginary frequencies is employed, yielding[117]

$$\chi_{\alpha}(\mathbf{x}_1, \mathbf{x}_2, \mathrm{i}\omega) = \sum_{n \neq 0} \frac{-2\Omega_{0n}^{\alpha}}{\omega^2 + (\Omega_{0n}^{\alpha})^2} \rho_{0n}^{\alpha}(\mathbf{x}_1) \rho_{0n}^{\alpha}(\mathbf{x}_2). \qquad 2.75$$

Since the excitations are always positive ($\Omega_{0n}^{\alpha} > 0$) and

$$\int_0^{\infty} \mathrm{d}\omega \frac{a}{a^2 + \omega^2} = \frac{\pi}{2} \qquad \forall a > 0, \qquad 2.76$$

the following relation is obtained:[33]

$$-\frac{1}{2\pi} \int_0^{\infty} \mathrm{d}\omega \, \chi_{\alpha}(\mathbf{x}_1, \mathbf{x}_2, \mathrm{i}\omega) = \frac{1}{2} \sum_{n \neq 0} \rho_{0n}^{\alpha}(\mathbf{x}_1) \rho_{0n}^{\alpha}(\mathbf{x}_2) = \frac{1}{2} \langle \Psi_0^{\alpha} | \Delta \hat{\rho}(\mathbf{x}_1) \Delta \hat{\rho}(\mathbf{x}_2) | \Psi_0^{\alpha} \rangle.$$

$$2.77$$

19

Equation 2.77 relates internal density fluctuations to the response function in the imaginary-frequency domain and is known as the *zero-temperature fluctuation-dissipation theorem*.[26] Combining Equation 2.77 with the adiabatic-connection expression (Equation 2.66) yields

$$E_c = -\frac{1}{2\pi} \int_0^1 d\alpha \int_0^\infty d\omega \iint d\mathbf{x}_1 \, d\mathbf{x}_2 \, \frac{\chi_\alpha(\mathbf{x}_1, \mathbf{x}_2, i\omega) - \chi_{KS}(\mathbf{x}_1, \mathbf{x}_2, i\omega)}{r_{12}}, \qquad 2.78$$

which is called the *adiabatic-connection fluctuation-dissipation theorem*.[24,25]

The question is now: How to obtain the response functions of all the systems with scaled electron-electron interactions along the adiabatic-connection path? This question will be addressed in the next section.

2.7 Density-Density Linear Response Functions

The response of the density to a small perturbation $\delta v_{\text{ext}}(\mathbf{x}, \omega)$ with frequency ω can be expressed by a Taylor series with respect to $\delta v_{\text{ext}}(\mathbf{x}, \omega)$ according to[116]

$$\rho(\mathbf{x}, \omega) = \rho^{(0)}(\mathbf{x}) + \rho^{(1)}(\mathbf{x}, \omega) + \rho^{(2)}(\mathbf{x}, \omega) + \dots. \qquad 2.79$$

In the following, only the linear response

$$\rho^{(1)}(\mathbf{x}_1, \omega) = \int d\mathbf{x}_2 \chi(\mathbf{x}_1, \mathbf{x}_2, \omega) \delta v_{\text{ext}}(\mathbf{x}_2, \omega) \qquad 2.80$$

is considered. Note that Equation 2.80 is for the interacting system. However, since the exact time-dependent density $\rho(\mathbf{x}, t)$ can also be computed from a noninteracting time-dependent effective one-particle potential — the time-dependent KS potential — the same is true for the first-order change of the density[116]

$$\rho^{(1)}(\mathbf{x}_1, \omega) = \int d\mathbf{x}_2 \chi_{KS}(\mathbf{x}_1, \mathbf{x}_2, \omega) \delta v_{KS}(\mathbf{x}_2, \omega), \qquad 2.81$$

where $\delta v_{\mathrm{KS}}(\mathbf{x}_2, \omega)$ denotes the first-order change in the time-dependent KS potential (formulated in the frequency domain). Since for the noninteracting system the excitation energies are simply the KS orbital energy differences $\Omega_{ia}^{\mathrm{KS}} = \varepsilon_a - \varepsilon_i$ and for real KS orbitals the transition densities are trivially given by[33,36]

$$\rho_{ia}^{\mathrm{KS}}(\mathbf{x}) = \phi_i(\mathbf{x})\phi_a(\mathbf{x}), \tag{2.82}$$

the KS response function can be expressed exactly according to

$$\chi_{\mathrm{KS}}(\mathbf{x}_1, \mathbf{x}_2, \omega) = \sum_i^{N_{\mathrm{occ}}} \sum_a^{N_{\mathrm{virt}}} \frac{2(\varepsilon_a - \varepsilon_i)\phi_i(\mathbf{x}_1)\phi_a(\mathbf{x}_1)\phi_i(\mathbf{x}_2)\phi_a(\mathbf{x}_2)}{\omega^2 - (\varepsilon_a - \varepsilon_i)^2}, \tag{2.83}$$

where N_{virt} denotes the number of virtual (unoccupied) orbitals. However, the change in the time-dependent KS potential given by[116]

$$\delta v_{\mathrm{KS}}(\mathbf{x}_1, \omega) = \delta v_{\mathrm{ext}}(\mathbf{x}_1, \omega) + \int \mathrm{d}\mathbf{x}_2 \frac{\rho^{(1)}(\mathbf{x}_2, \omega)}{r_{12}} + \int \mathrm{d}\mathbf{x}_2 f_{\mathrm{xc}}(\mathbf{x}_1, \mathbf{x}_2, \omega)\rho^{(1)}(\mathbf{x}_2, \omega), \tag{2.84}$$

where $f_{\mathrm{xc}}(\mathbf{x}_1, \mathbf{x}_2, \omega)$ denotes the frequency-dependent exchange-correlation kernel, which is the Fourier transform of

$$f_{\mathrm{xc}}(\mathbf{x}_1, t_1, \mathbf{x}_2, t_2) = \frac{\partial v_{\mathrm{xc}}(\mathbf{x}_1, t_1)}{\partial \rho(\mathbf{x}_2, t_2)}, \tag{2.85}$$

is unknown since the exchange-correlation potential and hence also its change with respect to the density are unknown. Combining Equations 2.80, 2.81, and 2.84 yields the Dyson-like equation for the interacting response function in real space:[118]

$$\chi(\mathbf{x}_1, \mathbf{x}_2, \omega) = \chi_{\mathrm{KS}}(\mathbf{x}_1, \mathbf{x}_2, \omega)$$
$$+ \iint \mathrm{d}\mathbf{x}_3 \mathrm{d}\mathbf{x}_4 \chi_{\mathrm{KS}}(\mathbf{x}_1, \mathbf{x}_3, \omega) \left[\frac{1}{r_{34}} + f_{\mathrm{xc}}(\mathbf{x}_3, \mathbf{x}_4, \omega) \right] \chi(\mathbf{x}_4, \mathbf{x}_2, \omega). \tag{2.86}$$

Since in quantum chemistry it is more common to work with matrices in the molecular-orbital or particle-hole space instead of the real space, Equation 2.86 is rewritten according to

$$\mathbf{\Pi}(\omega) = \mathbf{\Pi}_{\mathrm{KS}}(\omega) + \mathbf{\Pi}_{\mathrm{KS}}(\omega) \left[\mathbf{V} + \mathbf{F}_{\mathrm{xc}}(\omega) \right] \mathbf{\Pi}(\omega), \tag{2.87}$$

with

$$\Pi^{\text{KS}}_{ia,jb}(\omega) = \delta_{ij}\delta_{ab}\frac{2(\varepsilon_a - \varepsilon_i)}{\omega^2 - (\varepsilon_a - \varepsilon_i)^2} \tag{2.88}$$

$$V_{ia,jb} = (ia|jb) \tag{2.89}$$

$$F^{\text{xc}}_{ia,jb}(\omega) = \iint d\mathbf{x}_1\,d\mathbf{x}_2\,\phi_i(\mathbf{x}_1)\phi_a(\mathbf{x}_1)f_{\text{xc}}(\mathbf{x}_1,\mathbf{x}_2,\omega)\phi_j(\mathbf{x}_2)\phi_b(\mathbf{x}_2). \tag{2.90}$$

As mentioned before, the exchange-correlation kernel is unknown and hence approximations are necessary to compute the interacting response function. The simplest approximation in this regard is to neglect the exchange-correlation kernel completely and keep only the known Hartree kernel $\mathbf{V}$:

$$\mathbf{\Pi}_{\text{RPA}}(\omega) = \mathbf{\Pi}_{\text{KS}}(\omega) + \mathbf{\Pi}_{\text{KS}}(\omega)\mathbf{V}\mathbf{\Pi}_{\text{RPA}}(\omega). \tag{2.91}$$

This approximation is called the *random phase approximation* and is the reason why it is sometimes also referred to as the Hartree approximation within TDDFT.[7,59] Note, however, that the derivation shown until now is not just a complicated way to shift the problem of approximating the exchange-correlation potential to the problem of approximating the exchange-correlation kernel since in the random phase approximation important physical phenomena like dispersion interactions are already captured.[7,59,119]

The next section is dedicated to the derivation of actual working equations based on the random phase approximation, implemented in modern quantum chemistry program packages.

2.8 Random-Phase-Approximation Methods

2.8.1 Plasmon Formula

The derivation of the plasmon formula[36] presented here starts from an expression of the correlation energy in terms of transition densities (combination of Equations 2.66 and 2.71) given by

$$E_c = \frac{1}{2} \int_0^1 d\alpha \sum_{n \neq 0} \iint d\mathbf{x}_1 d\mathbf{x}_2 \frac{\rho_{0n}^{\alpha}(\mathbf{x}_1)\rho_{n0}^{\alpha}(\mathbf{x}_2) - \rho_{0n}^{KS}(\mathbf{x}_1)\rho_{n0}^{KS}(\mathbf{x}_2)}{r_{12}}. \qquad 2.92$$

In order to obtain the transition densities for the systems with scaled electron-electron interactions, a generalization of Equation 2.91 to the interacting density-matrix density-matrix linear response function (also called retarded polarization propagator)[7] is considered:[35,91,120]

$$\underline{\underline{\mathbf{\Pi}}}_{r,RPA}^{\alpha}(\omega) = \underline{\underline{\mathbf{\Pi}}}_{KS}(\omega) + \underline{\underline{\mathbf{\Pi}}}_{KS}(\omega)\alpha\underline{\underline{\mathbf{V}}}\,\underline{\underline{\mathbf{\Pi}}}_{r,RPA}^{\alpha}(\omega), \qquad 2.93$$

with

$$\underline{\underline{\mathbf{\Pi}}}_{KS}(\omega) = \begin{pmatrix} -(\mathbf{\Omega}^{KS} - \omega\mathbf{1})^{-1} & \mathbf{0} \\ \mathbf{0} & -(\mathbf{\Omega}^{KS} + \omega\mathbf{1})^{-1} \end{pmatrix} \qquad 2.94$$

$$\Omega_{ia,jb}^{KS} = \delta_{ij}\delta_{ab}\Omega_{ia}^{KS} \qquad 2.95$$

$$\underline{\underline{\mathbf{V}}} = \begin{pmatrix} \mathbf{V} & \mathbf{V} \\ \mathbf{V} & \mathbf{V} \end{pmatrix}, \qquad 2.96$$

where $\underline{\underline{\mathbf{\Pi}}}_{KS}(\omega)$ denotes the KS polarization propagator. Equation 2.93 is called the Bethe–Salpeter equation.[121] Rearranging Equation 2.93 yields

$$(\underline{\underline{\mathbf{1}}} - \underline{\underline{\mathbf{\Pi}}}_{KS}(\omega)\alpha\underline{\underline{\mathbf{V}}})\underline{\underline{\mathbf{\Pi}}}_{r,RPA}^{\alpha}(\omega) = \underline{\underline{\mathbf{\Pi}}}_{KS}(\omega) \qquad 2.97$$

$$\left[\underline{\underline{\mathbf{\Pi}}}_{r,RPA}^{\alpha}(\omega)\right]^{-1} = \underline{\underline{\mathbf{\Pi}}}_{KS}^{-1}(\omega) - \alpha\underline{\underline{\mathbf{V}}} \qquad 2.98$$

and hence

$$\underline{\underline{\mathbf{\Pi}}}_{r,RPA}^{\alpha}(\omega) = \left[\underline{\underline{\mathbf{\Pi}}}_{KS}^{-1}(\omega) - \alpha\underline{\underline{\mathbf{V}}}\right]^{-1}. \qquad 2.99$$

As mentioned above, the response function and thus also the polarization propagator diverge when the frequency ω equals an excitation energy Ω_{0n}^{α}. Considering Equation 2.99 it follows that for these frequencies the eigenvalues of $\left[\underline{\underline{\mathbf{\Pi}}}_{\mathrm{KS}}^{-1}(\omega) - \alpha\underline{\underline{\mathbf{V}}}\right]$ equal zero, leading to

$$\left[\underline{\underline{\mathbf{\Pi}}}_{\mathrm{KS}}^{-1}(\Omega_{0n}^{\alpha}) - \alpha\underline{\underline{\mathbf{V}}}\right] \begin{pmatrix} \mathbf{X}_{0n}^{\alpha} \\ \mathbf{Y}_{0n}^{\alpha} \end{pmatrix} = 0. \tag{2.100}$$

Equation 2.100 can then be rewritten to yield the well-known RPA eigenvalue problem[27,122]

$$\left[\begin{pmatrix} \mathbf{A}_{\alpha} & \mathbf{B}_{\alpha} \\ \mathbf{B}_{\alpha} & \mathbf{A}_{\alpha} \end{pmatrix} - \Omega_{0n}^{\alpha} \begin{pmatrix} \mathbf{1} & \mathbf{0} \\ \mathbf{0} & -\mathbf{1} \end{pmatrix}\right] \begin{pmatrix} \mathbf{X}_{0n}^{\alpha} \\ \mathbf{Y}_{0n}^{\alpha} \end{pmatrix} = 0, \tag{2.101}$$

with $\mathbf{X}_{0n}^{\alpha}$ and $\mathbf{Y}_{0n}^{\alpha}$ denoting the transition vectors and

$$A_{ia,jb}^{\alpha} = \delta_{ij}\delta_{ab}(\varepsilon_a - \varepsilon_i) + \alpha V_{ia,jb} \tag{2.102}$$

$$B_{ia,jb}^{\alpha} = \alpha V_{ia,jb}. \tag{2.103}$$

With the transition vectors at hand, the transition densities can be expanded in terms of KS orbital products according to[36]

$$\rho_{0n}^{\alpha}(\mathbf{x}) = \sum_{i}^{N_{\mathrm{occ}}} \sum_{a}^{N_{\mathrm{virt}}} (\mathbf{X}_{0n}^{\alpha} + \mathbf{Y}_{0n}^{\alpha})_{ia} \phi_i(\mathbf{x})\phi_a(\mathbf{x}). \tag{2.104}$$

Using the shorthand-notation

$$\Lambda_{\alpha} = \begin{pmatrix} \mathbf{A}_{\alpha} & \mathbf{B}_{\alpha} \\ \mathbf{B}_{\alpha} & \mathbf{A}_{\alpha} \end{pmatrix} \tag{2.105}$$

$$\left|\mathbf{X}_{0n}^{\alpha}, \mathbf{Y}_{0n}^{\alpha}\right\rangle = \begin{pmatrix} \mathbf{X}_{0n}^{\alpha} \\ \mathbf{Y}_{0n}^{\alpha} \end{pmatrix}, \tag{2.106}$$

the excitation energies can be expressed as

$$\Omega_{0n}^{\alpha} = \langle \mathbf{X}_{0n}^{\alpha}, \mathbf{Y}_{0n}^{\alpha} | \Lambda_{\alpha} | \mathbf{X}_{0n}^{\alpha}, \mathbf{Y}_{0n}^{\alpha} \rangle. \tag{2.107}$$

According to the Hellmann–Feynman theorem, the derivative of the excitation energy with respect to the coupling-strength is given by[36]

$$\frac{\partial \Omega_{0n}^{\alpha}}{\partial \alpha} = \langle \mathbf{X}_{0n}^{\alpha}, \mathbf{Y}_{0n}^{\alpha} | \frac{\partial \Lambda_{\alpha}}{\partial \alpha} | \mathbf{X}_{0n}^{\alpha}, \mathbf{Y}_{0n}^{\alpha} \rangle \qquad 2.108$$

$$= \iint \mathrm{d}\mathbf{x}_1 \, \mathrm{d}\mathbf{x}_2 \, \frac{\rho_{0n}^{\alpha}(\mathbf{x}_1)\rho_{n0}^{\alpha}(\mathbf{x}_2)}{r_{12}} \qquad 2.109$$

and hence

$$E_{\mathrm{c}}^{\mathrm{RPA}} = \frac{1}{2} \int_0^1 \mathrm{d}\alpha \sum_{n \neq 0} \left[\frac{\partial \Omega_{0n}^{\alpha}}{\partial \alpha} - \frac{\partial \Omega_{0n}^{\alpha}}{\partial \alpha} \Big|_{\alpha=0} \right]. \qquad 2.110$$

The coupling-strength integration can now be performed analytically, resulting in the plasmon formula[36]

$$E_{\mathrm{c}}^{\mathrm{RPA}} = \frac{1}{2} \sum_{n \neq 0} \left[\Omega_{0n} - \Omega_{0n}^{(1)} \right], \qquad 2.111$$

where

$$\Omega_{0n}^{(1)} = \Omega_{0n}^{\mathrm{KS}} + \frac{\partial \Omega_{0n}^{\alpha}}{\partial \alpha} \Big|_{\alpha=0} = (\varepsilon_a - \varepsilon_i) + (ia|ia) \qquad 2.112$$

is a first-order approximation of the RPA excitation energy.

Since this method requires the calculation of the RPA excitation energies obtained by diagonalizing Λ, it shows a prohibitive $O(M^6)$ scaling with respect to the system size. In the next section, a reformulation of RPA using the resolution of the identity and a numerical frequency-integration is presented, which lowers the overall scaling of the method to $O(M^4)$ and in this way greatly increases its applicability.

2.8.2 Molecular-Orbital Resolution-of-the-Identity RPA

Dielectric Matrix Formulation

To derive a RI-based formulation of RPA in the molecular-orbital space, first consider the expression for the response function in the imaginary-frequency domain for a system with scaled electron-electron interactions:

$$\mathbf{\Pi}_{\mathrm{RPA}}^{\alpha}(\mathrm{i}\omega) = \mathbf{\Pi}_{\mathrm{KS}}(\mathrm{i}\omega) + \mathbf{\Pi}_{\mathrm{KS}}(\mathrm{i}\omega)\alpha \mathbf{V} \mathbf{\Pi}_{\mathrm{RPA}}^{\alpha}(\mathrm{i}\omega). \qquad 2.113$$

Rearranging yields

$$\boldsymbol{\Pi}_{\mathrm{RPA}}^{\alpha}(\mathrm{i}\omega) = (\mathbf{1} - \boldsymbol{\Pi}_{\mathrm{KS}}(\mathrm{i}\omega)\alpha\mathbf{V})^{-1}\boldsymbol{\Pi}_{\mathrm{KS}}(\mathrm{i}\omega) \qquad 2.114$$

$$= (\kappa_{\alpha}(\mathrm{i}\omega))^{-1}\boldsymbol{\Pi}_{\mathrm{KS}}(\mathrm{i}\omega), \qquad 2.115$$

where $\kappa_{\alpha}(\mathrm{i}\omega)$ is the matrix representation of the generalized dielectric function,[7] which, from a physical perspective, captures screening effects of the bare KS particle-hole pairs arising from other particle-hole pairs via the Hartree kernel. Inserting Equation 2.114 into Equation 2.78 represented in the particle-hole space gives

$$E_{\mathrm{c}}^{\mathrm{RPA}} = -\frac{1}{2\pi}\int_0^1 \mathrm{d}\alpha \int_0^{\infty} \mathrm{d}\omega\, \mathrm{Tr}\left\{\left[\left[\mathbf{1} - \boldsymbol{\Pi}_{\mathrm{KS}}(\mathrm{i}\omega)\alpha\mathbf{V}\right]^{-1}\boldsymbol{\Pi}_{\mathrm{KS}}(\mathrm{i}\omega) - \boldsymbol{\Pi}_{\mathrm{KS}}(\mathrm{i}\omega)\right]\mathbf{V}\right\},$$

$$2.116$$

where the coupling-strength integration can now be performed analytically to yield[91]

$$E_{\mathrm{c}}^{\mathrm{RPA}} = \frac{1}{2\pi}\int_0^{\infty} \mathrm{d}\omega\, \mathrm{Tr}\left\{\ln(\mathbf{1} - \boldsymbol{\Pi}_{\mathrm{KS}}(\mathrm{i}\omega)\mathbf{V}) + \boldsymbol{\Pi}_{\mathrm{KS}}(\mathrm{i}\omega)\mathbf{V}\right\} \qquad 2.117$$

$$= \frac{1}{2\pi}\int_0^{\infty} \mathrm{d}\omega\, \mathrm{Tr}\left\{\ln(\kappa(\mathrm{i}\omega)) + \boldsymbol{\Pi}_{\mathrm{KS}}(\mathrm{i}\omega)\mathbf{V}\right\}. \qquad 2.118$$

This expression is sometimes also referred to as the dielectric matrix formulation.[91]

Resolution of the Identity

The next step is to introduce the resolution of the identity[123–128] to reduce the order of the electron repulsion integral (ERI) tensor by replacing it with a product of lower-order tensors. In this context, RI is also frequently referred to as density-fitting, although the two approaches — while leading to the same result — are, strictly speaking, not identical since they argue from different perspectives. In the following, the concept will be briefly explained from the density-fitting point of view.

The fourth-order ERI tensor in the atomic-orbital basis is given by

$$V_{\mu\nu,\lambda\sigma} = (\mu\nu|\lambda\sigma), \qquad 2.119$$

where μ, ν, λ, and σ denote atomic orbitals. The basis-function product $|\mu\nu)$ can be seen as a N_{basis}^2-dimensional function space to represent densities (transition densities in case of RPA), where N_{basis} denotes the total number of basis functions.

Fitting this product in the space of auxiliary functions $|M)$ according to

$$|\mu\nu) \approx |\widetilde{\mu\nu}) = \sum_M^{N_{\text{aux}}} |M) \, c_{\mu\nu}^M, \qquad \qquad 2.120$$

with fitting coefficients $c_{\mu\nu}^M$ and N_{aux} denoting the number of auxiliary basis functions, yields for the complete ERI tensor

$$(\mu\nu|\lambda\sigma) \approx (\widetilde{\mu\nu}|\widetilde{\lambda\sigma}) = \sum_{MN}^{N_{\text{aux}}} c_{\mu\nu}^M \, (M|N) \, c_{\lambda\sigma}^N. \qquad \qquad 2.121$$

The fitting coefficients are obtained by minimizing the residual self-repulsion[123]

$$\frac{\partial}{\partial c_{\mu\nu}^M} (\mu\nu - \widetilde{\mu\nu} | m_{12} | \mu\nu - \widetilde{\mu\nu}) \overset{!}{=} 0 \qquad \qquad 2.122$$

in a chosen metric m_{12} and are given by

$$c_{\mu\nu}^M = \sum_N^{N_{\text{aux}}} (\mu\nu | m_{12} | N) \, (N | m_{12} | M)^{-1}, \qquad \qquad 2.123$$

where matrix operations are to be taken before indexing. The final result for the ERI tensor is hence

$$(\mu\nu|\lambda\sigma) \approx (\widetilde{\mu\nu}|\widetilde{\lambda\sigma}) = \sum_{MNPQ}^{N_{\text{aux}}} (\mu\nu | m_{12} | M) \, (M | m_{12} | N)^{-1} \, (N | P) \, (P | m_{12} | Q)^{-1} \, (Q | m_{12} | \lambda\sigma)$$

$$2.124$$

$$= \sum_{MN}^{N_{\text{aux}}} B_{\mu\nu}^M \tilde{V}_{MN} B_{\lambda\sigma}^N, \qquad \qquad 2.125$$

where

$$B_{\mu\nu}^M = (\mu\nu | m_{12} | M) \qquad \qquad 2.126$$

$$\tilde{V}_{MN} = \sum_{PQ}^{N_{\text{aux}}} (M | m_{12} | P)^{-1} \, (P | Q) \, (Q | m_{12} | N)^{-1}. \qquad \qquad 2.127$$

As can be seen in Equation 2.124, using the density-fitting approach, the fourth-order tensor can be factorized into products of second- and third-order tensors, which greatly reduces the computational cost and hence led to extensive use in quantum chemistry.[127–132]

MO-RI-RPA

Using the result of Equation 2.125 to factorize the ERI tensor in the particle-hole space $\mathbf{V}$ in Equation 2.117 gives

$$E_c^{\text{RPA}} = \frac{1}{2\pi} \int_0^\infty d\omega \, \text{Tr} \left\{ \ln(\mathbf{1} - \mathbf{\Pi}_{\text{KS}}(\text{i}\omega)\mathbf{B}\tilde{\mathbf{V}}\mathbf{B}^T) + \mathbf{\Pi}_{\text{KS}}(\text{i}\omega)\mathbf{B}\tilde{\mathbf{V}}\mathbf{B}^T \right\}. \qquad 2.128$$

Since the matrix logarithm can be expanded as[133]

$$\ln(\mathbf{1} - \mathbf{\Pi}_{\text{KS}}(\text{i}\omega)\mathbf{B}\tilde{\mathbf{V}}\mathbf{B}^T) = - \sum_{n=1}^\infty \frac{1}{n}(\mathbf{\Pi}_{\text{KS}}(\text{i}\omega)\mathbf{B}\tilde{\mathbf{V}}\mathbf{B}^T)^n \qquad 2.129$$

and the trace over a matrix product is invariant with respect to cyclic permutation of the matrices, Equation 2.128 can be expressed in the space of the auxiliary basis functions according to

$$E_c^{\text{RPA}} = \frac{1}{2\pi} \int_0^\infty d\omega \, \text{Tr} \left\{ \ln(\mathbf{1} - \mathbf{X}_{\text{KS}}(\text{i}\omega)\tilde{\mathbf{V}}) + \mathbf{X}_{\text{KS}}(\text{i}\omega)\tilde{\mathbf{V}} \right\}, \qquad 2.130$$

with

$$X_{MN}^{\text{KS}}(\text{i}\omega) = \sum_{ij}^{N_{\text{occ}}} \sum_{ab}^{N_{\text{virt}}} B_{ia}^M \Pi_{ia,jb}^{\text{KS}}(\text{i}\omega) B_{jb}^N. \qquad 2.131$$

Note that the formulation in Equation 2.130 is not identical to the originally published MO-RI-RPA formulation[34] since a different factorization of the ERI tensor is used in the present work. Conceptually, however, the two formulations are identical.

Compared to the $O(M^6)$ scaling of the plasmon method, evaluation of Equation 2.130 only scales as $O(M^4)$, which significantly extends the applicability of RPA. However, for very large systems $O(M^4)$ scaling is still prohibitively steep, making further improvements necessary. In the next section, a formulation of the RPA correlation functional in the AO space is derived, which can be evaluated with effective linear time-complexity.

28

2.8.3 Atomic-Orbital Resolution-of-the-Identity RPA

The time-determining step of MO-RI-RPA is the calculation of the noninteracting response function in the imaginary-frequency domain

$$X_{MN}^{\text{KS}}(\text{i}\omega) = \sum_{ij}^{N_{\text{occ}}} \sum_{ab}^{N_{\text{virt}}} B_{ia}^M \Pi_{ia,jb}^{\text{KS}}(\text{i}\omega) B_{jb}^N \qquad 2.132$$

$$= \sum_{i}^{N_{\text{occ}}} \sum_{a}^{N_{\text{virt}}} B_{ia}^M \frac{-2(\varepsilon_a - \varepsilon_i)}{\omega^2 + (\varepsilon_a - \varepsilon_i)^2} B_{ia}^N \qquad 2.133$$

formally scaling as $O(N_{\text{occ}} N_{\text{virt}} N_{\text{aux}}^2)$. As can be seen in Equation 2.133, a straightforward reformulation purely in terms of atomic orbitals is prohibited by the structure of the response function in the imaginary-frequency domain, since the MO energies cannot be decoupled. However, expressing the response function in the imaginary-frequency domain by a Fourier transform[134] of its representation in the imaginary-time domain

$$\Pi_{ia,jb}^{\text{KS}}(\text{i}\omega) = -2 \int_0^\infty \text{d}\tau \, \cos(\omega\tau) \Pi_{ia,jb}^{\text{KS}}(\text{i}\tau) \qquad 2.134$$

$$= -2 \int_0^\infty \text{d}\tau \, \cos(\omega\tau) \delta_{ij} \delta_{ab} \exp(-(\varepsilon_a - \varepsilon_i)\tau) \qquad 2.135$$

allows to decouple the MO energies due to the properties of the exponential function. Note that the Fourier transform in this case reduces to a cosine transform since the response function is symmetric with respect to iω. Inserting Equation 2.134 into Equation 2.132 yields

$$X_{MN}^{\text{KS}}(\text{i}\omega) = -2 \int_0^\infty \text{d}\tau \, \cos(\omega\tau) \sum_{ij}^{N_{\text{occ}}} \sum_{ab}^{N_{\text{virt}}} B_{ia}^M \Pi_{ia,jb}^{\text{KS}}(\text{i}\tau) B_{jb}^N \qquad 2.136$$

$$= 2 \int_0^\infty \text{d}\tau \, \cos(\omega\tau) X_{MN}^{\text{KS}}(\text{i}\tau), \qquad 2.137$$

with $X_{MN}^{\text{KS}}(\text{i}\tau)$ denoting the auxiliary-basis representation of the KS response function in the imaginary-time domain. The expression for $X_{MN}^{\text{KS}}(\text{i}\tau)$ is trivially transformed into the AO space according to

$$X_{MN}^{\text{KS}}(\text{i}\tau) = - \sum_{\mu\nu\lambda\sigma}^{N_{\text{basis}}} \sum_{i}^{N_{\text{occ}}} \sum_{a}^{N_{\text{virt}}} C_{\mu i} C_{\nu a} B_{\mu\nu}^M \exp(-\varepsilon_a \tau) \exp(\varepsilon_i \tau) B_{\lambda\sigma}^N C_{\lambda i} C_{\sigma a}, \qquad 2.138$$

with the occupied $C_{\mu i}$ and virtual $C_{\mu a}$ MO coefficients. Introducing the one-particle Green's function in the imaginary-time domain

$$\mathbf{G}_0(i\tau) = \Theta(-i\tau)\underline{\mathbf{G}}_0(i\tau) + \Theta(i\tau)\overline{\mathbf{G}}_0(i\tau) \tag{2.139}$$

$$\underline{G}^0_{\mu\nu}(i\tau) = \sum_i^{N_{\text{occ}}} C_{\mu i}C_{\nu i}\exp(-\varepsilon_i\tau) \tag{2.140}$$

$$\overline{G}^0_{\mu\nu}(i\tau) = -\sum_a^{N_{\text{virt}}} C_{\mu a}C_{\nu a}\exp(-\varepsilon_a\tau), \tag{2.141}$$

with the Heaviside step-function Θ, the expression for $X^{\text{KS}}_{MN}(i\tau)$ can be further simplified to

$$X^{\text{KS}}_{MN}(i\tau) = \sum_{\mu\nu\lambda\sigma}^{N_{\text{basis}}} \underline{G}^0_{\mu\nu}(-i\tau)B^M_{\nu\lambda}\overline{G}^0_{\lambda\sigma}(i\tau)B^N_{\sigma\mu}. \tag{2.142}$$

Note that Equation 2.142 in combination with the Fourier transform (Equation 2.137) is equivalent to one of two integral transforms decoupling the MO energies in the original derivation of AO-RI-RPA by Schurkus and Ochsenfeld,[50] however, derived in a different way. The second integral transform was introduced in the original formulation since numerical problems arose when only one transform was used. In **Publication I**, the above-mentioned equivalence is used to establish a connection between AO-RI-RPA and the work of Kaltak *et al.*[134] on cubic-scaling RPA in the plane-wave basis. Based on that connection, optimized quadrature schemes[134] for the Fourier transform and the final frequency-integration (Equation 2.130) are introduced, making the second integral transform of the original AO-RI-RPA formulation obsolete.

Since all quantities in Equation 2.142 get sparse for large systems with a nonvanishing gap between the highest occupied and the lowest unoccupied molecular orbital, it can be evaluated with an asymptotic linear time-complexity, opening the door for large-scale applications of RPA.

2.9 Beyond the Random Phase Approximation

As already mentioned in Chapter 1, a major problem of RPA is the inherent self-correlation error, occurring due to the neglect of exchange-effects in the Dyson-like equation for the interacting response function (cf. Equation 2.91).[7,60–63] Since self-correlation is, of course, especially pronounced at short interelectronic distances,

processes introducing large changes in that region — as for example atomization reactions — are described poorly by RPA methods. The most rigorous way to remedy this problem is to include the missing exchange-effects, at least to some extent. This section is intended to briefly outline, how the beyond-RPA equations, forming the basis of **Publication V**, are obtained.

All of the beyond-RPA methods used in this work are derived starting from the Bethe–Salpeter equation[121] (BSE) for the causal polarization propagator of a system with scaled electron-electron interactions

$$\underline{\underline{\mathbf{\Pi}}}_\alpha(\omega) = \underline{\underline{\mathbf{\Pi}}}_{\mathrm{KS}}(\omega) + \underline{\underline{\mathbf{\Pi}}}_{\mathrm{KS}}(\omega) \left[\alpha \underline{\underline{\mathbf{V}}} + \underline{\underline{\mathbf{K}}}_\alpha(\omega) \right] \underline{\underline{\mathbf{\Pi}}}_\alpha(\omega). \qquad 2.143$$

It should be noted that the causal polarization propagator discussed here is not equal to the retarded polarization propagator (obtained by generalizing Equation 2.87 to the interacting density-matrix density-matrix linear response function), although they yield the same density-density response function and hence also the same correlation energy within the ACFDT.[7,35] The difference between the two stems from the fact that the frequency-dependent exchange-correlation kernel in case of the retarded polarization propagator known from TDDFT corresponds to local interactions — as it should be in the KS framework — while the frequency-dependent BSE kernel $\underline{\underline{\mathbf{K}}}_\alpha(\omega)$ in case of the causal polarization propagator corresponds to nonlocal interactions.[35] Further, it should be noted that Equation 2.143 is given in terms of 2×2 supermatrices with dimensions $2N_{\mathrm{ph}} \times 2N_{\mathrm{ph}}$, where N_{ph} denotes the number of particle-hole pairs. However, since all final equations are of dimensions $N_{\mathrm{ph}} \times N_{\mathrm{ph}}$, it is sufficient for the discussion here to work with reduced dimensions right from the beginning. The analog of Equation 2.143 is then given by

$$\mathbf{\Pi}_\alpha(\omega) = \mathbf{\Pi}_{\mathrm{KS}}(\omega) + \mathbf{\Pi}_{\mathrm{KS}}(\omega) \left[\alpha \mathbf{V} + \mathbf{K}_\alpha(\omega) \right] \mathbf{\Pi}_\alpha(\omega) \qquad 2.144$$

and the correlation energy within the adiabatic-connection fluctuation-dissipation framework (Equation 2.78) in the particle-hole space is

$$E_{\mathrm{c}} = -\frac{1}{2\pi} \int_0^1 \mathrm{d}\alpha \int_0^\infty \mathrm{d}\omega \, \mathrm{Tr} \left\{ \mathbf{\Pi}_\alpha(\mathrm{i}\omega)\mathbf{V} - \mathbf{\Pi}_{\mathrm{KS}}(\mathrm{i}\omega)\mathbf{V} \right\}. \qquad 2.145$$

A relatively simple approach to include exchange-effects is the second-order screened-exchange (SOSEX) correction in the ACFDT.[70,91] Note that the SOSEX correction was originally introduced in the direct-ring coupled-cluster doubles framework,[87,90] which was shown to be identical to the random phase approximation, but is not discussed in the present work.[47] The idea of the SOSEX correction is to calculate the interacting response function like in standard RPA (only keeping the Hartree kernel) and use integrals with exchanged particles in the ACFDT correlation energy expression:

$$\Delta E_{\mathrm{c}}^{\mathrm{SOSEX}} = \frac{1}{2\pi} \int_0^1 \mathrm{d}\alpha \int_0^\infty \mathrm{d}\omega \, \mathrm{Tr} \left\{ \mathbf{\Pi}_{\mathrm{RPA}}^{\alpha}(\mathrm{i}\omega)\mathbf{K} - \mathbf{\Pi}_{\mathrm{KS}}(\mathrm{i}\omega)\mathbf{K} \right\}, \qquad 2.146$$

with

$$K_{ia,jb} = (ib|ja). \qquad 2.147$$

Insertion of the interacting RPA response function (Equation 2.114) and analytical coupling-strength integration as described in Section 2.8 then yields

$$\Delta E_{\mathrm{c}}^{\mathrm{SOSEX}} = -\frac{1}{2\pi} \int_0^\infty \mathrm{d}\omega \, \mathrm{Tr} \left\{ \ln(\mathbf{1} - \mathbf{\Pi}_{\mathrm{KS}}(\mathrm{i}\omega)\mathbf{V})\mathbf{V}^{-1}\mathbf{K} + \mathbf{\Pi}_{\mathrm{KS}}(\mathrm{i}\omega)\mathbf{K} \right\}. \qquad 2.148$$

The other two approaches which will be discussed in the present work leave the Hartree kernel in the ACFDT correlation energy expression unchanged and aim to approximately account for exchange-effects in the calculation of the interacting response function (Equation 2.144). The RPA with exchange (RPAx) method[91] approximates the frequency-dependent BSE kernel $\mathbf{K}_\alpha(\omega)$ in Equation 2.144 by the static Hartree–Fock like exchange-kernel $\mathbf{K}$ already introduced in the SOSEX correction, however, in a different fashion. That is, the RPAx interacting response function is given by

$$\mathbf{\Pi}_{\mathrm{RPAx}}^{\alpha}(\omega) = \mathbf{\Pi}_{\mathrm{KS}}(\omega) + \mathbf{\Pi}_{\mathrm{KS}}(\omega)\alpha\mathbf{W}\,\mathbf{\Pi}_{\mathrm{RPAx}}^{\alpha}(\omega), \qquad 2.149$$

with

$$\mathbf{W} = \mathbf{V} - \mathbf{K}, \qquad 2.150$$

and the ACFDT correlation energy expression becomes[91]

$$E_{\mathrm{c}}^{\mathrm{RPAx}} = -\frac{1}{2\pi} \int_0^1 \mathrm{d}\alpha \int_0^\infty \mathrm{d}\omega \, \mathrm{Tr} \left\{ \mathbf{\Pi}_{\mathrm{RPAx}}^{\alpha}(\mathrm{i}\omega)\mathbf{V} - \mathbf{\Pi}_{\mathrm{KS}}(\mathrm{i}\omega)\mathbf{V} \right\}. \qquad 2.151$$

Reformulating Equation 2.151 along the lines of Section 2.8 finally yields

$$E_c^{\text{RPAx}} = \frac{1}{2\pi} \int_0^\infty d\omega \, \text{Tr} \left\{ \ln(\mathbf{1} - \mathbf{\Pi}_{\text{KS}}(i\omega)\mathbf{W})\mathbf{W}^{-1}\mathbf{V} + \mathbf{\Pi}_{\text{KS}}(i\omega)\mathbf{V} \right\}. \qquad 2.152$$

The approximate exchange-kernel (AXK) correction proposed by Furche and co-workers[35] uses in a first step the random phase approximation for the interacting response function

$$\mathbf{\Pi}_{\text{RPA}}^\alpha(\omega) = \left[\mathbf{\Pi}_{\text{KS}}^{-1}(\omega) - \alpha\mathbf{V} \right]^{-1} \qquad 2.153$$

and afterwards expands $\mathbf{\Pi}_\alpha(\omega)$ in terms of $\mathbf{\Pi}_{\text{RPA}}^\alpha(\omega)$ in a geometric series according to

$$\mathbf{\Pi}_\alpha(\omega) = \left[\left(\mathbf{\Pi}_{\text{RPA}}^\alpha(\omega)\right)^{-1} - \mathbf{K}_\alpha(\omega) \right]^{-1} \qquad 2.154$$

$$= \mathbf{\Pi}_{\text{RPA}}^\alpha(\omega) + \mathbf{\Pi}_{\text{RPA}}^\alpha(\omega)\mathbf{K}_\alpha(\omega)\mathbf{\Pi}_{\text{RPA}}^\alpha(\omega) + \dots \qquad 2.155$$

Truncating the expansion in second order and using the static Hartree–Fock like exchange-kernel to approximate $\mathbf{K}_\alpha(\omega)$ as in the RPAx method discussed above yields the AXK correction:[35]

$$\Delta E_c^{\text{AXK}} = \frac{1}{2\pi} \int_0^1 d\alpha \int_0^\infty d\omega \, \text{Tr} \left\{ \mathbf{\Pi}_{\text{RPA}}^\alpha(i\omega)\alpha\mathbf{K}\mathbf{\Pi}_{\text{RPA}}^\alpha(i\omega)\mathbf{V} \right\}. \qquad 2.156$$

Insertion of the interacting response function within the random phase approximation (Equation 2.114) and analytical coupling-strength integration then yields

$$\Delta E_c^{\text{AXK}} = \frac{1}{2\pi} \int_0^\infty d\omega \, \text{Tr} \left\{ \ln(\mathbf{1} - \mathbf{\Pi}_{\text{KS}}(i\omega)\mathbf{V})\mathbf{V}^{-1}\mathbf{K} + (\mathbf{1} - \mathbf{\Pi}_{\text{KS}}(i\omega)\mathbf{V})^{-1}\mathbf{\Pi}_{\text{KS}}(i\omega)\mathbf{K} \right\}.$$
$$2.157$$

All beyond-RPA methods discussed in this section yield the well-known MP2 correlation energy expression (in terms of KS orbitals) in a second-order approximation and hence are correct up to this order. This can be easily shown, e.g., for the RPAx method. Expanding the matrix logarithm (cf. Equation 2.129) lets the first-order term vanish and yields for the second-order term

$$E_c^{\text{RPAx},(2)} = -\frac{1}{4\pi} \int_0^\infty d\omega \, \text{Tr} \left\{ \mathbf{\Pi}_{\text{KS}}(i\omega)\mathbf{W}\mathbf{\Pi}_{\text{KS}}(i\omega)\mathbf{V} \right\}. \qquad 2.158$$

Since

$$\int_0^\infty d\omega \frac{-2a}{a^2 + \omega^2} \frac{-2b}{b^2 + \omega^2} = \frac{2\pi}{a + b} \qquad \forall a, b > 0 \qquad 2.159$$

Equation 2.158 becomes

$$E_{\rm c}^{\rm RPAx,(2)} = -\frac{1}{2} \sum_{ij}^{N_{\rm occ}} \sum_{ab}^{N_{\rm virt}} \frac{W_{ia,jb}V_{ia,jb}}{\Omega_{ia}^{\rm KS} + \Omega_{jb}^{\rm KS}} = E_{\rm c}^{\rm MP2},$$

2.160

which connects the discussed beyond-RPA method(s) with MP2 and thus enables to transfer all of the insights obtained in the development of efficient beyond-RPA methods to MP2 as it is done in **Publication VI**.

3

Publications

3.1 Accurate and Efficient Parallel Implementation of an Effective Linear-Scaling Direct Random Phase Approximation Method

D. Graf, M. Beuerle, H. F. Schurkus, A. Luenser, G. Savasci, C. Ochsenfeld

Abstract

An efficient algorithm for calculating the random phase approximation (RPA) correlation energy is presented that is as accurate as the canonical molecular orbital resolution-of-the-identity RPA (RI-RPA) with the important advantage of an effective linear-scaling behavior (instead of quartic) for large systems due to a formulation in the local atomic orbital space. The high accuracy is achieved by utilizing optimized minimax integration schemes and the local Coulomb metric attenuated by the complementary error function for the RI approximation. The memory bottleneck of former atomic orbital (AO)-RI-RPA implementations (Schurkus, H. F.; Ochsenfeld, C. *J. Chem. Phys.* **2016**, *144*, 031101 and Luenser, A.; Schurkus, H. F.; Ochsenfeld, C. *J. Chem. Theory Comput.* **2017**, *13*, 1647–1655) is addressed by precontraction of the large 3-center integral matrix with the Cholesky factors of the ground state density reducing the memory requirements of that matrix by a factor of $\frac{N_{\text{basis}}}{N_{\text{occ}}}$. Furthermore, we present a parallel implementation of our method, which not only leads to faster RPA correlation energy calculations but also to a scalable decrease in memory requirements, opening the door for investigations of large molecules even on small- to medium-sized computing clusters. Although it is known that AO methods are highly efficient for extended

systems, where sparsity allows for reaching the linear-scaling regime, we show that our work also extends the applicability when considering highly delocalized systems for which no linear scaling can be achieved. As an example, the interlayer distance of two covalent organic framework pore fragments (comprising 384 atoms in total) is analyzed.

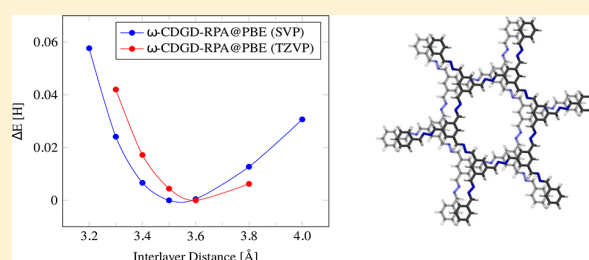# Accurate and Efficient Parallel Implementation of an Effective Linear-Scaling Direct Random Phase Approximation Method

Daniel Graf,[†] Matthias Beuerle,[†] Henry F. Schurkus,[†] Arne Luenser,[†] Gökcen Savasci,[‡,†] and Christian Ochsenfeld[*,†,‡]

[†]Chair of Theoretical Chemistry and Center for Integrated Protein Science Munich (CIPSM), Department of Chemistry, University of Munich (LMU), D-81377 Munich, Germany

[‡]Max Planck Institute for Solid State Research, Heisenbergstraße 1, 70569 Stuttgart, Germany

ABSTRACT: An efficient algorithm for calculating the random phase approximation (RPA) correlation energy is presented that is as accurate as the canonical molecular orbital resolution-of-the-identity RPA (RI-RPA) with the important advantage of an effective linear-scaling behavior (instead of quartic) for large systems due to a formulation in the local atomic orbital space. The high accuracy is achieved by utilizing optimized minimax integration schemes and the local Coulomb metric attenuated by the complementary error function for the RI approximation. The memory bottleneck of former atomic orbital (AO)-RI-RPA implementations (Schurkus, H. F.; Ochsenfeld, C. *J. Chem. Phys.* **2016**, *144*, 031101 and Luenser, A.; Schurkus, H. F.; Ochsenfeld, C. *J. Chem. Theory Comput.* **2017**, *13*, 1647−1655) is addressed by precontraction of the large 3-center integral matrix with the Cholesky factors of the ground state density reducing the memory requirements of that matrix by a factor of $\frac{N_{\text{basis}}}{N_{\text{occ}}}$.

Furthermore, we present a parallel implementation of our method, which not only leads to faster RPA correlation energy calculations but also to a scalable decrease in memory requirements, opening the door for investigations of large molecules even on small- to medium-sized computing clusters. Although it is known that AO methods are highly efficient for extended systems, where sparsity allows for reaching the linear-scaling regime, we show that our work also extends the applicability when considering highly delocalized systems for which no linear scaling can be achieved. As an example, the interlayer distance of two covalent organic framework pore fragments (comprising 384 atoms in total) is analyzed.

1. INTRODUCTION

Density functional theory (DFT) is the most widely used electronic structure method in chemistry, physics, and materials sciences. This is mainly because of the excellent cost-performance ratios and good accuracies of its parametrized functionals for certain types of compounds and properties. However, the high sensitivity of semilocal DFT results to the parametrization has led to the development of many hundreds of different functionals, which not only makes the selection of a suitable functional for a specific problem challenging[1] but also limits its predictive power. Additionally, the general failure of GGA functionals in describing noncovalent interactions[2,3] necessitates the development of more broadly applicable correlation models.

One theory to describe electron correlation, which has become increasingly popular over the past decade, is the random phase approximation (RPA). RPA is a post Kohn–Sham[4] method that was originally introduced by Bohm and Pines in 1953.[5] It contains an ab initio description of dispersion effects,[6] is size consistent,[7] and does not depend on any empirical parameters. Additionally, it is applicable to vanishing electronic gap systems,[7−9] making it highly interesting for a wide range of applications in the field of quantum chemistry.

However, in its original form,[10,11] the calculation of RPA correlation energies of molecular systems scales as $O(M^6)$ with system size M, making it impractical for larger molecules. In 2010, Furche and co-workers[12−14] successfully employed the resolution-of-the-identity (RI) approximation to reduce the scaling to effective $O(M^4)$, which can be viewed as a breakthrough because it opened the door for RPA calculations beyond the few atoms scale. In 2014, Kresse and co-workers[15] presented an algorithm for the RPA that employed minimax grids for the time as well as the frequency domain and a Fourier transform scheme to reduce the scaling to cubic. Effective linear-scaling of RPA calculations for molecules with non-vanishing band gaps was achieved by Kállay[16] as well as Schurkus and Ochsenfeld:[17] The approach of Kállay[16] is based on local correlation theory, which finds its origin in the 1980s,[18−20] whereas the method of Schurkus et al.[17] builds upon the transformation into the local atomic orbital space. Recently, Hutter and co-workers[21] presented a different approach toward large-scale RPA calculations by a cubic scaling but highly parallel implementation, opening the door to

calculations comprising up to 8000 electrons on a Cray XC40 supercomputer.

To obtain the desired linear-scaling behavior, Schurkus et al.[17] employed the local but with canonical auxiliary basis sets less accurate overlap RI metric[22] instead of the longe-range Coulomb metric. Additionally, the pilot implementation was strongly hampered in its applicability to larger basis sets because the scaling with basis set size N_{basis} and auxiliary basis set size N_{aux} is increased from $O(N_{aux}^2 N_{basis} N_{occ})$ to $O(N_{aux}^2 N_{basis}^2)$ for a fixed molecular size. In 2017, Luenser et al.[23] remedied these drawbacks by switching to the Coulomb metric attenuated by the complementary error function[24−26] as well as utilizing pivoted Cholesky decomposition[27−31] of density and pseudodensity matrices, which brought the scaling with basis set size back to $O(N_{aux}^2 N_{basis} N_{occ})$ while scaling linearly with molecular size. The improved implementation was termed ω-CDD-RPA.[23]

However, in both the original atomic orbital RI-RPA as well as the ω-CDD method, the complete 3-center integral matrix **B** in the atomic orbital (AO) basis needs to be stored in memory, which is a bottleneck when aiming for large systems. Additionally, two different formulations for constructing the frequency-dependent energy kernel $\mathbf{Q}(u)$ are necessary to avoid numerical problems arising from the use of unoptimized weights and roots for the numerical quadratures. Furthermore, the final frequency integration is carried out with the Clenshaw−Curtis scheme[32] with optimization of the scaling parameter as described by Furche and co-workers,[13] where at least 60 node points are necessary to obtain μHartree accuracy.

The focus of the present work is to overcome the drawbacks described above: The use of an optimized minimax grid for the frequency integration as described by Kresse and co-workers[15] reduces the number of necessary quadrature points from 60−100 to 10−20. Utilizing optimized weights and roots for the integrated double-Laplace expansion[17] enables us to obtain $\mathbf{Q}(u)$ without using the second equation, decreasing the prefactor of our RPA reformulation by a factor of 4 and, additionally, increasing the accuracy of the calculations by up to 4 orders of magnitude. Reformulating the formation of $\mathbf{F}_{INT}$ as described in this work reduces the memory effort of the algorithm by a factor of $\frac{N_{basis}}{N_{occ}}$ and yields an additional speed-up. Besides improved integration schemes, a parallel implementation of the new method is presented, which not only reduces the evaluation time of correlation energies significantly but also leads to a scalable decrease in memory requirements. Here, the focus of our present parallel implementation is on small- to medium-sized computing clusters typically available in local research groups.

In the following, we first give a brief review of the derivation of our ω-CDD-RI-RPA method[23] in section 2.1. We then establish the connection of our double-Laplace approach[17] and the cosine transformation of Kresse and co-workers[15] in section 2.2. In section 2.3, the memory efficient reformulation of evaluating $\mathbf{F}_{INT}$ is outlined before we present the parallel implementation of the method to further reduce the memory requirements and speed up the calculations in section 2.4. Computational details are given in section 3. Accuracy and performance benchmarks as well as a illustrative application of the new implementation are reported in section 4, followed by the conclusions in section 5.

2. THEORY

2.1. Linear-Scaling Atomic Orbital Random Phase Approximation. To create a complete picture of our new effective linear-scaling atomic orbital RPA method, we will briefly review the most important steps in the derivation of our recently reported ω-CDD method.[23] In this work, the following notation has been adopted: μ, ν, λ, σ denote atomic orbitals (AOs); i, j denote occupied molecular orbitals (MOs); a, b denote virtual MOs; $\underline{i}$, $\underline{j}$ denote Cholesky orbitals; and M, N denote auxiliary RI functions. The number of basis functions is represented by N_{basis}; the number of auxiliary RI functions is represented by N_{aux}; and the numbers of occupied and virtual molecular orbitals are represented by N_{occ} and N_{virt}, respectively. For 2-, 3-, and 4-center integrals, the Mulliken notation will be employed. Furthermore, Einstein's sum convention[33] is used, and the spin index is dropped for convenience.

Within the adiabatic connection formalism,[34] the total energy can be expressed as[10,11]

$$E = E_T[\{\phi_{KS}\}] + E_J[\{\phi_{KS}\}] + E_X[\{\phi_{KS}\}] + E_C \quad (1)$$

where E_T, E_J, and E_X denote the kinetic, Coulomb, and exact exchange energies, respectively. The expression for the correlation energy[35] E_C, obtained by using the zero-temperature fluctuation−dissipation theorem and the RPA,[36] is given by

$$E_C = \int_{-\infty}^{+\infty} \frac{du}{4\pi} \mathrm{Tr}[\ln(1 - v\chi_0(iu)) + v\chi_0(iu)] \quad (2)$$

where v represents the Coulomb operator

$$v(\mathbf{r}, \mathbf{r}') = \frac{1}{|\mathbf{r} - \mathbf{r}'|} \quad (3)$$

with the electronic coordinates $\mathbf{r}$ and $\mathbf{r}'$, and χ_0 denotes the noninteracting density−density response function in the occupied and virtual orbital representation in the zero-temperature case[37]

$$\chi_0(\mathbf{r}, \mathbf{r}', iu) = -\frac{\phi_i^*(\mathbf{r})\phi_a(\mathbf{r})\phi_a^*(\mathbf{r}')\phi_i(\mathbf{r}')}{\varepsilon_a - \varepsilon_i - iu}$$
$$- \frac{\phi_i^*(\mathbf{r}')\phi_a(\mathbf{r}')\phi_a^*(\mathbf{r})\phi_i(\mathbf{r})}{\varepsilon_a - \varepsilon_i + iu} \quad (4)$$

with the occupied and virtual molecular spin orbitals ϕ_i and ϕ_a and their respective orbital energies ε_i and ε_a. Note that v and $\chi_0(iu)$ denote matrices of which $v(\mathbf{r}, \mathbf{r}')$ and $\chi_0(\mathbf{r}, \mathbf{r}', iu)$ represent the respective $(\mathbf{r}, \mathbf{r}')$-th element and that

$$\mathrm{Tr}[v\chi_0(iu)] = \int\int d\mathbf{r} d\mathbf{r}' v(\mathbf{r}, \mathbf{r}')\chi_0(\mathbf{r}, \mathbf{r}', iu) \quad (5)$$

The correlation energy can also be expressed in a supermatrix formalism[38,39]

$$E_C = \int_{-\infty}^{+\infty} \frac{du}{4\pi} \mathrm{Tr}[\ln(\mathbf{1} - \mathbf{\Pi}_0(iu)\underline{\mathbf{V}}) + \mathbf{\Pi}_0(iu)\underline{\mathbf{V}}] \quad (6)$$

where we introduced the Kohn−Sham (KS) polarization propagator in the canonical orbital space

$$\mathbf{\Pi}_0(iu) = \begin{pmatrix} \boldsymbol{\pi}^-(iu) & 0 \\ 0 & \boldsymbol{\pi}^+(iu) \end{pmatrix} \quad (7)$$

with

$$\pi^{\pm}(iu) = -(\Delta \pm iu\mathbf{1})^{-1} \tag{8}$$

$$\Delta_{ia,jb} = \delta_{ij}\delta_{ab}(\varepsilon_a - \varepsilon_i) \tag{9}$$

and the Hartree kernel matrix

$$\underline{\underline{\mathbf{V}}} = \int\int d\mathbf{r}d\mathbf{r}'\mathbf{b}(\mathbf{r})v(\mathbf{r}, \mathbf{r}')\mathbf{b}^{\dagger}(\mathbf{r}') = \begin{pmatrix} \mathbf{V}_{11} & \mathbf{V}_{12} \\ \mathbf{V}_{12}^* & \mathbf{V}_{11}^* \end{pmatrix} \tag{10}$$

with

$$\mathbf{b}^T(\mathbf{r}) = (\cdots, \phi_i(\mathbf{r})\phi_a^*(\mathbf{r}), \cdots, \phi_i^*(\mathbf{r})\phi_a(\mathbf{r}), \cdots) \tag{11}$$

and its submatrices

$$V_{11,iajb} = (ia|jb) \tag{12}$$

$$V_{12,iajb} = (ia|bj) \tag{13}$$

For real-valued orbitals

$$\mathbf{V}_{11} = \mathbf{V}_{11}^* = \mathbf{V}_{12} = \mathbf{V}_{12}^* \tag{14}$$

holds and, therefore, the Hartree kernel matrix simplifies to

$$\underline{\underline{\mathbf{V}}} = \begin{pmatrix} \mathbf{V} & \mathbf{V} \\ \mathbf{V} & \mathbf{V} \end{pmatrix} \tag{15}$$

The matrices appearing in eq 6 have dimensions ($2N_{\text{PH}} \times 2N_{\text{PH}}$) with N_{PH} denoting the number of products between occupied and virtual orbitals (particle-hole). To reduce the dimensions to ($N_{\text{PH}} \times N_{\text{PH}}$), we use the series expansion of the matrix logarithm

$$\text{Tr}[\ln(\mathbf{1} - \underline{\underline{\mathbf{\Pi}}}_0(iu)\underline{\underline{\mathbf{V}}})] = -\sum_{n=1}^{\infty} \frac{1}{n}\text{Tr}[(\underline{\underline{\mathbf{\Pi}}}_0(iu)\underline{\underline{\mathbf{V}}})^n] \tag{16}$$

Application of the unitary transformation[40]

$$\mathbf{U} = \frac{1}{\sqrt{2}}\begin{pmatrix} \mathbf{1} & \mathbf{1} \\ \mathbf{1} & -\mathbf{1} \end{pmatrix} \tag{17}$$

cyclic permutation of the matrix products and considering that only the trace is relevant leads to

$$-\sum_{n=1}^{\infty} \frac{1}{n}\text{Tr}[(\mathbf{U}^{\dagger}\underline{\underline{\mathbf{\Pi}}}_0(iu)\underline{\underline{\mathbf{V}}}\mathbf{U})^n] = -\sum_{n=1}^{\infty} \frac{1}{n}\text{Tr}[(\{\pi^-(iu) + \pi^+(iu)\}\mathbf{V})^n] \tag{18}$$

$$-\sum_{n=1}^{\infty} \frac{1}{n}\text{Tr}[(\mathbf{U}^{\dagger}\underline{\underline{\mathbf{\Pi}}}_0(iu)\underline{\underline{\mathbf{V}}}\mathbf{U})^n] = -\sum_{n=1}^{\infty} \frac{1}{n}\text{Tr}[(-2\mathbf{G}(u)\mathbf{V})^n] \tag{19}$$

where

$$\mathbf{G}(u) = \frac{\Delta}{\Delta^2 + u^2\mathbf{1}} \tag{20}$$

Applying the Coulomb-RI metric attenuated by the complementary error function[24,26] as described by Luenser et al.[23]

$$(ia|jb) \approx B_{ia}^M \tilde{C}_{MN} B_{jb}^N \tag{21}$$

$$B_{ia}^M = \left(ia \left| \frac{\text{erfc}(\omega r_{12})}{r_{12}} \right| M \right) \tag{22}$$

$$\tilde{\mathbf{C}} = \mathbf{S}^{-1}\mathbf{C}\mathbf{S}^{-1} \tag{23}$$

$$C_{MN} = (M|r_{12}^{-1}|N) \tag{24}$$

$$S_{MN} = \left(M \left| \frac{\text{erfc}(\omega r_{12})}{r_{12}} \right| N \right) \tag{25}$$

to factorize the 4-center integrals into 3-center integrals B_{ia}^M, and 2-center-2-electron integrals $\tilde{C}_{MN}$ leads to

$$-\sum_{n=1}^{\infty} \frac{1}{n}\text{Tr}[(-2\mathbf{G}(u)\mathbf{V})^n] = -\sum_{n=1}^{\infty} \frac{1}{n}\text{Tr}[(-2\mathbf{G}(u)\mathbf{B}\tilde{\mathbf{C}}\mathbf{B}^T)^n] \tag{26}$$

Cyclic permutation of the matrix products and defining

$$\mathbf{Q}(u) = 2\mathbf{B}^T\mathbf{G}(u)\mathbf{B} \tag{27}$$

finally yields[17]

$$E_{\text{C}} = 2\int_0^{+\infty} \frac{du}{4\pi}\text{Tr}[\ln(\mathbf{1} + \mathbf{Q}(u)\tilde{\mathbf{C}}) - \mathbf{Q}(u)\tilde{\mathbf{C}}] \tag{28}$$

As shown by Schurkus and Ochsenfeld,[17] the Kohn–Sham energy-based $\mathbf{G}(u)$ can be decoupled by a contracted double-Laplace expansion

$$(\mathbf{G}(u))_{ia,jb} = \frac{\Delta_{ia,jb}}{\Delta_{ia,jb}^2 + u^2} \tag{29}$$

$$(\mathbf{G}(u))_{ia,jb} = \Delta_{ia,jb}\int_0^{\infty} \frac{\sin(up)}{u}\exp(-\Delta_{ia,jb}p)\,dp \tag{30}$$

yielding two different equations for calculating $\mathbf{Q}(u)$

$$\mathbf{Q}(u) = 2\int_0^{\infty} \cos(up)\mathbf{F}_{\text{INT}}^{(p)}\,dp \tag{31}$$

$$\mathbf{Q}(u) = 2\frac{\mathbf{F}^{(0)}}{u^2} + 2\int_0^{\infty} \frac{\cos(up)}{u^2}\mathbf{F}_{\text{D}}^{(p)}\,dp \tag{32}$$

after partial integration with three different forms of $\mathbf{F}$ matrices defined in ref 23. As evaluating the trace of the matrix logarithm in the final frequency integration (eq 28) has a very small prefactor, the time determining step of the algorithm is the calculation of these three $\mathbf{F}$ matrices. Rewriting the expressions for these matrices in the local atomic orbital basis allows for a linear-scaling calculation because all occurring quantities become sparse for large systems.[17]

2.2. Polarization Propagators in the Imaginary Frequency and Time Domain in AO-RI-RPA Theory. As mentioned in the section above, within the ω-CDD method two equations for the calculation of $\mathbf{Q}(u)$ are necessary because eq 31 suffers from numerical instability when u approaches infinity and eq 32 becomes numerically unstable where u tends to zero.[17] It is assumed that these problems occur because weights and roots are used for the numerical quadratures, which are not optimized for these specific transformations.[17] Therefore, determining optimized weights and roots for the integrated double-Laplace expansion should allow for using eq 31 alone for calculating $\mathbf{Q}(u)$. This would decrease the computational cost significantly while at the same time increasing the accuracy of the quadrature. Kresse and co-workers[15] have described in great detail a procedure for finding optimal weights and roots for their nonuniform cosine transformation, which is based on minimax grids and allows for transforming the polarizability $\hat{\chi}$ from the imaginary time domain into the imaginary frequency domain and vice versa. We show in the following that the described cosine transformation is equivalent to eq 31 stemming from the

double-Laplace transform, which enables us to follow the procedure outlined by Kresse and co-workers to obtain optimized weights and roots for this transformation.

Therefore, consider the definition of $\mathbf{Q}(u)$

$$\mathbf{Q}_{MN}(u) = 2B_{ia}^M \frac{\varepsilon_a - \varepsilon_i}{u^2 + (\varepsilon_a - \varepsilon_i)^2} B_{ia}^N \tag{33}$$

Combination of the two indices i and a according to $\kappa = (i, a)$ and defining

$$x_\kappa = \varepsilon_a - \varepsilon_i \tag{34}$$

results in

$$\mathbf{Q}_{MN}(u) = B_\kappa^M \Phi(u, x_\kappa) B_\kappa^N \tag{35}$$

where

$$\Phi(u, x_\kappa) = \frac{2x_\kappa}{u^2 + x_\kappa^2} \tag{36}$$

Next, consider the definition of $\mathbf{F}_{\mathrm{INT}}$, which is given by[23]

$$(\mathbf{F}_{\mathrm{INT}}^{(p)})_{MN} = \mathrm{Tr}(\underline{\mathbf{P}}^{(p)} \mathbf{B}^M \overline{\mathbf{P}}^{(p)} \mathbf{B}^N) \tag{37}$$

$$(\mathbf{F}_{\mathrm{INT}}^{(p)})_{MN} = \underline{P}_{\mu\nu}^{(p)} B_{\nu\sigma}^M \overline{P}_{\sigma\lambda}^{(p)} B_{\lambda\mu}^N \tag{38}$$

Inserting the definition for the occupied and virtual pseudodensities, $\underline{P}^{(p)}$ and $\overline{P}^{(p)}$[17] and transforming $\mathbf{B}$ back into the molecular orbital space yields

$$(\mathbf{F}_{\mathrm{INT}}^{(p)})_{MN} = B_{ia}^M \exp(+\varepsilon_i p)\exp(-\varepsilon_a p) B_{ia}^N \tag{39}$$

Considering the definitions for κ and x_κ finally leads to

$$(\mathbf{F}_{\mathrm{INT}}^{(p)})_{MN} = B_\kappa^M \hat{\Phi}(p, x_\kappa) B_\kappa^N \tag{40}$$

where

$$\hat{\Phi}(p, x_\kappa) = \exp(-x_\kappa p) \tag{41}$$

Comparison of eqs 35−40 with eqs 14−17 in ref 15 shows that $\mathbf{F}_{\mathrm{INT}}$ is the representation of $\mathbf{Q}(u)$ in the imaginary time domain. Therefore, the cosine transformation described by Kresse and co-workers[15] is equivalent to the double-Laplace transformation in its integral formulation (eq 31), and we can follow the procedure of ref 15 to obtain optimized weights and roots for the transformation.

Additionally, the minimax grid for the imaginary frequency domain will be utilized for the final frequency integration replacing the Clenshaw−Curtis quadrature[32] to obtain the RPA correlation energy according to eq 28, which decreases the number of necessary quadrature points from 60−100 to 10−20.

2.3. Memory Efficient Calculation of the $\mathbf{F}_{\mathrm{INT}}$ Matrix.
One of the major bottlenecks of the ω-CDD method is the huge memory requirement of the complete 3-center integrals in the AO basis. To find a strategy to reduce this memory requirement, we consider the formation of the $\mathbf{F}_{\mathrm{INT}}$ matrix according to[23]

$$(\mathbf{F}_{\mathrm{INT}}^{(p)})_{MN} = \mathrm{Tr}(\mathbf{Z}_M^{(p)T} \overline{\mathbf{P}}^{(p)} \mathbf{Z}_N^{(p)}) \tag{42}$$

where the pivoted Cholesky factorization of a given matrix $\mathbf{A}$ is abbreviated by $\mathbf{A} = \mathbf{L}\mathbf{L}^T$ and[23]

$$\mathbf{Z}_M^{(p)} = \mathbf{B}^M \underline{\mathbf{L}}^{(p)} \text{ with } \underline{\mathbf{P}}^{(p)} = \underline{\mathbf{L}}^{(p)} \underline{\mathbf{L}}^{(p)T} \tag{43}$$

The Cholesky factor $\underline{\mathbf{L}}^{(p)}$ is a transformation matrix to a local Cholesky basis,[30,31] and therefore, transformation of the 3-

center integrals $\mathbf{B}^M$ to this local basis reduces the dimensions of each $\mathbf{B}^M$ from $N_{\mathrm{basis}} \times N_{\mathrm{basis}}$ to $N_{\mathrm{basis}} \times N_{\mathrm{occ}}$ while preserving all sparsity of the original matrix.[23] However, because $\mathbf{Z}_M^{(p)}$ is required for each Laplace point p, precontraction of each $\mathbf{B}^M$ with the Cholesky factors requires $N_{\mathrm{aux}} N_{\mathrm{basis}} N_{\mathrm{occ}} \tau$ memory, where τ is the number of Laplace points and, therefore, quickly becomes unfeasible.

Reformulating the calculation of $\mathbf{F}_{\mathrm{INT}}$ using the idempotency relation of the ground state density $\mathbf{P}$

$$\mathbf{P} = \mathbf{P}\mathbf{S}\mathbf{P} \tag{44}$$

with the 2-center overlap $\mathbf{S}$ and the extension to pseudodensity matrices

$$\underline{\mathbf{P}} = \underline{\mathbf{P}}\mathbf{S}\mathbf{P} \tag{45}$$

according to

$$(\mathbf{F}_{\mathrm{INT}}^{(p)})_{MN} = \mathrm{Tr}(\underline{\mathbf{P}}^{(p)} \mathbf{B}^M \overline{\mathbf{P}}^{(p)} \mathbf{B}^N) \tag{46}$$

$$(\mathbf{F}_{\mathrm{INT}}^{(p)})_{MN} = \mathrm{Tr}(\underline{\mathbf{P}}^{(p)} \mathbf{S}\mathbf{P}\mathbf{B}^M \overline{\mathbf{P}}^{(p)} \mathbf{B}^N \mathbf{P}\mathbf{S}) \tag{47}$$

$$(\mathbf{F}_{\mathrm{INT}}^{(p)})_{MN} = \mathrm{Tr}(\underline{\mathbf{P}}^{(p)} \mathbf{S}\mathbf{L}\mathbf{L}^T \mathbf{B}^M \overline{\mathbf{P}}^{(p)} \mathbf{B}^N \mathbf{L}\mathbf{L}^T \mathbf{S}) \tag{48}$$

$$(\mathbf{F}_{\mathrm{INT}}^{(p)})_{MN} = \mathrm{Tr}(\mathbf{L}^T \mathbf{S}\underline{\mathbf{P}}^{(p)} \mathbf{S}\mathbf{L}\mathbf{L}^T \mathbf{B}^M \overline{\mathbf{P}}^{(p)} \mathbf{B}^N \mathbf{L}) \tag{49}$$

$$(\mathbf{F}_{\mathrm{INT}}^{(p)})_{MN} = \tilde{\underline{P}}_{ji}^{(p)} \tilde{B}_{i\nu}^M \overline{P}_{\nu\mu}^{(p)} \tilde{B}_{\mu j}^N \tag{50}$$

allows to precontract each $\mathbf{B}^M$ with the Cholesky factor $\mathbf{L}$ of the occupied one-particle density $\mathbf{P}$, which is not dependent on the Laplace points. Again, the dimensions are reduced from $N_{\mathrm{basis}} \times N_{\mathrm{basis}}$ to $N_{\mathrm{basis}} \times N_{\mathrm{occ}}$ while all sparsity of the original matrix is preserved, which will be shown in section 4. In this way, the required memory for saving the 3-center integrals is reduced by a factor of $\frac{N_{\mathrm{basis}}}{N_{\mathrm{occ}}}$ (with the total memory requirement being $N_{\mathrm{aux}} N_{\mathrm{basis}} N_{\mathrm{occ}}$), which is highly beneficial, especially for large basis sets. The final step for obtaining $\mathbf{F}_{\mathrm{INT}}$ is given by

$$(\mathbf{F}_{\mathrm{INT}}^{(p)})_{MN} = \underline{\tilde{\underline{B}}}_{j\mu}^{(p),M} \tilde{B}_{\mu j}^N \tag{51}$$

As the reformulation of $\mathbf{F}_{\mathrm{INT}}$ presented in this section makes use of only the Cholesky decomposed ground state density (CDGD) $\mathbf{P}$, we will term the algorithm ω-CDGD-RPA.

2.4. Parallel Implementation.
In the previous section, we showed that the memory requirements of the 3-center integral matrix can be decreased significantly by precontraction with the Cholesky factor of the ground state density. However, for large systems the 3-center integral matrix easily exceeds the available memory on a single node even with reduced dimensions. Therefore, our parallel implementation not only focuses on reducing calculation times of RPA correlation energies but also on a scalable decrease in memory requirements of the large 3-center integral matrix per node. The implementation presented here is a MPI/OpenMP hybrid parallelization of the ω-CDGD method, where OpenMP is mainly used for linear algebra and is therefore not discussed. The pseudocode of our implementation is shown in Figure 2.

The two most time-consuming steps in the ω-CDGD algorithm are, first, the formation of $\mathbf{F}_{\mathrm{INT}}$ according to eq 51 and, second, evaluation of the 3-center integrals $B_{\nu\sigma}^M$. For tackling all three of the bottlenecks mentioned above at once, a parallelization with respect to auxiliary basis functions is obvious. Therefore, each node calculates the 3-center integrals of a specific batch of RI basis functions (AUX$_1$...AUX$_n$) and
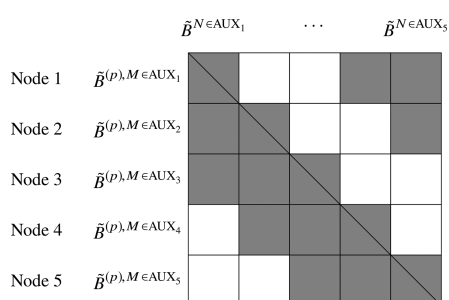
Figure 1. Schematic description of calculated unique blocks per node. Only the gray boxes are calculated; the white boxes are not calculated due to symmetry reasons.

keeps this part in memory (if enough memory is available) throughout the complete calculation. On each node, the 3-center integrals in the atomic orbital space are additionally evaluated in batches of RI basis functions, which are transformed into the Cholesky space by contraction with the Cholesky factor of the ground state density right after evaluation to reduce memory requirements. For evaluating the $\mathbf{F}_{INT}$ matrix, the nodes are set up in a cyclic topology. Each node calculates its specific diagonal block of the matrix $((\mathbf{F}_{INT})_{M\in AUX_1, N\in AUX_1})$ according to eq 51 and then sends a

copy of its batch of 3-center integrals $(\tilde{B}_{\mu i}^{N\in AUX_1})$ to the neighboring node. In the next cycle, each node calculates the next unique part of the $\mathbf{F}_{INT}$ matrix $((\mathbf{F}_{INT})_{M\in AUX_1, N\in AUX_2})$ and passes the batch (AUX_2) on to the next neighbor. As $\mathbf{F}_{INT}$ is symmetric, there are $\frac{n(n-1)}{2}$ unique nondiagonal parts of the matrix, where n is the total number of computing nodes, which is also the minimum number of send operations (see Figure 1). Note, however, that the send operations are conducted in parallel and the number of cycles $\left(N_{cycle} = \frac{n-1}{2}\right)$ is of more interest.

To prevent repetitive recalculation of $\underline{\tilde{B}}_{\underline{j}\mu}^{(p),M}$ in eq 51 or increasing the number of cycles by a factor of τ, a variable number of these matrices are precomputed. For computational efficiency, all τ matrices should be precomputed. However, to reduce memory requirements, it would be best to precompute only one of these matrices. In our implementation, the complete available memory is exploited to precompute as many of these matrices as possible. In the case of dense matrices, the approximation of the required memory is trivial because the memory requirements of all matrices are known beforehand. To approximate the required memory in case of sparse matrices, we use the fact that $\underline{\tilde{B}}_{\underline{j}\mu}^{(p),M}$ becomes less sparse when the value of the respective Laplace point p becomes
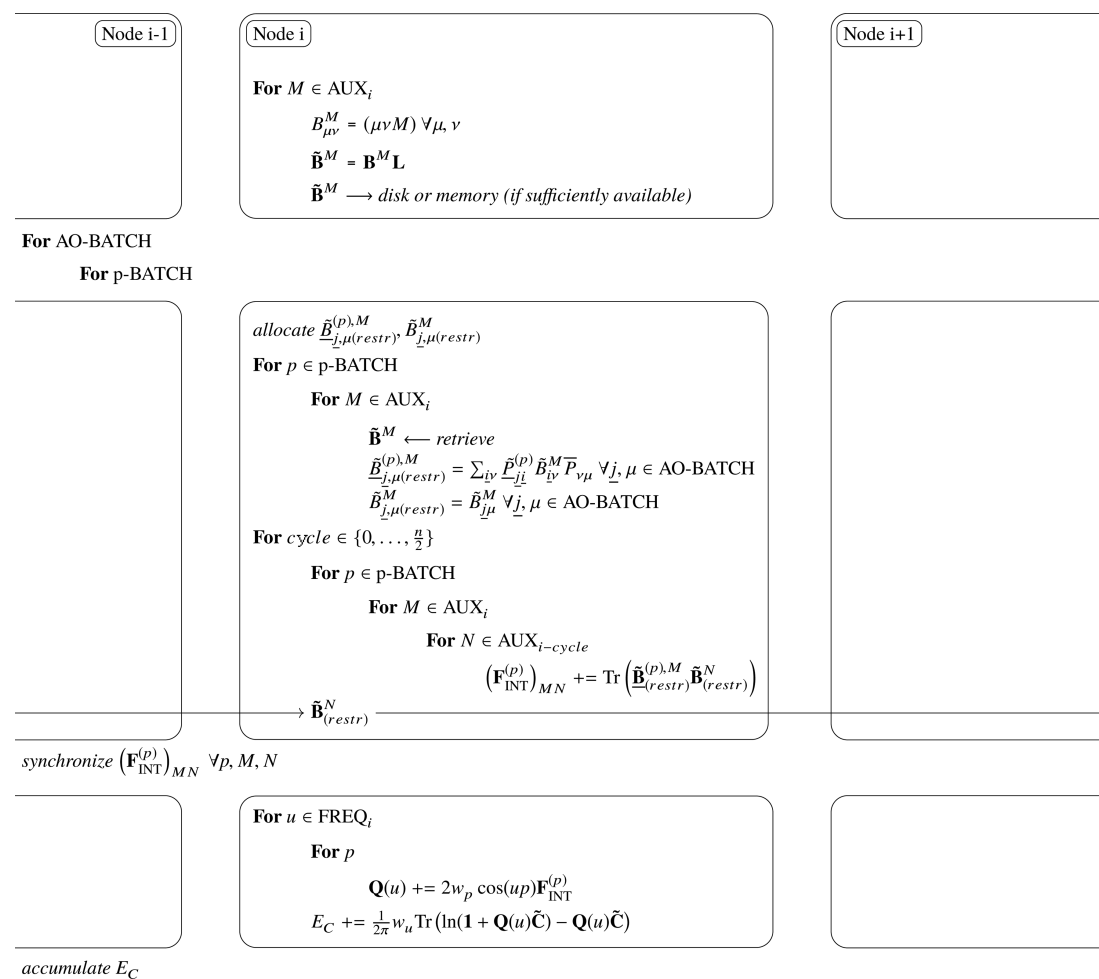

Figure 2. Pseudocode for the parallel calculation of the RPA correlation energy.

Table 1. Mean Absolute Deviations (MAD) and Maximum Absolute Deviations (MAX) of the Calculated Absolute Energies (Upper Part) as well as the Interaction Energies (Lower Part) Obtained with the ω-CDD and the New ω-CDGD Method from the Reference MO-RI-RPA Calculations for the S66 (Left) and L7 (Right) Test Sets

		S66		L7	
		MAD [H]	MAX [H]	MAD [H]	MAX [H]
absolute energies	ω-CDD	2×10^{-03}	1×10^{-02}	9×10^{-03}	4×10^{-02}
	ω-CDGD	7×10^{-07}	5×10^{-06}	9×10^{-07}	1×10^{-05}
interaction energies	ω-CDD	5×10^{-04}	3×10^{-03}	3×10^{-03}	1×10^{-02}
	ω-CDGD	9×10^{-07}	5×10^{-06}	2×10^{-06}	1×10^{-05}

smaller. Therefore, we calculate $\underline{\tilde{B}}_{j\mu}^{(p),M}$ with the smallest value of p and approximate the required memory by considering the number of allocated blocks of all necessary matrices. Note that we do not need to recalculate this matrix in the following evaluation of $\mathbf{F}_{INT}$ and, hence, this approximation does not decrease the efficiency of our algorithm. The final frequency integration (eq 28) is parallelized with respect to frequency points, which necessitates having the complete $\mathbf{F}_{INT}$ matrix on all nodes because $\mathbf{Q}(u)$ has to be computed on the fly from all $\mathbf{F}_{INT}^{(p)}$ according to eq 31. For the complete matrix to be formed on all nodes, the rotary scheme described above is again used. This time, however, at least $n-1$ cycles are necessary.

The parallel implementation described so far reduces the memory requirements of the large 3-center matrix by a factor of $\frac{n}{2}$ because two batches of $\tilde{B}_{\mu i}^{N}$ are necessary on every node. To further reduce the required memory of the algorithm (if necessary), we implemented an additional loop over batches of atomic orbitals $(AO_1...AO_c)$ on each node. Note that in this case batching with respect to atomic orbitals is superior because each batch $(\underline{\tilde{B}}_{\underline{i},\mu \in AO_1}^{(p),M \in AUX_1})$ only needs to be combined with the same AO batch of matrices $(\tilde{B}_{\mu \in AO_1,\underline{i}}^{N \in AUX_n})$ and not with all other AO batches because only the trace over atomic orbitals is necessary in the calculation of $\mathbf{F}_{INT}$. The final result for the unique part of $\mathbf{F}_{INT}$ $((\mathbf{F}_{INT})_{M \in AUX_1, N \in AUX_n})$ is then obtained by summing all results of the c AO batches.

3. COMPUTATIONAL DETAILS

The new ω-CDGD method as well as the ω-CDD[23] and the MO-RI-RPA[13] methods were implemented in the FermiONs++ program package.[41,42] Kohn–Sham orbitals used for the RPA energy calculations were obtained by preceding DFT calculations employing the generalized gradient approximation of Perdew, Burke, and Ernzerhof[43,44] (PBE) with def2-SVP, def2-TZVP, and def2-QZVP basis sets.[45,46] The RI approximation, which is only used for 4-center integrals in the correlation part of the RPA energy, uses the corresponding auxiliary basis sets[47,48] with the attenuated Coulomb metric with attenuation parameter $\omega = 0.1$. For the Laplace expansion in the AO implementations, 13–15 quadrature points were used. In the case of the ω-CDD algorithm, pretabulated values for the weights and roots of ref 49 are employed. Within the ω-CDGD method, we implemented the *sloppy Remez*[15] algorithm to obtain optimized weights for the integrated double-Laplace expansion to switch between the representation of $\mathbf{Q}$ in the imaginary time domain to the representation in the imaginary frequency domain. The MO-RI-RPA as well as the ω-CDD methods use the Clenshaw–Curtis scheme[13] with 60–100 quadrature points for the final frequency integration, whereas the ω-CDGD algorithm utilizes a minimax grid[15] with 13–15 frequency points.

For obtaining the minimax grids for the imaginary time and frequency domain, a Remez algorithm as described by Kresse and co-workers[15] was implemented. As a starting guess for the imaginary time domain, pretabulated values by Hackbusch and co-workers[49] are used. For obtaining a starting guess for the weights and roots in the imaginary frequency domain, a least-squares fit was performed utilizing the Levenberg–Marquardt algorithm[50] after the starting values were initialized randomly.

Total energies were obtained by adding the correlation energy to the exact Hamiltonian expectation value calculated from the PBE reference orbitals. Core orbitals were frozen in all RPA calculations.

For accuracy benchmarks, the full S66[51] test set of small-molecule interaction energies and the L7[52] test set of dispersion-dominated molecules of larger size were used. Investigations on performance and scaling behavior were conducted with a test set of linear n-alkanes and DNA fragments of increasing size. For the efficiency of the parallel implementation to be tested, the L7 test set was used again because the contained molecules can be seen as a representative selection of molecular sizes (15–112 atoms) for many applications. As an illustrative example for the applicability of our new method, the layer distance between two covalent organic framework (COF) pores was calculated.

4. RESULTS AND DISCUSSION

4.1. Accuracy: S66 and L7 Test Sets. First, the accuracy of the newly implemented ω-CDGD method is investigated and compared to that of the ω-CDD method.[23] Therefore, the full S66[51] test set of small-molecule interaction energies and the L7[52] benchmark set of dispersion-dominated molecules of larger size were calculated.

As reference serves our implementation of the canonical MO-RI-RPA method described by Furche and co-workers[13] using the Clenshaw–Curtis quadrature with optimization of the scaling parameter and 60 quadrature points. For the Laplace expansion in the two AO implementations, 15 quadrature points were employed. Correspondingly, 15 quadrature points were used for the final frequency integration in the ω-CDGD-RI-RPA method, and the ω-CDD algorithm used the Clenshaw–Curtis quadrature with settings equal to those of the MO-RI-RPA calculations. Note that the ω-CDD method yields better results for interaction energies when a fixed integration interval of $u \in [0;400]$ au is used.[23] However, for comparison reasons, the same settings for the frequency integration were used as for the reference calculations. The calculations of the full S66 test set were performed using the def2-QZVP basis set, whereas for the L7 test set, the def2-TZVP basis set was employed. All other settings remained equal in all calculations to facilitate comparison.

Table 1 shows the mean absolute deviation (MAD) and the maximum absolute deviation (MAX) of the calculated

correlated energies (upper part) as well as the interaction energies (lower part) using the two AO implementations from the MO reference calculations for both test sets. Starting with the S66 test set, the ω-CDGD method shows a significantly increased accuracy in absolute energies by 4 orders of magnitude with respect to both deviation measures due to the optimized integration schemes. Considering the interaction energies, the gain in accuracy is less dramatic but still lies within 3 orders of magnitude for the mean absolute as well as the maximum absolute deviation. Similar observations can be made when considering the L7 test set. The observed accuracy in the calculation of absolute energies is again increased significantly using the new ω-CDGD method. For both measures of deviation from the reference results, the occurring error is decreased by at least 3 orders of magnitude. As for the S66 test set, the difference in accuracy is smaller between the ω-CDD and the ω-CDGD implementation when referring to interaction energies. Still, the mean absolute as well as the maximum absolute deviation from the reference are lowered by 3 orders of magnitude.

4.2. Performance and Scaling Behavior. Next, the performance improvements and the scaling behavior of our new method are investigated in comparison with the preceding ω-CDD-RPA method. To do so, we calculated RPA correlation energies of a set of linear n-alkanes and DNA fragments of increasing size. The calculations on linear n-alkanes using the ω-CDD algorithm were conducted with 13 quadrature points for the Laplace expansion and 100 quadrature nodes for the frequency integration on a fixed integration interval of $u \in [0;300]$ au. The ω-CDGD method used 13 points for the frequency integration as well as the integrated double-Laplace expansion. For the calculations on the DNA fragments, we employed 15 instead of 13 quadrature points for the Laplace expansion as well as the minimax grid-based frequency integration. All calculations employed the def2-SVP basis set and were performed on an Intel Xeon E5-2667 processor using 16 threads.

4.2.1. Linear n-Alkanes. As a first test, we calculated a set of linear n-alkanes of increasing length. The results are shown in Table 2. Note that the calculations up to $C_{80}H_{162}$ were performed with standard dense matrix algebra, whereas all calculations of alkanes with larger size were conducted using sparse matrix algebra.

Considering the timings shown in Table 2, it becomes obvious that the newly implemented ω-CDGD method is asymptotically 4-times faster than the ω-CDD method for dense as well as sparse matrix algebra. This speed-up can be explained by the fact that, in the case of the ω-CDGD method, only the $\mathbf{F}_{INT}$ matrix needs to be calculated, whereas in the ω-CDD algorithm, all three expensive $\mathbf{F}$ matrices ($\mathbf{F}_0$, $\mathbf{F}_{INT}$, and $\mathbf{F}_D$) need to be evaluated. As the formation of $\mathbf{F}_0$ is independent of the Laplace points p, the time consumption is almost negligible compared to those of the other two $\mathbf{F}$ matrices. However, because the formation of $\mathbf{F}_D$ is ∼3-times as expensive as the formation of $\mathbf{F}_{INT}$ (see ref 23), a speed-up of approximately 4 is to be expected when only $\mathbf{F}_{INT}$ is computed.

A linear plot of the wall times against the number of AO basis functions is shown in Figure 3 (left). As can be seen, both implementations show a linear increase in the wall times for calculations using sparse matrix algebra (more than 1930 basis functions). In addition, the dashed line in the graph shows the wall times for the cubic-scaling frequency integration in the ω-CDGD algorithm. The contribution to the total wall time is

Table 2. Wall Times for the Calculation of RI-RPA Correlation Energies of Linear n-Alkanes with Increasing Length Using the ω-CDD and ω-CDGD Methods with the Last Column Giving the Speed-up of the Computation Time Using the ω-CDGD Method Compared to the ω-CDD Method

	molecule	N_{basis}	time [s] ω-CDD	time [s] ω-CDGD	speed-up
dense	C_5H_{12}	130	1	1	1.0
	$C_{10}H_{22}$	250	5	2	2.5
	$C_{15}H_{32}$	370	17	5	3.4
	$C_{20}H_{42}$	490	43	12	3.6
	$C_{30}H_{62}$	730	168	42	4.0
	$C_{40}H_{82}$	970	459	111	4.1
	$C_{50}H_{102}$	1210	978	232	4.2
	$C_{60}H_{122}$	1450	1887	443	4.3
	$C_{70}H_{142}$	1690	3221	763	4.2
	$C_{80}H_{162}$	1930	5329	1241	4.3
sparse	$C_{90}H_{182}$	2170	7111	1860	3.8
	$C_{100}H_{202}$	2410	7914	2072	3.8
	$C_{120}H_{242}$	2890	11348	3008	3.8
	$C_{160}H_{322}$	3850	15351	3974	3.9
	$C_{200}H_{402}$	4810	21444	5564	3.9
	$C_{300}H_{602}$	7210	40239	10003	4.0

very small even for the largest system under investigation (902 atoms) due to the small prefactor. On the right-hand side of Figure 3, a log−log plot of the wall times against the number of basis functions is shown. It shows that the scaling behavior for small as well as large systems remains roughly the same in the new implementation, however, with a significant decrease in the prefactor compared to the original implementation. As already stated above, an effective linear-scaling behavior can be observed for systems having more than 1930 basis functions in both algorithms.

4.2.2. DNA Fragments. To further investigate the performance improvements of our new method, we calculated RPA correlation energies of DNA fragments of increasing size. All calculations were performed using dense matrix algebra because no performance improvements were observed for the fairly moderate system sizes when sparse matrix algebra was applied. The results are shown in Table 3 and visualized in Figure 4. As for the set of linear n-alkanes, the ω-CDGD method is asymptotically 4-times faster than the ω-CDD algorithm. Note that the wall time for the ω-CDD-RPA calculation on the four base pair DNA fragment (DNA$_4$) was extrapolated because the memory requirements of the large 3-center integral matrix exceeded the available memory.

In conclusion, the ω-CDGD algorithm, which only makes use of the $\mathbf{F}_{INT}$ matrix calculated by just decomposing the ground state density, preserves sparsity as well as the ω-CDD method while at the same time reducing the memory requirements by a factor of $\frac{N_{basis}}{N_{occ}}$ and the run-time prefactor by a factor of 4.

4.3. Parallel Implementation. As described in section 2.4, a parallelization of the ω-CDGD method was implemented to further reduce the memory requirement of the algorithm and to speed up the calculation of RPA correlation energies to open the way for investigations of larger systems. In the following, the parallel efficiency of the implementation, defined as the observed speed-up divided by the number of nodes, is
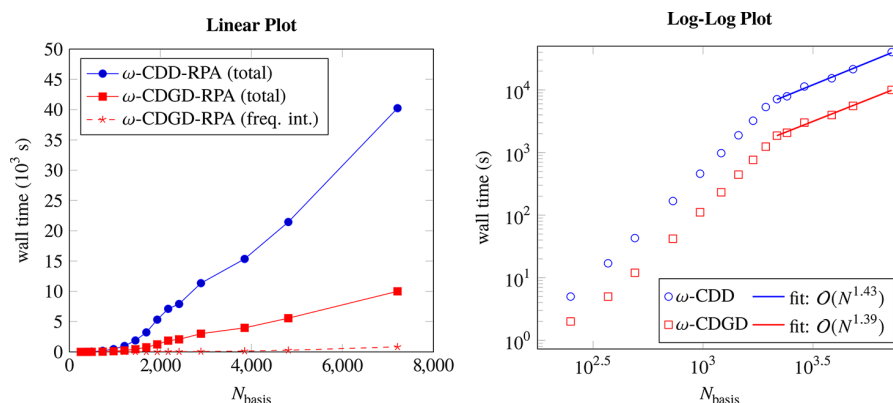
Figure 3. Linear plot (left) and the respective log−log plot (right) of the wall times for calculating RI-RPA correlation energies of linear n-alkanes using the ω-CDD (blue) and ω-CDGD (red) methods against the number of basis functions. Additionally, the wall time for the final frequency integration in the ω-CDGD method is shown (red, dashed). The log−log plot further shows linear fits for the ω-CDD (blue line) and ω-CDGD (red line) methods. For the linear fits, only data points are used, which were calculated using sparse matrix algebra.

Table 3. Wall Times for the Calculation of RI-RPA Correlation Energies of DNA Fragments with Increasing Size Using the ω-CDD and ω-CDGD Methods with the Last Column Giving the Speed-up of the Computation Time Using the ω-CDGD Method Compared to the ω-CDD Method[a]

molecule	N_{basis}	time [s]		speed-up
		ω-CDD	ω-CDGD	
DNA_1	625	126	35	3.6
DNA_2	1332	2018	528	3.8
DNA_4	2746	*32288	7755	4.2

[a]The value marked with an asterisk (*) was extrapolated conservatively.

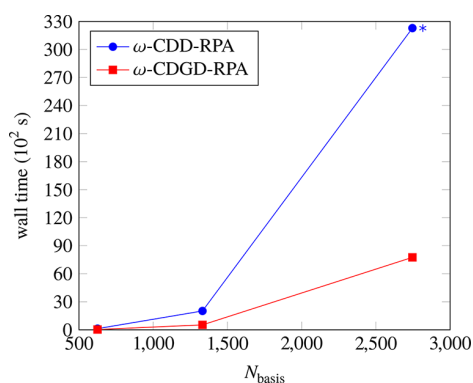**Figure 4.** Linear plot of the wall times for calculating RI-RPA correlation energies of DNA fragments (DNA_1, DNA_2, and DNA_4) using the ω-CDD (blue) and ω-CDGD (red) methods against the number of basis functions. The data point marked with an asterisk (*) was extrapolated conservatively.

investigated. To examine the changes in the parallel efficiency by varying the number of computation nodes, correlated energies of the complete L7 test set[52] were calculated on 1, 5, and 10 nodes using the def2-TZVP basis set on dual-core processor Intel Xeon E5-2620 machines using 12 threads per node. Note that these calculations do not only include the RPA correlation energy but also the Hamiltonian expectation value to give the total correlated energy of the system. The results are shown in Table 4.

Table 4. Cumulative Wall Times, Speed-ups, and Parallel Efficiencies for the Calculation of Correlated Energies of the Complete L7 Test Set Using 1, 5, and 10 Nodes

number of nodes	time [s]	speed-up	efficiency
1	33343		
5	6824	4.9	0.98
10	3840	8.7	0.87

As can be seen, using 5 compute nodes results in a speed-up in the cumulative calculation time of the complete L7 test set by 4.9, which corresponds to a parallel efficiency of 98%. On 10 computing nodes, however, the parallel efficiency decreases to 87%. This can be explained by the increase in communication over the network, which is particularly a problem for smaller systems where the ratio between communication and calculation time is large. However, because the calculation times for the relatively small systems in the L7 test set are very short even on only 1 node, the lower parallel efficiency for 10 nodes is less significant.

Focusing on larger systems, e.g., the circumcoronene guanine-cytosine base pair complex (Table 5), which is the

Table 5. Wall Times, Speed-ups, and Parallel Efficiencies for Calculating the Correlated Energy of the Circumcoronene Guanine-Cytosine Base Pair Complex (101 Atoms, 2431 Basis Functions, 5968 Auxiliary Basis Functions) from the L7 Test Set Using 1−10 Computing Nodes

number of nodes	time [s]	speed-up	efficiency
1	10074		
2	4974	2.0	1.00
4	2582	3.9	0.98
6	1673	6.0	1.00
8	1280	7.9	0.99
10	1046	9.6	0.96

system with the largest number of basis functions in the test set, shows that even with 10 nodes a parallel efficiency of 96% is observed. This means that, especially for large systems for which the parallel efficiency matters most, significant speed-ups are observed.

4.4. Illustrative Application. Efficient carbon capture and storage as well as atmospheric water capture are important

societal challenges and necessitate the development of materials with specific sorption properties. In 2015, Stegbauer et al.[53] reported that COFs show very high CO_2 and water uptake capacities at low pressures, making them highly interesting for environmental applications.

For understanding the absorption characteristics of COFs, detailed structural analyses are indispensable. One of the properties of intereset is the distance between two layers of the COF. As the interlayer distance is strongly influenced by dispersion interactions, a good description of these effects is essential for obtaining reliable computational results. We calculated total RPA energies of two azine-benzene-COF (AB-COF, see Figure 5) pores with eclipsed stacking (384
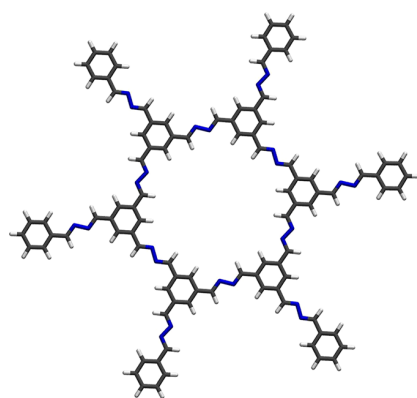

Figure 5. Structure representation of one AB-COF pore.

atoms) and distances between the two pores ranging from 3.2 to 4.0 Å using our ω-CDGD algorithm. All calculations were conducted using dense matrix algebra because no useful sparsity could be expected due to the highly delocalized electronic structure of the system. Note that the use of dense linear algebra prevents linear-scaling behavior, which relies on the sparsity of density matrices. The results are shown in Figure 6.

Although the preceding PBE calculations do not show a minimum in the calculated range with both the def2-SVP as well as the def2-TZVP basis sets, the RPA calculations clearly improve upon the PBE results and show a minimum at ~3.5 Å

using the def2-SVP basis set and a slightly right-shifted minimum at 3.6 Å with the def2-TZVP basis set. Both results for this model system are in good agreement with the experimental value of Stegbauer et al.[53] who reported an interlayer distance of 3.44 Å. As expected, the DFT calculations using the PBE functional are not sufficient to obtain reliable results for the interlayer distance of the COF due to the missing description of dispersion effects. However, with the methodology presented in this work, we are now able to correctly describe noncovalent interactions without necessitating additional parameters.

5. CONCLUSION

The memory bottleneck of our first linear-scaling RPA formulations has been overcome by a reformulation of the $\mathbf{F}_{INT}$ matrix, which only uses the Cholesky factors of the ground state density. This new formulation preserves sparsity as well as the previous Cholesky decomposition of the pseudodensities method but reduces the memory requirements of the large 3-center integral matrix by a factor of $\frac{N_{basis}}{N_{occ}}$. This is essential to further extend the applicability of this method to ever larger systems. Additionally, we have presented a parallel implementation of our method, which is shown to be highly efficient and also enables a further scalable decrease in memory requirements, opening the door for investigations of large molecules even on small- to medium-sized computing clusters. While our previous formulations required two different equations for the calculation of $\mathbf{Q}(u)$, which necessitates evaluating three different forms of $\mathbf{F}$ matrices, we have overcome this issue by utilizing minimax grids for the imaginary time and frequency domain as well as an optimized transform scheme to switch between the two domains. To this end, we have shown that $\mathbf{F}_{INT}$ is the representation of $\mathbf{Q}(u)$ in the imaginary time domain and that the integrated double-Laplace expansion is equivalent to a Fourier transform of the frequency-dependent noninteracting polarization propagator into the imaginary time domain. Employing optimized weights and roots for this transformation thus allows for using only the "INT"-formulation (eq 31). This decreases the run-time prefactor of our algorithm by a factor of 4 and at the same time increases the accuracy of our method by up to 4 orders of magnitude. Replacing the Clenshaw−Curtis scheme for the final frequency
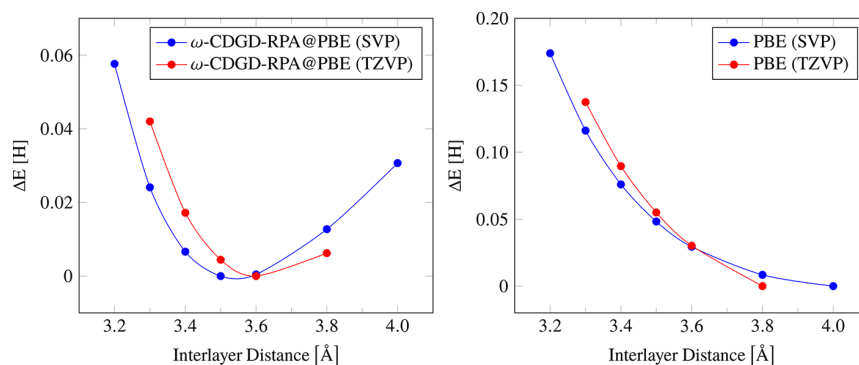
Figure 6. Plot of the relative energies of the AB-COF pore dimer calculated with the ω-CDGD method using PBE reference orbitals (left) and the PBE functional (right) employing the def2-SVP (blue) as well as the def2-TZVP (red) basis set against the interlayer distance. All data points were referenced with respect to the lowest computed value. The total wall time for each RPA correlation energy calculation using the def2-TZVP basis set is 130014 s on 10 computing nodes. The time for the communication between the nodes is 8307 s, which is approximately 6% of the total calculation time.

integration with a minimax quadrature decreases the number of quadrature points from 60−100 to 10−20 without losing accuracy. In conclusion, we have described an accurate linear-scaling RPA theory that is efficiently parallelized, has a low prefactor, is numerically very stable, and has low memory requirements that can be further lowered by distribution over multiple compute nodes. This enables calculations of large molecular systems in a fraction of the time of former theories on compute clusters typically available in local research groups. As an illustrative application, we used our new method to calculate the distance between two COF pores comprising 384 atoms and found the equilibrium distance to be in good agreement with experimental results.

■ AUTHOR INFORMATION

Corresponding Author
*E-mail: christian.ochsenfeld@uni-muenchen.de.

ORCID 🔟
Gökcen Savasci: 0000-0002-6183-7715
Christian Ochsenfeld: 0000-0002-4189-6558

Notes
The authors declare no competing financial interest.

■ REFERENCES

(1) Mardirossian, N.; Head-Gordon, M. Thirty years of density functional theory in computational chemistry: an overview and extensive assessment of 200 density functionals. *Mol. Phys.* **2017**, *115*, 2315−2372.

(2) Kristyán, S.; Pulay, P. Can (semi)local density functional theory account for the London dispersion forces? *Chem. Phys. Lett.* **1994**, *229*, 175−180.

(3) Pérez-Jordá, J.; Becke, A. A density-functional study of van der Waals forces: rare gas diatomics. *Chem. Phys. Lett.* **1995**, *233*, 134−137.

(4) Kohn, W.; Sham, L. J. Self-Consistent Equations Including Exchange and Correlation Effects. *Phys. Rev.* **1965**, *140*, A1133.

(5) Bohm, D.; Pines, D. A Collective Description of Electron Interactions: III. Coulomb Interactions in a Degenerate Electron Gas. *Phys. Rev.* **1953**, *92*, 609−625.

(6) Dobson, J. *Time-Dependent Density Functional Theory*; Springer: Berlin, Germany, 2006; Vol. 706.

(7) Fuchs, M.; Niquet, Y. M.; Gonze, X.; Burke, K. Describing static correlation in bond dissociation by Kohn-Sham density functional theory. *J. Chem. Phys.* **2005**, *122*, 094116.

(8) Harl, J.; Kresse, G. Cohesive energy curves for noble gas solids calculated by adiabatic connection fluctuation-dissipation theory. *Phys. Rev. B: Condens. Matter Mater. Phys.* **2008**, *77*, 1−8.

(9) Kresse, G.; Harl, J. Accurate Bulk Properties from Approximate Many-Body Techniques. *Phys. Rev. Lett.* **2009**, *103*, 4−7.

(10) Langreth, D. C.; Perdew, J. P. The Exchange-Correlation Energy of a Metallic Surface. *Solid State Commun.* **1975**, *17*, 1425−1429.

(11) Lume, V. O.; Langreth, D. C.; Perdew, J. P. Exchange-correlation energy of a metallic surface: Wave-vector analysis*. *Phys. Rev. B* **1977**, *15*, 2884−2901.

(12) Furche, F. Developing the random phase approximation into a practical post-Kohn-Sham correlation model. *J. Chem. Phys.* **2008**, *129*, 114105.

(13) Eshuis, H.; Yarkony, J.; Furche, F. Fast computation of molecular random phase approximation correlation energies using resolution of the identity and imaginary frequency integration. *J. Chem. Phys.* **2010**, *132*, 234114.

(14) Eshuis, H.; Furche, F. Basis set convergence of molecular correlation energy differences within the random phase approximation. *J. Chem. Phys.* **2012**, *136*, 084105.

(15) Kaltak, M.; Klimeš, J.; Kresse, G. Low Scaling Algorithms for the Random Phase Approximation: Imaginary Time and Laplace Transformations. *J. Chem. Theory Comput.* **2014**, *10*, 2498−2507.

(16) Kállay, M. Linear-scaling implementation of the direct random-phase approximation. *J. Chem. Phys.* **2015**, *142*, 204105.

(17) Schurkus, H. F.; Ochsenfeld, C. Communication: An effective linear-scaling atomic-orbital reformulation of the random-phase approximation using a contracted double-Laplace transformation. *J. Chem. Phys.* **2016**, *144*, 031101.

(18) Pulay, P. Localizability of Dynamic Electron Correlation. *Chem. Phys. Lett.* **1983**, *100*, 151−154.

(19) Kapuy, E.; Csépes, Z.; Kozmutza, C. Application of the Many-Body Perturbation Theory by Using Localized Orbitals. *Int. J. Quantum Chem.* **1983**, *23*, 981−990.

(20) Förner, W.; Ladik, J.; Otto, P.; Čížek, J. Coupled-Cluster Studies. II. The Role of Localization in Correlation Calculations on Extended Systems. *Chem. Phys.* **1985**, *97*, 251−262.

(21) Wilhelm, J.; Seewald, P.; Del Ben, M.; Hutter, J. Large-Scale Cubic-Scaling Random Phase Approximation Correlation Energy Calculations Using a Gaussian Basis. *J. Chem. Theory Comput.* **2016**, *12*, 5851−5859.

(22) Vahtras, O.; Almlöf, J.; Feyereisen, M. Integral approximations for LCAO-SCF calculations. *Chem. Phys. Lett.* **1993**, *213*, 514−518.

(23) Luenser, A.; Schurkus, H. F.; Ochsenfeld, C. Vanishing-Overhead Linear-Scaling Random Phase Approximation by Cholesky Decomposition and an Attenuated Coulomb-Metric. *J. Chem. Theory Comput.* **2017**, *13*, 1647−1655.

(24) Jung, Y.; Sodt, A.; Gill, P. M. W.; Head-Gordon, M. Auxiliary basis expansions for large-scale electronic structure calculations. *Proc. Natl. Acad. Sci. U. S. A.* **2005**, *102*, 6692−6697.

(25) Jung, Y.; Shao, Y.; Head-Gordon, M. Fast Evaluation of Scaled Opposite Spin Second-Order Møller-Plesset Correlation Energies Using Auxiliary Basis Expansions and Exploiting Sparsity. *J. Comput. Chem.* **2007**, *28*, 1953−1964.

(26) Reine, S.; Tellgren, E.; Krapp, A.; Kjærgaard, T.; Helgaker, T.; Jansik, B.; Høst, S.; Salek, P. Variational and robust density fitting of four-center two-electron integrals in local metrics. *J. Chem. Phys.* **2008**, *129*, 104101.

(27) Koch, H.; Sánchez De Merás, A.; Pedersen, T. B. Reduced scaling in electronic structure calculations using Cholesky decompositions. *J. Chem. Phys.* **2003**, *118*, 9481−9484.

(28) Higham, N. J. Cholesky factorization. *Wiley Interdiscip. Rev. Comput. Stat.* **2009**, *1*, 251−254.

(29) Harbrecht, H.; Peters, M.; Schneider, R. On the low-rank approximation by the pivoted Cholesky decomposition. *Appl. Numer. Math.* **2012**, *62*, 428−440.

(30) Zienau, J.; Clin, L.; Doser, B.; Ochsenfeld, C. Cholesky-decomposed densities in Laplace-based second-order Møller-Plesset perturbation theory. *J. Chem. Phys.* **2009**, *130*, 204112.

(31) Maurer, S. A.; Clin, L.; Ochsenfeld, C. Cholesky-decomposed density MP2 with density fitting: Accurate MP2 and double-hybrid DFT energies for large systems. *J. Chem. Phys.* **2014**, *140*, 224112.

(32) Boyd, J. P. Exponentially Convergent Fourier-Chebshev Quadrature Schemes on Bounded and Infinite Intervals. *J. Sci. Comput.* **1987**, *2*, 99−109.

(33) Einstein, A. Die Grundlage der allgemeinen Relativitätstheorie. *Ann. Phys.* **1916**, *354*, 769−822.

(34) Gunnarsson, O.; Lundqvist, B. I. Exchange and correlation in atoms, molecules, and solids by the spin-density-functional formalism. *Phys. Rev. B* **1976**, *13*, 4274−4298.

(35) Niquet, Y. M.; Fuchs, M.; Gonze, X. Exchange-correlation potentials in the adiabatic connection fluctuation-dissipation framework. *Phys. Rev. A: At., Mol., Opt. Phys.* **2003**, *68*, 032507.

(36) Furche, F.; Van Voorhis, T. Fluctuation-dissipation theorem density-functional theory. *J. Chem. Phys.* **2005**, *122*, 164106.

(37) Ullrich, C.-A. *Time-Dependent Density-Functional Theory - Concepts and Applications*; Oxford University Press: Oxford, U.K., 2012.

(38) Grundei, M. M.; Burow, A. M. Random Phase Approximation for Periodic Systems Employing Direct Coulomb Lattice Summation. *J. Chem. Theory Comput.* **2017**, *13*, 1159−1175.

(39) Bates, J. E.; Furche, F. Communication: Random phase approximation renormalized many-body perturbation theory. *J. Chem. Phys.* **2013**, *139*, 171103.

(40) Mussard, B.; Rocca, D.; Jansen, G.; Ángyán, J. G. Dielectric Matrix Formulation of Correlation Energies in the Random Phase Approximation: Inclusion of Exchange Effects. *J. Chem. Theory Comput.* **2016**, *12*, 2191−2202.

(41) Kussmann, J.; Ochsenfeld, C. Pre-selective screening for matrix elements in linear-scaling exact exchange calculations. *J. Chem. Phys.* **2013**, *138*, 134114.

(42) Kussmann, J.; Ochsenfeld, C. Preselective Screening for Linear-Scaling Exact Exchange-Gradient Calculations for Graphics Processing Units and General Strong-Scaling Massively Parallel Calculations. *J. Chem. Theory Comput.* **2015**, *11*, 918−922.

(43) Perdew, J. P.; Burke, K.; Ernzerhof, M. Generalized Gradient Approximation Made Simple [Phys. Rev. Lett. 77, 3865 (1996)]. *Phys. Rev. Lett.* **1997**, *78*, 1396−1396.

(44) Perdew, J. P.; Burke, K.; Ernzerhof, M. Generalized Gradient Approximation Made Simple. *Phys. Rev. Lett.* **1996**, *77*, 3865−3868.

(45) Weigend, F.; Furche, F.; Ahlrichs, R. Gaussian basis sets of quadruple zeta valence quality for atoms H-Kr. *J. Chem. Phys.* **2003**, *119*, 12753−12762.

(46) Weigend, F.; Ahlrichs, R. Balanced basis sets of split valence, triple zeta valence and quadruple zeta valence quality for H to Rn: Design and assessment of accuracy. *Phys. Chem. Chem. Phys.* **2005**, *7*, 3297.

(47) Weigend, F.; Häser, M.; Patzelt, H.; Ahlrichs, R. RI-MP2: optimized auxiliary basis sets and demonstration of efficiency. *Chem. Phys. Lett.* **1998**, *294*, 143−152.

(48) Hättig, C. Optimization of auxiliary basis sets for RI-MP2 and RI-CC2 calculations: Core-valence and quintuple-ζ basis sets for H to Ar and QZVPP basis sets for Li to Kr. *Phys. Chem. Chem. Phys.* **2005**, *7*, 59−66.

(49) Takatsuka, A.; Ten-No, S.; Hackbusch, W. Minimax approximation for the decomposition of energy denominators in Laplace-transformed Møller-Plesset perturbation theories. *J. Chem. Phys.* **2008**, *129*, 044112.

(50) Press, W. H.; Teukolsky, S. A.; Vetterling, W. T.; Flannery, B. P. *Numerical Recipes 3rd ed.: The Art of Scientific Computing*, 3rd ed.; Cambridge University Press: New York, NY, USA, 2007.

(51) Řezáč, J.; Riley, K. E.; Hobza, P. S66: A Well-balanced Database of Benchmark Interaction Energies Relevant to Biomolecular Structures. *J. Chem. Theory Comput.* **2011**, *7*, 2427−2438.

(52) Sedlak, R.; Janowski, T.; Pitoňák, M.; Řezáč, J.; Pulay, P.; Hobza, P. Accuracy of Quantum Chemical Methods for Large Noncovalent Complexes. *J. Chem. Theory Comput.* **2013**, *9*, 3364−3374.

(53) Stegbauer, L.; Hahn, M. W.; Jentys, A.; Savasci, G.; Ochsenfeld, C.; Lercher, J. A.; Lotsch, B. V. Tunable Water and CO_2 Sorption Properties in Isostructural Azine-Based Covalent Organic Frameworks through Polarity Engineering. *Chem. Mater.* **2015**, *27*, 7874−7881.

3.2 Low-Scaling Self-Consistent Minimization of a Density Matrix Based Random Phase Approximation Method in the Atomic Orbital Space

D. Graf, M. Beuerle, C. Ochsenfeld

J. Chem. Theory Comput. **15**, 4468 (2019).

Abstract

An efficient minimization of the random phase approximation (RPA) energy with respect to the one-particle density matrix in the atomic orbital space is presented. The problem of imposing full self-consistency on functionals depending on the potential itself is bypassed by approximating the RPA Hamiltonian on the basis of the well-known Hartree–Fock Hamiltonian making our self-consistent RPA method completely parameter-free. It is shown that the new method not only outperforms post-Kohn–Sham RPA in describing noncovalent interactions but also gives accurate dipole moments demonstrating the high quality of the calculated densities. Furthermore, the main drawback of atomic orbital based methods, in increasing the prefactor as compared to their canonical counterparts, is overcome by introducing Cholesky decomposed projectors allowing the use of large basis sets. Exploiting the locality of atomic and/or Cholesky orbitals enables us to present a self-consistent RPA method which shows asymptotically quadratic scaling opening the door for calculations on large molecular systems.
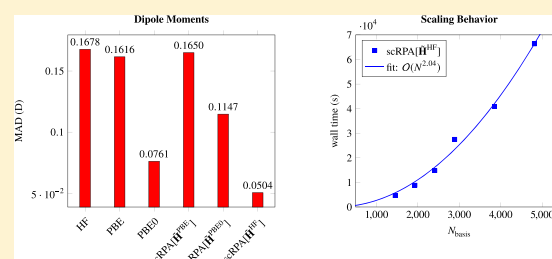
Low-Scaling Self-Consistent Minimization of a Density Matrix Based Random Phase Approximation Method in the Atomic Orbital Space

Daniel Graf, Matthias Beuerle, and Christian Ochsenfeld*

Chair of Theoretical Chemistry and Center for Integrated Protein Science Munich (CIPSM), Department of Chemistry, University of Munich (LMU), D-81377 Munich, Germany

S Supporting Information

ABSTRACT: An efficient minimization of the random phase approximation (RPA) energy with respect to the one-particle density matrix in the atomic orbital space is presented. The problem of imposing full self-consistency on functionals depending on the potential itself is bypassed by approximating the RPA Hamiltonian on the basis of the well-known Hartree−Fock Hamiltonian making our self-consistent RPA method completely parameter-free. It is shown that the new method not only outperforms post-Kohn−Sham RPA in describing noncovalent interactions but also gives accurate dipole moments demonstrating the high quality of the calculated densities. Furthermore, the main drawback of atomic orbital based methods, in increasing the prefactor as compared to their canonical counterparts, is overcome by introducing Cholesky decomposed projectors allowing the use of large basis sets. Exploiting the locality of atomic and/or Cholesky orbitals enables us to present a self-consistent RPA method which shows asymptotically quadratic scaling opening the door for calculations on large molecular systems.

1. INTRODUCTION

One of the most challenging tasks in quantum chemistry is the calculation of the electronic correlation energy. The most widely used pragmatic approach to tackle this problem is density functional theory (DFT) due to its excellent cost-performance ratio and good accuracies for certain types of compounds and properties. However, since the pioneering work of Kohn and Sham[1] in 1965, hundreds of density functionals have been developed which makes the selection of a suitable functional for a specific problem challenging[2] and also limits its predictive power. Therefore, the development of a broadly applicable and efficient correlation model is highly desirable.

Within the Kohn−Sham (KS) framework the adiabatic-connection fluctuation−dissipation theorem (ACFD)[3,4] gives an exact expression for the correlation energy. This expression depends on the density−density response function of the noninteracting (KS) system and on the response functions of the system with scaled electron−electron interactions. The KS response function is known exactly while the response functions of the interacting system need to be calculated approximately. The quantity to be approximated is the frequency-dependent exchange-correlation kernel, and in the most simple approximation it is neglected completely. This approximation is called the direct random phase approximation (dRPA) and is often denoted as RPA with the term "direct" dropped. RPA was originally introduced by Bohm and Pines in 1953[5] and contains an *ab initio* description of dispersion effects,[6] is size consistent,[7] does not depend on any empirical parameters, and, additionally, is applicable to systems with

vanishing electronic gaps.[7−9] However, in its original form,[3,4] RPA correlation energy calculations scale as $O(M^6)$ with system size M making them impractical for calculations on systems of larger size. Much work has been put in the development of efficient RPA algorithms in recent years[10−18] allowing for RPA calculations on systems with more than 1000 atoms.[14−18]

RPA calculations are in most cases performed in a post-KS fashion, which means that the RPA functional is evaluated using orbitals and respective orbital energies stemming from a self-consistent semilocal DFT calculation. This, however, leads to nonvariational total energies and unrelaxed orbitals which cause large density-driven errors.[19,20]

The optimized effective potential approach[21−24] (OEP) to evaluate the RPA functional self-consistently yields accurate local exchange-correlation (XC) potentials and KS orbital energies which showed to give good estimates for ionization potentials and band gaps.[22] However, the reported results for bond energies and noncovalent interactions are less accurate than their non-self-consistent counterparts.[22] The generalized optimized effective potential method developed by Yang and co-workers,[25] however, yields improved energetics compared to standard RPA but the orbital energies do not have physical meanings. Furche and co-workers[26] very recently put forward a variational generalized Kohn−Sham approach which combines both improved energetics as well as accurate orbital energies.

In this work we present a minimization of the RPA correlation energy with respect to the one-particle density matrix in the atomic orbital (AO) space. The presented method shows a low-scaling behavior and not only leads to improved energetics but also to accurate dipole moments indicating the high quality of the calculated densities.

2. THEORY

2.1. Atomic Orbital Direct Random Phase Approximation. In this work the following notation has been adopted: μ, ν, λ, σ denote atomic orbitals (AOs); i, j, occupied molecular orbitals (MOs); a, b, virtual MOs; $\underline{i}$, $\underline{j}$, Cholesky orbitals; M, N, auxiliary resolution-of-the-identity (RI) functions. The number of basis functions is represented by N_{basis}, the number of auxiliary RI functions by N_{aux}, and the numbers of occupied and virtual molecular orbitals by N_{occ} and N_{virt}, respectively. For 2-, 3-, and 4-center integrals, the Mulliken notation is employed. Furthermore, Einstein's sum convention[27] is used and the spin index is dropped for convenience.

Within the adiabatic connection formalism,[28] the total energy can be expressed as[3,4]

$$E = E_{\text{h}}[\{\phi_{\text{KS}}\}] + E_{\text{J}}[\{\phi_{\text{KS}}\}] + E_{\text{X}}[\{\phi_{\text{KS}}\}] + E_{\text{c}} \qquad (1)$$

where E_{h}, E_{J}, and E_{X} denote the one-electron, Coulomb, and the exact exchange energy, respectively. Using the zero-temperature fluctuation−dissipation theorem and the RPA[29] together with the RI approximation,[10−12] the correlation energy E_{c} is given by

$$E_{\text{c}}^{\text{RPA}} = \frac{1}{2\pi} \int_{0}^{+\infty} d\omega \, \text{Tr}[\ln(1 - \mathbf{X}_0(i\omega)\mathbf{V}) + \mathbf{X}_0(i\omega)\mathbf{V}] \qquad (2)$$

where $\mathbf{V}$ represents the Coulomb operator in the auxiliary basis

$$V_{MN} = (M|m_{12}|P)^{-1}(P|r_{12}^{-1}|Q)(Q|m_{12}|N)^{-1} \qquad (3)$$

with the RI metric m_{12} and the interelectronic distance r_{12}. $\mathbf{X}_0$ denotes the noninteracting density−density response function in the auxiliary basis in the zero-temperature case.[30] For the sake of efficiency, the response function is calculated in the imaginary time domain

$$X_{0,MN}(i\tau) = G_{0,\mu\nu}(-i\tau)B_{\nu\lambda}^{M}G_{0,\lambda\sigma}(i\tau)B_{\sigma\mu}^{N} \qquad (4)$$

and afterward transformed with a contracted double-Laplace[15] or cosine[13] transformation

$$\mathbf{X}_0(i\omega) = \int_{-\infty}^{+\infty} d\tau \, \cos(\omega\tau)\mathbf{X}_0(i\tau) \qquad (5)$$

to obtain the respresentation in the imaginary frequency domain. In eq 4, $\mathbf{G}_0(i\tau)$ denotes the one-particle Green's function in the imaginary time domain and is given by

$$\mathbf{G}_0(i\tau) = \Theta(-i\tau)\underline{\mathbf{G}}_0(i\tau) + \Theta(i\tau)\overline{\mathbf{G}}_0(i\tau) \qquad (6)$$

$$\underline{\mathbf{G}}_0(i\tau) = C_{\mu i}C_{\nu i}\exp(-(\varepsilon_i - \varepsilon_{\text{F}})\tau) \qquad (7)$$

$$\overline{\mathbf{G}}_0(i\tau) = -C_{\mu a}C_{\nu a}\exp(-(\varepsilon_a - \varepsilon_{\text{F}})\tau) \qquad (8)$$

with the occupied ($C_{\mu i}$) and unoccupied ($C_{\mu a}$) MO coefficients and the respective MO energies ε_i and ε_a. $\Theta(i\tau)$ denotes the Heaviside step function, and ε_{F}, the Fermi level. The three-center integral matrix $\mathbf{B}$ is given by

$$B_{\mu\nu}^{M} = (\mu\nu|m_{12}|M) \qquad (9)$$

The most time-consuming step in AO-RI-RPA is the formation of the response function in the imaginary time domain (eq 4). To reduce the scaling with the basis set size, Luenser et al.[16] introduced pivoted Cholesky-decomposition[31−35] of density and pseudodensity matrices which brings the scaling with basis set size back to $O(N_{\text{aux}}^2 N_{\text{basis}} N_{\text{occ}})$.

Very recently, the AO-RI-RPA algorithm was improved even further by our group[17] where we arrived at a formulation for the calculation of the response function in the imaginary time domain given by

$$X_{0,MN}(i\tau) = \text{Tr}(\mathbf{L}^{\text{T}}\mathbf{S}\underline{\mathbf{G}}_0(-i\tau)\mathbf{S}\mathbf{L}\mathbf{L}^{\text{T}}\mathbf{B}^{M}\overline{\mathbf{G}}_0(i\tau)\mathbf{B}^{N}\mathbf{L}) \qquad (10)$$

$$= \underline{G}_{0,\underline{j}\,\underline{i}}(-i\tau)B_{\underline{i}\nu}^{M}\overline{G}_{0,\nu\mu}(i\tau)B_{\mu\underline{j}}^{N} \qquad (11)$$

with the two-center overlap $\mathbf{S}$ and the Cholesky factor $\mathbf{L}$ of the occupied one-particle density $\mathbf{P}$. Note that all quantities in eq 11 become sparse for large systems with nonvanishing band gaps when a local metric is employed, and therefore, the calculation scales linearly with the system size.

2.2. Minimization of the AO-RI-RPA Functional with Respect to the Occupied One-Particle Density Matrix. In order to calculate the gradient with respect to the occupied one-particle density matrix $\mathbf{P}$, we express the RPA functional in terms of that quantity

$$E^{\text{RPA}}[\mathbf{P}] = E_{\text{h}}[\mathbf{P}] + E_{\text{J}}[\mathbf{P}] + E_{\text{X}}[\mathbf{P}] + E_{\text{c}}^{\text{RPA}}[\mathbf{P}]$$

$$= E^{\text{HF}}[\mathbf{P}] + E_{\text{c}}^{\text{RPA}}[\mathbf{P}] \qquad (12)$$

Note that the sum of the one-particle, the Coulomb, and the exact exchange energy contributions is the well-known Hartree−Fock (HF) energy. To obtain an RPA functional of the one-particle density matrix, we express the one-particle Green's functions as

$$\mathbf{G}_0(i\tau) = \mathbf{P}\exp(-\tau(\mathbf{H} - \varepsilon_{\text{F}}\mathbf{S})\mathbf{P}) \qquad (13)$$

$$\overline{\mathbf{G}}_0(i\tau) = -\mathbf{P}^{\text{virt}}\exp(-\tau(\mathbf{H} - \varepsilon_{\text{F}}\mathbf{S})\mathbf{P}^{\text{virt}}) \qquad (14)$$

with the unoccupied/virtual one-particle density matrix $\mathbf{P}^{\text{virt}}$ and the Hamiltonian $\mathbf{H}$. Differentiating the total RPA energy with respect to the one-particle density matrix $\mathbf{P}$ results in the RPA Hamiltonian

$$\frac{\partial E^{\text{RPA}}[\mathbf{P}]}{\partial \mathbf{P}} = \frac{\partial E^{\text{HF}}[\mathbf{P}]}{\partial \mathbf{P}} + \frac{\partial E_{\text{c}}^{\text{RPA}}[\mathbf{P}]}{\partial \mathbf{P}} = \mathbf{H}_0^{\text{HF}} + \mathbf{V}_{\text{c}}^{\text{RPA}}$$

$$= \mathbf{H}_0^{\text{RPA}} \qquad (15)$$

with the well-known Hartree−Fock Hamiltonian $\mathbf{H}_0^{\text{HF}}$ and the nonlocal RPA correlation potential $\mathbf{V}_{\text{c}}^{\text{RPA}}$. As can be seen in the definition of the one-particle Green's functions, the RPA functional depends on the potential itself and for complete functional self-consistency the Hamiltonian in eqs 13 and 14 should be replaced by the RPA Hamiltonian. To bypass this dilemma we follow the idea of Furche and co-workers[26] and construct an approximated RPA Hamiltonian which is forced to yield the exact same density after diagonalization as the RPA Hamiltonian. To achieve this, the approximated Hamiltonian is built using the density obtained by diagonalizing the RPA Hamiltonian and projecting out the occupied-virtual and virtual-occupied parts according to

$$\tilde{\mathbf{H}} = \mathbf{SPHPS} + \mathbf{SP}^{\text{virt}}\mathbf{HP}^{\text{virt}}\mathbf{S} \qquad (16)$$

Inserting this Hamiltonian in eqs 13 and 14 yields the final expressions for calculating the one-particle Green's functions

$$\underline{\mathbf{G}}_0(i\tau) = \mathbf{P}\exp(-\tau(\tilde{\mathbf{H}} - \varepsilon_{\mathrm{F}}\mathbf{S})\mathbf{P}) \tag{17}$$

$$\overline{\mathbf{G}}_0(i\tau) = -\mathbf{P}^{\mathrm{virt}}\exp(-\tau(\tilde{\mathbf{H}} - \varepsilon_{\mathrm{F}}\mathbf{S})\mathbf{P}^{\mathrm{virt}}) \tag{18}$$

To obtain the conceptually most correct result, the approximated Hamiltonian should give an eigenvalue spectrum which resembles the one of the RPA Hamiltonian as accurately as possible. In section 4 we will compare and discuss different choices of approximated Hamiltonians and investigate the effect on the obtained results.

In the following, we will present the derivation of the equations for the efficient calculation of the RPA correlation potential in the atomic orbital space. The derivative of the RPA correlation energy with respect to one density matrix element is given by

$$V_{\mathrm{c},\mu\nu}^{\mathrm{RPA}} = \mathrm{Tr}\left(\frac{\partial E_{\mathrm{c}}^{\mathrm{RPA}}}{\partial \mathbf{X}_0(i\omega)} \frac{\partial \mathbf{X}_0(i\omega)}{\partial \mathbf{G}_0(i\tau)} \frac{\partial \mathbf{G}_0(i\tau)}{\partial P_{\mu\nu}}\right) \tag{19}$$

with the trace implying integration over imaginary frequency and imaginary time. Since the derivative of the RPA correlation energy with respect to the one-particle Green's function is the correlation part of the RPA self-energy[36] which also occurs in the calculation of nuclear gradients[37] and is obtained according to

$$\Sigma_{\mu\nu}(i\tau) = -B_{\mu\lambda}^M G_{0,\lambda\sigma}(i\tau) W_{\mathrm{c}}^{MN}(i\tau) B_{\sigma\nu}^N \tag{20}$$

with W_{c} denoting the correlated screened Coulomb interaction given by

$$\mathbf{W}_{\mathrm{c}}(i\omega) = \mathbf{V}[(1 - \mathbf{X}_0(i\omega)\mathbf{V})^{-1} - 1] \tag{21}$$

$$\mathbf{W}_{\mathrm{c}}(i\tau) = \frac{1}{2\pi} \int_{-\infty}^{+\infty} d\omega \, \cos(\omega\tau) \mathbf{W}_{\mathrm{c}}(i\omega) \tag{22}$$

we can simplify eq 19 yielding

$$V_{\mathrm{c},\mu\nu}^{\mathrm{RPA}} = \mathrm{Tr}\left(\int_{-\infty}^{+\infty} d\tau \, \boldsymbol{\Sigma}(-i\tau)\frac{\partial \mathbf{G}_0(i\tau)}{\partial P_{\mu\nu}}\right) \tag{23}$$

$$= \mathrm{Tr}\left(\int_0^{+\infty} d\tau \left(\boldsymbol{\Sigma}(i\tau)\frac{\partial \underline{\mathbf{G}}_0(-i\tau)}{\partial P_{\mu\nu}} + \boldsymbol{\Sigma}(-i\tau)\right.\right. \tag{24}$$
$$\left.\left.\frac{\partial \overline{\mathbf{G}}_0(i\tau)}{\partial P_{\mu\nu}}\right)\right)$$

The derivative of the one-particle Green's function with respect to the ground state density matrix $\mathbf{P}$ can be split into three parts. The first part accounts for changes of the Green's functions while keeping the approximated Hamiltonian fixed. The second part includes the changes in the projection of the underlying Hamiltonian $\mathbf{H}$ and the last part arises from changes in the density entering the underlying Hamiltonian. In the following we will present the most important steps of the derivation of the terms for negative imaginary time. The terms for positive imaginary time can be obtained analogously.

The first part of the derivative of the one-particle Green's function in negative imaginary times with respect to one density matrix element is given by

$$\left(\frac{\partial \underline{G}_{0,\mu\nu}(-i\tau)}{\partial P_{\lambda\sigma}}\right)_1 = \frac{\partial P_{\mu\kappa}}{\partial P_{\lambda\sigma}}(\exp\{+\tau(\tilde{\mathbf{H}} - \varepsilon_{\mathrm{F}}\mathbf{S})\mathbf{P}\})_{\kappa\nu}$$
$$+ P_{\mu\kappa}\exp\left\{+\tau(\tilde{H}_{\kappa\gamma} - \varepsilon_{\mathrm{F}}S_{\kappa\gamma})\frac{\partial P_{\gamma\nu}}{\partial P_{\lambda\sigma}}\right\} \tag{25}$$

To calculate the second term of eq 25 we employ the series expansion of the matrix exponential[38−40]

$$\underline{\mathbf{G}}_0(-i\tau) = \mathbf{P}\exp(+\tau(\tilde{\mathbf{H}} - \varepsilon_{\mathrm{F}}\mathbf{S})\mathbf{P})$$
$$= \mathbf{P}\sum_{k=0}^{\infty}\frac{1}{k!}(+\tau(\tilde{\mathbf{H}} - \varepsilon_{\mathrm{F}}\mathbf{S})\mathbf{P})^k \tag{26}$$

yielding

$$\left(\frac{\partial \underline{G}_{0,\mu\nu}(-i\tau)}{\partial P_{\lambda\sigma}}\right)_1 = \frac{\partial P_{\mu\kappa}}{\partial P_{\lambda\sigma}}(\exp\{+\tau(\tilde{\mathbf{H}} - \varepsilon_{\mathrm{F}}\mathbf{S})\mathbf{P}\})_{\kappa\nu}$$
$$+ P_{\mu\kappa}\sum_{k=1}^{\infty}\sum_{l=0}^{k-1}\frac{\tau^k}{k!}((\tilde{\mathbf{H}} - \varepsilon_{\mathrm{F}}\mathbf{S})\mathbf{P})_{\kappa\mu'}^l(\tilde{H}_{\mu'\gamma} - \varepsilon_{\mathrm{F}}S_{\mu'\gamma})\frac{\partial P_{\gamma\nu'}}{\partial P_{\lambda\sigma}}$$
$$((\tilde{\mathbf{H}} - \varepsilon_{\mathrm{F}}\mathbf{S})\mathbf{P})_{\nu'\nu}^{k-1-l} \tag{27}$$

With

$$\frac{\partial P_{\mu\kappa}}{\partial P_{\lambda\sigma}} = \delta_{\mu\lambda}\delta_{\kappa\sigma} \tag{28}$$

$$\underline{\mathbf{Y}}(-i\tau) = \sum_{k=1}^{\infty}\sum_{l=0}^{k-1}\frac{\tau^k}{k!}((\tilde{\mathbf{H}} - \varepsilon_{\mathrm{F}}\mathbf{S})\mathbf{P})^{k-1-l}\boldsymbol{\Sigma}(i\tau)\mathbf{P}$$
$$((\tilde{\mathbf{H}} - \varepsilon_{\mathrm{F}}\mathbf{S})\mathbf{P})^l \tag{29}$$

and inserting into

$$\mathrm{Tr}\left(\int_0^{+\infty} d\tau \, \boldsymbol{\Sigma}(i\tau)\frac{\partial \underline{\mathbf{G}}_0(-i\tau)}{\partial P_{\mu\nu}}\right) \tag{30}$$

we finally get

$$\underline{\mathbf{V}}_{\mathrm{c},1}^{\mathrm{RPA}} = \int_0^{+\infty} d\tau \, (\exp\{+\tau(\tilde{\mathbf{H}} - \varepsilon_{\mathrm{F}}\mathbf{S})\mathbf{P}\}\boldsymbol{\Sigma}(i\tau)$$
$$+ \underline{\mathbf{Y}}(-i\tau)(\tilde{\mathbf{H}} - \varepsilon_{\mathrm{F}}\mathbf{S})) \tag{31}$$

To calculate the derivative of the virtual density matrix $\mathbf{P}^{\mathrm{virt}}$ occurring in the Green's function for positive imaginary times, we make use of the completeness relation[38]

$$1 = \mathbf{P}\mathbf{S} + \mathbf{P}^{\mathrm{virt}}\mathbf{S} \tag{32}$$

to obtain

$$\frac{\partial P_{\mu\kappa}^{\mathrm{virt}}}{\partial P_{\lambda\sigma}} = -\delta_{\mu\lambda}\delta_{\kappa\sigma} \tag{33}$$

Therefore, part one of the RPA correlation potential for positive imaginary times is given by

$$\overline{\mathbf{V}}_{\mathrm{c},1}^{\mathrm{RPA}} = \int_0^{+\infty} d\tau(\exp\{-\tau(\tilde{\mathbf{H}} - \varepsilon_{\mathrm{F}}\mathbf{S})\mathbf{P}^{\mathrm{virt}}\}\boldsymbol{\Sigma}(-i\tau)$$
$$+ \overline{\mathbf{Y}}(i\tau)(\tilde{\mathbf{H}} - \varepsilon_{\mathrm{F}}\mathbf{S})) \tag{34}$$

with

$$\overline{\mathbf{Y}}(i\tau) = \sum_{k=1}^{\infty} \sum_{l=0}^{k-1} \frac{(-\tau)^k}{k!} ((\tilde{\mathbf{H}} - \varepsilon_{\mathrm{F}}\mathbf{S})\mathbf{P}^{\mathrm{virt}})^{k-1-l} \Sigma(-i\tau)\mathbf{P}^{\mathrm{virt}}$$

$$((\tilde{\mathbf{H}} - \varepsilon_{\mathrm{F}}\mathbf{S})\mathbf{P}^{\mathrm{virt}})^l \tag{35}$$

The second part of the Green's function derivative focuses on the change in the projection of the underlying Hamiltonian $\mathbf{H}$ and is given by

$$\left(\frac{\partial \underline{G}_{0,\mu\nu}(-i\tau)}{\partial P_{\lambda\sigma}}\right)_2 = P_{\mu\kappa}\exp\left\{+\tau\left(S_{\kappa\mu'}\frac{\partial P_{\mu'\nu'}}{\partial P_{\lambda\sigma}}H_{\nu'\gamma'}P_{\gamma'\kappa}S_{\kappa'\gamma}\right)P_{\gamma\nu}\right\}$$

$$+ P_{\mu\kappa}\exp\left\{+\tau\left(S_{\kappa\mu'}\frac{\partial P^{\mathrm{virt}}_{\mu'\nu'}}{\partial P_{\lambda\sigma}}H_{\nu'\gamma'}P^{\mathrm{virt}}_{\gamma'\kappa}S_{\kappa'\gamma}\right)P_{\gamma\nu}\right\} + \text{transpose} \tag{36}$$

Since

$$\mathbf{PSP}^{\mathrm{virt}} = 0 \tag{37}$$

the second term and also its transpose vanish. Using the series expansion and inserting into eq 30 finally yields

$$\underline{\mathbf{V}}^{\mathrm{RPA}}_{c,2} = \int_0^{+\infty} \mathrm{d}\tau \, (\mathbf{SP}\underline{\mathbf{Y}}(-i\tau)\mathbf{SPH} + \mathbf{HPS}\underline{\mathbf{Y}}^{\mathrm{T}}(-i\tau)\mathbf{PS}) \tag{38}$$

Analogously, we obtain for positive imaginary times

$$\overline{\mathbf{V}}^{\mathrm{RPA}}_{c,2} = \int_0^{+\infty} \mathrm{d}\tau \, (\mathbf{SP}^{\mathrm{virt}}\overline{\mathbf{Y}}(i\tau)\mathbf{SP}^{\mathrm{virt}}\mathbf{H} + \mathbf{HP}^{\mathrm{virt}}\mathbf{S}\overline{\mathbf{Y}}^{\mathrm{T}}(i\tau)$$

$$\mathbf{P}^{\mathrm{virt}}\mathbf{S}) \tag{39}$$

The third and last part stems from changes in the density entering the underlying Hamiltonian $\mathbf{H}$ and is given by

$$\left(\frac{\partial \underline{G}_{0,\mu\nu}(-i\tau)}{\partial P_{\lambda\sigma}}\right)_3 = P_{\mu\kappa}\exp\left\{+\tau\left(S_{\kappa\mu'}P_{\mu'\nu'}\frac{H_{\nu'\gamma'}}{\partial P_{\lambda\sigma}}P_{\gamma'\kappa}S_{\kappa'\gamma}\right)P_{\gamma\nu}\right\}$$

$$+ P_{\mu\kappa}\exp\left\{+\tau\left(S_{\kappa\mu'}P^{\mathrm{virt}}_{\mu'\nu'}\frac{H_{\nu'\gamma'}}{\partial P_{\lambda\sigma}}P^{\mathrm{virt}}_{\gamma'\kappa}S_{\kappa'\gamma}\right)P_{\gamma\nu}\right\} \tag{40}$$

with

$$\frac{H_{\nu'\gamma'}}{\partial P_{\lambda\sigma}} = (\nu'\gamma'|\lambda\sigma) + (\nu'\gamma'|f_{\mathrm{XC}}|\lambda\sigma) \tag{41}$$

and f_{XC} denoting the exchange-correlation kernel of the underlying Hamiltonian. Again, the second term vanishes and by employing the series expansion and inserting into eq 30 we get

$$\underline{\mathbf{V}}^{\mathrm{RPA}}_{c,3} = \int_0^{+\infty} \mathrm{d}\tau \, P_{\mu\kappa}\underline{Y}_{\kappa\gamma}(-i\tau)S_{\gamma\kappa'}P_{\kappa'\nu}[(\mu\nu|\lambda\sigma)$$

$$+ (\mu\nu|f_{\mathrm{XC}}|\lambda\sigma)] \tag{42}$$

For positive imaginary times, we obtain

$$\overline{\mathbf{V}}^{\mathrm{RPA}}_{c,3} = \int_0^{+\infty} \mathrm{d}\tau \, P^{\mathrm{virt}}_{\mu\kappa}\overline{Y}_{\kappa\gamma}(i\tau)S_{\gamma\kappa}P^{\mathrm{virt}}_{\kappa'\nu}[(\mu\nu|\lambda\sigma)$$

$$+ (\mu\nu|f_{\mathrm{XC}}|\lambda\sigma)] \tag{43}$$

and the complete RPA correlation potential is then finally given by

$$\mathbf{V}^{\mathrm{RPA}}_{c} = \underline{\mathbf{V}}^{\mathrm{RPA}}_{c,1} + \overline{\mathbf{V}}^{\mathrm{RPA}}_{c,1} + \underline{\mathbf{V}}^{\mathrm{RPA}}_{c,2} + \overline{\mathbf{V}}^{\mathrm{RPA}}_{c,2} + \underline{\mathbf{V}}^{\mathrm{RPA}}_{c,3} + \overline{\mathbf{V}}^{\mathrm{RPA}}_{c,3} \tag{44}$$

2.3. Cholesky Decomposition of the Occupied One-Particle Density.

So far we presented the calculation of the RPA correlation potential in the atomic orbital space. While it is well-known that atomic orbital formulations show low- or even linear-scaling behaviors due to the local nature of atomic orbitals, a drawback is the significantly increased prefactor compared to molecular orbital formulations. One way to remedy the mentioned increased prefactor is to employ pivoted Cholesky decomposition of positive-semidefinite matrices.[31−35] Particularly useful is the decomposition of quantities corresponding to occupied orbitals such as the occupied one-particle density matrix $\mathbf{P}$ since the rank of the matrix can be lowered to at least N_{occ}. In the following discussion we will abbreviate the pivoted Cholesky factorization by $\mathbf{A} = \mathbf{L}\mathbf{L}^{\mathrm{T}}$ where $\mathbf{L}$ denotes the Cholesky factor of matrix $\mathbf{A}$ with dimensions rows $(\mathbf{A}) \times$ rank $(\mathbf{A})$.

The most time-consuming step in our algorithm is the contraction of the screened Coulomb interaction $\mathbf{W}_c$ with the three-center integral matrix $\mathbf{B}$ occurring in the calculation of the correlated self-energy (eq 20) and scales formally as $O(N^2_{\mathrm{aux}}N^2_{\mathrm{basis}})$. In the second term of eq 24, the correlated RPA self-energy for negative imaginary times occurs which is given by

$$\Sigma_{\mu\nu}(-i\tau) = -B^M_{\mu\lambda}G_{0,\lambda\sigma}(-i\tau)B^N_{\sigma\nu}W^{NM}_c(-i\tau) \tag{45}$$

Since the one-particle Green's function in the negative imaginary time domain is invariant with respect to projection onto the occupied space, we can reformulate the expression according to

$$\Sigma_{\mu\nu}(-i\tau) = -B^M_{\mu\lambda}G_{0,\lambda\sigma}(-i\tau)S_{\sigma\gamma}P_{\gamma\kappa}B^N_{\kappa\nu}W^{NM}_c(-i\tau) \tag{46}$$

$$= -B^M_{\mu\lambda}G_{0,\lambda\sigma}(-i\tau)S_{\sigma\gamma}L_{\gamma\underline{i}}L^{\mathrm{T}}_{\underline{i}\kappa}B^N_{\kappa\nu}W^{NM}_c(-i\tau) \tag{47}$$

$$= -B^M_{\mu\lambda}G_{0,\lambda\underline{i}}(-i\tau)B^N_{\underline{i}\nu}W^{NM}_c(-i\tau) \tag{48}$$

which reduces the formal scaling of the contraction to $O(N^2_{\mathrm{aux}}N_{\mathrm{basis}}N_{\mathrm{occ}})$. For the first term in eq 24 the self-energy in the positive imaginary time domain needs to be calculated which can be expressed as

$$\Sigma_{\mu\nu}(i\tau) = -B^M_{\mu\lambda}\overline{G}_{0,\lambda\sigma}(i\tau)B^N_{\sigma\nu}W^{NM}_c(i\tau) \tag{49}$$

Here, the one-particle Green's function for positive imaginary times occurs for which the projection onto the occupied space is not invariant and therefore prevents the application of the scheme described above to reduce the scaling behavior. Realizing, however, that for the minimization of the RPA energy only the occupied-occupied, occupied-virtual, and virtual-occupied part of the potential is necessary, we can calculate

$$\tilde{\mathbf{V}}^{\mathrm{RPA}}_{c,1} = \underline{\mathbf{V}}^{\mathrm{RPA}}_{c,1}\mathbf{PS} \tag{50}$$

instead of the complete matrix $\underline{\mathbf{V}}^{\mathrm{RPA}}_{c,1}$. Therefore, only

$$\Sigma_{\mu\nu}(i\tau)\mathbf{PS} = -B^M_{\mu\lambda}\overline{G}_{0,\lambda\sigma}(i\tau)W^{MN}_c(i\tau)B^N_{\sigma\gamma}P_{\gamma\kappa}S_{\kappa\nu} \tag{51}$$

$$= -B^M_{\mu\lambda}\overline{G}_{0,\lambda\sigma}(i\tau)W^{MN}_c(i\tau)B^N_{\sigma\gamma}L_{\gamma\underline{i}}L^{\mathrm{T}}_{\underline{i}\kappa}S_{\kappa\nu} \tag{52}$$

$$= -B^M_{\mu\lambda}\overline{G}_{0,\lambda\sigma}(i\tau)W^{MN}_c(i\tau)B^N_{\sigma\underline{i}}S_{\underline{i}\nu} \tag{53}$$

needs to be calculated which again scales as $O(N_{aux}^2 N_{basis} N_{occ})$. The necessary blocks of $\underline{\mathbf{V}}_{c,1}^{RPA}$ can then be obtained by the projections

$$\underline{\mathbf{V}}_{c,1,oo}^{RPA} = \mathbf{S}\mathbf{P}\underline{\tilde{V}}_{c,1}^{RPA} \tag{54}$$

$$\underline{\mathbf{V}}_{c,1,vo}^{RPA} = \mathbf{S}\mathbf{P}^{virt}\underline{\tilde{V}}_{c,1}^{RPA} \tag{55}$$

$$\underline{\mathbf{V}}_{c,1,ov}^{RPA} = (\underline{\mathbf{V}}_{c,1,vo}^{RPA})^T \tag{56}$$

Note that in cases where virtual orbital energies are necessary, e.g., for the calculation of band gaps, the occupied space we are projecting onto can be extended by a variable number of virtual orbitals while excluding them from the virtual space. The resulting matrix $\mathbf{P}^{proj}$ is still positive semidefinite and can be Cholesky decomposed. This of course increases the rank of the resulting Cholesky factor by the number of the included virtual orbitals.

3. COMPUTATIONAL DETAILS

The presented self-consistent RPA method was implemented analytically and numerically in the FermiONs++ program package developed in our group.[41−43] To investigate the dependence of the method on the chosen approximated Hamiltonian, we use the PBE,[44,45] PBE0,[46] and HF functionals to calculate the XC potential.

As atomic basis sets, the def2-SVP, def2-TZVP,[47,48] cc-pV5Z, aug-cc-pV5Z,[49,50] and aug-cc-pV6Z[51,52] basis sets are employed. For the resolution-of-the-identity which is used for four-center integrals in the calculation of the RPA correlation potential, the corresponding auxiliary basis sets[53,54] are used with the standard Coulomb metric. For efficient calculations of RPA correlation potentials of larger systems, the attenuated Coulomb metric[55−57] with attenuation parameter $\omega = 0.1$[16] is used along with sparse matrix algebra.

For integrations along imaginary time and frequency as well as transformations between the two domains, we use optimized minimax grids with in general 15 quadrature points.[13,17] Kohn−Sham orbitals used for ω-CDGD-RPA calculations were obtained by preceding DFT calculations using the PBE functional.

The convergence criterion for all self-consistent calculations is the root-mean-square of the $[\mathbf{H}, \mathbf{P}]$-commutator which needs to fall below a threshold of 1.0×10^{-7} in general.

4. RESULTS AND DISCUSSION

4.1. Comparison with Numerical Potentials. In this section we validate our implementation by comparison with numerical results. As a first step we compare the RPA correlation potentials obtained analytically as presented above with the respective numerical potentials for three small molecular systems. The numerical potentials were obtained by performing density matrix based RPA correlation energy calculations using density matrices with small perturbations (1.0×10^{-8}) in the respective density matrix elements and applying the five-point stencil method. To further prove correctness of our implementation, we performed full SCF calculations using the numerically calculated potentials and compare the resulting minimum total energies as well as orbital energies of the highest occupied molecular orbital (HOMO) and the lowest unoccupied molecular orbital (LUMO) with the analytical results. All calculations in this section were performed with the def2-SVP basis set.

Table 1 shows the mean absolute deviations (MAD) as well as the maximum errors (MAX) of the analytical RPA

Table 1. Mean Absolute Deviations and Maximum Errors of Analytical RPA Correlation Potential Matrices Compared to Numerical Results

	hydrogen	water	methane
MAD	3.8×10^{-8}	2.3×10^{-8}	4.0×10^{-7}
MAX	1.5×10^{-7}	3.5×10^{-7}	2.6×10^{-6}

correlation potentials compared to the ones obtained numerically. As can be seen, the maximum error in the potential matrix elements are on the order of 10^{-6} for methane and on the order of 10^{-7} for the other two examples.

The comparison of the minimum energies as well as the HOMO and LUMO energies are shown in Table 2. It shows that the resulting minimum total energies as well as orbital energies are in very good agreement for all three presented systems.

Table 2. Differences in Hartree of the Minimum Total Energies and the Energies of the HOMO and LUMO Calculated Analytically and Numerically[a]

	hydrogen	water	methane
ΔE	1.5×10^{-9}	1.6×10^{-9}	7.5×10^{-9}
$\Delta\varepsilon_{HOMO}$	1.0×10^{-7}	$<1.0 \times 10^{-7}$	-1.0×10^{-7}
$\Delta\varepsilon_{LUMO}$	-1.0×10^{-7}	$<1.0 \times 10^{-7}$	3.0×10^{-7}

[a]Shown are always the analytical results minus the numerical results.

4.2. Convergence with the Number of Included Virtual Orbitals. As mentioned in section 2.3, for an efficient calculation of the self-energy in the positive imaginary time domain using Cholesky decomposition, we need to neglect the virtual-virtual part of the contribution to the RPA correlation potential stemming from changes in the Green's functions while keeping the projected Hamiltonian fixed. In this section we show that this procedure does not introduce any errors in the calculated minimum total energy as well as in the energy of the HOMO.

In Table 3 we present total energies as well as HOMO and LUMO energies calculated with an increasing number of included virtual orbitals for two examplary systems using the def2-TZVP basis set. The reference calculations were performed without Cholesky decomposition. It shows that the total energy as well as the HOMO energy are not affected by the number of included virtual orbitals while the LUMO energy of course is. However, as can be seen also, the LUMO energy is calculated correctly when including only one virtual orbital into the calculation.

4.3. Comparison with Post-KS RPA and Influence of the Approximated Hamiltonian. After validating our implementation, this section is intended to show the effect of self-consistency compared to standard post-KS RPA as well as to investigate the effect of the choice of the approximated Hamiltonian. The PBE, PBE0, and HF Hamiltonians serve as a basis for the approximated Hamiltonians. In the following, the three different variants are abbreviated by scRPA[$\tilde{\mathbf{H}}^{PBE}$], scRPA[$\tilde{\mathbf{H}}^{PBE0}$], and scRPA[$\tilde{\mathbf{H}}^{HF}$], respectively.

4.3.1. Eigenvalue Spectra of the Approximated Hamiltonians and the RPA Hamiltonian. This section is intended to compare the eigenvalue spectra of the different approxi-

Table 3. Convergence of the Total Energy and the HOMO and LUMO Energy in Hartree with the Number of Included Virtual Orbitals

no. virts	water			methane		
	E	ε_{HOMO}	ε_{LUMO}	E	ε_{HOMO}	ε_{LUMO}
0	−76.474782	−0.427739	0.146769	−40.576788	−0.497835	0.163197
1	−76.474782	−0.427739	0.090904	−40.576788	−0.497835	0.107917
2	−76.474782	−0.427739	0.090904	−40.576788	−0.497835	0.107917
3	−76.474782	−0.427739	0.090904	−40.576788	−0.497835	0.107917
4	−76.474782	−0.427739	0.090904	−40.576788	−0.497835	0.107917
5	−76.474782	−0.427739	0.090904	−40.576788	−0.497835	0.107917
ref	−76.474782	−0.427739	0.090904	−40.576788	−0.497835	0.107917

mated Hamiltonians with the ones obtained from the RPA Hamiltonian. Since the approximated Hamiltonians are designed to give the same density after diagonalization as the RPA Hamiltonian, investigating the eigenvalue spectra is important to decide on which approximation gives the most consistent results.

Therefore, we performed self-consistent RPA calculations using the PBE, PBE0, and HF functionals to calculate the exchange-correlation part of the approximated Hamiltonian for 44 different molecules and compare the difference of the eigenvalue spectra of the RPA Hamiltonian with the ones obtained with the respective approximated Hamiltonian. All calculations in this section were performed with the cc-pV5Z basis set. The results are shown in Table 4.

Table 4. Total Mean Absolute Deviations in Hartree of the Eigenvalue Spectra of the Three Approximated Hamiltonians from the Ones of the RPA Hamiltonian for 44 Molecules[a]

	scRPA[$\tilde{\mathbf{H}}^{PBE}$]	scRPA[$\tilde{\mathbf{H}}^{PBE0}$]	scRPA[$\tilde{\mathbf{H}}^{HF}$]
MAD	0.421245	0.323187	0.011351

[a]The complete list of all calculated deviations is provided in the Supporting Information.

As can be seen, the eigenvalue spectra of the approximated Hamiltonian based on PBE show in total a mean absolute deviation of 0.42 H from the ones obtained from the RPA Hamiltonian and therefore differ most. Including some exact exchange in the calculation of the XC potential (PBE0) improves the consistency with the RPA Hamiltonian (total MAD of 0.32 H), however, only slightly. By far the best agreement is achieved using the approximated Hamiltonian based on HF where the total MAD for all 44 molecules reduces to 0.01 H. This was to be expected since the RPA functional is based on the HF functional which of course has an important impact on the RPA Hamiltonian.

Therefore, in our opinion it is the most consistent choice to use the HF Hamiltonian to approximate the RPA Hamiltonian needed to construct the one-particle Green's functions. In the following, we will compare the performance of the three different self-consistent RPA variants scRPA[$\tilde{\mathbf{H}}^{PBE}$], scRPA-[$\tilde{\mathbf{H}}^{PBE0}$], and scRPA[$\tilde{\mathbf{H}}^{HF}$] in more detail.

4.3.2. S22 Test Set. As a first test, the S22 test set[58] of small-molecule interaction energies was calculated using our post-KS ω-CDGD-RPA method[17] as well as the self-consistent RPA variants. All calculations were performed with the def2-TZVP basis set. The results are shown in Table 5: The self-consistent RPA method using an approximated Hamiltonian based on PBE does not significantly improve upon the post-KS method.

Table 5. Mean Absolute Deviations and Maximum Errors (kcal/mol) of the ω-CDGD and the Self-Consistent RPA Method Using Three Different Approximated Hamiltonians Compared to CCSD(T) Reference Values for the S22 Test Set[a]

	ω-CDGD	scRPA[$\tilde{\mathbf{H}}^{PBE}$]	scRPA[$\tilde{\mathbf{H}}^{PBE0}$]	scRPA[$\tilde{\mathbf{H}}^{HF}$]
MAD	0.76	0.76	0.56	0.60
MAX	2.85	2.60	1.83	1.46

[a]All calculations were performed with the def2-TZVP basis set.

The MAD of 0.76 kcal/mol remains unchanged, whereas the maximum error is decreased from 2.85 to 2.60 kcal/mol. The improvement of the self-consistent approach compared to the post-KS method is more significant when PBE0 or HF Hamiltonians are used as a basis for the approximation. While scRPA[$\tilde{\mathbf{H}}^{PBE0}$] gives the smallest MAD (0.56 kcal/mol) of all three methods, the maximum error is decreased most (1.46 kcal/mol) by the variant abbreviated as scRPA[$\tilde{\mathbf{H}}^{HF}$].

4.3.3. He$_2$ and Be$_2$ Potential Energy Curves. Second, the dissociation of a helium dimer was calculated with the three different scRPA variants as well as our most recent ω-CDGD-RPA method. All calculations were performed with the aug-cc-pV6Z basis set. The results are shown in Figure 1.

While the post-KS method (ω-CDGD-RPA) hardly produces any binding, all three self-consistent variants improve significantly upon the post-KS results and show proper binding potential energy curves. The variant which uses the PBE Hamiltonian as basis for the approximation gives the best results, followed by scRPA[$\tilde{\mathbf{H}}^{PBE0}$] and scRPA[$\tilde{\mathbf{H}}^{HF}$]. As could
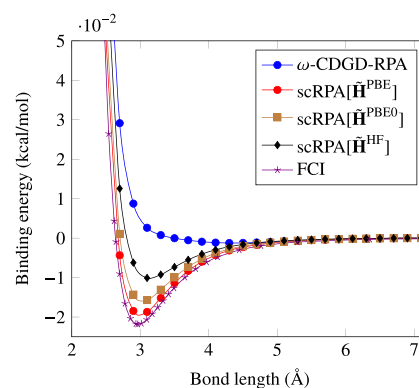
Figure 1. Dissociation curve of a helium dimer calculated with the ω-CDGD-RPA and self-consistent RPA method using three different approximated Hamiltonians (aug-cc-pV6Z basis). An estimated full CI, complete basis set dissociation curve serves as reference.[59]

be assumed, the results of scRPA[$\tilde{\mathbf{H}}^{\text{PBE0}}$] lie between the results of scRPA[$\tilde{\mathbf{H}}^{\text{PBE}}$] and scRPA[$\tilde{\mathbf{H}}^{\text{HF}}$].

To further test our self-consistent RPA method, the challenging dissociation curve of a beryllium dimer was calculated. All calculations were performed with the aug-cc-pV5Z basis set. The results are shown in Figure 2.
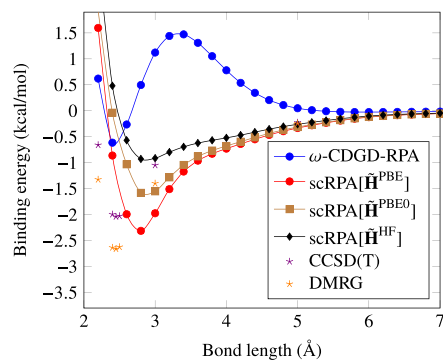
Figure 2. Dissociation curve of a beryllium dimer calculated with ω-CDGD-RPA and self-consistent RPA using three different approximated Hamiltonians (aug-cc-pV5Z basis). Core orbitals were frozen in all ω-CDGD calculations. Additionally, complete basis set extrapolated CCSD(T) and cc-pCVQZ-F12 DMRG values are shown, where the DMRG values are in very good agreement with experimental data.[60]

Again, it becomes obvious that all self-consistent variants improve upon the post-KS variant and remove the unphysical bump occurring in the region between 2.7−5.0 Å in the potential energy curve calculated with the ω-CDGD method. As for the dissociation of the helium dimer, the variant abbreviated by scRPA[$\tilde{\mathbf{H}}^{\text{PBE}}$] gives the best results followed by the results of scRPA[$\tilde{\mathbf{H}}^{\text{PBE0}}$] which lie between the scRPA-[$\tilde{\mathbf{H}}^{\text{PBE}}$] and scRPA[$\tilde{\mathbf{H}}^{\text{HF}}$] curve. Compared to the DMRG results, which are in very good agreement with experimental data,[60] it shows that also the CCSD(T) method differs quite significantly due to the missing description of static correlation effects present at short bond distances.

As shown above, although giving the worst results, the variant using the HF Hamiltonian to approximate the RPA Hamiltonian is the most consistent one since the eigenvalue spectra of the approximated Hamiltonian resemble the ones obtained with the RPA Hamiltonian best. We assume that the superior results of scRPA[$\tilde{\mathbf{H}}^{\text{PBE}}$] are due to a fortuitous error compensation since the approximated Hamiltonian gives electronic gaps which are too small leading to too large polarizabilities which in turn deepen the minima of the potential energy curves.

4.3.4. Dipole Moments. As shown in the sections before, there is a significant dependence of the method on the choice of the approximated Hamiltonian which is used to build the Green's functions. In this section we investigate the quality of the densities obtained with the different variants by comparing the respective calculated dipole moments with complete basis set extrapolated CCSD(T) reference values for 44 molecules. All calculations were performed with the cc-pV5Z basis set.

The results presented in Figure 3 again underline the importance of the approximated Hamiltonian. The scRPA-[$\tilde{\mathbf{H}}^{\text{PBE}}$] variant yields dipole moments with a MAD of 0.1650 D compared to the reference CCSD(T) values which are comparable to the ones obtained with the HF (0.1678 D)
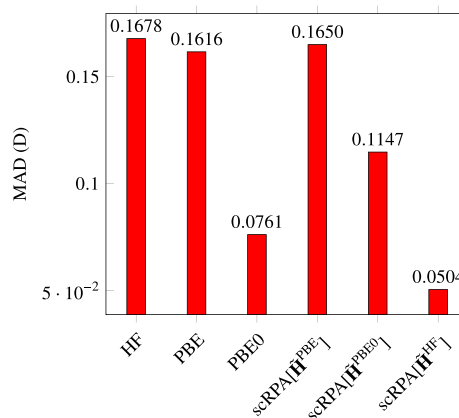
Figure 3. Mean absolute deviations of dipole moments in Debye for 44 molecules calculated with the HF, PBE, and PBE0, as well as the three different scRPA variants compared to reference CCSD(T)/CBS values.[61] All calculations were performed with the cc-pV5Z basis set. The complete list of all calculated dipole moments is provided in the Supporting Information.

and the PBE (0.1616 D) method. Replacing the PBE XC potential with a PBE0 XC potential to approximate the RPA Hamiltonian results in a significant improvement of the calculated dipole moments and decreases the MAD to 0.1147 D. Utilizing the HF Hamiltonian as basis for the approximation lowers the MAD even further to 0.0504 D. This finding is very encouraging since the method is completely free of any empirical parameters and also outperforms the PBE0 functional which gives dipole moments with a MAD of 0.0761 D compared to the CCSD(T) reference results.

4.4. Scaling Behavior. To test the scaling behavior of our self-consistent RPA method we calculated minimum total energies for a set of linear *n*-alkanes of increasing length using the def2-SVP basis set. The number of gridpoints for the imaginary time and frequency grid was set to 13 in all calculations. Additionally, Cholesky decomposition as described in section 2.3 without including any virtual orbitals was applied. For the RI we use the local attenuated Coulomb metric (ω = 0.1) along with sparse algebra. All calculations were performed on one Intel Xeon Gold 6134 CPU machine using 16 threads.

A linear (left) and a log−log (right) plot of the wall times of one iteration against the number of basis functions is shown in Figure 4. As can be seen, the self-consistent RPA method shows asymptotically a quadratic-scaling behavior as compared to the sixth-power scaling of conventional post-KS RPA. This was to be expected since the most time-consuming step in the calculation is the contraction of the sparse three-center integral matrix **B** with the screened Coulomb interaction $\mathbf{W}_c$, which does not show any useful sparsity, and should scale quadratically with the system size in the asymptotic limit.

In the following we briefly compare the computational effort of the presented self-consistent RPA method with our post-KS ω-CDGD-RPA method: the time-determining step of calculating the self-energy presently scales quadratically in the asymptotic limit which is to be contrasted to the linear-scaling calculation of the noninteraction response function in case of the ω-CDGD method. Therefore, the computational cost of one iteration of our self-consistent RPA method is comparable to the present cost of calculating RPA level molecular gradients.[37] The prefactor equals the number of SCF

Figure 4. Linear plot (left) and the respective log−log plot (right) of the wall times for one iteration of our self-consistent RPA method on linear *n*-alkanes calculated with the def2-SVP basis set against the number of basis functions.

cycles needed until convergence is reached, which in general is on the same order as for standard PBE calculations (roughly 10 iterations).
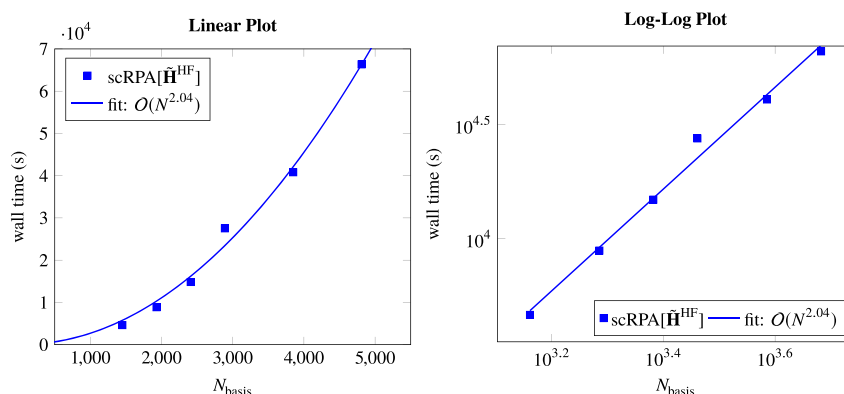
5. CONCLUSION

The minimization of the RPA functional with respect to the one-particle density matrix in the atomic orbital space was derived and implemented analytically as well as numerically. It was shown that the analytical results are in very good agreement with results obtained numerically demonstrating the correctness of our implementation. The problem of imposing full self-consistency on functionals with explicit dependence on the potential is bypassed by approximating the RPA Hamiltonian using a semicanonical projection scheme. Investigation of the eigenvalue spectra of the approximated Hamiltonians shows that the approximation gives the conceptually most consistent results when performed on the basis of the HF Hamiltonian, which makes our self-consistent RPA abbreviated as scRPA[$\tilde{\mathbf{H}}^{HF}$] a completely parameter-free electronic structure method. The presented method not only outperforms standard post-KS RPA in describing noncovalent interactions but also gives accurate dipole moments under-lining the high quality of the calculated densities. The increased prefactor of AO formulations compared to their canonical counterparts is overcome by introduction of Cholesky decomposed projectors onto the occupied orbital space enabling the use of large basis sets. Finally, exploiting the local nature of atomic and/or Cholesky orbitals results in an asymptotically quadratic-scaling algorithm opening the door for self-consistent RPA calculations on systems with hundreds of atoms.

ASSOCIATED CONTENT

Ⓢ Supporting Information

The Supporting Information is available free of charge on the ACS Publications website at DOI: 10.1021/acs.jctc.9b00444.

> Complete list of calculated MADs of the eigenvalue spectra of the three approximated Hamiltonians from the ones of the RPA Hamiltonian as well as calculated dipole moments (PDF)

AUTHOR INFORMATION

Corresponding Author
*E-mail: christian.ochsenfeld@uni-muenchen.de.

ORCID Ⓞ
Christian Ochsenfeld: 0000-0002-4189-6558

Notes
The authors declare no competing financial interest.

REFERENCES

(1) Kohn, W.; Sham, L. J. Self-Consistent Equations Including Exchange and Correlation Effects. *Phys. Rev.* **1965**, *140*, A1133−A1138.
(2) Mardirossian, N.; Head-Gordon, M. Thirty years of density functional theory in computational chemistry: an overview and extensive assessment of 200 density functionals. *Mol. Phys.* **2017**, *115*, 2315−2372.
(3) Langreth, D. C.; Perdew, J. P. The Exchange-Correlation Energy of a Metallic Surface. *Solid State Commun.* **1975**, *17*, 1425−1429.
(4) Langreth, D. C.; Perdew, J. P. Exchange-correlation energy of a metallic surface: Wave-vector analysis. *Phys. Rev. B* **1977**, *15*, 2884−2901.
(5) Bohm, D.; Pines, D. A Collective Description of Electron Interactions: III. Coulomb Interactions in a Degenerate Electron Gas. *Phys. Rev.* **1953**, *92*, 609−625.
(6) Dobson, J. *Time-Dependent Density Functional Theory*; Springer: Berlin, 2006; Vol. 706.
(7) Fuchs, M.; Niquet, Y. M.; Gonze, X.; Burke, K. Describing static correlation in bond dissociation by Kohn-Sham density functional theory. *J. Chem. Phys.* **2005**, *122*, 094116.
(8) Harl, J.; Kresse, G. Cohesive energy curves for noble gas solids calculated by adiabatic connection fluctuation-dissipation theory. *Phys. Rev. B* **2008**, *77*, 1−8.
(9) Harl, J.; Kresse, G. Accurate Bulk Properties from Approximate Many-Body Techniques. *Phys. Rev. Lett.* **2009**, *103*, 4−7.
(10) Furche, F. Developing the random phase approximation into a practical post-Kohn-Sham correlation model. *J. Chem. Phys.* **2008**, *129*, 114105.
(11) Eshuis, H.; Yarkony, J.; Furche, F. Fast computation of molecular random phase approximation correlation energies using resolution of the identity and imaginary frequency integration. *J. Chem. Phys.* **2010**, *132*, 234114.

(12) Eshuis, H.; Furche, F. Basis set convergence of molecular correlation energy differences within the random phase approximation. *J. Chem. Phys.* **2012**, *136*, 084105.

(13) Kaltak, M.; Klimeš, J.; Kresse, G. Low Scaling Algorithms for the Random Phase Approximation: Imaginary Time and Laplace Transformations. *J. Chem. Theory Comput.* **2014**, *10*, 2498−2507.

(14) Kállay, M. Linear-scaling implementation of the direct random-phase approximation. *J. Chem. Phys.* **2015**, *142*, 204105.

(15) Schurkus, H. F.; Ochsenfeld, C. An effective linear-scaling atomic-orbital reformulation of the random-phase approximation using a contracted double-Laplace transformation. *J. Chem. Phys.* **2016**, *144*, 031101.

(16) Luenser, A.; Schurkus, H. F.; Ochsenfeld, C. Vanishing-Overhead Linear-Scaling Random Phase Approximation by Cholesky Decomposition and an Attenuated Coulomb-Metric. *J. Chem. Theory Comput.* **2017**, *13*, 1647−1655.

(17) Graf, D.; Beuerle, M.; Schurkus, H. F.; Luenser, A.; Savasci, G.; Ochsenfeld, C. Accurate and Efficient Parallel Implementation of an Effective Linear-Scaling Direct Random Phase Approximation Method. *J. Chem. Theory Comput.* **2018**, *14*, 2505−2515.

(18) Wilhelm, J.; Seewald, P.; Del Ben, M.; Hutter, J. Large-Scale Cubic-Scaling Random Phase Approximation Correlation Energy Calculations Using a Gaussian Basis. *J. Chem. Theory Comput.* **2016**, *12*, 5851−5859.

(19) Kim, M.-C.; Sim, E.; Burke, K. Understanding and Reducing Errors in Density Functional Calculations. *Phys. Rev. Lett.* **2013**, *111*, 073003.

(20) Wasserman, A.; Nafziger, J.; Jiang, K.; Kim, M.-C.; Sim, E.; Burke, K. The Importance of Being Inconsistent. *Annu. Rev. Phys. Chem.* **2017**, *68*, 555−581.

(21) Verma, P.; Bartlett, R. J. Increasing the applicability of density functional theory. II. Correlation potentials from the random phase approximation and beyond. *J. Chem. Phys.* **2012**, *136*, 044105.

(22) Bleiziffer, P.; Heßelmann, A.; Görling, A. Efficient self-consistent treatment of electron correlation within the random phase approximation. *J. Chem. Phys.* **2013**, *139*, 084113.

(23) Nguyen, N. L.; Colonna, N.; de Gironcoli, S. Ab initio self-consistent total-energy calculations within the EXX/RPA formalism. *Phys. Rev. B* **2014**, *90*, 045138.

(24) Hellgren, M.; Caruso, F.; Rohr, D. R.; Ren, X.; Rubio, A.; Scheffler, M.; Rinke, P. Static correlation and electron localization in molecular dimers from the self-consistent RPA and *GW* approximation. *Phys. Rev. B* **2015**, *91*, 165110.

(25) Jin, Y.; Zhang, D.; Chen, Z.; Su, N. Q.; Yang, W. Generalized Optimized Effective Potential for Orbital Functionals and Self-Consistent Calculation of Random Phase Approximations. *J. Phys. Chem. Lett.* **2017**, *8*, 4746−4751.

(26) Voora, V. K.; Balasubramani, S. G.; Furche, F. Variational generalized Kohn-Sham approach combining the random-phase-approximation and Green's-function methods. *Phys. Rev. A* **2019**, *99*, 012518.

(27) Einstein, A. Die Grundlage der allgemeinen Relativitätstheorie. *Ann. Phys.* **1916**, *354*, 769−822.

(28) Gunnarsson, O.; Lundqvist, B. I. Exchange and correlation in atoms, molecules, and solids by the spin-density-functional formalism. *Phys. Rev. B* **1976**, *13*, 4274−4298.

(29) Furche, F.; Van Voorhis, T. Fluctuation-dissipation theorem density-functional theory. *J. Chem. Phys.* **2005**, *122*, 164106.

(30) Ullrich, C.-A. *Time-Dependent Density-Functional Theory−Concepts and Applications*; Oxford University Press: Oxford, 2012.

(31) Koch, H.; Sánchez De Merás, A.; Pedersen, T. B. Reduced scaling in electronic structure calculations using Cholesky decompositions. *J. Chem. Phys.* **2003**, *118*, 9481−9484.

(32) Higham, N. J. Cholesky factorization. *Wiley Interdiscip. Rev. Comput. Stat.* **2009**, *1*, 251−254.

(33) Harbrecht, H.; Peters, M.; Schneider, R. On the low-rank approximation by the pivoted Cholesky decomposition. *Appl. Numer. Math.* **2012**, *62*, 428−440.

(34) Zienau, J.; Clin, L.; Doser, B.; Ochsenfeld, C. Cholesky-decomposed densities in Laplace-based second-order Møller-Plesset perturbation theory. *J. Chem. Phys.* **2009**, *130*, 204112.

(35) Maurer, S. A.; Clin, L.; Ochsenfeld, C. Cholesky-decomposed density MP2 with density fitting: Accurate MP2 and double-hybrid DFT energies for large systems. *J. Chem. Phys.* **2014**, *140*, 224112.

(36) Hellgren, M.; von Barth, U. Correlation potential in density functional theory at the GWA level: Spherical atoms. *Phys. Rev. B* **2007**, *76*, 075107.

(37) Beuerle, M.; Ochsenfeld, C. Low-scaling analytical gradients for the direct random phase approximation using an atomic orbital formalism. *J. Chem. Phys.* **2018**, *149*, 244111.

(38) Schweizer, S.; Doser, B.; Ochsenfeld, C. An atomic orbital-based reformulation of energy gradients in second-order Møller-Plesset perturbation theory. *J. Chem. Phys.* **2008**, *128*, 154101.

(39) Ayala, P. Y.; Scuseria, G. E. Linear scaling second-order Møller-Plesset theory in the atomic orbital basis for large molecular systems. *J. Chem. Phys.* **1999**, *110*, 3660.

(40) Surján, P. R. The MP2 energy as a functional of the Hartree-Fock density matrix. *Chem. Phys. Lett.* **2005**, *406*, 318−320.

(41) Kussmann, J.; Ochsenfeld, C. Pre-selective screening for matrix elements in linear-scaling exact exchange calculations. *J. Chem. Phys.* **2013**, *138*, 134114.

(42) Kussmann, J.; Ochsenfeld, C. Preselective Screening for Linear-Scaling Exact Exchange-Gradient Calculations for Graphics Processing Units and General Strong-Scaling Massively Parallel Calculations. *J. Chem. Theory Comput.* **2015**, *11*, 918−922.

(43) Kussmann, J.; Ochsenfeld, C. Hybrid CPU/GPU Integral Engine for Strong-Scaling *Ab Initio* Methods. *J. Chem. Theory Comput.* **2017**, *13*, 3153−3159.

(44) Perdew, J. P.; Burke, K.; Ernzerhof, M. Generalized Gradient Approximation Made Simple [Phys. Rev. Lett. 77, 3865 (1996)]. *Phys. Rev. Lett.* **1997**, *78*, 1396−1396.

(45) Perdew, J. P.; Burke, K.; Ernzerhof, M. Generalized Gradient Approximation Made Simple. *Phys. Rev. Lett.* **1996**, *77*, 3865−3868.

(46) Perdew, J. P.; Ernzerhof, M.; Burke, K. Rationale for mixing exact exchange with density functional approximations. *J. Chem. Phys.* **1996**, *105*, 9982−9985.

(47) Weigend, F.; Furche, F.; Ahlrichs, R. Gaussian basis sets of quadruple zeta valence quality for atoms H−Kr. *J. Chem. Phys.* **2003**, *119*, 12753−12762.

(48) Weigend, F.; Ahlrichs, R. Balanced basis sets of split valence, triple zeta valence and quadruple zeta valence quality for H to Rn: Design and assessment of accuracy. *Phys. Chem. Chem. Phys.* **2005**, *7*, 3297.

(49) Peterson, K. A.; Woon, D. E.; Dunning, T. H. Benchmark calculations with correlated molecular wave functions. IV. The classical barrier height of the H + H$_2$ → H$_2$ + H reaction. *J. Chem. Phys.* **1994**, *100*, 7410−7415.

(50) Prascher, B. P.; Woon, D. E.; Peterson, K. A.; Dunning, T. H.; Wilson, A. K. Gaussian basis sets for use in correlated molecular calculations. VII. Valence, core-valence, and scalar relativistic basis sets for Li, Be, Na, and Mg. *Theor. Chem. Acc.* **2011**, *128*, 69−82.

(51) Wilson, A. K.; van Mourik, T.; Dunning, T. H. Gaussian basis sets for use in correlated molecular calculations. VI. Sextuple zeta correlation consistent basis sets for boron through neon. *J. Mol. Struct.: THEOCHEM* **1996**, *388*, 339−349.

(52) Van Mourik, T.; Wilson, A. K.; Dunning, T. H. Benchmark calculations with correlated molecular wavefunctions. XIII. Potential energy curves for He2, Ne2 and Ar2 using correlation consistent basis sets through augmented sextuple zeta. *Mol. Phys.* **1999**, *96*, 529−547.

(53) Weigend, F.; Häser, M.; Patzelt, H.; Ahlrichs, R. RI-MP2: optimized auxiliary basis sets and demonstration of efficiency. *Chem. Phys. Lett.* **1998**, *294*, 143−152.

(54) Hättig, C. Optimization of auxiliary basis sets for RI-MP2 and RI-CC2 calculations: Core-valence and quintuple-ζ basis sets for H to Ar and QZVPP basis sets for Li to Kr. *Phys. Chem. Chem. Phys.* **2005**, *7*, 59−66.

(55) Jung, Y.; Sodt, A.; Gill, P. M. W.; Head-Gordon, M. Auxiliary basis expansions for large-scale electronic structure calculations. *Proc. Natl. Acad. Sci. U. S. A.* **2005**, *102*, 6692−6697.

(56) Jung, Y.; Shao, Y.; Head-Gordon, M. Fast Evaluation of Scaled Opposite Spin Second-Order Møller−Plesset Correlation Energies Using Auxiliary Basis Expansions and Exploiting Sparsity. *J. Comput. Chem.* **2007**, *28*, 1953−1964.

(57) Reine, S.; Tellgren, E.; Krapp, A.; Kjærgaard, T.; Helgaker, T.; Jansik, B.; Høst, S.; Salek, P. Variational and robust density fitting of four-center two-electron integrals in local metrics. *J. Chem. Phys.* **2008**, *129*, 104101.

(58) Jurečka, P.; Šponer, J.; Černý, J.; Hobza, P. Benchmark database of accurate (MP2 and CCSD(T) complete basis set limit) interaction energies of small model complexes, DNA base pairs, and amino acid pairs. *Phys. Chem. Chem. Phys.* **2006**, *8*, 1985−1993.

(59) van Mourik, T.; Dunning, T. H. A new ab initio potential energy curve for the helium dimer. *J. Chem. Phys.* **1999**, *111*, 9248−9258.

(60) Sharma, S.; Yanai, T.; Booth, G. H.; Umrigar, C. J.; Chan, G. K.-L. Spectroscopic accuracy directly from quantum chemistry: Application to ground and excited states of beryllium dimer. *J. Chem. Phys.* **2014**, *140*, 104112.

(61) Hait, D.; Head-Gordon, M. How Accurate Is Density Functional Theory at Predicting Dipole Moments? An Assessment Using a New Database of 200 Benchmark Values. *J. Chem. Theory Comput.* **2018**, *14*, 1969−1981.

Supporting Information: Low-Scaling Self-Consistent Minimization of a Density Matrix Based Random Phase Approximation Method in the Atomic Orbital Space

Daniel Graf, Matthias Beuerle, and Christian Ochsenfeld*

Chair of Theoretical Chemistry and Center for Integrated Protein Science Munich (CIPSM), Department of Chemistry, University of Munich (LMU), D-81377 Munich, Germany

E-mail: christian.ochsenfeld@uni-muenchen.de

1 Eigenvalue Spectra of the Approximated Hamiltonians and the RPA Hamiltonian

Table 1: Mean absolute deviations in Hartree of the eigenvalue spectra of the three approximated Hamiltonians from the ones of the RPA Hamiltonian for 44 molecules.

molecule	scRPA[$\tilde{\mathbf{H}}^{\mathrm{PBE}}$]	scRPA[$\tilde{\mathbf{H}}^{\mathrm{PBE0}}$]	scRPA[$\tilde{\mathbf{H}}^{\mathrm{HF}}$]
BH_2Cl	0.410626	0.314479	0.009522
BH_2F	0.44629	0.34254	0.00965
$BHCl_2$	0.450631	0.343705	0.014459
BHF_2	0.517411	0.395838	0.014028
CH_3Cl	0.428917	0.328835	0.008865
CH_3F	0.463563	0.355809	0.008685
CH_3OH	0.43177	0.332265	0.007307
ClCN	0.48826	0.372891	0.013544
ClF	0.578205	0.439101	0.023271
CO	0.495106	0.37877	0.012769
CS	0.442126	0.337223	0.014945
FCN	0.533763	0.407841	0.011937
H_2O-H_2O	0.45783	0.351073	0.009956
H_2O-NH_3	0.436086	0.335705	0.008134
H_2O	0.457004	0.351073	0.009801
H_2S-H_2S	0.415645	0.318268	0.010752
H_2S-HCl	0.436209	0.333374	0.012517
HCCF	0.483387	0.370564	0.009641
HCl$-$HCl	0.463429	0.353341	0.014874
HCl	0.461788	0.351914	0.015092
HCN	0.443651	0.340674	0.006957
HF$-$HF	0.539533	0.412479	0.014623
HF	0.537048	0.41037	0.014948
HOOH	0.497001	0.380374	0.01107
$LiBH_4$	0.315028	0.243353	0.003591
LiCl	0.325303	0.247803	0.013301
LiCN	0.350942	0.269983	0.00714

Table 1 Continued.

molecule	scRPA[$\tilde{\boldsymbol{H}}^{\text{PBE}}$]	scRPA[$\tilde{\boldsymbol{H}}^{\text{PBE0}}$]	scRPA[$\tilde{\boldsymbol{H}}^{\text{HF}}$]
LiF	0.374755	0.287507	0.015355
LiH	0.215769	0.168318	0.002967
LiOH	0.341812	0.264857	0.011317
N_2H_4	0.434003	0.334158	0.007403
NaCl	0.335281	0.254466	0.017267
NaCN	0.357377	0.274389	0.010052
NaF	0.373639	0.292038	0.019897
NaH	0.225461	0.179105	0.00859
NaLi	0.165358	0.130699	0.006611
NaOH	0.346033	0.269366	0.014772
NH_3-BH_3	0.392471	0.302738	0.005272
NH_3-NH_3	0.4179	0.322133	0.006786
NH_3	0.417724	0.32184	0.006566
PH_3	0.390945	0.299887	0.008593
SF_2	0.583451	0.444077	0.023029
SiH_3Cl	0.412585	0.315366	0.011744
SiH_3F	0.443665	0.339619	0.011847
Mean	0.421245	0.323187	0.011351

2 Dipole Moments

Table 2: Dipole moments in Debye for 44 molecules calculated with the HF, PBE, PBE0, as well as the three different scRPA variants along the reference CCSD(T)/CBS values.[1] All calculations were performed with the cc-pV5Z basis set.

molecule	CCSD(T)	HF	PBE	PBE0	scRPA[$\tilde{\mathbf{H}}^{\text{PBE}}$]	scRPA[$\tilde{\mathbf{H}}^{\text{PBE0}}$]	scRPA[$\tilde{\mathbf{H}}^{\text{HF}}$]
BH_2Cl	0.6838	0.9247	0.4342	0.5899	0.3391	0.3955	0.5317
BH_2F	0.8269	1.0129	0.6061	0.7445	0.6560	0.6985	0.7950
$BHCl_2$	0.6684	0.8699	0.4828	0.5976	0.4429	0.4649	0.5437
BHF_2	0.9578	1.1157	0.7705	0.8867	0.8045	0.8399	0.9195
CH_3Cl	1.8981	2.0524	1.8211	1.8911	1.6656	1.7004	1.7750
CH_3F	1.8083	1.9607	1.6432	1.7421	1.7456	1.7643	1.8155
CH_3OH	1.7091	1.8101	1.6004	1.6680	1.6761	1.6867	1.7203
ClCN	2.8496	3.1102	2.9592	2.9889	2.8171	2.8293	2.8976
ClF	0.8802	1.1347	0.7530	0.8507	1.0021	0.9678	0.9748
CO	0.1172	-0.2666	0.2209	0.0995	0.1928	0.2109	0.1775
CS	1.9692	1.6194	1.9971	1.9280	1.9877	2.0652	2.1233
FCN	2.1756	2.3383	2.3245	2.3054	2.1171	2.1005	2.1176
H_2O-H_2O	2.7303	2.8540	2.7624	2.7896	2.6638	2.6853	2.7322
H_2O-NH_3	3.5004	3.6342	3.5410	3.5757	3.4256	3.4519	3.5070
H_2O	1.8601	2.0025	1.8422	1.8945	1.8040	1.8261	1.8750
H_2S-H_2S	0.9181	0.9298	1.0690	1.0279	0.8768	0.8852	0.9004
H_2S-HCl	2.1328	2.1976	2.3368	2.3038	2.0358	2.0577	2.1008
HCCF	0.7452	0.8830	0.4541	0.6053	0.6408	0.6716	0.7425
HCl-HCl	1.7766	1.8705	1.8744	1.8770	1.6708	1.6911	1.7359
HCl	1.1055	1.2060	1.1133	1.1492	1.0326	1.0471	1.0830
HCN	3.0065	3.2911	2.9397	3.0364	2.9089	2.9161	2.9828
HF-HF	3.3991	3.5736	3.3836	3.4377	3.2814	3.3120	3.3808
HF	1.8059	1.9319	1.7685	1.8192	1.7296	1.7511	1.7989
HOOH	1.5732	1.6931	1.5511	1.5958	1.5065	1.5294	1.5762
$LiBH_4$	6.1281	6.2089	5.9477	6.0288	6.0713	6.1043	6.1561
LiCl	7.0960	7.2569	6.8193	6.9737	6.8220	6.8516	7.0107
LiCN	6.9851	7.1007	6.8077	6.9174	6.7647	6.8516	6.9600

5

Table 2 Continued.

molecule	CCSD(T)	HF	PBE	PBE0	scRPA[$\widetilde{\mathbf{H}}^{\mathrm{PBE}}$]	scRPA[$\widetilde{\mathbf{H}}^{\mathrm{PBE0}}$]	scRPA[$\widetilde{\mathbf{H}}^{\mathrm{HF}}$]
LiF	6.2879	6.4490	6.0670	6.2011	6.0250	6.1048	6.2184
LiH	5.8286	5.9984	5.6100	5.7480	5.4698	5.6789	5.8495
LiOH	4.5664	4.6570	4.3182	4.4464	4.2973	4.3862	4.4897
N_2H_4	2.7179	2.8404	2.6585	2.7242	2.6273	2.6547	2.7138
NaCl	9.0066	9.2513	8.4834	8.7977	8.6244	8.7658	8.9326
NaCN	8.8903	9.0933	8.5817	8.7930	8.6043	8.7429	8.8898
NaF	8.1339	8.3700	7.7178	8.0147	7.5291	7.8596	8.0701
NaH	6.3966	7.0082	5.7572	6.2135	5.5441	5.9263	6.4434
NaLi	0.4837	0.6662	0.2059	0.3720	0.6701	0.3058	0.1906
NaOH	6.7690	6.8628	6.5010	6.6530	6.4933	6.6126	6.7199
NH_3-BH_3	5.2810	5.3729	5.2678	5.3029	5.1943	5.2160	5.2556
NH_3-NH_3	2.1345	2.2186	2.1642	2.1826	2.0670	2.0867	2.1256
NH_3	1.5289	1.6259	1.4932	1.5408	1.4590	1.4811	1.5242
PH_3	0.6069	0.6581	0.6369	0.6631	0.4723	0.4882	0.5214
SF_2	1.0555	1.3294	0.8414	0.9939	1.0988	1.0875	1.1403
SiH_3Cl	1.3645	1.4541	1.2187	1.3032	1.2116	1.2324	1.2869
SiH_3F	1.3123	1.4177	1.1785	1.2728	1.2344	1.2577	1.3133
MAD		0.1678	0.1616	0.0761	0.1650	0.1147	0.0504

References

(1) Hait, D.; Head-Gordon, M. How Accurate Is Density Functional Theory at Predicting Dipole Moments? An Assessment Using a New Database of 200 Benchmark Values. *J. Chem. Theory Comput.* **2018**, *14*, 1969–1981.

3.3 Range-Separated Density-Functional Theory in Combination with the Random Phase Approximation: An Accuracy Benchmark

A. Kreppel, D. Graf, H. Laqua, C. Ochsenfeld

J. Chem. Theory Comput. **16**, 2985 (2020).

Abstract

A formulation of range-separated random phase approximation (RPA) based on our efficient ω-CDGD-RI-RPA [*J. Chem. Theory Comput.* **2018**, *14*, 2505] method and a large scale benchmark study are presented. By application to the GMTKN55 data set, we obtain a comprehensive picture of the performance of range-separated RPA in general main group thermochemistry, kinetics, and noncovalent interactions. The results show that range-separated RPA performs stably over the broad range of molecular chemistry included in the GMTKN55 set. It improves significantly over semilocal DFT but it is still less accurate than modern dispersion corrected double-hybrid functionals. Furthermore, range-separated RPA shows a faster basis set convergence compared to standard full-range RPA making it a promising applicable approach with only one empirical parameter.

Reprinted with permission from:

Range-Separated Density-Functional Theory in Combination with the Random Phase Approximation: An Accuracy Benchmark

Andrea Kreppel, Daniel Graf, Henryk Laqua, and Christian Ochsenfeld*
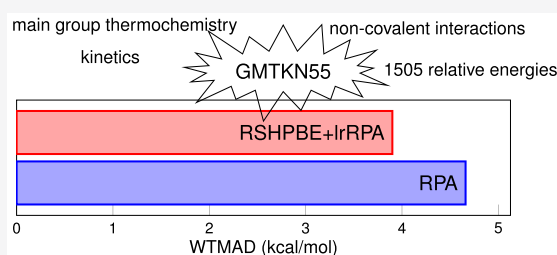
Read Online

ACCESS | 📊 Metrics & More | 📰 Article Recommendations | 🆂�🅸 Supporting Information

ABSTRACT: A formulation of range-separated random phase approximation (RPA) based on our efficient ω-CDGD-RI-RPA [*J. Chem. Theory Comput.* **2018**, *14*, 2505] method and a large scale benchmark study are presented. By application to the GMTKN55 data set, we obtain a comprehensive picture of the performance of range-separated RPA in general main group thermochemistry, kinetics, and noncovalent interactions. The results show that range-separated RPA performs stably over the broad range of molecular chemistry included in the GMTKN55 set. It improves significantly over semilocal DFT but it is still less accurate than modern dispersion corrected double-hybrid functionals. Furthermore, range-separated RPA shows a faster basis set convergence compared to standard full-range RPA making it a promising applicable approach with only one empirical parameter.

1. INTRODUCTION

The random phase approximation (RPA)[1−6] has become an increasingly popular post-Kohn−Sham (KS)[7] approach. RPA can be considered as a parameter-free density functional and it stands on the fifth and highest rung of the Jacob's ladder of density-functional theory (DFT).[8] RPA overcomes several failures of semilocal density functionals, among which one of the most important issues are the poorly described long-range van der Waals interactions.[9] This means that RPA gives more accurate interaction and cohesion energies.[10−14] Even though the long-range part of the dispersion interactions is described well, RPA gives a poor approximation for small interelectronic distances.[3,15−17]

For this reason the idea of treating the short-range interactions with semilocal DFT arose some time ago.[16,18−20] Recently, a scheme that combines the long-range part of the RPA correlation energy with the short-range part of a density functional via the error function has been established.[21−23] This range-separated RPA approach has been shown to improve the RPA correlation energy in various cases. One example is the improvement of dissociation curves for rare-gas dimers and alkaline-earth dimers compared to full-range RPA.[22,23] It also has been shown that the range-separation approach provides accurate interaction energies for a range of noncovalent complexes.[24,25] Furthermore, the range-separation scheme improves atomization energies and barrier heights of small test sets.[26]

Here, we present a range-separated RPA method which is based on our efficient linear-scaling ω-CDGD-RI-RPA method[27−30] in the local atomic orbital space that uses a Cholesky decomposed ground state density (CDGD) and makes use of the resolution-of-the-identity (RI) with the attenuated ω-Coulomb metric.[31] The use of our efficient ω-CDGD-RI-RPA algorithm within the range-separation approach enables us to test range-separated RPA on a large scale and to provide a comprehensive picture of the performance of range-separated RPA. Hence, we compare range-separated RPA to full-range RPA for the GMTKN55 data set.[32] This large benchmark set comprises 1505 relative energies based on 2462 single-point calculations on molecules with up to 72 atoms and gives a broad overview of general main group thermochemistry, kinetics, and noncovalent interactions.

2. THEORY

Several schemes for range-separated RPA have been proposed so far.[22,23,23] The formalism of the range-separation scheme used in this work is described by Toulouse et al. in detail in ref 23. Here, we give a brief overview and rather focus on the description of the long-range formulation of our ω-CDGD-RI-RPA method.[28] In the subsequent description μ, ν, λ, σ refer to atomic orbitals (AOs) i, j and a, b refer to occupied and virtual molecular orbitals (MOs), respectively, and $\underline{i}$, $\underline{j}$ refer to Cholesky orbitals. M, N, P, Q denote auxiliary RI functions. Moreover, Einstein's sum convention[34] is used.

2.1. Range Separation. The separation of the electron−electron interaction into long-range (lr) and short-range (sr) contributions can be achieved by dividing the electron−electron operator v_{ee} into a long-range electron−electron operator v_{ee}^{lr} and a short-range electron−electron operator v_{ee}^{sr} using the error function and its complementary function as

$$v_{ee} = v_{ee}^{lr} + v_{ee}^{sr} = \frac{erf(\mu r_{12})}{r_{12}} + \frac{erfc(\mu r_{12})}{r_{12}} \tag{1}$$

where the adjustable range-separation parameter μ defines the range of the separation.

Until now, multiple formulations of short-range PBE were presented in the literature.[35−37] In this work the range-separated hybrid PBE functional (RSHPBE) of Goll et al.[38] is used, which utilizes the range-separation scheme in eq 1. A detailed description of this functional is given in ref 38. Its energy

$$E^{RSHPBE} = E_H + E_x^{PBE,sr} + E_x^{HF,lr} + E_c^{PBE,sr} \tag{2}$$

is composed of the Hartree energy E_H, the short-range exchange $E_x^{PBE,sr}$, and correlation energy $E_c^{PBE,sr}$ given by the short-range PBE-like functional and the long-range exact exchange energy $E_x^{HF,lr}$. E^{RSHPBE} lacks long-range correlation effects and thus can be corrected with the long-range part of the RPA correlation energy $E_c^{RPA,lr}$ in a *post*-KS calculation:

$$E^{RSHPBE+lrRPA} = E^{RSHPBE} + E_c^{RPA,lr} \tag{3}$$

2.2. Long-Range Formulation of the RPA Correlation Energy. The standard full-range RPA total energy within the adiabatic connection formalism[39] is given by

$$E^{RPA} = E^{HF} + E_c^{RPA} \tag{4}$$

where E^{HF} is the Hartree−Fock energy evaluated non-self-consistently on the reference orbitals and E_c^{RPA} is the RPA correlation energy. Using the fluctuation−dissipation theorem together with the RI approximation, the RPA correlation energy can be expressed after coupling-strength integration as[4−6]

$$E_c^{RPA} = \frac{1}{2\pi} \int_0^{+\infty} d\omega \, Tr[\ln(1 - X_0(i\omega)V) + X_0(i\omega)V] \tag{5}$$

where

$$V_{MN} = (C^{-1})_{MP} \tilde{V}_{PQ} (C^{-1})_{QN} \tag{6}$$

represents the Coulomb operator in the auxiliary basis with

$$C_{MN} = (M|m_{12}|N) \tag{7}$$

$$\tilde{V}_{MN} = (M|v_{ee}(r_{12})|N) \tag{8}$$

and the RI metric m_{12}. In the presented method the attenuated Coulomb metric

$$m_{12} = \frac{erfc(\omega_{att} r_{12})}{r_{12}} \tag{9}$$

with $\omega_{att} = 0.1 \, a_0^{-1}$ is used, since it has been shown to constitute a good trade-off between accuracy and locality for fitting the full-range Coulomb operator.[31] X_0 denotes the noninteracting density−density response function in the zero-temperature case, also represented in the auxiliary basis. For

the sake of efficiency, X_0 is calculated in the imaginary time domain

$$X_{0,MN}(i\tau) = G_{0,\mu\nu}(-i\tau) B_{\nu\lambda}^M G_{0,\lambda\sigma}(i\tau) B_{\sigma\mu}^N \tag{10}$$

where $G_0(i\tau)$ is the one-particle Green's function

$$G_0(i\tau) = \Theta(-i\tau)\underline{G}_0(i\tau) + \Theta(i\tau)\bar{G}_0(i\tau) \tag{11}$$

$$\underline{G}_{0,\mu\nu}(i\tau) = C_{\mu i} C_{\nu i} \exp(-(\varepsilon_i - \varepsilon_F)\tau)$$

$$\bar{G}_{0,\mu\nu}(i\tau) = -C_{\mu a} C_{\nu a} \exp(-(\varepsilon_a - \varepsilon_F)\tau)$$

with the Heaviside step function $\Theta(i\tau)$, the MO coefficients $C_{\mu i}$ and $C_{\mu a}$, as well as the MO energies ε_i and ε_a of the occupied and unoccupied MOs, respectively, and the Fermi level ε_F. The three-center integrals $B_{\mu\nu}^M$ are given in Mulliken notation by

$$B_{\mu\nu}^M = (\mu\nu|m_{12}|M) \tag{12}$$

The response function of eq 10 is then transformed into the imaginary frequency domain by a contracted double Laplace[27] or, equivalently, cosine[40] transform according to

$$X_0(i\omega) = \int_{-\infty}^{+\infty} d\tau \, \cos(\omega\tau) X_0(i\tau) \tag{13}$$

to perform the final frequency integration.

The main drawback of pure AO formulations is the unfavorable scaling with the size of the basis set compared to MO formulations. To address this problem, pivoted Cholesky decomposition[41−43] can be applied to density-type matrices[28,31] in order to obtain local Cholesky vectors/orbitals which can then be used to transform important quantities in the time-determining steps. In the following, pivoted Cholesky decomposition of a given matrix A is abbreviated by $A = LL^T$.

Since the one-particle Green's function in the negative imaginary time domain is invariant with respect to projection onto the occupied space, eq 10 can equivalently be expressed as

$$X_{0,MN}(i\tau) = Tr(PSG_0(-i\tau)SPB^M G_0(i\tau)B^N) \tag{14}$$

Cholesky decomposition of the ground state density matrix P and cyclic permutation within the trace result in

$$X_{0,MN}(i\tau) = Tr(L^T SG_0(-i\tau)SLL^T B^M G_0(i\tau)B^N L) \tag{15}$$

and allow the dimensions of the important quantities to be reduced yielding

$$X_{0,MN}(i\tau) = G_{0,\underline{j}\,\underline{i}}(-i\tau) B_{\underline{i}\nu}^M G_{0,\nu\mu}(i\tau) B_{\mu\underline{j}}^N \tag{16}$$

where we defined

$$G_{0,\underline{j}\,\underline{i}}(-i\tau) = (L^T S)_{\underline{j}\mu} G_{0,\mu\nu}(-i\tau)(SL)_{\nu\underline{i}} \tag{17}$$

$$B_{\underline{i}\nu}^M = (L^T)_{\underline{i}\mu} B_{\mu\nu}^M \tag{18}$$

The final and most expensive step in the calculation of the response function is then given by

$$X_{0,MN}(i\tau) = B_{\underline{j}\mu}^M(i\tau) B_{\mu\underline{j}}^N \tag{19}$$

with

$$B_{\underline{j}\mu}^M(i\tau) = G_{0,\underline{j}\,\underline{i}}(-i\tau) B_{\underline{i}\nu}^M G_{0,\nu\mu}(i\tau) \tag{20}$$

The evaluation of eq 19 formally scales as $O(N_{aux}^2 N_{basis} N_{occ})$ but can be implemented in an asymptotically linear-scaling fashion using sparse matrix algebra.

To account for the long-range part of the RPA correlation energy only, as required by the presented range-separated functional, the standard Coulomb operator in eq 8 is substituted by the long-range electron−electron operator defined in eq 1 to obtain

$$\tilde{V}_{MN}^{lr} = (M|v_{ee}^{lr}(r_{12})|N) \tag{21}$$

and hence

$$V_{MN}^{lr} = (\mathbf{C}^{-1})_{MP} \tilde{V}_{PQ}^{lr} (\mathbf{C}^{-1})_{QN} \tag{22}$$

This long-range Coulomb operator in the auxiliary basis $\mathbf{V}^{lr}$ is then used in the final expression for the long-range RPA correlation energy according to

$$E_c^{RPA,lr} = \frac{1}{2\pi} \int_0^{+\infty} d\omega \, \mathrm{Tr}[\ln(1 - \mathbf{X}_0(i\omega)\mathbf{V}^{lr}) + \mathbf{X}_0\mathbf{V}^{lr}] \tag{23}$$

In our standard full-range RPA algorithm, the trace of the matrix logarithm is evaluated using Cholesky decomposition of $\mathbf{V}$ in combination with the Mercator series for $\ln(1 + x)$ according to

$$\mathrm{Tr}[\ln(1 + \mathbf{X}_0(i\omega)\mathbf{V})] = \mathrm{Tr}[\ln(1 + \mathbf{L}^T\mathbf{X}_0(i\omega)\mathbf{L})] \tag{24}$$

$$= 2 \ln\left(\prod_n L'_{nn}\right) \tag{25}$$

where we absorbed the minus sign into the response function and abbreviated the Cholesky decomposition of $1 + \mathbf{L}^T\mathbf{X}_0(i\omega)\mathbf{L}$ by $\mathbf{L}'$. In the presented range-separated RPA algorithm, Cholesky decomposition of the long-range Coulomb operator $\mathbf{V}^{lr}$ has turned out to be problematic in some cases due to very small negative eigenvalues occurring as a reason for numerical inaccuracies. Therefore, Cholesky decomposition of $\mathbf{V}^{lr}$ is avoided by evaluating the trace of the matrix logarithm according to

$$\mathrm{Tr}[\ln(1 + \mathbf{X}_0(i\omega)\mathbf{V}^{lr})] \tag{26}$$
$$= \mathrm{Tr}[\ln(1 + (\mathbf{V}^{lr})^{1/2}\mathbf{X}_0(i\omega)(\mathbf{V}^{lr})^{1/2})]$$

$$= 2 \ln\left(\prod_n L_{nn}\right) \tag{27}$$

where this time $\mathbf{L}$ stems from Cholesky-decomposing $1 + (\mathbf{V}^{lr})^{1/2}\mathbf{X}_0(i\omega)(\mathbf{V}^{lr})^{1/2}$. Another alternative avoiding Cholesky decomposition of $\mathbf{V}^{lr}$ is, of course, to simply evaluate the matrix logarithm via diagonalization, which works in any case but comes along with an increased computational cost.

3. COMPUTATIONAL DETAILS

All calculations were performed using the FermiONs++ program package.[44−46] The self-consistent range-separated hybrid DFT calculations were performed using the short-range PBE functional of ref 38, which was implemented in a development-version of libxc,[47] and long-range exact exchange. This approach is referred to as "RSHPBE" in the following. The long-range RPA correlation correction to the RSHPBE energy was calculated based on these RSHPBE reference

orbitals using the long-range formulation of the ω-CDGD-RI-RPA method as described above. This range-separated RPA approach is termed "RSHPBE+lrRPA". For all range-separated calculations a range-separation parameter of $\mu = 0.5 \, a_0^{-1}$ was used (see also discussion below), unless stated otherwise. Full-range RPA calculations performed on PBE[48,49] reference orbitals are simply named "RPA" in the following.

All calculations on the GMTKN55 were performed with the Ahlrichs-type split-valence triple-ζ basis set def2-TZVP[50] and the corresponding auxiliary basis set.[51] The basis set was augmented by diffuse functions for the WATER27, G21EA, AHB21, and IL16 subsets in the same way as for the original calculations on the GMTKN55[32] to ensure best possible comparability to already existing results of other density functionals. In the WATER27 test set, Dunning's diffuse s and p functions were applied to oxygen; diffuse s and p functions were applied to non-hydrogen atoms and diffuse s functions to hydrogen in the G21EA, AHB21, and IL16 sets.

Effective-core potentials[50] were used to replace the core electrons of heavy elements in the HEAVYSB11, HEAVY28, and HAL59 subsets.

For all molecules in the singlet state, closed-shell calculations were performed.

4. RESULTS AND DISCUSSION

4.1. Choice of the Basis Set. Several investigations on the basis set dependence of RSHPBE+lrRPA indicated that within the range-separated framework a smaller number of basis functions is required for convergence of the RPA energy with respect to the basis set size.[22,23,26,52] This convergence behavior is caused by the expected exponential convergence of the long-range part of the RPA correlation energy[53] and the replacement of the relatively slowly converging short-range part of the RPA correlation by faster converging PBE. As the studies concerning basis set behavior of range-separated RPA rely on a small number of molecular systems, we investigate here the basis set convergence of range-separated RPA energies compared to full-range RPA energies using a larger set of molecules.

We compared RSHPBE+lrRPA to full-range RPA on the BH76 (barrier heights), BH76RC (reaction energies), and S22 (noncovalent interactions) test sets for different basis sets (detailed results can be found in the Supporting Information). For full-range RPA a rather pronounced basis set dependence can be observed (Figure 1) as the MAD decreases significantly for each of the three subsets going from the triple- to quadruple-ζ basis. The MADs for RSHPBE+lrRPA, in contrast, vary at most in a range of 0.17 kcal/mol going from def2-TZVP to the larger quadruple-ζ basis set and thus can be considered as sufficiently converged with the def2-TZVP basis set. Further, we want to note that the introduced error by fitting the long-range Coulomb operator with the short-range Coulomb metric is, like for fitting the full-range Coulomb operator, orders of magnitude below the orbital basis set error and the intrinsic error of RPA (see Table S2, Supporting Information). Therefore, the dependence of the results on the quality of the auxiliary basis is assumed to be similar to that of standard RI-RPA which was investigated in ref 5.

Even though the results of full-range RPA are clearly not yet converged with the triple-ζ basis sets, we compare both methods using def2-TZVP as we want to have a fair comparison for practical usage. This means using a basis set that is affordable for many applications. For the performance of
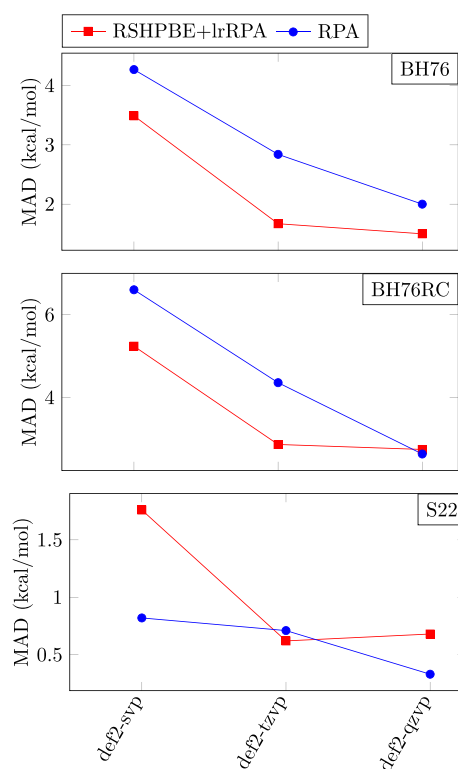
Figure 1. Basis set dependence of the mean absolute deviation (MAD) in kcal/mol for the BH76, BH76RC, and S22 data sets of range-separated RSHPBE+lrRPA (red) and full-range RPA (blue).

Figure 2. Mean absolute deviation (MAD) for the BH76, BH76RC, and S22 data sets as a function of the range-separation parameter μ for range-separated RSHPBE+lrRPA calculations using the def2-TZVP basis set. In the limit of $\mu \to \infty$ RSHPBE+lrRPA converges to standard RPA evaluated on HF reference orbitals (RPA@HF) and for $\mu \to 0$ it corresponds to PBE.

full-range RPA with larger basis sets we refer the interested reader to already existing benchmarks.[6,54−57]

4.2. Choice of the Range-Separation Parameter. Prior studies investigating the range-separation parameter μ in range-separated methods revealed that its optimal value lies around $0.5\ a_0^{-1}$. These prior studies comprise the investigation of the enthalpies of formation for a series of molecules with a combination of srLDA and lrHF exchange[58] and calculations on atomization energy and barrier height data sets with range-separated RPA.[26]

It is worth noting here that in the limit $\mu \to \infty$ the results of RSHPBE+lrRPA do not converge to the results of conventional full-range RPA based on PBE reference orbitals. In fact, the lrRPA$_{\mu \to \infty}$ correlation energy formally corresponds to the full-range formulation, but the RSHPBE (see eq 2) reference orbitals converge to HF orbitals rather than PBE orbitals for $\mu \to \infty$. This means that RSHPBE+lrRPA$_{\mu \to \infty}$ is equal to full-range RPA using HF reference orbitals (RPA@HF, see Figure 2). In the limit of $\mu \to 0$ the lrRPA correlation energy approaches 0. Thus, RSHPBE+lrRPA$_{\mu \to 0}$ approaches the energy of the RSHPBE reference orbitals, which are identical to those of full-range PBE in the case of $\mu \to 0$.

To investigate whether a range-separation parameter of $0.5\ a_0^{-1}$ is indeed an appropriate choice for a broader range of molecules and properties of molecular systems, we complemented these studies by calculations on the BH76RC, BH76, and S22 data sets with varying range-separation parameter in RSHPBE+lrRPA. The results (Figure 2, detailed results can be found in the Supporting Information) reveal that the optimal value for μ slightly varies depending on the examined property or system. While for the BH76 and S22 test sets the optimum

of μ lies at $0.5\ a_0^{-1}$, it is shifted to a slightly higher value of $0.8\ a_0^{-1}$ for the BH76RC test set. A shift of the optimal value of the range-separation parameter to a larger value has also been observed for calculations on reaction energies with a range-separated RPA variant.[59]

Since the results show a quite distinct dependence of the optimal range-separation parameter on the molecular system, we decided to investigate the parameter for an even broader range of molecular systems. We therefore created the set "RAND2x55" which contains two randomly chosen items of each subset of the GMTKN55. The detailed list of contained relative energies can be found in the Supporting Information (Table S1). The absolute values of the relative energies $|\Delta E|$ contained in this test set vary significantly as these describe completely different chemical properties. Items with larger $|\Delta E|$ are expected to give a larger absolute deviation, which in turn leads to a larger change between different μ values. In order to consider each item of the RAND2x55 in the same way for obtaining an optimal range-separation parameter, the absolute deviations of every item are weighted using the weighting factors of weighting scheme 1 of ref 32 for the respective subset. The weighted MADs of the RAND2x55 subset show that there is a broad minimum around $\mu = 0.45\ a_0^{-1}$ (see Figure 3) with a deviation of maximally 0.1 kcal/mol in the MADs over the range $\mu = 0.4\ a_0^{-1}$ to $\mu = 0.55\ a_0^{-1}$. On average, RSHPBE+lrRPA seems to be quite robust with respect to the choice of μ, reassuring us that the

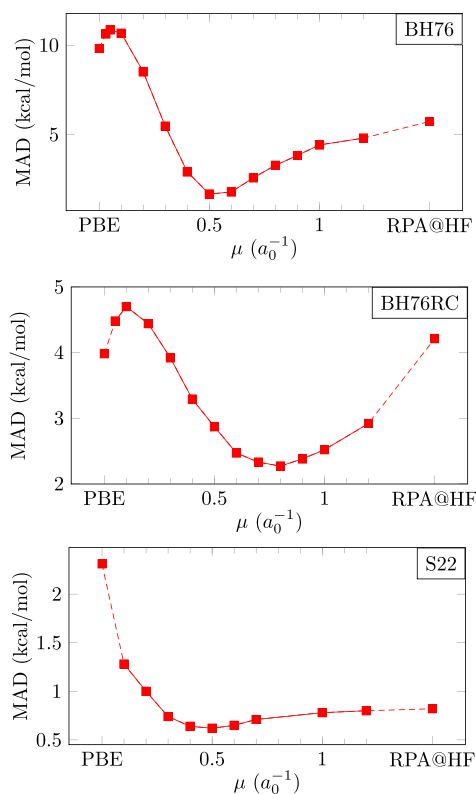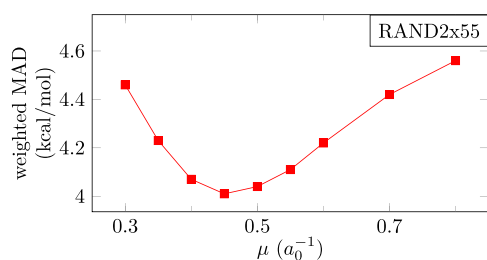**Figure 3.** Weighted mean absolute deviation (MAD) for the RAND2×55 data set as a function of the range-separation parameter μ for range-separated RSHPBE+lrRPA calculations using the def2-TZVP basis set.

choice of $\mu = 0.5\ a_0^{-1}$ in previous studies[23,25,26,58] is reasonable. For this reason a range-separation parameter of 0.5 a_0^{-1} was used in the following.

4.3. Results of the GMTKN55 Data Set. The subsets included in the GMTKN55 data set can be grouped into five categories. The first category "basic + small" targets basic properties and reaction energies for small systems. The subsets of the second category "iso + large" comprise reaction energies for large systems and isomerizations. In the third category "barrier", barrier height test sets are united. The last two subcategories "intermol. NCIs" and "intramol. NCIs" focus on inter- and intramolecular noncovalent interactions, respectively.

As shown in Table 1, RSHPBE+lrRPA yields a weighted mean absolute deviation according to weighting scheme 1 of

Table 1. Comparison of the WTMAD-1 for the GMTKN55 obtained by RSHPBE+lrRPA and Full-Range RPA to Density Functionals Grouped by the Rank of the Jacob's Ladder

RSHPBE+lrRPA	3.86[a]
RPA	4.72[a]
GGA	10.70[b]
meta-GGA	7.31[b]
hybrid	6.56[b]
double-hybrid	3.60[b]

[a]def-TZVP basis set, this work. [b]def2-QZVP basis set and no empirical dispersion correction. Average value taken from ref 32.

ref 32 (WTMAD-1) of 3.86 kcal/mol for the total GMTKN55 data set. With this result RSHPBE+lrRPA is among the 15% best density functionals tested in ref 32 using the def2-QZVP basis set (see Figure 4) and can be ranked in between the average hybrid and average double-hybrid density functional (see Table 1). It has to be further stressed that the compared (MP2-based) double-hybrid functionals are, due to the inclusion of exchange terms, computationally more expensive than the here presented RPA methods.

The results grouped by category (see Table 2 and Figure 5) show that RSHPBE+lrRPA is not as good as the average double-hybrid density functional for "basic + small" and "barriers" but is significantly better for NCIs. However, the deficiencies of double-hybrid density functionals in describing noncovalent interactions can be compensated by the inclusion of the empirical "D3" dispersion correction of Grimme.[60,61]

RSHPBE+lrRPA gives a slightly better result than full-range RPA (WTMAD-1 of 3.86 kcal/mol vs 4.72 kcal/mol) for the complete GMTKN55 test set. Furthermore, RSHPBE+lrRPA
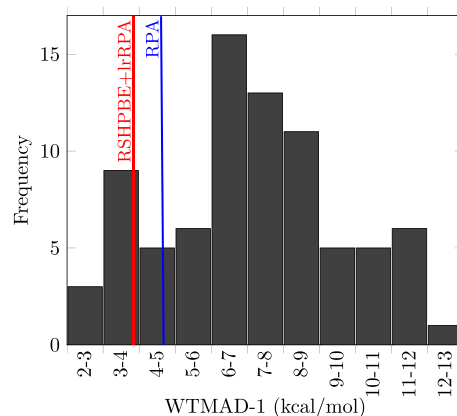
Figure 4. Histogram showing the WTMAD-1 distribution for all tested density functionals without empirical dispersion correction (def2-QZVP) in ref 32 on the total GMTKN55 test set. The red and blue lines illustrate where RSHPBE+lrRPA and full-range RPA def2-TZVP are placed among the density functionals according to the WTMAD-1.

Table 2. WTMAD-1 Values in kcal/mol for the GMTKN55 Test Set and Its Categories[a]

	RSHPBE	PBE	RSHPBE +lrRPA	RPA	average double-hybrid	
					no D3	D3
GMTKN55	8.33	8.17	3.86	4.72	3.60	2.05
basic + small	4.92	5.56	3.48	5.41	2.21	1.87
iso. + large	4.97	7.38	3.76	3.10	3.40	2.50
barriers	5.72	7.64	3.56	2.63	1.43	1.59
intermol. NCIs	13.87	10.41	4.27	6.54	5.90	2.02
intramlo. NCIs	13.13	11.64	4.40	4.16	5.17	2.39
all NCIs	13.55	10.94	4.33	5.52	5.59	2.18

[a]All calculations were performed using the def2-TZVP basis set. Values for the average double-hybrid functional with and without Grimme's D3 dispersion correction[60,61] were obtained using the def2-QZVP basis set and are taken from ref 32.

performs more stably over all categories. The WTMAD-1 of RSHPBE+lrRPA is for all categories about the same and does not show as high fluctuations as the full-range variant. In both cases, range-separated and full-range, the RPA correlation energy on average improves the results of the respective Kohn−Sham reference calculations, RSHPBE and PBE.

The improvement of the RPA approaches over the respective Kohn−Sham reference is most prominent for the categories concerning noncovalent interactions. Within the subsets of "intermol. NCIs" and "intramol. NCIs" the improvement is most obvious for the IDISP subset which targets intermolecular dispersion interactions (see Table 3). This is not surprising, as RSHPBE and PBE do not account for any dispersion interactions. Moreover, the remarkably high MAD of RSHPBE+lrRPA for the WATER27 (hydrogen bonds) subset has to be noted. Apparently, this test set is quite sensitive to the basis set size as all tested methods have a significant deviation in the MAD between the def2-TZVP and def2-QZVP results (see Table 3, values in brackets). This means that for this test set the results of all studied methods, including the references RSHPBE and PBE, are not sufficiently
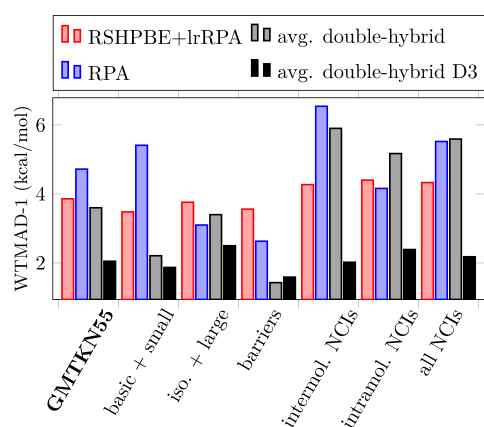
Figure 5. Graphical representation of the WTMAD-1 values for the GMTKN55 test set and its categories. The def2-TZVP basis set was used for RSHPBE+lrRPA and full-range RPA (this work). The average WTMAD-1s for all tested double-hybrid functionals in ref 32 with (avg. double-hybrid D3) and without (avg. double-hybrid) Grimme's D3 dispersion correction[60,61] were obtained using the def2-QZVP basis set and are taken from ref 32.

converged with respect to the basis set size at triple-ζ level and are thus not reliable.

For all noncovalent interactions (all NCIs, Table 2), RSHPBE+lrRPA has a slightly lower WTMAD-1 compared to full-range RPA. This is in line with the observation of Zhu et al.[25] that range-separated RPA improves interaction energies of weakly interacting intermolecular complexes. Also, several studies suggest[17,25,52,62] that a range-separated RPA approach improves interaction energies in rare-gas dimers which we can confirm by the results of the RG18 subset (Table 3).

For reaction barrier heights, varying results for RSHPBE +lrRPA were obtained. In fact, RSHPBE+lrRPA has a slightly lower MAD in some reaction barrier height subsets but has also a remarkably higher MAD for the two subsets, PX13 and WCPT18, containing reaction barriers of proton-transfer and -exchange reactions, where water−water interactions, which are also present in the WATER27 test set, play a crucial role. This suggests that the results of PX13 and WCPT18 might also be not sufficiently converged with respect to the basis set size at the triple-ζ level. This is one of the reasons why we have not observed a significant improvement in the description of reaction barrier heights for RSHPBE+lrRPA over full-range RPA, contradicting the finding of Mussard et al.[26] Another reason might be the larger test volume investigated in our present work.

For the category "iso. + large", a slightly inferior performance of RSHPBE+lrRPA compared to the full-range variant is observed (3.76 kcal/mol vs 3.10 kcal/mol). In this category, the MADs for the MB16-43 (decomposition of artificial molecules) and DARC (Diels−Alder reaction energies) subsets stand out in particular (Table 3). For the DARC test set the difference in the MADs between RSHPBE+lrRPA and full-range RPA is remarkable. It should be noted that the errors for this rather specialized test set are mainly systematic as all relative energies contained in this test set describe one single property: the relative stability of a C−C σ bond vs a C−C π bond. The low MAD of full-range RPA arises from a fortuitous error cancellation for this very specific type of reactions. PBE significantly underestimates the relative stability of C−C σ bonds (signed error +6.12 kcal/mol), and the addition of the

full-range RPA correlation compensates this deficiency nearly exactly (signed error +0.48 kcal/mol). In contrast, RSHPBE already overestimates the relative strength of C−C σ bonds (signed error −1.27 kcal/mol), so that the addition of the long-range RPA correlation results in an even stronger comparative overbinding of σ bonds (signed error −6.79 kcal/mol). However, this error is not unusually large compared to other functionals. The average MAD for all double-hybrid functionals tested in ref 32 without empirical dispersion correction is 4.62 kcal/mol. We also tested the influence of the basis set on this specific test set employing the def2-QZVP basis set instead. The differences in the MADs of RSHPBE +lrRPA and full-range RPA, however, were found to be smaller than 1 kcal/mol, i.e., this test set is not dominated by basis set incompleteness errors.

For the MB16-43 test set large MADs are not unusual due to the large average of absolute energy differences $|\overline{\Delta E}|$ of 414.73 kcal/mol. The result of RSHPBE+lrRPA for this test set is as good as the average result of all double-hybrid functionals tested in ref 32 with 22.91 kcal/mol (without empirical dispersion correction). The MAD of full-range RPA, however, is exceptionally large displaying the deficiency of standard full-range RPA to describe the strength of covalent bonds which is well-known concerning atomization energies.[54,63−65]

RSHPBE+lrPBE seems to have an improved performance in basic properties as compared to full-range RPA ("basic + small", Table 2 and Figure 5). This difference in the WTMAD-1s arises from the stable performance of RSHPBE +lrRPA compared to the varying results of standard RPA. Here, especially the noticeable high MADs of the W4-11 (atomization energies), SIE4x4 (self-interaction-error related problems), and ALKBDE10 (dissociation energies of group-1 and -2 diatomics) subsets stand out. The obtained results for the atomization energies subset W4-11 are in line with those of Mussard et al.,[26] who also observed that range-separated RPA gives more precise atomization energies than the full-range variant. It has to be noted that the large MADs of full-range RPA for atomization energies and dissociation energies arise from the systematical underbinding of standard full-range RPA caused by deficiencies in the description of short-range correlation.[54,63,65] The poor performance of standard RPA for the self-interaction-error related problems is also not surprising as it is a well-known deficiency of direct RPA. However, the range-separation approach somewhat alleviates this problem, as indicated by the significantly better performance of RSHPBE+lrRPA in the SIE4x4 test set, confirming the findings of previous work on range-separated RPA.[33,66] In this context, range-separated RPA may also be regarded as a cost-effective alternative to beyond RPA methods.[29,67−72]

5. CONCLUSION

In this work we presented a range-separated RPA method, RSHPBE+lrRPA, based on our efficient linear-scaling ω-CDGD-RI-RPA algorithm.[28] Investigations on the basis set dependence revealed that energies obtained by this range-separated method converge faster with respect to the basis set size than full-range RPA energies. For most systems, RSHPBE+lrRPA yields reliable results with the def2-TZVP basis set. The weaker basis set dependence compared to full-range RPA and the fact that the presented RSHPBE+lrRPA method is exactly as efficient as the underlying ω-CDGD-RI-RPA algorithm opens up the possibility for efficiently applying

Table 3. Detailed List of the Mean Absolute Deviation in kcal/mol for All Subsets of the GMTKN55 Data Base[a]

set	description	RSHPBE	PBE	RSHPBE+lrRPA	RPA
Basic Properties and Reaction Energies for Small Systems					
W4-11[b]	total atomization energies	15.34	14.69	6.94	27.06
G21EA	adiabatic electron affinities	6.43	2.80	3.66	3.39
G21IP	adiabatic ionization potentials	5.09	3.91	4.29	3.41
DIPCS10	double-ionization potentials of closed-shell systems	6.15	4.59	2.94	6.32
PA26	adiabatic proton affinities (incl. of amino acids)	2.53	1.92	1.29	3.88
SIE4x4	self-interaction-error related problems	4.64	23.73	8.63	22.19
ALKBDE10	dissociation energies in group-1 and -2 diatomics	6.19	4.93	4.83	25.00
YBDE18	bond-dissociation energies in ylides	6.99	5.68	2.56	5.28
AL2x6	dimerization energies of AlX_x compounds	6.27	4.04	1.79	2.82
HEAVYSB11	dissociation energies in heavy-element compounds	12.53	4.34	4.97	6.66
NBPRC	oligomerizations and H_2 fragmentation of NH_3/BH_3 systems	2.62	2.77	1.95	2.53
ALK8	dissociation and other reactions of alkaline compounds	7.09	3.05	3.69	7.79
RC21	fragmentations and rearrangements in radical cations	2.71	6.03	4.09	2.79
G2RC	reaction energies of selected G2/97 systems	5.48	7.50	5.67	7.04
BH76RC	reaction energies of the BH76 set	2.38	3.98	2.87	4.51
FH51	reaction energies in various (in-) organic systems	3.27	4.03	3.31	3.40
TAUT15	relative energies in tautomers	1.18	1.91	0.90	1.19
DC13	13 difficult cases for DFT methods	12.76	10.00	8.49	10.47
Reaction Energies for Large Systems and Isomerization Reactions					
MB16-43	decomposition energies of artificial molecules	49.92	24.24	21.72	60.96
DARC	reaction energies of Diels−Alder reactions	1.61	6.39	6.79	0.92
RSE43	radical-stabilization energies	0.46	3.16	0.53	0.48
BSR36	bond-separation reaction of satured hydrocarbons	8.43	8.15	0.90	1.88
CDIE20	double-bond isomerization energies in cyclic systems	1.00	1.90	0.69	0.46
ISO34	isomerization energies of small and medium-sized organic molecules	1.70	1.95	1.51	1.43
ISOL24	isomerization energies of large organic molecules	4.74	6.71	3.79	2.01
C60ISO	relative energies between C_{60} isomers	23.05	10.48	7.55	7.71
PArel	relative energies in protonated isomers	1.05	1.76	1.05	0.97
Reaction Barrier Heights					
BH76	barrier heights of hydrogen transfer, heavy atom transfer, nucleophilic substitution, unimolecular, and association reactions	3.17	9.82	1.67	2.84
BHPERI	barrier heights of pericyclic reactions	10.74	4.18	1.85	0.73
BHDIV10	diverse reaction barrier heights	5.10	8.24	1.39	1.89
INV24	inversion/racemization barrier heights	3.39	2.95	2.11	1.21
BHROT27	barrier heights for rotation around single bonds	0.90	0.54	0.70	0.75
PX13	proton-exchange barriers in H_2O, NH_3, and HF clusters	5.07	13.16	7.67	2.36
WCPT18	proton-transfer barriers in uncatalyzed and water-catalyzed reactions	3.59	9.66	3.19	1.68
Intermolecular Noncovalent Interactions					
RG18	interaction energies in rare-gas complexes	0.51	0.36	0.14	0.41
ADIM6	interaction energies of n-alkane dimers	4.54	3.37	1.24	0.30
S22	binding energies of noncovalently bound dimers	3.01	2.31	0.62	0.71
S66	binding energies of noncovalently bound dimers	2.57	1.94	0.72	0.42
HEAVY28	noncovalent interaction energies between heavy element hydrides	1.30	0.49	0.45	0.65
WATER27	binding energies in $(H_2O)_n$, $H^+(H_2O)_n$, and $OH^-(H_2O)_n$	2.27 (5.08)	9.06 (2.84)	11.64 (5.70)	0.89 (3.86)
CARBH12	hydrogen-bonded complexes between carbene analogues and H_2O, NH_3, or HCl	0.63	1.45	0.59	2.07
PNICO23	interaction energies in pnicogen-containing dimers	1.77	0.86	0.53	1.43
HAL59	binding energies in halogenated dimers (incl. halogen bonds)	1.94	1.36	0.37	1.62
AHB21	interaction energies in anion-neutral dimers	1.22	1.10	1.52	1.33
CHB6	interaction energies in cation-neutral dimers	1.76	1.34	1.68	0.87
IL16	interaction energies in anion−cation dimers	4.29	1.77	0.66	0.95
Intramolecular Dispersion Interactions					
IDISP	intramolecular disperison interaction	10.72	10.62	2.81	2.63
ICONF	relative energies in conformers of inorganic systems	0.79	0.41	0.43	0.46
ACONF	Relative energies of alkane conformers	0.92	0.58	0.19	0.06
AMINO20x4	Relative energies in amino acid conformers	0.62	0.47	0.27	0.35

Table 3. continued

set	description	RSHPBE	PBE	RSHPBE+lrRPA	RPA
Intramolecular Dispersion Interactions					
PCONF21	relative energies in tri- and tetrapeptide conformers	3.14	3.20	0.68	1.04
MCONF	relative energies in melatonin conformers	1.83	1.64	0.19	0.64
SCONF	Relative energies of sugar conformers	0.75	0.70	0.49	0.24
UPU23	relative energies between RNA-backbone conformers	2.51	1.87	0.83	0.55
BUT14DIOL	relative energies in butane-1,4-diol conformers	0.19	0.54	0.60	0.14

[a]All calculations were performed using the def2-TZVP basis set. For the WATER27 test set aug-def2-QZVP results are given in brackets. [b]Without the atomization energy of C_2.

range-separated RPA onto relevant systems with several hundred atoms, as illustrated for the ω-CDGD-RI-RPA method in ref 28 where the largest system comprised 902 atoms.

Investigations on the range-separation parameter μ revealed a shallow minimum between 0.4 a_0^{-1} and 0.55 a_0^{-1}, which is in good agreement with previous findings of $\mu = 0.5$ a_0^{-1} to be optimal.[21,23,25,26,38,62]

To give a comprehensive picture of the performance of RSHPBE+lrRPA we compared this method to standard RPA on the GMTKN55 data set[32] and placed it among previously tested density functionals. The results for GMTKN55 show that RSHPBE+lrRPA yields stable results for a broad range of thermochemical and kinetic properties as well as noncovalent interactions. Although the overall performance of RSHPBE+lrRPA is comparable to that of full-range RPA, it shows less variance in the WTMAD-1s of the subcategories. It was found that the range-separation approach especially gives better results compared to those of the full-range variant for atomization energies (W4-11), problems that are prone to the self-interaction-error (SIE4x4), and systems containing group-1 and -2 elements (ALKBDE10, ALK8).

Overall, the results of RSHPBE+lrRPA are promising considering that only one empirical parameter was employed. In the future, the method could further be improved by including exchange into the response function, e.g., along the lines of the second order screened exchange (SOSEX) RPA method.[29,67,68,72] Alternatively, more empirical approaches could be explored in a similar fashion as done by Mardirossian and Head-Gordon,[73] i.e., employing more empirical semilocal exchange-correlation functionals (e.g., B97[74]), more complicated range-separation schemes, or adding empirical dispersion interaction corrections.

Due to the lower computational cost compared to standard MP2 and the stable results of range-separated RPA over a broad range of chemical problems, this avenue is in our opinion worth considering for future developments.

ASSOCIATED CONTENT

Supporting Information

The Supporting Information is available free of charge at https://pubs.acs.org/doi/10.1021/acs.jctc.9b01294.

Details on the "RAND2x55" test set (PDF)

Detailed list of the relative energies for all subsets (XLSX)

AUTHOR INFORMATION

Corresponding Author

Christian Ochsenfeld − *Chair of Theoretical Chemistry, Department of Chemistry, University of Munich (LMU), D-81377 Munich, Germany; Max Planck Institute for Solid State Research, D-70569 Stuttgart, Germany;* orcid.org/0000-0002-4189-6558; Email: c.ochsenfeld@fkf.mpg.de

Authors

Andrea Kreppel − *Chair of Theoretical Chemistry, Department of Chemistry, University of Munich (LMU), D-81377 Munich, Germany*

Daniel Graf − *Chair of Theoretical Chemistry, Department of Chemistry, University of Munich (LMU), D-81377 Munich, Germany*

Henryk Laqua − *Chair of Theoretical Chemistry, Department of Chemistry, University of Munich (LMU), D-81377 Munich, Germany*

Complete contact information is available at:
https://pubs.acs.org/10.1021/acs.jctc.9b01294

Notes

The authors declare no competing financial interest.

REFERENCES

(1) Bohm, D.; Pines, D. A collective description of electron interactions: III. Coulomb interactions in a degenerate electron gas. *Phys. Rev.* **1953**, *92*, 609−625.

(2) Langreth, D. C.; Perdew, J. P. The Exchange-Correlation Energy of a Metallic Surface. *Solid State Commun.* **1975**, *17*, 1425−1429.

(3) Langreth, D. C.; Perdew, J. P. Exchange-correlation energy of a metallic surface: Wave-vector analysis. *Phys. Rev. B* **1977**, *15*, 2884−2901.

(4) Furche, F. Developing the random phase approximation into a practical post-Kohn-Sham correlation model. *J. Chem. Phys.* **2008**, *129*, 114105.

(5) Eshuis, H.; Yarkony, J.; Furche, F. Fast computation of molecular random phase approximation correlation energies using resolution of the identity and imaginary frequency integration. *J. Chem. Phys.* **2010**, *132*, 234114.

(6) Eshuis, H.; Furche, F. Basis set convergence of molecular correlation energy differences within the random phase approximation. *J. Chem. Phys.* **2012**, *136*, 084105.

(7) Kohn, W.; Sham, L. J. Self-Consistent Equations Including Exchange and Correlation Effects. *Phys. Rev.* **1965**, *140*, A1133−A1138.

(8) Perdew, J. P.; Schmidt, K. Jacob's ladder of density functional approximations for the exchange-correlation energy. *AIP Conf. Proc.* **2000**, *577*, 1−20.

(9) Andersson, Y.; Langreth, D. C.; Lundqvist, B. I. Van der Waals interactions in density-functional theory. *Phys. Rev. Lett.* **1996**, *76*, 102−105.

(10) Dobson, J. F.; Wang, J. Successful test of a seamless van der Waals density functional. *Phys. Rev. Lett.* **1999**, *82*, 2123−2126.

(11) Dobson, J. F.; Wang, J.; Dinte, B. P.; McLennan, K.; Le, H. M. Soft cohesive forces. *Int. J. Quantum Chem.* **2005**, *101*, 579−598.

(12) Harl, J.; Kresse, G. Cohesive energy curves for noble gas solids calculated by adiabatic connection fluctuation-dissipation theory. *Phys. Rev. B: Condens. Matter Mater. Phys.* **2008**, *77*, 045136.

(13) Nguyen, H. V.; Galli, G. A first-principles study of weakly bound molecules using exact exchange and the random phase approximation. *J. Chem. Phys.* **2010**, *132*, 044109.

(14) Lebègue, S.; Harl, J.; Gould, T.; Ángyán, J. G.; Kresse, G.; Dobson, J. F. Cohesive properties and asymptotics of the dispersion interaction in graphite by the random phase approximation. *Phys. Rev. Lett.* **2010**, *105*, 196401.

(15) Singwi, K. S.; Tosi, M. P.; Land, R. H.; Sjolander, A. Electron Correlations at Metallic Densities. *Phys. Rev.* **1968**, *176*, 589−599.

(16) Kurth, S.; Perdew, J. Density-functional correction of random-phase-approximation correlation with results for jellium surface energies. *Phys. Rev. B: Condens. Matter Mater. Phys.* **1999**, *59*, 10461−10468.

(17) Ángyán, J. G.; Liu, R. F.; Toulouse, J.; Jansen, G. Correlation energy expressions from the adiabatic-connection fluctuation-dissipation theorem approach. *J. Chem. Theory Comput.* **2011**, *7*, 3116−3130.

(18) Perdew, J. P. Local density and gradient-corrected functionals for short-range correlation: Antiparallel-spin and non-RPA contributions. *Int. J. Quantum Chem.* **1993**, *48*, 93−100.

(19) Savin, A. A Combined Density Functional and Configuration Interaction Method. *Int. J. Quantum Chem.* **1988**, *34*, 59−69.

(20) Kohn, W.; Meir, Y.; Makarov, D. E. Van der Waals Energies in Density Functional Theory. *Phys. Rev. Lett.* **1998**, *80*, 4153−4156.

(21) Toulouse, J.; Gerber, I. C.; Jansen, G.; Savin, A.; Ángyán, J. G. Adiabatic-connection fluctuation-dissipation density-functional theory based on range separation. *Phys. Rev. Lett.* **2009**, *102*, 096404.

(22) Janesko, B. G.; Henderson, T. M.; Scuseria, G. E. Long-range-corrected hybrids including random phase approximation correlation. *J. Chem. Phys.* **2009**, *130*, 081105.

(23) Toulouse, J.; Zhu, W.; Angyan, J. G.; Savin, A. Range-separated density-functional theory with random phase approximation: detailed formalism and illustrative applications. *Phys. Rev. A: At., Mol., Opt. Phys.* **2010**, *82*, 032502.

(24) Janesko, B. G.; Henderson, T. M.; Scuseria, G. E. Long-range-corrected hybrid density functionals including random phase approximation correlation: Application to noncovalent interactions. *J. Chem. Phys.* **2009**, *131*, 034110.

(25) Zhu, W.; Toulouse, J.; Savin, A.; Ángyán, J. G. Range-separated density-functional theory with random phase approximation applied to noncovalent intermolecular interactions. *J. Chem. Phys.* **2010**, *132*, 244108.

(26) Mussard, B.; Reinhardt, P.; Ángyán, J. G.; Toulouse, J. Spin-unrestricted random-phase approximation with range separation: Benchmark on atomization energies and reaction barrier heights. *J. Chem. Phys.* **2015**, *142*, 154123.

(27) Schurkus, H. F.; Ochsenfeld, C. Communication: An effective linear-scaling atomic-orbital reformulation of the random-phase approximation using a contracted double-Laplace transformation. *J. Chem. Phys.* **2016**, *144*, 031101.

(28) Graf, D.; Beuerle, M.; Schurkus, H. F.; Luenser, A.; Savasci, G.; Ochsenfeld, C. Accurate and Efficient Parallel Implementation of an Effective Linear-Scaling Direct Random Phase Approximation Method. *J. Chem. Theory Comput.* **2018**, *14*, 2505−2515.

(29) Beuerle, M.; Graf, D.; Schurkus, H. F.; Ochsenfeld, C. Efficient calculation of beyond RPA correlation energies in the dielectric matrix formalism. *J. Chem. Phys.* **2018**, *148*, 204104.

(30) Graf, D.; Beuerle, M.; Ochsenfeld, C. Low-Scaling Self-Consistent Minimization of a Density Matrix Based Random Phase

(31) Luenser, A.; Schurkus, H. F.; Ochsenfeld, C. Vanishing-Overhead Linear-Scaling Random Phase Approximation by Cholesky Decomposition and an Attenuated Coulomb-Metric. *J. Chem. Theory Comput.* **2017**, *13*, 1647−1655.

(32) Goerigk, L.; Hansen, A.; Bauer, C.; Ehrlich, S.; Najibi, A.; Grimme, S. A look at the density functional theory zoo with the advanced GMTKN55 database for general main group thermochemistry, kinetics and noncovalent interactions. *Phys. Chem. Chem. Phys.* **2017**, *19*, 32184−32215.

(33) Mezei, P. D.; Kállay, M. Construction of a Range-Separated Dual-Hybrid Direct Random Phase Approximation. *J. Chem. Theory Comput.* **2019**, *15*, 6678−6687.

(34) Einstein, A. Die Grundlage der allgemeinen Relativitätstheorie. *Ann. Phys.* **1916**, *354*, 769−822.

(35) Iikura, H.; Tsuneda, T.; Yanai, T.; Hirao, K. A long-range correction scheme for generalized-gradient-approximation exchange functionals. *J. Chem. Phys.* **2001**, *115*, 3540−3544.

(36) Toulouse, J.; Colonna, F.; Savin, A. Short-range exchange and correlation energy density functionals: Beyond the local-density approximation. *J. Chem. Phys.* **2005**, *122*, 014110.

(37) Laikov, D. N. Simple exchange hole models for long-range-corrected density functionals. *J. Chem. Phys.* **2019**, *151*, 094106.

(38) Goll, E.; Werner, H.-J.; Stoll, H.; Leininger, T.; Gori-giorgi, P.; Savin, A. A short-range gradient-corrected spin density functional in combination with long-range coupled-cluster methods: Application to alkali-metal rare-gas dimers. *Chem. Phys.* **2006**, *329*, 276−282.

(39) Gunnarsson, O.; Lundqvist, B. I. Exchange and correlation in atoms, molecules, and solids by the spin-density-functional formalism. *Phys. Rev. B* **1976**, *13*, 4274−4298.

(40) Kaltak, M.; Klimeš, J.; Kresse, G. Low scaling algorithms for the random phase approximation: Imaginary time and Laplace transformations. *J. Chem. Theory Comput.* **2014**, *10*, 2498.

(41) Koch, H.; Sánchez De Merás, A.; Pedersen, T. B. Reduced scaling in electronic structure calculations using Cholesky decompositions. *J. Chem. Phys.* **2003**, *118*, 9481−9484.

(42) Higham, N. J. Cholesky factorization. *Wiley Interdiscip. Rev. Comput. Stat.* **2009**, *1*, 251−254.

(43) Harbrecht, H.; Peters, M.; Schneider, R. On the low-rank approximation by the pivoted Cholesky decomposition. *Appl. Numer. Math.* **2012**, *62*, 428−440.

(44) Kussmann, J.; Ochsenfeld, C. Pre-selective screening for matrix elements in linear-scaling exact exchange calculations. *J. Chem. Phys.* **2013**, *138*, 134114.

(45) Kussmann, J.; Ochsenfeld, C. Preselective screening for linear-scaling exact exchange-gradient calculations for graphics processing units and general strong-scaling massively parallel calculations. *J. Chem. Theory Comput.* **2015**, *11*, 918−922.

(46) Kussmann, J.; Ochsenfeld, C. Hybrid CPU/GPU Integral Engine for Strong-Scaling Ab Initio Methods. *J. Chem. Theory Comput.* **2017**, *13*, 3153−3159.

(47) Marques, M. A. L.; Oliveira, M. J. T.; Burnus, T. Libxc: a library of exchange and correlation functionals for density functional theory. *Comput. Phys. Commun.* **2012**, *183*, 2272.

(48) Perdew, J. P.; Burke, K.; Ernzerhof, M. Generalized gradient approximation made simple. *Phys. Rev. Lett.* **1996**, *77*, 3865−3868.

(49) Perdew, J. P.; Ernzerhof, M.; Burke, K. (ERRATA) Generalized Gradient Approximation Made Simple. *Phys. Rev. Lett.* **1996**, *77*, 3865−3868.

(50) Weigend, F.; Ahlrichs, R. Balanced basis sets of split valence, triple zeta valence and quadruple zeta valence quality for H to Rn: Design and assessment of accuracy. *Phys. Chem. Chem. Phys.* **2005**, *7*, 3297−3305.

(51) Weigend, F.; Häser, M.; Patzelt, H.; Ahlrichs, R. RI-MP2: optimized auxiliary basis sets and demonstration of efficiency. *Chem. Phys. Lett.* **1998**, *294*, 143−152.

(52) Irelan, R. M.; Henderson, T. M.; Scuseria, G. E. Long-range-corrected hybrids using a range-separated Perdew-Burke-Ernzerhof

functional and random phase approximation correlation. *J. Chem. Phys.* **2011**, *135*, 094105.

(53) Franck, O.; Mussard, B.; Luppi, E.; Toulouse, J. Basis convergence of range-separated density-functional theory. *J. Chem. Phys.* **2015**, *142*, 074107.

(54) Eshuis, H.; Bates, J. E.; Furche, F. Electron correlation methods based on the random phase approximation. *Theor. Chem. Acc.* **2012**, *131*, 1084.

(55) Ren, X.; Rinke, P.; Scuseria, G. E.; Scheffler, M. Renormalized second-order perturbation theory for the electron correlation energy: Concept, implementation, and benchmarks. *Phys. Rev. B: Condens. Matter Mater. Phys.* **2013**, *88*, 035120.

(56) Ruzsinszky, A.; Zhang, I. Y.; Scheffler, M. Insight into organic reactions from the direct random phase approximation and its corrections. *J. Chem. Phys.* **2015**, *143*, 144115.

(57) Grimme, S.; Steinmetz, M. A computationally efficient double hybrid density functional based on the random phase approximation. *Phys. Chem. Chem. Phys.* **2016**, *18*, 20926−20937.

(58) Gerber, I. C.; Ángyán, J. G. Hybrid functional with separated range. *Chem. Phys. Lett.* **2005**, *415*, 100−105.

(59) Heßelmann, A.; Ángyán, J. Assessment of a range-separated orbital-optimized random-phase approximation electron correlation method. *Theor. Chem. Acc.* **2018**, *137*, 155.

(60) Grimme, S.; Antony, J.; Ehrlich, S.; Krieg, H. A consistent and accurate ab initio parametrization of density functional dispersion correction (DFT-D) for the 94 elements H-Pu. *J. Chem. Phys.* **2010**, *132*, 154104.

(61) Grimme, S.; Ehrlich, S.; Goerigk, L. Effect of the Damping Function in Dispersion Corrected Density Functional Theory. *J. Comput. Chem.* **2011**, *32*, 1456−1465.

(62) Toulouse, J.; Zhu, W.; Savin, A.; Jansen, G.; Ángyán, J. G. Closed-shell ring coupled cluster doubles theory with range separation applied on weak intermolecular interactions. *J. Chem. Phys.* **2011**, *135*, 084119.

(63) Furche, F. Molecular tests of the random phase approximation to the exchange-correlation energy functional. *Phys. Rev. B: Condens. Matter Mater. Phys.* **2001**, *64*, 195120.

(64) Dobson, J. F.; Gould, T. Calculation of dispersion energies. *J. Phys.: Condens. Matter* **2012**, *24*, 073201.

(65) Chen, G. P.; Voora, V. K.; Agee, M. M.; Balasubramani, S. G.; Furche, F. Random-Phase Approximation Methods. *Annu. Rev. Phys. Chem.* **2017**, *68*, 421−445.

(66) Mezei, P. D.; Csonka, G. I.; Ruzsinszky, A.; Kállay, M. Construction and Application of a New Dual-Hybrid Random Phase Approximation. *J. Chem. Theory Comput.* **2015**, *11*, 4615−4626.

(67) Freeman, D. L. Coupled-cluster expansion applied to the electron gas: Inclusion of ring and exchange effects. *Phys. Rev. B* **1977**, *15*, 5512−5521.

(68) Grüneis, A.; Marsman, M.; Harl, J.; Schimka, L.; Kresse, G. Making the random phase approximation to electronic correlation accurate. *J. Chem. Phys.* **2009**, *131*, 154115.

(69) Bates, J. E.; Furche, F. Communication: Random phase approximation renormalized many-body perturbation theory. *J. Chem. Phys.* **2013**, *139*, 171103.

(70) Mussard, B.; Rocca, D.; Jansen, G.; Ángyán, J. G. Dielectric Matrix Formulation of Correlation Energies in the Random Phase Approximation: Inclusion of Exchange Effects. *J. Chem. Theory Comput.* **2016**, *12*, 2191−2202.

(71) Dixit, A.; Ángyán, J. G.; Rocca, D. Improving the accuracy of ground-state correlation energies within a plane-wave basis set: The electron-hole exchange kernel. *J. Chem. Phys.* **2016**, *145*, 104105.

(72) Beuerle, M.; Ochsenfeld, C. Short-range second order screened exchange correction to RPA correlation energies. *J. Chem. Phys.* **2017**, *147*, 204107.

(73) Mardirossian, N.; Head-Gordon, M. Survival of the most transferable at the top of Jacob's ladder: Defining and testing the ωB97M(2) double hybrid density functional. *J. Chem. Phys.* **2018**, *148*, 241736.

(74) Becke, A. D. Density-functional thermochemistry. V. Systematic optimization of exchange- correlation functionals. *J. Chem. Phys.* **1997**, *107*, 8554−8560.

Supporting Information for: Range-Separated Density-Functional Theory in Combination with the Random Phase Approximation: An Accuracy Benchmark

Andrea Kreppel,[†] Daniel Graf,[†] Henryk Laqua,[†] and Christian Ochsenfeld[*,†,‡]

†*Chair of Theoretical Chemistry, Department of Chemistry, University of Munich (LMU), D-81377 Munich, Germany*

‡*Max Planck Institute for Solid State Research, Heisenbergstr. 1, D-70569 Stuttgart, Germany*

E-mail: c.ochsenfeld@fkf.mpg.de

The detailed results of RSHPBE, PBE, RSHBPE+lrRPA, and full-range RPA on the GMTKN55 obtained in this work can be found in the enclosed file 'GMTKN55.xlsx'.

Table S1: Detailed list of the RAND2x55 test set. For each item its number in the original subset (#) is given. The system names correspond to the geometry files of the corresponding test set. The reference values are given in kcal/mol. In the last column, the weighting factor of the corresponding test set in the WTMAD-1 scheme is given.

subset	#	systems	stoichiometry	ref.	$w1$
W4-11	8	sih si h	-1 1 1	73.921	0.1
W4-11	90	hocl h o cl	-1 1 1 1	166.229	0.1
G21EA	20	EA_20n EA_20	1 -1	9.5	1
G21EA	2	EA_o EA_o-	1 -1	33.7	1
G21IP	36	IP_80 48	1 -1	261.153	0.1
G21IP	22	IP_65 IP_n65	1 -1	234.107	0.1
DIPCS10	2	c2h6 c2h6_2+	-1 1	667.1	0.1
DIPCS10	7	h2s h2s_2+	-1 1	733	0.1
PA26	15	ch3cooh ch3coohp	1 -1	190.9	0.1
PA26	10	h2s h2sp	1 -1	174.3	0.1
SIE4x4	5	he he+ he2+_1.0	1 1 -1	56.9	1
SIE4x4	8	he he+ he2+_1.75	1 1 -1	19.1	1
ALKBDE10	2	beo be o	-1 1 1	106.6	0.1
ALKBDE10	7	lio li o	-1 1 1	82.5	0.1
YBDE18	6	me2s-ch2 me2s ch2	-1 1 1	51.74	1
YBDE18	16	ph3-ch2 ph3 ch2	-1 1 1	60.11	1
AL2x6	4	al2me4 alme2	-1 2	38.4	1
AL2x6	3	al2cl6 alcl3	-1 2	32.5	1
HEAVYSB11	11	br br2	2 -1	53.17	1
HEAVYSB11	4	sh h2s2	2 -1	67.85	1
NBPRC	7	BH3PH3 BH3 PH3	1 -1 -1	-25.2	1
NBPRC	5	nh2-bh2 bz h2	-3 1 3	-48.9	1

ALK8	6	li5_ch li4_c li_h	-1 1 1	66.28	1
ALK8	2	na8 na2	-1 4	53.15	1
RC21	5	3e 3p1 3p2	-1 1 1	57.93	1
RC21	13	6e 6p1 ethylene	-1 1 1	21.21	1
G2RC	10	58 59 57 60	-1 -1 1 1	-27.15	1
G2RC	6	128 13 126 22	-1 -1 1 1	-10.7	1
BH76RC	29	C2H6 NH2 C2H5 NH3	-1 -1 1 1	-6.52	1
BH76RC	13	hnc hcn	-1 1	-15.06	1
FH51	13	2-pentyne H2 trans-2-pentene	-1 -1 1	-44.82	1
FH51	4	C4H9SO2H H2O2 C4H9SO3H H2O	-1 -1 1 1	-82.55	1
TAUT15	9	6a 6b	-1 1	-0.17	10
TAUT15	10	6a 6c	-1 1	-0.87	10
DC13	12	o3 c2h4 o3_c2h4_add	-1 -1 1	-58.7	1
DC13	2	c20cage c20bowl	-1 1	-7.7	1
MB16-43	13	13 H2 CH4 N2 O2 MgH2 S2	-2 -5 4 4 2 2 2	19.8751	0.1
MB16-43	32	32 H2 LiH BH3 N2 F2 AlH3 SiH4 S2	-2 -11 2 6 1 2 2 2 1	685.5818	0.1
DARC	6	ethine chdiene P6	-1 -1 1	-49	1
DARC	3	ethene cpdiene P3	-1 -1 1	-29.9	1
RSE43	42	E44 P1 E1 P44	-1 -1 1 1	-6.7	1
RSE43	13	E15 P1 E1 P15	-1 -1 1 1	-6.4	1
BSR36	26	c2h6 r11 ch4	11 -1 -12	8.93	1
BSR36	21	c2h6 r6 ch4	7 -1 -7	9.78	1
CDIE20	6	R28 P26	-1 1	4	10
CDIE20	20	R60 P60	-1 1	8.6	10
ISO34	20	E20 P20	-1 1	18.12	1
ISO34	24	E24 P24	-1 1	12.26	1

ISOL24	24	i24e i24p	-1 1	15.4	1
ISOL24	9	i9e i9p	-1 1	21.09	1
C60ISO	8	1 9	-1 1	143.96	0.1
C60ISO	7	1 8	-1 1	142.18	0.1
PArel	19	c2cl43 c2cl42	-1 1	2.47	10
PArel	12	sugar0 sugar3	-1 1	3.21	10
BH76	75	C5H8 RKT22	-1 1	39.7	1
BH76	63	h H2S RKT16	-1 -1 1	3.9	1
BHPERI	15	13r_5 13_c2h4 13ts_5a	-1 -1 1	6.5	1
BHPERI	26	09r 00r 09ts	-1 -1 1	31.3	1
BHDIV10	1	ed1 ts1	-1 1	25.65	1
BHDIV10	5	ed5 ts5	-1 1	15.94	1
INV24	3	SO2 SO2_TS	-1 1	60.6	1
INV24	12	Dibenzocycloheptene Dibenzocycloheptene_TS	-1 1	10.3	1
BHROT27	24	ethylthiourea_180 ethylthiourea_TS1	-1 1	10.36	10
BHROT27	22	butadiene_strans butadiene_TS	-1 1	6.3	10
PX13	6	h2o_4 h2o_4_ts	-1 1	26.6	1
PX13	9	hf_2 hf_2_ts	-1 1	42.3	1
WCPT18	8	reac8 ts8	-1 1	28.97	1
WCPT18	7	reac7 ts7	-1 1	32	1
RG18	15	c2h6Ne ne c2h6	-1 1 1	0.24	10
RG18	17	bzNe ne bz	-1 1 1	0.4	10
ADIM6	5	AM6 AD6	2 -1	4.6	10
ADIM6	6	AM7 AD7	2 -1	5.55	10
S22	10	10 10a 10b	-1 1 1	1.448	10
S22	7	7 07a 07b	-1 1 1	16.66	10

S66	2	02A 02B 2	1 1 -1	5.59	10
S66	53	53A 53B 53	1 1 -1	4.36	10
HEAVY28	21	sbh3_nh3 sbh3 nh3	-1 1 1	2.84	10
HEAVY28	11	pbh4_hcl pbh4 hcl	-1 1 1	0.75	10
WATER27	20	OHmH2O OHm H2O	-1 1 1	26.687	0.1
WATER27	3	H2O4 H2O	-1 4	27.353	0.1
CARBH12	1	1O 1O_A 1O_B	-1 1 1	5.37	10
CARBH12	10	2CL 2CL_A 2CL_B	-1 1 1	10.483	10
PNICO23	5	5 5a 5b	-1 1 1	2.86	10
PNICO23	1	1 1a p1b	-1 1 1	1.43	10
HAL59	32	BrBr_FCCH BrBr FCCH	-1 1 1	0.74	10
HAL59	38	BrBr_OCH2 BrBr OCH2	-1 1 1	4.41	10
AHB21	15	15 15A 15B	1 -1 -1	-8.62	1
AHB21	5	5 5A 5B	1 -1 -1	-15.61	1
CHB6	6	27 27A 27B	1 -1 -1	-19.9	1
CHB6	3	24 24A 24B	1 -1 -1	-17.83	1
IL16	1	008 008A 008B	1 -1 -1	-100.41	0.1
IL16	7	187 187A 187B	1 -1 -1	-114	0.1
IDISP	1	antdimer ant	1 -2	-9.15	1
IDISP	4	undecan1 undecan2	1 -1	9.1	1
ICONF	3	N4H6_1 N4H6_2	-1 1	0.13	10
ICONF	4	N4H6_1 N4H6_3	-1 1	2.33	10
ACONF	8	H_ttt H_gtg	-1 1	1.178	10
ACONF	11	H_ttt H_g+x-t+	-1 1	2.632	10
AMINO20x4	59	PRO_xae PRO_xaf	-1 1	4.187	10
AMINO20x4	66	THR_xaq THR_xag	-1 1	3.08	10

PCONF	15	SER_ab SER_aR	-1 1	1.47	10
PCONF	7	99 412	-1 1	2.18	10
MCONF	51	1 52	-1 1	8.75	10
MCONF	41	1 42	-1 1	6.39	10
SCONF	8	C1 C9	-1 1	6.19	10
SCONF	1	C1 C2	-1 1	0.86	10
UPU23	2	2p u1b	-1 1	2.97	10
UPU23	17	2p 7p	-1 1	3.9	10
BUT14DIOL	45	B1 B46	-1 1	3.18	10
BUT14DIOL	21	B1 B22	-1 1	2.74	10

Table S2: Comparison of the WTMAD-1 (kcal/mol) for the RAND2x55 test set using the attenuated Coulomb metric ($\omega = 0.1$) and the standard Coulomb metric to fit the long-range Coulomb operator in the auxiliary basis for two different range-separation values.

μ	ω-Coulomb	Coulomb	Δ
0.45	4.00618	4.00590	-2.74E-04
0.5	4.04240	4.04217	-2.37E-04

A detailed list of all relative energies included in this work can be downloaded from: `https://pubs.acs.org/doi/suppl/10.1021/acs.jctc.9b01294/suppl_file/ct9b01294_si_002.xlsx`

3.4 A range-separated generalized Kohn–Sham method including a long-range nonlocal random phase approximation correlation potential

D. Graf, C. Ochsenfeld
J. Chem. Phys. **153**, 244118 (2020).

Abstract

Based on our recently published range-separated random phase approximation (RPA) functional [Kreppel *et al.*, "Range-separated density-functional theory in combination with the random phase approximation: An accuracy benchmark," J. Chem. Theory Comput. **16**, 2985–2994 (2020)], we introduce self-consistent minimization with respect to the one-particle density matrix. In contrast to the range-separated RPA methods presented so far, the new method includes a long-range nonlocal RPA correlation potential in the orbital optimization process, making it a full-featured variational generalized Kohn–Sham (GKS) method. The new method not only improves upon all other tested RPA schemes including the standard post-GKS range-separated RPA for the investigated test cases covering general main group thermochemistry, kinetics, and noncovalent interactions but also significantly outperforms the popular G_0W_0 method in estimating the ionization potentials and fundamental gaps considered in this work using the eigenvalue spectra obtained from the GKS Hamiltonian.

A range-separated generalized Kohn–Sham method including a long-range nonlocal random phase approximation correlation potential

View Online   Export Citation   CrossMark

Daniel Graf [iD] and Christian Ochsenfeld[a] [iD]

AFFILIATIONS

Chair of Theoretical Chemistry, Department of Chemistry, University of Munich (LMU), D-81377 Munich, Germany

[a]Author to whom correspondence should be addressed: christian.ochsenfeld@uni-muenchen.de

ABSTRACT

Based on our recently published range-separated random phase approximation (RPA) functional [Kreppel *et al.*, "Range-separated density-functional theory in combination with the random phase approximation: An accuracy benchmark," J. Chem. Theory Comput. **16**, 2985–2994 (2020)], we introduce self-consistent minimization with respect to the one-particle density matrix. In contrast to the range-separated RPA methods presented so far, the new method includes a long-range nonlocal RPA correlation potential in the orbital optimization process, making it a full-featured variational generalized Kohn–Sham (GKS) method. The new method not only improves upon all other tested RPA schemes including the standard post-GKS range-separated RPA for the investigated test cases covering general main group thermochemistry, kinetics, and noncovalent interactions but also significantly outperforms the popular G_0W_0 method in estimating the ionization potentials and fundamental gaps considered in this work using the eigenvalue spectra obtained from the GKS Hamiltonian.

I. INTRODUCTION

Density functional theory (DFT) is among the most popular approaches for electronic structure calculations in the fields of solid state physics, computational chemistry, and materials science. However, standard density functionals show several shortcomings. For example, the unphysical Coulomb self-interaction is typically only incompletely corrected by approximate exchange–correlation (xc) functionals.[1–10] This spurious self-interaction results in a wrong asymptotic decay of the xc-potential,[2,11,12] which, in turn, results in a poor description of molecular properties such as ionization potentials.[13] Another well-known problem of standard density functionals is the missing description of long-range dispersion effects due to their nonlocal nature.[14] Furthermore, it should be mentioned that since the pioneering work of Kohn and Sham[15] in 1965, hundreds of density functionals have been developed, which makes the selection of a suitable functional for a specific problem challenging[16] and additionally limits its predictive power. Therefore,

the development of a more broadly applicable method is highly desirable.

Electronic structure methods based on the random phase approximation (RPA) have become increasingly popular in the last decade, providing a promising route toward a qualitative and quantitative improvement of standard density functional theory.[17–48] RPA methods contain an *ab initio* description of dispersion interactions,[49,50] do not depend on any empirical parameters, and are applicable to vanishing electronic gap systems.[22,51,52] The random phase approximation belongs to the family of adiabatic-connection fluctuation-dissipation (ACFD) methods[53,54] that calculate the correlation energy using density–density response functions. The quantity to be approximated within these approaches is the frequency-dependent exchange–correlation kernel. The direct random phase approximation is the most simple approximation one can think of in this regard as it neglects the frequency-dependent exchange–correlation kernel entirely. It is hence often considered as the Hartree approximation for time-dependent density functional

theory (TDDFT).[24,55] As a consequence, same-spin electron–hole pairs do not experience Pauli repulsion, making the direct RPA correlation hole too negative, which, in turn, results in an overcorrelation of electrons at short interelectronic distances.[17,24,56–58] Furthermore, RPA methods show slow convergence with respect to the size of the basis set[19,59] arising due to the explicit description of the correlation hole near the electron–electron cusp,[60] which requires a lot of one-electron basis functions with high angular momentum. As is common practice in the literature, we will, in the following, drop the "direct" term and use the terms direct RPA and RPA synonymously.

Since DFT describes short-range electron–electron interaction well without the need for large basis sets, the idea of combining DFT and *ab initio* approaches arose some time ago.[61–63] The combination of short-range DFT with long-range RPA methods is especially attractive in this regard. Not only do RPA methods describe long-range correlation exceptionally well,[50] but they are also perfectly compatible with the (nonlocal) exact exchange that corrects the spurious Coulomb self-interaction of standard DFT and leads to the correct asymptotic $-1/r$ decay of the exchange-potential. This should be contrasted with standard global hybrids that decay as $-a_x/r_{12}$, where a_x is the fraction of exact exchange that leads to an underestimation of ionization potentials.[64,65]

In the last few years, a lot of work has gone into range-separated approaches based on the RPA by the Paris–Nancy group[59,66–73] and Scuseria and co-workers.[74–79] It was shown that the range-separated approaches show faster convergence with the basis set while at the same time improving the accuracy of intermolecular interactions, atomization energies, and barrier heights compared to their full-range versions. Very recently, our group contributed to this promising field with a detailed benchmark of an efficient range-separated RPA method in the atomic/Cholesky orbital space.[41] It was shown that range-separated RPA performs more stably over the broad range of molecular chemistry included in the GMTKN55 dataset[80] than standard full-range RPA, and the finding that range-separation leads to faster convergence with respect to the size of the basis set was confirmed.

So far, range-separated RPA was performed almost exclusively in a post-generalized-Kohn–Sham (GKS) fashion where the orbitals are obtained by solving the GKS equations[81] including a short-range density functional combined with long-range (nonlocal) exact exchange. In these approaches, the long-range correlation part is completely omitted within the orbital optimization process. It was shown, however, that the reference orbitals and orbital energies have a strong impact on the performance of RPA.[51,76,82–84] Therefore, it might be advisable to include a long-range correlation potential compatible with the long-range exact exchange. Heßelmann and Ángyán[85] recently presented a range-separated self-consistent RPA method based on the optimized effective potential (OEP) approach,[82,86–102] yielding a completely local potential as required by a real Kohn–Sham (KS) method.

In this work, we present a method that self-consistently minimizes the total energy of our range-separated RPA functional[41] with respect to the one-particle density matrix in the atomic orbital (AO) space. This leads to a variational generalized Kohn–Sham method that includes a nonlocal long-range xc-potential consisting of the exact exchange and the RPA correlation potential and hence accounts for all parts of the potential in the orbital optimization process (full-featured).

II. THEORY

A. Range-separated atomic orbital random phase approximation

In this section, we briefly review the theory underlying the range-separated atomic orbital (AO) resolution-of-the-identity (RI) RPA method presented recently by our group.[41] For a detailed description of range-separated RPA, the reader is referred to the paper of Toulouse *et al.*[69]

In the following, μ, v, λ, σ denote atomic orbitals, i, j denote occupied molecular orbitals (MOs), a, b denote virtual MOs, $\underline{i},\underline{j}$ denote Cholesky orbitals, and M, N denote auxiliary resolution-of-the-identity functions. N_{basis} denotes the number of basis functions, N_{aux} denotes the number of auxiliary RI functions, and N_{occ} and N_{virt} denote the numbers of occupied and virtual molecular orbitals, respectively. Integrals are expressed in the Mulliken notation. Furthermore, Einstein's sum convention[103] is used and the spin index is dropped for convenience.

Our range-separated RPA method is based on the range-separated hybrid PBE (RSHPBE) functional of Goll *et al.*,[104] which calculates the energy according to

$$E^{\text{RSHPBE}} = E_{\text{H}} + E_{\text{c}}^{\text{PBE,sr}} + E_{\text{x}}^{\text{PBE,sr}} + E_{\text{x}}^{\text{HF,lr}} \tag{1}$$

with the Hartree energy E_{H}, the short-range PBE-like exchange $E_{\text{x}}^{\text{PBE,sr}}$ and correlation energy $E_{\text{c}}^{\text{PBE,sr}}$, and the long-range exact Hartree–Fock (HF) exchange energy $E_{\text{x}}^{\text{HF,lr}}$. The separation of the electron–electron interaction is achieved by partitioning the standard electron–electron interaction operator $v_{\text{ee}} = 1/r_{12}$ into a short-range $v_{\text{ee}}^{\text{sr}}$ part and a long-range $v_{\text{ee}}^{\text{lr}}$ part using the error function and its complement[61,62,105]

$$v_{\text{ee}} = v_{\text{ee}}^{\text{sr}} + v_{\text{ee}}^{\text{lr}} = \frac{\text{erfc}(\mu r_{12})}{r_{12}} + \frac{\text{erf}(\mu r_{12})}{r_{12}} \tag{2}$$

with the range-separation parameter μ and the interelectronic distance r_{12}.

The RSHPBE functional, which is minimized in a standard generalized Kohn–Sham scheme, does not contain long-range correlation and is thus in a second step corrected by a post-GKS long-range RPA correlation energy calculation using the RSHPBE orbitals and orbital energies. The long-range RI-RPA energy is given by

$$E_{\text{c}}^{\text{RPA,lr}} = \frac{1}{2\pi} \int_0^{+\infty} d\omega \, \text{Tr}\left[\ln\left(\mathbf{1} - \mathbf{X}_0(i\omega)\mathbf{V}^{\text{lr}} \right) + \mathbf{X}_0 \mathbf{V}^{\text{lr}} \right], \tag{3}$$

where $\mathbf{V}^{\text{lr}}$ represents the long-range electron–electron interaction in the auxiliary basis

$$V_{MN}^{\text{lr}} = \left(\mathbf{C}^{-1} \right)_{MP} \tilde{V}_{PQ}^{\text{lr}} \left(\mathbf{C}^{-1} \right)_{QN}, \tag{4}$$

$$C_{MN} = (M|m_{12}|N), \tag{5}$$

$$\tilde{V}_{MN}^{\text{lr}} = \left(M|v_{\text{ee}}^{\text{lr}}|N \right), \tag{6}$$

and m_{12} is the RI-metric. In the present method, the attenuated Coulomb metric

$$m_{12} = \frac{\mathrm{erfc}(\omega_{\mathrm{att}} r_{12})}{r_{12}} \tag{7}$$

with $\omega_{\mathrm{att}} = 0.1\, a_0^{-1}$ is used since it has been shown to constitute a good trade-off between accuracy and locality for fitting the full-range electron-electron interaction operator.[48] $\mathbf{X}_0$ denotes the noninteracting density–density response function in the zero-temperature case and is calculated in the imaginary time domain according to

$$X_{0,MN}(\mathrm{i}\tau) = G_{0,\mu\nu}(-\mathrm{i}\tau) B_{\nu\lambda}^{M} G_{0,\lambda\sigma}(\mathrm{i}\tau) B_{\sigma\mu}^{N}, \tag{8}$$

where $\mathbf{G}_0(\mathrm{i}\tau)$ is the one-particle Green's function in the imaginary time domain,

$$\mathbf{G}_0(\mathrm{i}\tau) = \Theta(-\mathrm{i}\tau)\underline{\mathbf{G}}_0(\mathrm{i}\tau) + \Theta(\mathrm{i}\tau)\overline{\mathbf{G}}_0(\mathrm{i}\tau), \tag{9}$$

$$\underline{\mathbf{G}}_0(\mathrm{i}\tau) = C_{\mu i} C_{\nu i} \exp(-(\varepsilon_i - \varepsilon_{\mathrm{F}})\tau), \tag{10}$$

$$\overline{\mathbf{G}}_0(\mathrm{i}\tau) = -C_{\mu a} C_{\nu a} \exp(-(\varepsilon_a - \varepsilon_{\mathrm{F}})\tau) \tag{11}$$

with the occupied ($C_{\mu i}$) and unoccupied ($C_{\mu a}$) MO coefficients and the respective MO energies ε_i and ε_a. $\Theta(\mathrm{i}\tau)$ denotes the Heaviside step function, and ε_{F} denotes the Fermi level. The three-center integral matrix $\mathbf{B}$ is given by

$$B_{\mu\nu}^{M} = (\mu\nu|m_{12}|M). \tag{12}$$

The response function of Eq. (8) is then transformed into the imaginary frequency domain by a contracted double-Laplace[47] or equivalently cosine[106] transform according to

$$\mathbf{X}_0(\mathrm{i}\omega) = \int_{-\infty}^{+\infty} \mathrm{d}\tau \cos(\omega\tau)\mathbf{X}_0(\mathrm{i}\tau) \tag{13}$$

to perform the final frequency integration given in Eq. (3).

B. Extending the RSHPBE functional by a long-range nonlocal random phase approximation correlation potential

In Sec. II A, we reviewed our recently published range-separated AO-RI-RPA method. As mentioned earlier, this scheme lacks long-range correlation within the self-consistent optimization of the orbitals and orbital energies. In this section, we remedy this problem by extending the RSHPBE functional by a long-range nonlocal RPA correlation potential.

The long-range RPA correlation potential is obtained by differentiation of the long-range RPA correlation energy with respect to the one-particle density-matrix $\mathbf{P}$,

$$\mathbf{V}_{\mathrm{c}}^{\mathrm{RPA,lr}} = \frac{\partial E_{\mathrm{c}}^{\mathrm{RPA,lr}}[\mathbf{P}]}{\partial \mathbf{P}}. \tag{14}$$

To perform this differentiation, we first need to express the long-range RPA correlation energy in terms of the one-particle density

matrix. This is easily achieved by expressing the one-particle Green's functions according to

$$\underline{\mathbf{G}}_0(\mathrm{i}\tau) = \mathbf{P}\exp(-\tau(\mathbf{H} - \varepsilon_{\mathrm{F}}\mathbf{S})\mathbf{P}), \tag{15}$$

$$\overline{\mathbf{G}}_0(\mathrm{i}\tau) = -\mathbf{P}^{\mathrm{virt}}\exp(-\tau(\mathbf{H} - \varepsilon_{\mathrm{F}}\mathbf{S})\mathbf{P}^{\mathrm{virt}}) \tag{16}$$

with the two-center overlap matrix $\mathbf{S}$, the unoccupied/virtual one-particle density matrix $\mathbf{P}^{\mathrm{virt}}$, and the total Hamiltonian $\mathbf{H}$. The total Hamiltonian of the present range-separated GKS method is given by

$$\mathbf{H} = \mathbf{h} + \mathbf{J} + \mathbf{V}_{\mathrm{xc}}^{\mathrm{PBE,sr}} + \mathbf{V}_{\mathrm{x}}^{\mathrm{HF,lr}} + \mathbf{V}_{\mathrm{c}}^{\mathrm{RPA,lr}} = \mathbf{H}^{\mathrm{RSHPBE}} + \mathbf{V}_{\mathrm{c}}^{\mathrm{RPA,lr}}, \tag{17}$$

where $\mathbf{h}$ denotes the core-Hamiltonian, $\mathbf{J}$ denotes the Coulomb potential, $\mathbf{V}_{\mathrm{xc}}^{\mathrm{PBE,sr}}$ denotes the short-range PBE-like exchange–correlation potential, $\mathbf{V}_{\mathrm{x}}^{\mathrm{HF,lr}}$ denotes the long-range exact (HF) exchange potential, and $\mathbf{V}_{\mathrm{c}}^{\mathrm{RPA,lr}}$ denotes the long-range nonlocal RPA correlation potential.

As can be seen in Eqs. (15) and (16), the Green's functions depend on the total Hamiltonian and hence on the long-range RPA correlation potential itself, making a straightforward differentiation impossible. This dilemma can be bypassed by a semicanonical projection as described by Furche and co-workers.[30] We therefore construct an intermediate Hamiltonian $\tilde{\mathbf{H}}$ by first calculating $\mathbf{H}^{\mathrm{RSHPBE}}$ using the density obtained by diagonalizing the total Hamiltonian and in a second step removing the occupied-virtual and virtual-occupied parts by projection according to

$$\tilde{\mathbf{H}} = \mathbf{S}\mathbf{P}\mathbf{H}^{\mathrm{RSHPBE}}\mathbf{P}\mathbf{S} + \mathbf{S}\mathbf{P}^{\mathrm{virt}}\mathbf{H}^{\mathrm{RSHPBE}}\mathbf{P}^{\mathrm{virt}}\mathbf{S} \tag{18}$$

to ensure that both the total and the intermediate Hamiltonian yield the same density. Having two different Hamiltonians, $\mathbf{H}$ and $\tilde{\mathbf{H}}$, of course means that there is an inconsistency in the GKS potential defining the exchange–correlation energy of the functional and the derivative thereof resulting in two different GKS systems. Without semicanonical projection, the two systems would in general differ in the potential *and* the respective density. Therefore, semicanonical projection is a straightforward approach to impose the weaker condition of requiring the two GKS systems to only yield the same density instead of being identical and hence a step toward full self-consistency. In order to keep the difference between the potentials of the two GKS systems as small as possible, we use the RSHPBE Hamiltonian as a basis of the intermediate Hamiltonian, which differs from the total Hamiltonian only by the long-range RPA correlation potential. That omitting the RPA correlation potential in the construction of the intermediate Hamiltonian is a reasonable choice was already shown in previous work of our group.[42]

In the following, we will give the working equations for the calculation of the long-range RPA correlation potential in the atomic orbital space.

The derivative of the long-range RPA correlation energy with respect to one element of the density matrix $\mathbf{P}$ is given by

$$V_{\mathrm{c},\mu\nu}^{\mathrm{RPA,lr}} = \mathrm{Tr}\left(\frac{\partial E_{\mathrm{c}}^{\mathrm{RPA,lr}}}{\partial \mathbf{X}_0(\mathrm{i}\omega)} \frac{\partial \mathbf{X}_0(\mathrm{i}\omega)}{\partial \mathbf{G}_0(\mathrm{i}\tau)} \frac{\partial \mathbf{G}_0(\mathrm{i}\tau)}{\partial P_{\mu\nu}} \right) \tag{19}$$

with the trace implying integration over imaginary frequency and imaginary time. The change in the long-range RPA correlation energy due to the variation of the one-particle Green's function is described by the long-range correlation part of the RPA self-energy[107] denoted by $\mathbf{\Sigma}_c^{lr}$. Therefore, we can rewrite Eq. (19) as

$$V_{c,\mu\nu}^{RPA} = \mathrm{Tr}\left\{ \int_{-\infty}^{+\infty} d\tau \mathbf{\Sigma}_c^{lr}(-i\tau) \frac{\partial \mathbf{G}_0(i\tau)}{\partial P_{\mu\nu}} \right\}, \quad (20)$$

with

$$\Sigma_{c,\mu\nu}^{lr}(i\tau) = -B_{\mu\lambda}^M G_{0,\lambda\sigma}(i\tau) W_c^{lr,MN}(i\tau) B_{\sigma\nu}^N \quad (21)$$

and $\mathbf{W}_c^{lr}$ denoting the long-range correlated screened Coulomb interaction given by

$$\mathbf{W}_c^{lr}(i\omega) = \mathbf{V}^{lr}\left[\left(\mathbf{1} - \mathbf{X}_0(i\omega)\mathbf{V}^{lr}\right)^{-1} - \mathbf{1} \right], \quad (22)$$

$$\mathbf{W}_c^{lr}(i\tau) = \frac{1}{2\pi} \int_{-\infty}^{+\infty} d\omega \cos(\omega\tau) \mathbf{W}_c^{lr}(i\omega). \quad (23)$$

The derivative of the one-particle Green's function with respect to the ground state density matrix $\mathbf{P}$ can be split into three parts. The first part accounts for changes in the Green's function while keeping the intermediate Hamiltonian fixed and is given by

$$\begin{aligned} \mathbf{V}_{c,1}^{RPA,lr} = &\int_0^{+\infty} d\tau \Big(\exp\{+\tau(\tilde{\mathbf{H}} - \varepsilon_F\mathbf{S})\mathbf{P}\} \mathbf{\Sigma}_c^{lr}(i\tau) + \underline{\mathbf{Y}}(-i\tau)(\tilde{\mathbf{H}} - \varepsilon_F\mathbf{S}) \Big) \\ &+ \int_0^{+\infty} d\tau \Big(\exp\{-\tau(\tilde{\mathbf{H}} - \varepsilon_F\mathbf{S})\mathbf{P}^{virt}\} \mathbf{\Sigma}_c^{lr}(-i\tau) \\ &+ \overline{\mathbf{Y}}(i\tau)(\tilde{\mathbf{H}} - \varepsilon_F\mathbf{S}) \Big), \end{aligned} \quad (24)$$

with

$$\underline{\mathbf{Y}}(-i\tau) = \sum_{k=1}^{\infty} \sum_{l=0}^{k-1} \frac{\tau^k}{k!} \left((\tilde{\mathbf{H}} - \varepsilon_F\mathbf{S})\mathbf{P} \right)^{k-1-l} \mathbf{\Sigma}_c^{lr}(i\tau) \mathbf{P} \left((\tilde{\mathbf{H}} - \varepsilon_F\mathbf{S})\mathbf{P} \right)^{l} \quad (25)$$

$$\begin{aligned} \overline{\mathbf{Y}}(i\tau) = &\sum_{k=1}^{\infty} \sum_{l=0}^{k-1} \frac{(-\tau)^k}{k!} \left((\tilde{\mathbf{H}} - \varepsilon_F\mathbf{S})\mathbf{P}^{virt} \right)^{k-1-l} \\ &\times \mathbf{\Sigma}_c^{lr}(-i\tau)\mathbf{P}^{virt}\left((\tilde{\mathbf{H}} - \varepsilon_F\mathbf{S})\mathbf{P}^{virt} \right)^{l}. \end{aligned} \quad (26)$$

The second part includes the changes in the projection of the Hamiltonian $\mathbf{H}^{RSHPBE}$ according to

$$\begin{aligned} \mathbf{V}_{c,2}^{RPA,lr} = &\int_0^{+\infty} d\tau \Big(\mathbf{SP}\underline{\mathbf{Y}}(-i\tau)\mathbf{SPH}^{RSHPBE} + \mathbf{H}^{RSHPBE}\mathbf{PS}\underline{\mathbf{Y}}^T(-i\tau)\mathbf{PS} \Big) \\ &+ \int_0^{+\infty} d\tau \Big(\mathbf{SP}^{virt}\overline{\mathbf{Y}}(i\tau)\mathbf{SP}^{virt}\mathbf{H}^{RSHPBE} \\ &+ \mathbf{H}^{RSHPBE}\mathbf{P}^{virt}\mathbf{S}\overline{\mathbf{Y}}^T(i\tau)\mathbf{P}^{virt}\mathbf{S} \Big). \end{aligned} \quad (27)$$

The third and last part arises from changes in the density entering $\mathbf{H}^{RSHPBE}$ and is given by

$$\begin{aligned} \mathbf{V}_{c,3}^{RPA,lr} = &\int_0^{+\infty} d\tau P_{\mu\kappa} \underline{Y}_{\kappa\gamma}(-i\tau) S_{\gamma\kappa'} P_{\kappa'\nu}[(\mu\nu|\lambda\sigma) + (\mu\nu|f_{xc}|\lambda\sigma)] \\ &+ \int_0^{+\infty} d\tau P_{\mu\kappa}^{virt} \overline{Y}_{\kappa\gamma}(i\tau) S_{\gamma\kappa'} P_{\kappa'\nu}^{virt}[(\mu\nu|\lambda\sigma) + (\mu\nu|f_{xc}|\lambda\sigma)], \end{aligned} \quad (28)$$

with f_{xc} denoting the exchange–correlation kernel of $\mathbf{H}^{RSHPBE}$. The complete RPA correlation potential is then finally given by

$$\mathbf{V}_c^{RPA,lr} = \mathbf{V}_{c,1}^{RPA,lr} + \mathbf{V}_{c,2}^{RPA,lr} + \mathbf{V}_{c,3}^{RPA,lr}. \quad (29)$$

III. COMPUTATIONAL DETAILS

The present range-separated self-consistent RPA method was implemented in the FermiONs++ program package developed in our group.[108–110] As mentioned above, we use the projection of the RSHPBE[104] Hamiltonian ($\mathbf{H}^{RSHPBE}$) of the standard GKS scheme in the post-SCF version as intermediate Hamiltonian. This approach is referred to as range-separated self-consistent RPA (rsscRPA) in the following. In Sec. IV, we will compare the method with the range-separated PBE-like functional of Goll et al.[104] (RSHPBE); our standard post-GKS range-separated RPA presented in Ref. 41 and abbreviated as "RSHPBE + lrRPA;" the PBE functional;[111,112] our ω-CDGD RPA method (RPA) based on PBE orbitals;[43] and our self-consistent RPA[42] (scRPA) using the projection of the HF-Hamiltonian as the intermediate Hamiltonian.

All range-separated methods employed in this work use a fixed range-separation parameter of $\mu = 0.5\,a_0^{-1}$. We used this value not only because it is a common and validated choice[41,59,63,66–70,113–115] but also because it is physically reasonable. The average distance of valence electrons in molecular systems is around 1 a.u.–2 a.u.[63] Since the inverse of the range-separation parameter approximately gives the distance where the range-separation is made, this would lead to values for μ between $0.5\,a_0^{-1}$ and $1.0\,a_0^{-1}$. There are also ways to determine the range-separation parameter non-empirically.[116–119] In this context, it is interesting to note that Brémond et al.[118] determined a value of $0.45\,a_0^{-1}$ for their RSX-PBE method, which is in good agreement with the empirically determined value of $\mu = 0.5\,a_0^{-1}$.

As atomic basis sets, the def2-TZVP, def2-TZVPP,[120,121] and aug-cc-pVQZ[122,123] basis sets are employed. For the resolution-of-the-identity that is used for 4-center integrals in the calculation of the RPA correlation energy/potential, the corresponding auxiliary basis sets[124–126] are used with the attenuated Coulomb metric[127–129] with an attenuation parameter $\omega_{att} = 0.1\,a_0^{-1}$.[48]

For integrations along imaginary time and frequency as well as transformations between the two domains, we use optimized minimax grids with, in general, 15 quadrature points.[43,106]

IV. RESULTS AND DISCUSSION

A. General main group thermochemistry, kinetics, and noncovalent interactions

In this section, we assess the performance of the present range-separated self-consistent RPA method for general main group thermochemistry, kinetics, as well as noncovalent interactions and compare it to several other RPA schemes. To do so, we picked three test sets of each category in the large GMTKN55 database targeting basic properties and reaction energies for small systems (basic + small), reaction energies for large systems and isomerization reactions (iso. + large), reaction barrier heights (barriers), intermolecular noncovalent interactions (intermol. NCIs), and intramolecular noncovalent interactions (intramol. NCIs), respectively. The def2-TZVP basis set was employed for all calculations in this section since larger basis sets are hardly usable for practical applications. A summary of the results is given in Tables I and II. The detailed results can be found in the supplementary material.

We start our discussion with the results of the full-range methods shown in Table I. As can be seen, standard RPA, with a total weighted mean absolute deviation according to weighting scheme 1 of Ref. 80 (WTMAD-1) of 4.10 kcal/mol, on average significantly improves upon the reference PBE calculations (WTMAD-1 of 9.58 kcal/mol). The largest improvement can be observed for noncovalent interactions, which is, of course, not surprising since it is well known that PBE lacks a correct description of dispersion interactions. Self-consistently minimizing the total RPA energy with respect to the one-particle density-matrix (scRPA) decreases the WTMAD-1 value for the investigated subset of the GMTKN55 database further to 3.46 kcal/mol. Considering the results for different categories shows that scRPA while on average improving upon post-KS RPA for the test cases included in the categories basic + small, iso. + large, and all NCIs has significant deficiencies in the calculation of barrier heights compared to standard post-KS RPA. An explanation for this observation might be that the intermediate Hamiltonian based on Hartree–Fock is not suitable for the description of the transition states. This assumption is supported by the fact that an evaluation of the barrier heights with the scRPA orbitals (RPA@scRPA) gives much better results. Note the difference between the two approaches scRPA and RPA@scRPA: In the first approach, the response function and therefore also the correlation energy are evaluated with orbitals and their respective energies

TABLE I. WTMAD-1 values for the full-range methods in kcal/mol for a subset of the GMTKN55 database grouped by categories. The def2-TZVP basis set was used for all calculations. A detailed list of the results can be found in the supplementary material.

	PBE	RPA@PBE	scRPA	RPA@scRPA
Basic + small	3.71	4.67	2.96	2.83
Iso. + large	9.70	2.64	1.77	4.03
Barriers	5.12	1.28	3.47	1.93
Intermol. NCIs	22.53	9.30	6.35	14.11
Intramol. NCIs	6.84	2.61	2.75	3.14
All NCIs	14.69	5.96	4.55	8.63
Total	9.58	4.10	3.46	5.21

TABLE II. WTMAD-1 values of the range-separated methods in kcal/mol for a subset of the GMTKN55 database grouped by categories. The def2-TZVP basis set was used for all calculations. A detailed list of the results can be found in the supplementary material.

	RSHPBE	RSHPBE + lrRPA	rsscRPA	rsRPA@ rsscRPA
Basic + small	5.54	2.93	2.72	2.36
Iso. + large	6.71	3.10	3.10	3.06
Barriers	6.41	1.78	1.74	1.52
Intermol. NCIs	25.80	8.50	8.26	6.42
Intramol. NCIs	9.27	3.00	2.89	2.31
All NCIs	17.54	5.75	5.58	4.36
Total	10.75	3.86	3.74	3.13

stemming from the intermediate Hamiltonian, whereas in the second approach, the orbitals and orbital energies of a converged self-consistent RPA calculation are employed. Interestingly, the second approach gives much worse results in almost all other cases, yielding a total WTMAD-1 of 5.21 kcal/mol, which is even worse than RPA on PBE orbitals. Notably, the poor performance on intermolecular interactions stands out in this respect. In order to understand this observation, we plotted the signed errors of different approaches for the calculation of interaction energies of n-alkane dimers included in the ADIM6 test set in Fig. 1. To ease the following discussion, we make use of a notation for hybrid RPA methods similar to that employed in Ref. 37. The theoretical scheme that evaluates the Hartree–Fock energy with orbitals obtained from a self-consistent approach SC1 and adds the RPA correlation energy evaluated with orbitals/orbital energies obtained from a self-consistent approach SC2 is denoted as HF@SC1 + cRPA@SC2. The standard RPA@PBE approach, e.g., would in this notation be referred to as HF@PBE + cRPA@PBE. As can be seen in Fig. 1, standard RPA@PBE (Fig. 1, blue) performs very well on this specific test set, however, showing the typical underestimation of the dimer stability (underbinding). Ren *et al.*[37] found that this underbinding can be corrected by replacing HF@PBE with HF@HF, which amounts, to a large extent, to the single excitation correction.[37] This can also be observed for the ADIM6 test set (Fig. 1, brown), however, in this case, systematically overcorrecting it. A similar behavior can be observed when replacing cRPA@PBE in the standard RPA with cRPA@scRPA (violet). Hence, it can be said that evaluating the HF energy with HF orbitals as well as evaluating the RPA correlation energy with scRPA orbitals/orbital energies increases the stability of the dimer compared to the monomers. When we now use the scheme HF@HF + cRPA@scRPA, a strong overcorrection can be observed, just as expected. In contrast, evaluating the RPA correlation energy with HF orbitals/orbital energies seems to decrease the stability of the dimer compared to the monomers, as can be seen by comparing RPA@HF, or in the other notation HF@HF + cRPA@HF (Fig. 1, red), with HF@HF + cRPA@PBE, demonstrating the significant dependence of the RPA functional on the reference potential. These findings can now be used to explain the behavior observed for the two self-consistent RPA approaches: RPA@scRPA is similar to the approach HF@HF + cRPA@scRPA and overcorrects in the HF as well as the cRPA part. The self-consistent RPA approach that uses
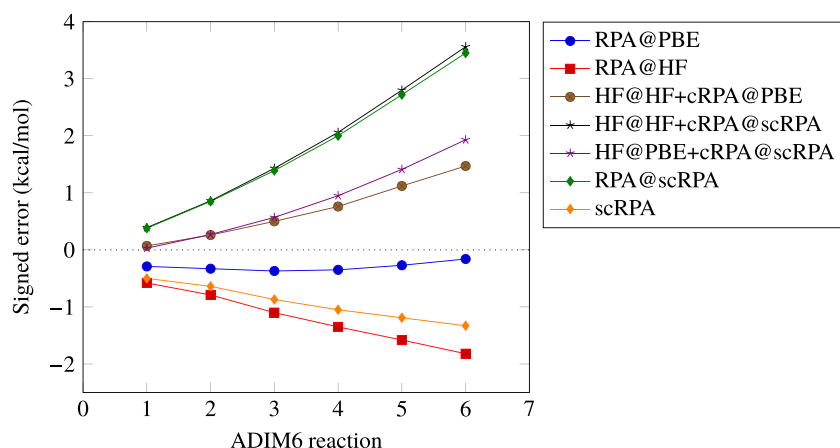
FIG. 1. Signed errors in kcal/mol for the ADIM6 test set using different methods.

the orbitals and orbital energies of the intermediate Hamiltonian (based on the HF Hamiltonian) shown in orange, however, increases the stability of the dimer in the HF part and decreases it in the cRPA part.

We now turn to the results of the range-separated methods presented in Table II. First of all, we note that, as expected, the addition of long-range RPA correlation to the RSHPBE energies significantly improves the performance in all cases and reduces the total WTMAD-1 from 10.75 kcal/mol for RSHPBE to 3.86 kcal/mol for RSHPBE + lrRPA. Note that the long-range RPA correlation energy in this case is evaluated using RSHPBE reference orbitals (see Sec. II A). Self-consistently minimizing the RSHPBE + lrRPA energy with respect to the one-particle density-matrix (rsscRPA) decreases the total WTMAD-1 to 3.74 kcal/mol although the effect on the single categories is sometimes small. Using the orbitals and orbital energies obtained by a converged rsscRPA calculation instead of the ones obtained by the intermediate Hamiltonian (rsRPA@rsscRPA) has a stronger impact and yields a total WTMAD-1 of 3.13 kcal/mol, which is the lowest value of all tested methods and can be seen as a first indication of the high quality of the underlying potential.

At this point, we want to add some words considering the computational effort of the self-consistent RPA methods compared to their post-SCF counterparts: The time-determining step in our post-SCF RPA implementations used in this work is the calculation of the noninteracting response function that shows asymptotically linear scaling[43] with the molecular size. This is to be contrasted to the asymptotically quadratic-scaling[42] calculation of the self-energy in the two self-consistent versions. In the case of the self-consistent versions, there is further an additional factor stemming from the number of SCF cycles needed until convergence is reached, which, in general, is on the same order as for standard PBE calculations. Note also that range-separation in both the self-consistent and the post-SCF variant does not have a significant impact on the computational efficiency.

B. Ionization potentials and band gaps

For a sound density functional, the negative of the highest occupied molecular orbital (HOMO) eigenvalue has to equal the

ionization potential in finite electron systems[4,11,130] and can hence be used as a test of the underlying exchange–correlation potential. Therefore, we compared the negatives of the HOMO eigenvalues obtained with several methods with experimental values for the GW27[131] test set. A summary of the results is given in Table III; detailed values can be found in the supplementary material. As mentioned above, the exchange–correlation functionals of standard density functional approximations such as PBE only partly correct for the unphysical Coulomb self-interaction, leading to a wrong asymptotic decay of the exchange–correlation potential. This spurious behavior is reflected in the poor quality of the HOMO energies as estimates of the ionization potentials with a MAD of 3.88 eV using the PBE functional. Within the RSHPBE functional, the asymptotic region of the potential is described by the exact (HF) exchange potential that shows the correct asymptotic decay. This results in a significant improvement of the HOMO energies, yielding a MAD of 0.45 eV. Inclusion of the long-range RPA correlation potential in the rsscRPA method improves the calculated HOMO energies further and reduces the MAD to 0.26 eV. The new rsscRPA method also improves upon scRPA (MAD of 0.36 eV), demonstrating the benefits of range-separation in the electron–electron interaction. It should also be mentioned at this point that both self-consistent RPA methods significantly outperform the popular G_0W_0 method (MAD of 0.59 eV) in approximating the ionization potentials considered in this work, which again gives rise to the

TABLE III. Mean absolute deviations as well as maximum errors in eV of the calculated ionization potentials compared to experimental values for the GW27[131] test set. The ionization potentials for RSHPBE, rsscRPA, PBE, and scRPA were calculated as negatives of the HOMO energies. All calculations were performed with the def2-TZVPP basis set. PBE, G_0W_0, and experimental values were taken from Ref. 131. Values for systems containing heavy elements such as Cs_2, Au_2, and Au_4 were excluded due to technical reasons.

	RSHPBE	rsscRPA	PBE	scRPA	G_0W_0
MAD	0.45	0.26	3.88	0.36	0.59
MAX	1.04	0.86	6.73	0.84	1.26

assumption that the potentials obtained by these methods are of high quality.

As a further test, gaps obtained as differences between the lowest unoccupied molecular orbital (LUMO) and the HOMO were calculated using the RSHPBE, rsscRPA, and the scRPA methods and compared to CCSD(T) total energy differences. The results are shown in Table IV. Again, both self-consistent RPA methods perform very well, significantly outperforming RSHPBE as well as G_0W_0. Also in this case, separation of the electron–electron interaction shows to be beneficial, decreasing the MAD from 0.29 eV (scRPA) to 0.27 eV (rsscRPA).

C. H$_2$ dissociation curve

It is well known that RPA captures static correlation to some extent and that this feature is connected to the spurious self-correlation inherent in RPA.[10,57] For example, RPA dissociates the H$_2$ molecule correctly in the sense that an infinitely stretched H$_2$ molecule has the same energy as two separate hydrogen atoms. However, this comes at the cost of an unphysical bump in the dissociation curve. Furthermore, the description of the hydrogen atom itself is wrong, yielding a non-zero correlation energy. The one-electron self-correlation within RPA can, for example, be removed from the energy by the second-order screened exchange (SOSEX) approximation.[44,132,133] Unfortunately, this leads to a larger static correlation error, underlining the connection between static correlation and self-correlation within RPA. We calculated the dissociation curve of the H$_2$ molecule, which can be considered as the standard test for the description of static correlation of a functional, to investigate the performance of the self-consistent RPA methods discussed in the present work. The results are shown in Figs. 2 and 3.

First of all, note the difference between the RPA@PBE (Fig. 2, right, blue) and the RPA-SOSEX@PBE (Fig. 2, right, black) curve. As can be seen, RPA-SOSEX describes the region around the minimum well but fails to capture static correlation effects at long bond lengths. In contrast, RPA shows a curve that is shifted to too negative values on the absolute scale but shows a better agreement with

TABLE IV. HOMO–LUMO gaps in eV and mean absolute deviations from reference CCSD(T) values[30] (total energy differences). RSHPBE, rsscRPA, and scRPA calculations were performed with the def2-TZVPP basis set; CCSD(T) and G_0W_0 calculations were performed with the aug-cc-pVTZ basis set. The CCSD(T) and G_0W_0 values were taken from Ref. 30.

	RSHPBE	rsscRPA	scRPA	G_0W_0	CCSD(T)
Li$_2$	5.36	4.90	4.62	4.43	4.76
Na$_2$	4.81	4.43	4.18	4.35	4.48
LiH	8.40	8.15	7.80	6.92	7.67
CH$_3$NO$_2$	11.97	11.03	10.84	9.82	11.41
MAD	0.55	0.27	0.29	0.70	. . .

the full configuration-interaction (FCI) curve on the scale relative to two separate hydrogen atoms (Fig. 3). As mentioned above, this behavior can be explained by the self-correlation within RPA, leading to a too deep correlation hole and a wrong description of the hydrogen atom itself. Note also the unphysical bump in the dissociation curve obtained with RPA@PBE. Considering the curve obtained with RSHPBE + lrRPA (Fig. 2, left, blue) it becomes obvious that the results are similar to those of RPA-SOSEX. The region around the minimum is described well; however, important correlation effects are missed in the long bond length regime. It is another appealing feature of range-separated RPA approaches that they are able to counteract the self-correlation problem within RPA, which is, of course, pronounced at short interelectronic distances. Therefore, range-separated RPA methods can be considered as cost-efficient alternatives to beyond-RPA methods including some kind of exchange. It should be mentioned, however, that range-separation is not able to remove the unphysical bump in the dissociation curve, although it is much less pronounced than in the full-range RPA.

We now turn to the self-consistent RPA approaches discussed in the present work. Self-consistently minimizing the total
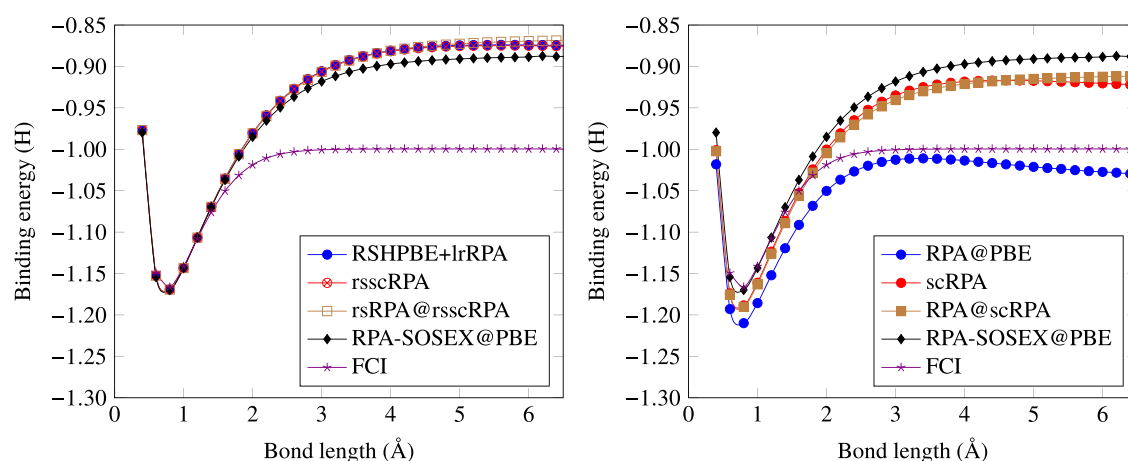

FIG. 2. Dissociation curve of the H$_2$ molecule calculated with different methods. All RPA calculations were performed with the aug-cc-pVQZ basis set. As reference serves a FCI/def2-TZVP dissociation curve.

FIG. 3. Dissociation curve of the H_2 molecule relative to two separate hydrogen atoms calculated with different methods. All RPA calculations were performed with the aug-cc-pVQZ basis set. As reference serves a FCI/def2-TZVP dissociation curve.
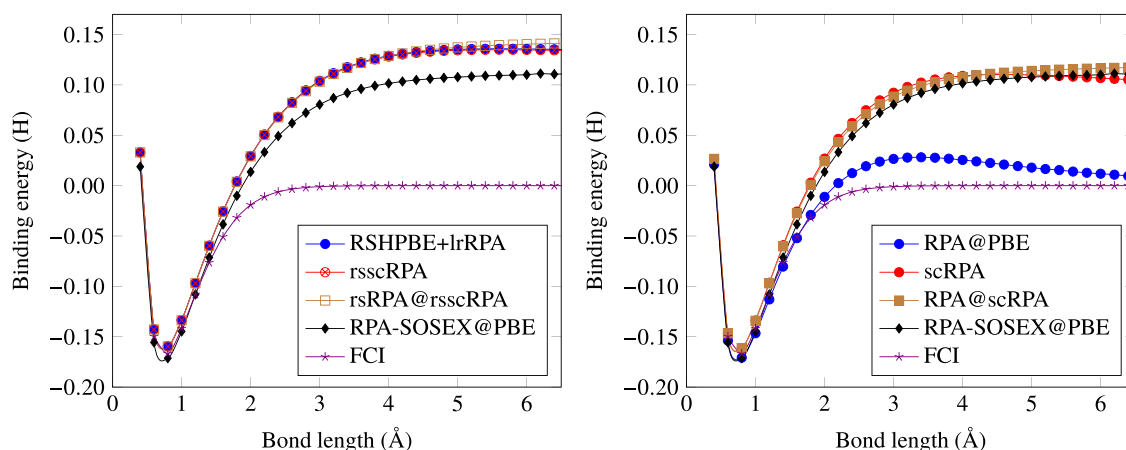
range-separated RPA energy (Fig. 2, left, red) hardly changes anything compared to the post-GKS variant. If orbitals and orbital energies of a converged rsscRPA calculation are used to evaluate the total range-separated RPA energy (Fig. 2, left, brown), however, it becomes obvious that the small unphysical bump is removed. This behavior is even more pronounced in the full-range scRPA approach (Fig. 2, right, red and brown). Another interesting observation is that RPA@scRPA shows a very similar dissociation curve compared to RPA-SOSEX@PBE, which becomes especially apparent on the relative scale in Fig. 3. The shift to more negative values on the absolute scale can again be explained by self-correlation, which is, of course, still present in the self-consistent version. As a final remark, we want to stress again the significant dependence of RPA on the reference or to be more specific on the orbital energies, which can be seen in the huge difference between RPA@PBE (Fig. 2, right, blue) and RPA@scRPA (Fig. 2, right, brown).

V. CONCLUSION

In this work, we presented the self-consistent minimization of our recently published range-separated RPA method (RSHPBE + lrRPA)[41] with respect to the one-particle density matrix in the atomic orbital space. The method extends the RSHPBE functional of Goll *et al.*[104] by a long-range nonlocal RPA correlation potential in the orbital optimization process, making it a full-featured variational generalized Kohn–Sham method. The problem of imposing self-consistency on the long-range RPA correlation functional, which depends on the total Hamiltonian and hence on its own derivative, was bypassed by semicanonical projection[30] of the RSHPBE Hamiltonian. The performance of the new method, termed rsscRPA, on general main group thermochemistry, kinetics, and noncovalent interactions was investigated using a subset of the large GMTKN55 database.[80] The overall performance of rsscRPA on this subset shows to be superior to that of the standard post-GKS variant although the improvement is sometimes small. The method that

evaluates the RSHPBE + lrRPA functional using rsscRPA orbitals and orbital energies, termed rsRPA@rsscRPA, outperforms all other tested methods in this work including PBE, RSHPBE, RPA, RSHPBE + lrRPA, and full-range self-consistent RPA, suggesting high quality of the orbitals, the orbital energies, and hence the underlying potential of rsscRPA. To further test the new method, ionization potentials and fundamental gaps calculated from the eigenvalue spectra of the GKS Hamiltonian were investigated. The method shows to give accurate results for the systems under investigation, significantly outperforming the popular G_0W_0 method, which again implies high quality of the underlying potential. Finally, the behavior of the new method upon bond dissociation was investigated using the example of the H_2 molecule. It showed that the performance is very similar to that of the post-GKS range-separated RPA. However, the unphysical bump well known from the standard full-range RPA, which can also be observed in the range-separated variant, is removed.

SUPPLEMENTARY MATERIAL

Complete lists of the mean absolute deviations for a subset of the GMTKN55 database and the calculated ionization potentials of the GW27 test set are given in the supplementary material.

ACKNOWLEDGMENTS

DATA AVAILABILITY

The data that support the findings of this study are available within the article and its supplementary material.

REFERENCES

[1] J. P. Perdew, "Orbital functional for exchange and correlation: Self-interaction correction to the local density approximation," Chem. Phys. Lett. **64**, 127–130 (1979).

[2] J. P. Perdew and A. Zunger, "Self-interaction correction to density-functional approximations for many-electron systems," Phys. Rev. B **23**, 5048–5079 (1981).

[3] L. A. Cole and J. P. Perdew, "Calculated electron affinities of the elements," Phys. Rev. A **25**, 1265–1271 (1982).

[4] C. Toher, A. Filippetti, S. Sanvito, and K. Burke, "Self-interaction errors in density-functional calculations of electronic transport," Phys. Rev. Lett. **95**, 146402 (2005).

[5] A. J. Cohen, P. Mori-Sánchez, and W. Yang, "Insights into current limitations of density functional theory," Science **321**, 792–794 (2008).

[6] Y. Zhang and W. Yang, "A challenge for density functionals: Self-interaction error increases for systems with a noninteger number of electrons," J. Chem. Phys. **109**, 2604 (1998).

[7] A. J. Cohen, P. Mori-Sánchez, and W. Yang, "Challenges for density functional theory," Chem. Rev. **112**, 289–320 (2012).

[8] P. Mori-Sánchez, A. J. Cohen, and W. Yang, "Localization and delocalization errors in density functional theory and implications for band-gap prediction," Phys. Rev. Lett. **100**, 146401 (2008).

[9] P. Mori-Sánchez, A. J. Cohen, and W. Yang, "Many-electron self-interaction error in approximate density functionals," J. Chem. Phys. **125**, 201102 (2006).

[10] T. M. Henderson and G. E. Scuseria, "The connection between self-interaction and static correlation: A random phase approximation perspective," Mol. Phys. **108**, 2511–2517 (2010).

[11] C.-O. Almbladh and U. Von Barth, "Exact results for the charge and spin densities, exchange-correlation potentials, and density-functional eigenvalues," Phys. Rev. B **31**, 3231–3244 (1985).

[12] R. Van Leeuwen and E. J. Baerends, "Exchange-correlation potential with correct asymptotic behavior," Phys. Rev. A **49**, 2421–2431 (1994).

[13] S. A. C. McDowell, R. D. Amos, and N. C. Handy, "Molecular polarisabilities—A comparison of density functional theory with standard *ab initio* methods," Chem. Phys. Lett. **235**, 1–4 (1995).

[14] J. Pérez-Jordá and A. D. Becke, "A density-functional study of van der Waals forces: Rare gas diatomics," Chem. Phys. Lett. **233**, 134–137 (1995).

[15] W. Kohn and L. J. Sham, "Self-consistent equations including exchange and correlation effects," Phys. Rev. **140**, A1133–A1138 (1965).

[16] N. Mardirossian and M. Head-Gordon, "Thirty years of density functional theory in computational chemistry: An overview and extensive assessment of 200 density functionals," Mol. Phys. **115**, 2315–2372 (2017).

[17] S. Kurth and J. P. Perdew, "Density-functional correction of random-phase-approximation correlation with results for jellium surface energies," Phys. Rev. B **59**, 10461–10468 (1999).

[18] J. F. Dobson and J. Wang, "Successful test of a seamless van der waals density functional," Phys. Rev. Lett. **82**, 2123–2126 (1999).

[19] F. Furche, "Molecular tests of the random phase approximation to the exchange-correlation energy functional," Phys. Rev. B **64**, 195120 (2001).

[20] M. Fuchs and X. Gonze, "Accurate density functionals: Approaches using the adiabatic-connection fluctuation-dissipation theorem," Phys. Rev. B **65**, 235109 (2002).

[21] Y. M. Niquet, M. Fuchs, and X. Gonze, "Exchange-correlation potentials in the adiabatic connection fluctuation-dissipation framework," Phys. Rev. A **68**, 032507 (2003).

[22] M. Fuchs, Y.-M. Niquet, X. Gonze, and K. Burke, "Describing static correlation in bond dissociation by Kohn-Sham density functional theory," J. Chem. Phys. **122**, 094116 (2005).

[23] F. Furche and T. Van Voorhis, "Fluctuation-dissipation theorem density-functional theory," J. Chem. Phys. **122**, 164106 (2005).

[24] G. P. Chen, V. K. Voora, M. M. Agee, S. G. Balasubramani, and F. Furche, "Random-phase approximation methods," Annu. Rev. Phys. Chem. **68**, 421–445 (2017).

[25] H. Eshuis and F. Furche, "Basis set convergence of molecular correlation energy differences within the random phase approximation," J. Chem. Phys. **136**, 084105 (2012).

[26] H. Eshuis, J. E. Bates, and F. Furche, "Electron correlation methods based on the random phase approximation," Theor. Chem. Acc. **131**, 1084 (2012).

[27] H. Eshuis, J. Yarkony, and F. Furche, "Fast computation of molecular random phase approximation correlation energies using resolution of the identity and imaginary frequency integration," J. Chem. Phys. **132**, 234114 (2010).

[28] J. E. Bates and F. Furche, "Communication: Random phase approximation renormalized many-body perturbation theory," J. Chem. Phys. **139**, 171103 (2013).

[29] F. Furche, "Developing the random phase approximation into a practical post-Kohn-Sham correlation model," J. Chem. Phys. **129**, 114105 (2008).

[30] V. K. Voora, S. G. Balasubramani, and F. Furche, "Variational generalized Kohn-Sham approach combining the random-phase-approximation and Green's-function methods," Phys. Rev. A **99**, 012518 (2019).

[31] A. M. Burow, J. E. Bates, F. Furche, and H. Eshuis, "Analytical first-order molecular properties and forces within the adiabatic connection random phase approximation," J. Chem. Theory Comput. **10**, 180–194 (2014).

[32] H. Eshuis and F. Furche, "A parameter-free density functional that works for noncovalent interactions," J. Phys. Chem. Lett. **2**, 983–989 (2011).

[33] A. Heßelmann and A. Görling, "Random phase approximation correlation energies with exact Kohn-Sham exchange," Mol. Phys. **108**, 359–372 (2010).

[34] A. Heßelmann and A. Görling, "Correct description of the bond dissociation limit without breaking spin symmetry by a random-phase-approximation correlation functional," Phys. Rev. Lett. **106**, 093001 (2011).

[35] A. Heßelmann and A. Görling, "Random-phase approximation correlation methods for molecules and solids," Mol. Phys. **109**, 2473–2500 (2011).

[36] J. Paier, X. Ren, P. Rinke, G. E. Scuseria, A. Grüneis, G. Kresse, and M. Scheffler, "Assessment of correlation energies based on the random-phase approximation," New J. Phys. **14**, 043002 (2012).

[37] X. Ren, A. Tkatchenko, P. Rinke, and M. Scheffler, "Beyond the random-phase approximation for the electron correlation energy: The importance of single excitations," Phys. Rev. Lett. **106**, 153003 (2011).

[38] P. Bleiziffer, A. Heßelmann, and A. Görling, "Resolution of identity approach for the Kohn-Sham correlation energy within the exact-exchange random-phase approximation," J. Chem. Phys. **136**, 134102 (2012).

[39] X. Ren, P. Rinke, C. Joas, and M. Scheffler, "Random-phase approximation and its applications in computational chemistry and materials science," J. Mater. Sci. **47**, 7447–7471 (2012).

[40] G. E. Scuseria, T. M. Henderson, and D. C. Sorensen, "The ground state correlation energy of the random phase approximation from a ring coupled cluster doubles approach," J. Chem. Phys. **129**, 231101 (2008).

[41] A. Kreppel, D. Graf, H. Laqua, and C. Ochsenfeld, "Range-separated density-functional theory in combination with the random phase approximation: An accuracy benchmark," J. Chem. Theory Comput. **16**, 2985–2994 (2020).

[42] D. Graf, M. Beuerle, and C. Ochsenfeld, "Low-scaling self-consistent minimization of a density matrix based random phase approximation method in the atomic orbital space," J. Chem. Theory Comput. **15**, 4468–4477 (2019).

[43] D. Graf, M. Beuerle, H. F. Schurkus, A. Luenser, G. Savasci, and C. Ochsenfeld, "Accurate and efficient parallel implementation of an effective linear-scaling direct random phase approximation method," J. Chem. Theory Comput. **14**, 2505–2515 (2018).

[44] M. Beuerle, D. Graf, H. F. Schurkus, and C. Ochsenfeld, "Efficient calculation of beyond RPA correlation energies in the dielectric matrix formalism," J. Chem. Phys. **148**, 204104 (2018).

[45] M. Beuerle and C. Ochsenfeld, "Short-range second order screened exchange correction to RPA correlation energies," J. Chem. Phys. **147**, 204107 (2017).

[46] M. Beuerle and C. Ochsenfeld, "Low-scaling analytical gradients for the direct random phase approximation using an atomic orbital formalism," J. Chem. Phys. **149**, 244111 (2018).

[47] H. F. Schurkus and C. Ochsenfeld, "Communication: An effective linear-scaling atomic-orbital reformulation of the random-phase approximation using

a contracted double-Laplace transformation," J. Chem. Phys. **144**, 031101 (2016).

[48] A. Luenser, H. F. Schurkus, and C. Ochsenfeld, "Vanishing-overhead linear-scaling random phase approximation by Cholesky decomposition and an attenuated Coulomb-metric," J. Chem. Theory Comput. **13**, 1647–1655 (2017).

[49] J. F. Dobson, *Time-Dependent Density Functional Theory* (Springer, Berlin, 2006).

[50] J. P. Perdew, "Local density and gradient-corrected functionals for short-range correlation: Antiparallel-spin and non-RPA contributions," Int. J. Quantum Chem. **48**, 93–100 (1993).

[51] J. Harl and G. Kresse, "Cohesive energy curves for noble gas solids calculated by adiabatic connection fluctuation-dissipation theory," Phys. Rev. B **77**, 045136 (2008).

[52] G. Kresse and J. Harl, "Accurate bulk properties from approximate many-body techniques," Phys. Rev. Lett. **103**, 056401 (2009).

[53] D. C. Langreth and J. P. Perdew, "The exchange-correlation energy of a metallic surface," Solid State Commun. **17**, 1425–1429 (1975).

[54] D. C. Langreth and J. P. Perdew, "Exchange-correlation energy of a metallic surface: Wave-vector analysis," Phys. Rev. B **15**, 2884–2901 (1977).

[55] J. F. Dobson, "Dispersion (van der Waals) forces and TDDFT," in *Fundamentals of Time-Dependent Density Functionl Theory*, edited by M. Marques, N. Maitra, F. Nogueira, E. Gross, and A. Rubio (Springer-Verlag, Berlin, 2012).

[56] K. S. Singwi, M. P. Tosi, R. H. Land, and A. Sjölander, "Electron correlations at metallic densities," Phys. Rev. **176**, 589–599 (1968).

[57] P. Mori-Sánchez, A. J. Cohen, and W. Yang, "Failure of the random-phase-approximation correlation energy," Phys. Rev. A **85**, 042507 (2012).

[58] Z. Yan, J. P. Perdew, and S. Kurth, "Density functional for short-range correlation: Accuracy of the random-phase approximation for isoelectronic energy changes," Phys. Rev. B **61**, 16430–16439 (2000).

[59] J. Toulouse, I. C. Gerber, G. Jansen, A. Savin, and J. G. Ángyán, "Adiabatic-connection fluctuation-dissipation density-functional theory based on range separation," Phys. Rev. Lett. **102**, 096404 (2009).

[60] T. Kato, "On the eigenfunctions of many-particle systems in quantum mechanics," Commun. Pure Appl. Math. **10**, 151–177 (1957).

[61] A. Savin, in *Recent Developments of Modern Density Functional Theory*, edited by J. M. Seminaria (Elsevier, Amsterdam, 1996), pp. 327–357.

[62] J. Toulouse, F. Colonna, and A. Savin, "Long-range–short-range separation of the electron-electron interaction in density-functional theory," Phys. Rev. A **70**, 062505 (2004).

[63] I. C. Gerber and J. G. Ángyán, "Hybrid functional with separated range," Chem. Phys. Lett. **415**, 100–105 (2005).

[64] J. L. Bao, Y. Wang, X. He, L. Gagliardi, and D. G. Truhlar, "Multiconfiguration pair-density functional theory is free from delocalization error," J. Phys. Chem. Lett. **8**, 5616–5620 (2017).

[65] N. Colonna, N. L. Nguyen, A. Ferretti, and N. Marzari, "Koopmans-compliant functionals and potentials and their application to the GW100 test set," J. Chem. Theory Comput. **15**, 1905–1914 (2019).

[66] J. Toulouse, W. Zhu, A. Savin, G. Jansen, and J. G. Ángyán, "Closed-shell ring coupled cluster doubles theory with range separation applied on weak intermolecular interactions," J. Chem. Phys. **135**, 084119 (2011).

[67] B. Mussard, P. Reinhardt, J. G. Ángyán, and J. Toulouse, "Spin-unrestricted random-phase approximation with range separation: Benchmark on atomization energies and reaction barrier heights," J. Chem. Phys. **142**, 154123 (2015).

[68] W. Zhu, J. Toulouse, A. Savin, and J. G. Ángyán, "Range-separated density-functional theory with random phase approximation applied to noncovalent intermolecular interactions," J. Chem. Phys. **132**, 244108 (2010).

[69] J. Toulouse, W. Zhu, J. G. Ángyán, and A. Savin, "Range-separated density-functional theory with the random-phase approximation: Detailed formalism and illustrative applications," Phys. Rev. A **82**, 032502 (2010).

[70] J. G. Ángyán, R.-F. Liu, J. Toulouse, and G. Jansen, "Correlation energy expressions from the adiabatic-connection fluctuation–dissipation theorem approach," J. Chem. Theory Comput. **7**, 3116–3130 (2011).

[71] E. Chermak, B. Mussard, J. G. Ángyán, and P. Reinhardt, "Short range DFT combined with long-range local RPA within a range-separated hybrid DFT framework," Chem. Phys. Lett. **550**, 162–169 (2012).

[72] B. Mussard, P. G. Szalay, and J. G. Ángyán, "Analytical energy gradients in range-separated hybrid density functional theory with random phase approximation," J. Chem. Theory Comput. **10**, 1968–1979 (2014).

[73] C. Kalai, B. Mussard, and J. Toulouse, "Range-separated double-hybrid density-functional theory with coupled-cluster and random-phase approximations," J. Chem. Phys. **151**, 074102 (2019).

[74] B. G. Janesko, T. M. Henderson, and G. E. Scuseria, "Long-range-corrected hybrids including random phase approximation correlation," J. Chem. Phys. **130**, 081105 (2009).

[75] B. G. Janesko, T. M. Henderson, and G. E. Scuseria, "Long-range-corrected hybrid density functionals including random phase approximation correlation: Application to noncovalent interactions," J. Chem. Phys. **131**, 034110 (2009).

[76] B. G. Janesko and G. E. Scuseria, "The role of the reference state in long-range random phase approximation correlation," J. Chem. Phys. **131**, 154106 (2009).

[77] J. Paier, B. G. Janesko, T. M. Henderson, G. E. Scuseria, A. Grüneis, and G. Kresse, "Hybrid functionals including random phase approximation correlation and second-order screened exchange," J. Chem. Phys. **132**, 094103 (2010).

[78] R. M. Irelan, T. M. Henderson, and G. E. Scuseria, "Long-range-corrected hybrids using a range-separated Perdew-Burke-Ernzerhof functional and random phase approximation correlation," J. Chem. Phys. **135**, 094105 (2011).

[79] A. J. Garza, I. W. Bulik, A. G. S. Alencar, J. Sun, J. P. Perdew, and G. E. Scuseria, "Combinations of coupled cluster, density functionals, and the random phase approximation for describing static and dynamic correlation, and van der Waals interactions," Mol. Phys. **114**, 997–1018 (2016).

[80] L. Goerigk, A. Hansen, C. Bauer, S. Ehrlich, A. Najibi, and S. Grimme, "A look at the density functional theory zoo with the advanced GMTKN55 database for general main group thermochemistry, kinetics and noncovalent interactions," Phys. Chem. Chem. Phys. **19**, 32184–32215 (2017).

[81] A. Seidl, A. Görling, P. Vogl, J. A. Majewski, and M. Levy, "Generalized Kohn-Sham schemes and the band-gap problem," Phys. Rev. B **53**, 3764–3774 (1996).

[82] P. Bleiziffer, A. Heßelmann, and A. Görling, "Efficient self-consistent treatment of electron correlation within the random phase approximation," J. Chem. Phys. **139**, 084113 (2013).

[83] A. Thierbach, D. Schmidtel, and A. Görling, "Robust and accurate hybrid random-phase-approximation methods," J. Chem. Phys. **151**, 144117 (2019).

[84] M. Modrzejewski, S. Yourdkhani, and J. Klimeš, "Random phase approximation applied to many-body noncovalent systems," J. Chem. Theory Comput. **16**, 427–442 (2020).

[85] A. Heßelmann and A. Ángyán, "Assessment of a range-separated orbital-optimised random-phase approximation electron correlation method," Theor. Chem. Acc. **137**, 155 (2018).

[86] A. Görling, "Orbital- and state-dependent functionals in density-functional theory," J. Chem. Phys. **123**, 062203 (2005).

[87] R. T. Sharp and G. K. Horton, "A variational approach to the unipotential many-electron problem," Phys. Rev. **90**, 317 (1953).

[88] J. D. Talman and W. F. Shadwick, "Optimized effective atomic central potential," Phys. Rev. A **14**, 36–40 (1976).

[89] M. Städele, J. A. Majewski, P. Vogl, and A. Görling, "Exact Kohn-Sham exchange potential in semiconductors," Phys. Rev. Lett. **79**, 2089–2092 (1997).

[90] A. Görling, "New KS method for molecules based on an exchange charge density generating the exact local KS exchange potential," Phys. Rev. Lett. **83**, 5459–5462 (1999).

[91] S. Ivanov, S. Hirata, and R. J. Bartlett, "Exact exchange treatment for molecules in finite-basis-set Kohn-Sham theory," Phys. Rev. Lett. **83**, 5455–5458 (1999).

[92] M. Städele, M. Moukara, J. A. Majewski, P. Vogl, and A. Görling, "Exact exchange Kohn-Sham formalism applied to semiconductors," Phys. Rev. B **59**, 10031–10043 (1999).

[93] S. Hirata, S. Ivanov, I. Grabowski, R. J. Bartlett, K. Burke, and J. D. Talman, "Can optimized effective potentials be determined uniquely?," J. Chem. Phys. **115**, 1635–1649 (2001).

[94]S. Kümmel and J. P. Perdew, "Simple iterative construction of the optimized effective potential for orbital functionals, including exact exchange," Phys. Rev. Lett. **90**, 043004 (2003).

[95]W. Yang and Q. Wu, "Direct method for optimized effective potentials in density-functional theory," Phys. Rev. Lett. **89**, 143002 (2002).

[96]Q. Wu and W. Yang, "Algebraic equation and iterative optimization for the optimized effective potential in density functional theory," J. Theor. Comput. Chem. **02**, 627–638 (2003).

[97]A. Heßelmann and A. Görling, "Comparison between optimized effective potential and Kohn–Sham methods," Chem. Phys. Lett. **455**, 110–119 (2008).

[98]A. Görling, A. Heßelmann, M. Jones, and M. Levy, "Relation between exchange-only optimized potential and Kohn-Sham methods with finite basis sets, and effect of linearly dependent products of orbital basis functions," J. Chem. Phys. **128**, 104104 (2008).

[99]P. Verma and R. J. Bartlett, "Increasing the applicability of density functional theory. II. Correlation potentials from the random phase approximation and beyond," J. Chem. Phys. **136**, 044105 (2012).

[100]N. L. Nguyen, N. Colonna, and S. de Gironcoli, "*Ab initio* self-consistent total-energy calculations within the EXX/RPA formalism," Phys. Rev. B **90**, 045138 (2014).

[101]M. Hellgren, F. Caruso, D. R. Rohr, X. Ren, A. Rubio, M. Scheffler, and P. Rinke, "Static correlation and electron localization in molecular dimers from the self-consistent RPA and GW approximation," Phys. Rev. B **91**, 165110 (2015).

[102]A. Görling, "Hierarchies of methods towards the exact Kohn-Sham correlation energy based on the adiabatic-connection fluctuation-dissipation theorem," Phys. Rev. B **99**, 235120 (2019).

[103]A. Einstein, "Die grundlage der allgemeinen relativitätstheorie," Ann. Phys. **354**, 769–822 (1916).

[104]E. Goll, H.-J. Werner, H. Stoll, T. Leininger, P. Gori-Giorgi, and A. Savin, "A short-range gradient-corrected spin density functional in combination with long-range coupled-cluster methods: Application to alkali-metal rare-gas dimers," Chem. Phys. **329**, 276–282 (2006).

[105]T. Leininger, H. Stoll, H.-J. Werner, and A. Savin, "Combining long-range configuration interaction with short-range density functional," Chem. Phys. Lett. **275**, 151–160 (1997).

[106]M. Kaltak, J. Klimeš, and G. Kresse, "Low scaling algorithms for the random phase approximation: Imaginary time and Laplace transformations," J. Chem. Theory Comput. **10**, 2498–2507 (2014).

[107]M. Hellgren and U. von Barth, "Correlation potential in density functional theory at the GWA level: Spherical atoms," Phys. Rev. B **76**, 075107 (2007).

[108]J. Kussmann and C. Ochsenfeld, "Pre-selective screening for matrix elements in linear-scaling exact exchange calculations," J. Chem. Phys. **138**, 134114 (2013).

[109]J. Kussmann and C. Ochsenfeld, "Preselective screening for linear-scaling exact exchange-gradient calculations for graphics processing units and general strong-scaling massively parallel calculations," J. Chem. Theory Comput. **11**, 918–922 (2015).

[110]J. Kussmann and C. Ochsenfeld, "Hybrid CPU/GPU integral engine for strong-scaling *ab initio* methods," J. Chem. Theory Comput. **13**, 3153–3159 (2017).

[111]J. P. Perdew, K. Burke, and M. Ernzerhof, "Generalized gradient approximation made simple [Phys. Rev. Lett. 77, 3865 (1996)]," Phys. Rev. Lett. **78**, 1396 (1997).

[112]J. P. Perdew, K. Burke, and M. Ernzerhof, "Generalized gradient approximation made simple," Phys. Rev. Lett. **77**, 3865–3868 (1996).

[113]J. G. Ángyán, I. C. Gerber, A. Savin, and J. Toulouse, "van der Waals forces in density functional theory: Perturbational long-range electron-interaction corrections," Phys. Rev. A **72**, 012510 (2005).

[114]B. Mussard and J. Toulouse, "Fractional-charge and fractional-spin errors in range-separated density-functional theory," Mol. Phys. **115**, 161–173 (2017).

[115]O. Franck, B. Mussard, E. Luppi, and J. Toulouse, "Basis convergence of range-separated density-functional theory," J. Chem. Phys. **142**, 074107 (2015).

[116]R. Baer, E. Livshits, and U. Salzner, "Tuned range-separated hybrids in density functional theory," Annu. Rev. Phys. Chem. **61**, 85–109 (2010).

[117]A. Karolewski, L. Kronik, and S. Kümmel, "Using optimally tuned range separated hybrid functionals in ground-state calculations: Consequences and caveats," J. Chem. Phys. **138**, 204115 (2013).

[118]É. Brémond, Á. J. Pérez-Jiménez, J. C. Sancho-García, and C. Adamo, "Range-separated hybrid density functionals made simple," J. Chem. Phys. **150**, 201102 (2019).

[119]Z. Lin and T. Van Voorhis, "Triplet tuning: A novel family of non-empirical exchange-correlation functionals," J. Chem. Theory Comput. **15**, 1226–1241 (2019).

[120]F. Weigend, F. Furche, and R. Ahlrichs, "Gaussian basis sets of quadruple zeta valence quality for atoms H–Kr," J. Chem. Phys. **119**, 12753–12762 (2003).

[121]F. Weigend and R. Ahlrichs, "Balanced basis sets of split valence, triple zeta valence and quadruple zeta valence quality for H to Rn: Design and assessment of accuracy," Phys. Chem. Chem. Phys. **7**, 3297 (2005).

[122]T. H. Dunning, "Gaussian basis sets for use in correlated molecular calculations. I. The atoms boron through neon and hydrogen," J. Chem. Phys. **90**, 1007–1023 (1989).

[123]R. A. Kendall, T. H. Dunning, and R. J. Harrison, "Electron affinities of the first-row atoms revisited. Systematic basis sets and wave functions," J. Chem. Phys. **96**, 6796–6806 (1992).

[124]F. Weigend, M. Häser, H. Patzelt, R. Ahlrichs, and " RI-MP2, "Optimized auxiliary basis sets and demonstration of efficiency," Chem. Phys. Lett. **294**, 143–152 (1998).

[125]F. Weigend, A. Köhn, and C. Hättig, "Efficient use of the correlation consistent basis sets in resolution of the identity MP2 calculations," J. Chem. Phys. **116**, 3175–3183 (2002).

[126]C. Hättig, "Optimization of auxiliary basis sets for RI-MP2 and RI-CC2 calculations: Core−valence and quintuple-ζ basis sets for H to Ar and QZVPP basis sets for Li to Kr," Phys. Chem. Chem. Phys. **7**, 59–66 (2005).

[127]Y. Jung, A. Sodt, P. M. W. Gill, and M. Head-Gordon, "Auxiliary basis expansions for large-scale electronic structure calculations," Proc. Natl. Acad. Sci. U. S. A. **102**, 6692–6697 (2005).

[128]Y. Jung, Y. Shao, and M. Head-Gordon, "Fast evaluation of scaled opposite spin second-order Møller−Plesset correlation energies using auxiliary basis expansions and exploiting sparsity," J. Comput. Chem. **28**, 1953–1964 (2007).

[129]S. Reine, E. Tellgren, A. Krapp, T. Kjærgaard, T. Helgaker, B. Jansik, S. Høst, and P. Salek, "Variational and robust density fitting of four-center two-electron integrals in local metrics," J. Chem. Phys. **129**, 104101 (2008).

[130]M. Levy, J. P. Perdew, and V. Sahni, "Exact differential equation for the density and ionization energy of a many-particle system," Phys. Rev. A **30**, 2745–2748 (1984).

[131]M. J. van Setten, F. Weigend, and F. Evers, "The GW-method for quantum chemistry applications: Theory and implementation," J. Chem. Theory Comput. **9**, 232–246 (2013).

[132]D. L. Freeman, "Coupled-cluster expansion applied to the electron gas: Inclusion of ring and exchange effects," Phys. Rev. B **15**, 5512–5521 (1977).

[133]A. Grüneis, M. Marsman, J. Harl, L. Schimka, and G. Kresse, "Making the random phase approximation to electronic correlation accurate," J. Chem. Phys. **131**, 154115 (2009).

102

Supporting Information: A Range-Separated Generalized Kohn-Sham Method Including a Long-Range Nonlocal Random Phase Approximation Correlation Potential

Daniel Graf[1] and Christian Ochsenfeld[1]

Chair of Theoretical Chemistry, Department of Chemistry,

University of Munich (LMU), D-81377 Munich, Germany

I. GENERAL MAIN GROUP THERMOCHEMISTRY, KINETICS, AND NONCOVALENT INTERACTIONS

TABLE I. Mean absolute deviations in kcal/mol for a subset of the GMTKN55[1] database. The def2-TZVP basis set was used for all calculations.

Set	RSHPBE	PBE	RSHPBE+lrRPA	rsscRPA	rsRPA@rsscRPA	RPA@PBE	scRPA	RPA@scRPA
basic + small								
AL2X6	6.27	4.04	1.79	1.43	1.04	2.82	1.64	1.05
ALK8	7.09	3.05	3.69	3.40	2.65	7.79	5.61	4.70
FH51	3.27	4.03	3.31	3.33	3.39	3.40	1.63	2.73
iso. + large								
BSR36	8.43	8.15	0.90	0.69	0.60	1.88	1.21	5.14
CDIE20	1.00	1.90	0.69	0.71	0.71	0.46	0.30	0.54
ISO34	1.70	1.95	1.51	1.50	1.50	1.43	1.06	1.52
barriers								
BHPERI	10.74	4.18	1.85	1.80	1.32	0.73	4.32	2.81
BHDIV10	5.10	8.24	1.39	1.31	1.18	1.89	3.43	1.15
INV24	3.39	2.95	2.11	2.10	2.06	1.21	2.65	1.83
intermol. NCIs								
ADIM6	4.54	3.37	1.24	1.15	0.57	0.30	0.93	1.80
S66	2.57	1.94	0.72	0.70	0.58	0.42	0.42	1.86
CARBH12	0.63	1.45	0.59	0.63	0.78	2.07	0.55	0.58
intramol. NCIs								
IDISP	10.72	10.62	2.81	2.67	1.90	2.63	2.17	6.80
ICONF	0.79	0.41	0.43	0.42	0.40	0.46	0.28	0.19
ACONF	0.92	0.58	0.19	0.18	0.10	0.06	0.33	0.07

II. IONIZATION POTENTIALS

TABLE II. Ionization potentials in eV for the GW27[2] test set. The values for RSHPBE, rsscRPA, PBE, as well as scRPA were calculated as negatives of the HOMO energies. All calculations were performed with the def2-TZVPP basis set. PBE, G_0W_0, and experimental values were taken from Ref. 2. Values for systems containing heavy elements like Cs_2, Au_2, and Au_4 were excluded due to technical reasons.

molecule	RSHPBE	rsscRPA	PBE	scRPA	G_0W_0	Exp
H_2	15.42	15.34	10.245	15.66	15.73	15.42
Li_2	5.07	4.90	3.213	4.67	4.91	5.11
Na_2	4.74	4.61	3.125	4.39	4.74	4.89
F_2	15.15	14.84	8.97	15.65	14.44	15.70
N_2	15.90	15.52	10.197	15.48	14.51	15.58
BF	11.09	10.84	6.795	10.42	10.50	11.00
LiH	8.21	8.05	4.363	7.69	6.64	7.90
CO_2	13.97	13.62	9.02	13.41	12.79	13.78
H_2O	12.58	12.37	7.019	12.58	11.76	12.62
NH_3	11.06	10.80	6.017	10.72	10.10	10.85
SiH_4	12.93	12.60	8.472	12.49	12.23	12.30
SF_4	13.06	12.58	8.094	12.44	11.79	12.30
Methane	14.35	14.07	9.441	14.09	13.84	13.60
Ethane	12.81	12.44	8.127	12.51	12.27	12.00
Propane	12.22	11.79	7.665	11.85	11.60	11.51
Butane	12.13	11.63	7.579	11.44	11.16	11.09
Isobutane	12.10	11.60	7.599	11.53	11.19	11.13
Ethylene	10.83	10.52	6.775	9.95	10.22	10.68
Acetone	10.41	9.91	5.586	9.84	8.58	9.70
Acrolein	10.81	10.34	5.956	10.07	8.91	10.11
Benzene	9.80	9.34	6.394	8.67	8.65	9.24
Naphthalene	8.63	8.14	5.497	7.52	7.49	8.09
Antracene	7.76	7.25	4.964	6.65	6.65	7.40
Naphthacene	7.23	6.71	4.648	6.13	6.12	6.97

REFERENCES

[1] L. Goerigk, A. Hansen, C. Bauer, S. Ehrlich, A. Najibi, and S. Grimme, "A look at the density functional theory zoo with the advanced GMTKN55 database for general main group thermochemistry, kinetics and noncovalent interactions," Phys. Chem. Chem. Phys. **19**, 32184–32215 (2017).

[2] M. J. van Setten, F. Weigend, and F. Evers, "The GW-Method for Quantum Chemistry Applications: Theory and Implementation," J. Chem. Theory Comput. **9**, 232–246 (2013).

3.5 Efficient calculation of beyond RPA correlation energies in the dielectric matrix formalism

M. Beuerle, D. Graf, H. F. Schurkus, C. Ochsenfeld
J. Chem. Phys. **148**, 204104 (2018).

Abstract

We present efficient methods to calculate beyond random phase approximation (RPA) correlation energies for molecular systems with up to 500 atoms. To reduce the computational cost, we employ the resolution-of-the-identity and a double-Laplace transform of the non-interacting polarization propagator in conjunction with an atomic orbital formalism. Further improvements are achieved using integral screening and the introduction of Cholesky decomposed densities. Our methods are applicable to the dielectric matrix formalism of RPA including second-order screened exchange (RPA-SOSEX), the RPA electron-hole time-dependent Hartree-Fock (RPA-eh-TDHF) approximation, and RPA renormalized perturbation theory using an approximate exchange kernel (RPA-AXK). We give an application of our methodology by presenting RPA-SOSEX benchmark results for the L7 test set of large, dispersion dominated molecules, yielding a mean absolute error below 1 kcal/mol. The present work enables calculating beyond RPA correlation energies for significantly larger molecules than possible to date, thereby extending the applicability of these methods to a wider range of chemical systems.

Efficient calculation of beyond RPA correlation energies in the dielectric matrix formalism

Matthias Beuerle, Daniel Graf, Henry F. Schurkus, and Christian Ochsenfeld[a)]

Chair of Theoretical Chemistry, Department of Chemistry, University of Munich (LMU), Butenandtstr. 7, D-81377 München, Germany and Center for Integrated Protein Science (CIPSM) at the Department of Chemistry, University of Munich (LMU), Butenandtstr. 5–13, D-81377 München, Germany

We present efficient methods to calculate beyond random phase approximation (RPA) correlation energies for molecular systems with up to 500 atoms. To reduce the computational cost, we employ the resolution-of-the-identity and a double-Laplace transform of the non-interacting polarization propagator in conjunction with an atomic orbital formalism. Further improvements are achieved using integral screening and the introduction of Cholesky decomposed densities. Our methods are applicable to the dielectric matrix formalism of RPA including second-order screened exchange (RPA-SOSEX), the RPA electron-hole time-dependent Hartree-Fock (RPA-eh-TDHF) approximation, and RPA renormalized perturbation theory using an approximate exchange kernel (RPA-AXK). We give an application of our methodology by presenting RPA-SOSEX benchmark results for the L7 test set of large, dispersion dominated molecules, yielding a mean absolute error below 1 kcal/mol. The present work enables calculating beyond RPA correlation energies for significantly larger molecules than possible to date, thereby extending the applicability of these methods to a wider range of chemical systems. *Published by AIP Publishing.* https://doi.org/10.1063/1.5025938

I. INTRODUCTION

Correlation energies obtained from the direct random phase approximation (dRPA) have proven to be a valuable post-Kohn-Sham (KS) correction (for an overview over recent developments, see, e.g., Refs. 1–3). While the original formulations for calculating dRPA correlation energies for molecules showed an $\mathcal{O}(\mathcal{N}^6)$ asymptotic scaling behavior,[4] where N denotes the molecular size, restricting the application to small molecules, several reformulations have been introduced recently for reducing the scaling behavior and allowing for calculating larger systems, some with more than 1000 atoms.[5–8] To reduce the computational cost, these methods employ, e.g., the resolution-of-the-identity (RI) technique,[9] tensor hyper contraction (THC),[10–13] local,[5] atomic,[6] and Cholesky orbital[7] formulations, and integral transforms of the non-interacting polarization propagator,[6–8,14,15] the latter being a central quantity in the calculation of dRPA correlation energies. For some methods, this brought the asymptotic scaling behavior down to linear,[5–8] enabling calculations for large systems of chemical interest.

While dRPA calculations provide significant improvements over conventional density functional theory (DFT) calculations for properties such as dispersion interactions,[16,17] dRPA delivers unsatisfactory results for non-isogyric processes such as atomization energies.[4,18–20] These failures can be traced back to the self-interaction error present in dRPA energies.[21] To circumvent these problems, approaches beyond the direct random phase approximation have been proposed that include exchange effects and higher order correlations.

In general, RPA-type methods can be derived from two frameworks, namely, those that resemble simplified coupled cluster doubles equations[22] or those derived from the adiabatic connection fluctuation dissipation theorem (ACFDT).[4,23–25] Here we focus on approaches derived from the latter framework. In the ACFDT, the direct random phase approximation represents the simplest approach to obtain an approximate interacting polarization propagator required for the calculation of ACFDT correlation energies. To further include exchange effects, several approaches have been suggested: Among those, a second-order screened exchange (RPA-SOSEX) type approach[26,27] replaces the Hartree kernel in the ACFDT formula with an antisymmetrised Hartree kernel.[28,29] The RPA electron-hole time-dependent Hartree-Fock (RPA-eh-TDHF) approximation uses an interacting polarization propagator obtained from a simplified time-dependent Hartree-Fock kernel.[29,30] RPA renormalized perturbation theory uses a low-order approximation to the approximate eh-TDHF polarization propagator as the leading correction to dRPA (this approach is denoted as RPA-AXK).[18] Furthermore, methods have been proposed using the exact-exchange kernel from time-dependent density functional theory,[31] also including a power series approximation to the correlation kernel.[32] Applications of these methods have been hampered so far by their steep computational scaling of up to $\mathcal{O}(\mathcal{N}^6)$ in their canonical formulation. Using the RI-technique, $\mathcal{O}(\mathcal{N}^5)$-scaling ACFDT-based formulations have been proposed,[29,30,33] which is however still too expensive to tackle

---

a)christian.ochsenfeld@uni-muenchen.de

large molecular systems. Further performance benefits have been obtained using a plane wave formulation in conjunction with a Gram-Schmidt orthogonalization scheme.[34] It is worthwhile to note that more efficient RPA with exchange methods have been proposed not only in the ACFDT but also the CCD framework.[35,36]

Here we present a framework that allows for a low scaling calculation of different RPA with exchange methods. In particular, we show that our methods are applicable for RPA-SOSEX, RPA-eh-TDHF, and RPA-AXK. We employ methods recently introduced by us in the context of low- and linear-scaling dRPA and MP2 methods,[6–8,37] namely, an RI-decomposition using a local metric in conjunction with an atomic orbital (AO) or Cholesky basis formulation using the integrated double-Laplace transform of the non-interacting polarization propagator,[6] which is equivalent to a Fourier transform of the non-interacting polarization propagator into the imaginary frequency domain.[14] In this way, RPA with exchange energies for significantly larger molecular systems become accessible.

II. THEORY

In the following, we present a derivation of the working equations for this manuscript. For detailed information on the different RPA with exchange methods and their derivations, we refer the reader to the original publications.[18,29,30] We use the Mulliken notation for two, three, and four center Coulomb integrals and enumerate quantities related to occupied orbitals as $i, j, \ldots$ and those related to virtual orbitals as $a, b, \ldots$.

The dRPA correlation energy in the ACFDT using real-valued spin orbitals after coupling strength integration is given as[23,24,29]

$$E_c^{\text{dRPA}} = \frac{1}{2} \int_{-\infty}^{\infty} \frac{d\omega}{2\pi} \text{Tr} \left\{ \log \left(\mathbf{1} - \mathbf{\Pi}_0(i\omega)\mathbf{V} \right) + \mathbf{\Pi}_0(i\omega)\mathbf{V} \right\}, \quad (1)$$

with $\mathbf{\Pi}_0(i\omega)$ being the non-interacting polarization propagator at imaginary frequency $i\omega$,

$$\Pi_0(i\omega)_{ia,jb} = \frac{-2\varepsilon_{ia}}{\varepsilon_{ia}^2 + \omega^2} \delta_{i,j} \delta_{a,b}, \quad (2)$$

and $V_{ia,jb} = (ia|jb)$ being the Hartree kernel. Here $\varepsilon_{ia} = \varepsilon_a - \varepsilon_i$ are particle-hole excitation energies, where $\varepsilon_i, \varepsilon_j, \ldots$ denote the occupied orbital energies and $\varepsilon_a, \varepsilon_b, \ldots$ denote the virtual orbital energies. Turning to the three beyond RPA methods used in this work, the canonical formulation for the SOSEX correction is given by[29]

$$E_c^{\text{SOSEX}} = -\frac{1}{2} \int_{-\infty}^{\infty} \frac{d\omega}{2\pi} \text{Tr} \left\{ \log \left(\mathbf{1} - \mathbf{\Pi}_0(i\omega)\mathbf{V} \right) \mathbf{V}^{-1} \mathbf{K} \right. $$
$$\left. + \mathbf{\Pi}_0(i\omega)\mathbf{K} \right\}, \quad (3)$$

the RPA-AXK correction is given by[18]

$$E_c^{\text{AXK}} = \frac{1}{2} \int_{-\infty}^{\infty} \frac{d\omega}{2\pi} \text{Tr} \left\{ \log \left(\mathbf{1} - \mathbf{\Pi}_0(i\omega)\mathbf{V} \right) \mathbf{V}^{-1} \mathbf{K} \right. $$
$$\left. + \left(\mathbf{1} - \mathbf{\Pi}_0(i\omega)\mathbf{V} \right)^{-1} \mathbf{\Pi}_0(i\omega)\mathbf{K} \right\}, \quad (4)$$

and the correlation energy expression for RPA-eh-TDHF is given by[29,30]

$$E_c^{\text{RPA-eh-TDHF}} = \frac{1}{2} \int_{-\infty}^{\infty} \frac{d\omega}{2\pi} \text{Tr} \left\{ \log \left(\mathbf{1} - \mathbf{\Pi}_0(i\omega)\mathbf{W} \right) \mathbf{W}^{-1} \mathbf{V} \right. $$
$$\left. + \mathbf{\Pi}_0(i\omega)\mathbf{V} \right\}. \quad (5)$$

Here $K_{ia,jb} = (ib|ja)$ represents an approximate exchange kernel and $\mathbf{W} = \mathbf{V} - \mathbf{K}$. It is worth to note that the SOSEX and AXK corrections have to be added to the dRPA correlation energy, while the formula for RPA-eh-TDHF delivers the entire correlation energy.

A. Resolution-of-the-identity formulations

The resolution-of-the-identity approximation is often used in quantum chemistry to decompose the four-index two-electron repulsion integral (ERI) tensor into two three-center tensors,[7,9,38–40]

$$(ia|jb) \approx \sum_{P,Q} (ia|m_{12}|P) C_{PQ} (Q|m_{12}|jb)$$
$$= \sum_{P,Q,R} (ia|m_{12}|P) C_{PR}^{1/2} C_{RQ}^{1/2} (Q|m_{12}|jb) = \sum_{R} B_{ia}^R B_{jb}^R, \quad (6)$$

where $(ia|m_{12}|P)$ are the three-center integrals and the RI matrix

$$C_{PQ} = \sum_{R,S} (P|m_{12}|R)^{-1} (R|S)(S|m_{12}|Q)^{-1}, \quad (7)$$

with the respective metric m_{12} employed for the RI-decomposition. Here $P, Q, R, \ldots$ denote the auxiliary basis functions.

Inserting the RI-approximation to decompose $\mathbf{V}$ leads to the following RI-dRPA expression introduced by Furche and co-workers:[9]

$$E_c^{\text{RI-dRPA}} = \frac{1}{2} \int_{-\infty}^{\infty} \frac{d\omega}{2\pi} \text{Tr} \left\{ \log \left(\mathbf{1} - \mathbf{Q}(i\omega) \right) + \mathbf{Q}(i\omega) \right\}, \quad (8)$$

where $\mathbf{Q}(i\omega)$ is a $N_{\text{Aux}} \times N_{\text{Aux}}$ matrix, with N_{Aux} being the size of the auxiliary space. $\mathbf{Q}(i\omega)$ is defined as

$$Q_{PQ}(i\omega) = \sum_{i,a} B_{ia}^P \Pi_0(i\omega)_{ia,ia} B_{ia}^Q. \quad (9)$$

Similar considerations allow decomposing both $\mathbf{V}$ and $\mathbf{K}$ with the RI-approximation for the beyond RPA expressions to obtain

$$E_c^{\text{RI-SOSEX}} = -\frac{1}{2} \int_{-\infty}^{\infty} \frac{d\omega}{2\pi} \text{Tr} \left\{ \log \left(\mathbf{1} - \mathbf{Q}(i\omega) \right) \mathbf{Q}^{-1}(i\omega) \right. $$
$$\left. \times \mathbf{Y}(i\omega) \mathbf{Q}^{-1}(i\omega) + \mathbf{Y}(i\omega) \mathbf{Q}^{-1}(i\omega) \right\}, \quad (10)$$

$$E_c^{\text{RI-AXK}} = \frac{1}{2} \int_{-\infty}^{\infty} \frac{d\omega}{2\pi} \text{Tr} \left\{ \log \left(\mathbf{1} - \mathbf{Q}(i\omega) \right) \mathbf{Q}^{-1}(i\omega) \mathbf{Y}(i\omega) \right. $$
$$\left. \times \mathbf{Q}^{-1}(i\omega) + \left(\mathbf{1} - \mathbf{Q}(i\omega) \right)^{-1} \mathbf{Y}(i\omega) \mathbf{Q}^{-1}(i\omega) \right\}, \quad (11)$$

$$E_c^{\text{RI-RPA-eh-TDHF}} = \frac{1}{2} \int_{-\infty}^{\infty} \frac{d\omega}{2\pi} \text{Tr} \left\{ \log \left(\mathbf{1} - \mathbf{Q}(i\omega) + \mathbf{Y}(i\omega)\mathbf{Q}^{-1}(i\omega) \right) \right. $$
$$\left. \times \left(\mathbf{Q}(i\omega) - \mathbf{Y}(i\omega)\mathbf{Q}^{-1}(i\omega) \right)^{-1} \mathbf{Q}(i\omega) + \mathbf{Q}(i\omega) \right\}. \quad (12)$$

The $\mathbf{Q}(i\omega)$ matrix is the same as the one appearing in the dRPA energy expression [Eq. (8)] and $\mathbf{Y}(i\omega)$ is given as

$$Y_{PQ}(i\omega) = \sum_{i,a,j,b} B_{ia}^P \Pi_0(i\omega)_{ia,ia} K_{ia,jb} \Pi_0(i\omega)_{jb,jb} B_{jb}^Q. \quad (13)$$

For the derivation of the RI-expression for RPA-SOSEX, see Ref. 29; for RPA-eh-TDHF, see Ref. 30; and for RPA-AXK,[18] see the Appendix.

B. Atomic orbital formulation

While in Refs. 6–8, efficient methods to calculate $\mathbf{Q}(i\omega)$ have been presented, the naive calculation of $\mathbf{Y}(i\omega)$ scales at least as $\mathcal{O}(\mathcal{N}_{occ}^2 \mathcal{N}_{virt}^2 \mathcal{N}_{Aux})$, where N_{occ} and N_{virt} denote the dimensions of the occupied and virtual space, respectively. Although this is more efficient than the canonical $\mathcal{O}(\mathcal{N}_{occ}^3 \mathcal{N}_{virt}^3)$ formulation for the beyond RPA methods, this scaling is still prohibitively steep for large molecules. To obtain an efficient method for calculating $\mathbf{Y}(i\omega)$, we use a double-Laplace transform of the non-interacting polarization propagator,[6,14]

$$\Pi_0(i\omega)_{ia,ia} = \frac{-2\varepsilon_{ia}}{\varepsilon_{ia}^2 + \omega^2} = -2 \int_0^\infty d\tau \cos(\omega\tau) e^{-\varepsilon_{ia}\tau}$$
$$= -2 \sum_\tau w_\tau \cos(\omega\tau) e^{-\varepsilon_{ia}\tau}, \quad (14)$$

with roots τ and weights w_τ, which allows calculating $\mathbf{Y}(i\omega)$ in an atomic orbital (AO) formulation analogous to the AO formulation of $\mathbf{Q}(i\omega)$ first shown in Ref. 6,

$$Y_{PQ}(i\omega) = \sum_{\mu,\nu,\lambda,\sigma} \sum_{\mu',\nu',\lambda',\sigma'} \sum_{\tau,\tau'} 4 w_\tau w_{\tau'} \cos(\omega\tau) \cos(\omega\tau')$$
$$\times \underline{P}_{\mu\mu'}^\tau B_{\mu\nu}^P \overline{P}_{\nu\nu'}^\tau (\mu'\sigma'|\lambda'\nu') \underline{P}_{\lambda\lambda'}^{\tau'} B_{\lambda\sigma}^Q \overline{P}_{\sigma\sigma'}^{\tau'}, \quad (15)$$

with $\underline{\mathbf{P}}^\tau$, $\overline{\mathbf{P}}^\tau$ representing the occupied and virtual pseudodensities, defined as

$$\underline{P}_{\mu\mu'}^\tau = \sum_i \mathcal{C}_{\mu i} e^{\varepsilon_i \tau} \mathcal{C}_{\mu' i} \quad (16)$$

and

$$\overline{P}_{\mu\mu'}^\tau = \sum_a \mathcal{C}_{\mu a} e^{-\varepsilon_a \tau} \mathcal{C}_{\mu' a}, \quad (17)$$

where $\mathcal{C}$ is the matrix of molecular orbital coefficients. We denote the AO basis functions as μ, μ', ν, ν', ...

The key idea of AO-based methods is a reformulation in a local Gaussian basis to obtain sparse quantities, which allow for an efficient calculation. Therefore, we also move the RI matrix $\mathbf{C}$ out of the $\mathbf{B}$ tensor[6] to obtain

$$Y_{PQ}(i\omega) = \sum_{R,S} C_{PR}^{1/2} \tilde{Y}_{RS}(i\omega) C_{SQ}^{1/2}, \quad (18)$$

$$\tilde{Y}_{PQ}(i\omega) = \sum_{\mu,\nu,\lambda,\sigma} \sum_{\mu',\nu',\lambda',\sigma'} \sum_{\tau,\tau'} 4 w_\tau w_{\tau'} \cos(\omega\tau) \cos(\omega\tau')$$
$$\times \underline{P}_{\mu\mu'}^\tau \tilde{B}_{\mu\nu}^P \overline{P}_{\nu\nu'}^\tau (\mu'\sigma'|\lambda'\nu') \underline{P}_{\lambda\lambda'}^{\tau'} \tilde{B}_{\lambda\sigma}^Q \overline{P}_{\sigma\sigma'}^{\tau'}, \quad (19)$$

where $\tilde{B}_{\mu\nu}^P = (\mu\nu|m_{12}|P)$ represent solely the three-center integrals. Now if one uses a local RI metric, such as the overlap[6] or attenuated Coulomb metric,[7,41–43] the number of elements of the three-center tensor $\tilde{\mathbf{B}}$ will grow only linearly with the system size, allowing for an efficient calculation of $\tilde{\mathbf{Y}}(i\omega)$.

Here we want to note that the contraction of $\tilde{\mathbf{Y}}(i\omega)$ with the RI-matrix and other operations on the $N_{Aux} \times N_{Aux}$ matrices $\mathbf{Q}(i\omega)$ and $\mathbf{Y}(i\omega)$ (matrix multiplications and eigendecompositions) have a very low prefactor and will therefore only become dominant for exceedingly large molecules,[6] which means that the calculation of $\tilde{\mathbf{Y}}(i\omega)$ determines the effective scaling behavior.

The AO formulation of $\tilde{\mathbf{Y}}(i\omega)$ allows for an efficient integral-direct calculation. Therefore, we first carry out the double-Laplace transform to rewrite $\tilde{\mathbf{Y}}(i\omega)$ as

$$\tilde{Y}_{PQ}(i\omega) = \sum_{\mu',\nu',\lambda',\sigma'} \tilde{M}_{\mu'\nu'}^P(i\omega) K_{\mu'\nu',\lambda'\sigma'} \tilde{M}_{\lambda'\sigma'}^Q(i\omega), \quad (20)$$

with

$$\tilde{M}_{\mu'\nu'}^P(i\omega) = \sum_{\mu,\nu} \sum_\tau -2 w_\tau \cos(\omega\tau) \underline{P}_{\mu\mu'}^\tau \tilde{B}_{\mu\nu}^P \overline{P}_{\nu\nu'}^\tau. \quad (21)$$

Since the occupied and unoccupied pseudodensities are sparse quantities, the number of elements of the three-index quantity $\tilde{\mathbf{M}}(i\omega)$ also grows only linearly with system size and is efficiently calculated using sparse algebra. Now $\tilde{\mathbf{Y}}(i\omega)$ can be calculated in a linear scaling fashion by an integral-direct contraction of the AO ERI's with one of the $\tilde{\mathbf{M}}(i\omega)$ tensors followed by a matrix product over the remaining AO indices,

$$K_{\mu'\nu'}^Q(i\omega) = \sum_{\lambda',\sigma'} K_{\mu'\nu',\lambda'\sigma'} \tilde{M}_{\lambda'\sigma'}^Q(i\omega), \quad (22)$$

$$\tilde{Y}_{PQ}(i\omega) = \sum_{\mu',\nu'} \tilde{M}_{\mu'\nu'}^P(i\omega) K_{\mu'\nu'}^Q(i\omega). \quad (23)$$

Linear scaling is achieved by the realization that the locality of the $\tilde{\mathbf{M}}(i\omega)$ tensor and the locality of AO basis function pairs within the ERI tensor renders only a linear number of ERIs significant. These are then contracted with $\tilde{\mathbf{M}}(i\omega)$ by a LinK type scheme.[44,45] To identify the significant ERIs, we use Schwarz estimates $Q_{\mu\nu} = (\mu\nu|\mu\nu)^{1/2}$ weighted with the corresponding $\tilde{M}_{\mu'\nu'}^{max}(i\omega)$ element, where *max* denotes the maximum absolute value over all auxiliary indices, and discard insignificant integrals according to a fixed threshold ϑ,

$$|\tilde{M}_{\mu'\nu'}^P(i\omega)(\mu'\sigma'|\lambda'\nu')| \le |\tilde{M}_{\mu'\nu'}^{max}(i\omega)| Q_{\mu'\sigma'} Q_{\lambda'\nu'} < \vartheta. \quad (24)$$

The remaining significant integrals are contracted with a constant number of $\tilde{M}_{\mu'\nu'}^P(i\omega)$ elements, determined by the block sparse algebra implementation. In practice, we perform the contraction in Eq. (22) for batches of auxiliary indices to store all necessary quantities in computer memory and to allow for fine grained screening. Per default, we set up the batching scheme by performing the contraction for all auxiliary indices belonging to one atom, where *max* then refers to the batch maximum. We note that the idea of an integral-direct computation of $\mathbf{K}$ along with an RI-decomposed Hartree kernel was first mentioned in the supplementary information of Ref. 18. Through the use of a local RI-metric in conjunction with a transformed non-interacting polarization propagator and the use of the LinK scheme, we arrive at an efficient scheme to calculate beyond RPA correlation energies, which we will refer to as AO-LinK in Sec. IV.

C. Cholesky decomposed density (CDD) RI formulation

The method presented above will scale efficiently for large molecules due to the sparsity of AO quantitites. An issue with AO-based methods is, however, their steep computational scaling with respect to the basis set size N_{Bas} due to the redundancy present in typical AO basis sets, as compared to canonical methods. A solution to this problem has been to exploit the rank deficiency of AO quantities by using pivoted Cholesky decomposition (CD).[7,37,46–50] Pivoted Cholesky decomposition allows decomposing a positive semi-definite matrix into a product of a lower and upper triangular matrix,

$$\mathbf{A} = \mathbf{L}\mathbf{L}^T. \tag{25}$$

The Cholesky factors $\mathbf{L}$ have the same number of rows as the original matrix $\mathbf{A}$ and $rank(\mathbf{A})$ columns. Since the rank of the occupied one-particle density matrix $\mathbf{P}_{\text{occ}}$ equals the number of occupied orbitals, CD allows for huge computational savings when large basis sets are employed. The rank of the virtual one particle density matrix $\mathbf{P}_{\text{virt}}$ equals the number of virtual orbitals. Since especially for large basis sets N_{virt} is of similar size as N_{Bas}, the computational benefits of decomposing $\mathbf{P}_{\text{virt}}$ are not as high. Furthermore, decomposing $\mathbf{P}_{\text{virt}}$ has been found to interfere negatively with matrix sparsity,[7] which is why we omit the decomposition of $\mathbf{P}_{\text{virt}}$ in this work. For a more detailed description of pivoted CD in the context of one particle density matrices, see, e.g., Ref. 7. While the rank discussion also applies to occupied and virtual pseudodensities (where the rank is sometimes even lower than N_{occ} and N_{virt}, respectively), we found it to be more efficient to introduce Cholesky decomposed densities (CDDs) into the calculation of $\tilde{\mathbf{Y}}(\mathrm{i}\omega)$, by decomposing the one-particle density matrix $\mathbf{P}_{\text{occ}} = \mathbf{L}\mathbf{L}^T$ in conjunction with the following equality for occupied pseudodensities:

$$\underline{\mathbf{P}}^\tau = \underline{\mathbf{P}}^\tau \mathbf{S}\mathbf{P}_{\text{occ}}, \tag{26}$$

where $\mathbf{S}$ is the AO overlap matrix. Thus, we can rewrite Eq. (20) by also inserting the RI for the remaining ERI as

$$\tilde{Y}_{PQ}(\mathrm{i}\omega) = \sum_{\underline{i},\underline{j},\nu',\sigma'} \sum_R \tilde{M}^P_{\underline{i}\nu'}(\mathrm{i}\omega)\tilde{B}^R_{\underline{i}\sigma'}\overline{B}^R_{\underline{j}\nu'}\tilde{M}^Q_{\underline{j}\sigma'}(\mathrm{i}\omega). \tag{27}$$

Here $\underline{i},\underline{j}$ denote the Cholesky vectors of $\mathbf{P}_{\text{occ}}$, $\tilde{B}^R_{\underline{i}\sigma'}$ $= \sum_{\mu'} L^T_{\underline{i}\mu'}\tilde{B}^R_{\mu'\sigma'}$, $\overline{\mathbf{B}} = \mathbf{C}\tilde{\mathbf{B}}$, and

$$\tilde{M}^P_{\underline{i}\nu'}(\mathrm{i}\omega) = \sum_\tau -2w_\tau \cos{(\omega\tau)}(\mathbf{L}^T\mathbf{S}\underline{\mathbf{P}}^\tau \tilde{\mathbf{B}}^P\overline{\mathbf{P}}^\tau)_{\underline{i}\nu'}. \tag{28}$$

Note that we used an asymmetric RI in Eq. (27). In this way, it is possible to significantly reduce the cost of forming $\tilde{\mathbf{Y}}(\mathrm{i}\omega)$ since the number of significant elements of $\underline{\tilde{\mathbf{B}}}$ scales linearly with system size as opposed to $\mathbf{B}$ and $\overline{\mathbf{B}}$, when a local RI metric is employed. To optimally exploit the locality of the quantities in Eq. (27), the order of summation is crucial. Optimizing the order of summation, subject to formal $\mathcal{O}(\mathcal{N}^3)$ memory requirements and lowest formal scaling behavior, in conjunction with efficient usage of matrix sparsity, we arrive at the sequence shown in the pseudocode in

Algorithm 1. Pseudocode to optimally exploit sparsity in the formation of $\tilde{\mathbf{Y}}(\mathrm{i}\omega)$ using the CDD-RI formulation.

1:   **function** Calculate $\tilde{\mathbf{Y}}(\mathrm{i}\omega)$
2:       **for** R **do**
3:           $X^{RQ}_{\underline{i}\underline{j}}(\mathrm{i}\omega) = \sum_{\sigma'} \tilde{B}^R_{\underline{i}\sigma'}\tilde{M}^Q_{\underline{j}\sigma'}(\mathrm{i}\omega)$
4:           $K^Q_{\underline{i}\nu'}(\mathrm{i}\omega)\mathrel{+}= \sum_{\underline{j}} \overline{B}^R_{\underline{j}\nu'}X^{RQ}_{\underline{i}\underline{j}}(\mathrm{i}\omega)$
5:       **end for**
6:       $\tilde{Y}_{PQ}(\mathrm{i}\omega) = \sum_{\underline{i},\nu'} \tilde{M}^P_{\underline{i}\nu'}(\mathrm{i}\omega)K^Q_{\underline{i}\nu'}(\mathrm{i}\omega)$
7:   **end function**

Algorithm 1. Obviously sparse algebra routines are required for efficiency.

We will refer to these methods as CDD-RI in Sec. IV.

D. Schwarz screened CDD-RI formulation

Memory layouts and caching of modern computers advocate for rather large block dimensions in the blocked sparse algebra routines which need to be traded off against the granularity at which the sparsity in the AO-CDD quantities can be captured. This means that with the most efficient large block sizes, an algorithm exploiting only block sparsity will translate into significant computational savings only for rather large molecules. Since the formal scaling behavior of the method in Sec. II C is $\mathcal{O}(\mathcal{N}^2_{\text{Aux}}\mathcal{N}^2_{\text{occ}}\mathcal{N}_{\text{Bas}})$, this would result in a noticeable prefactor. Screening of individual integrals allows circumventing this problem, and the derivation of the necessary integral estimates is given in the following. The method in this section is currently only applicable to the RPA-SOSEX and RPA-AXK correction and not to RPA-eh-TDHF. We show the derivation here explicitly for RPA-SOSEX.

Using the rotatory invariance of the trace and defining

$$\mathbf{W}(\mathrm{i}\omega) = \mathbf{Q}^{-1}(\mathrm{i}\omega)\log{(\mathbf{1} - \mathbf{Q}(\mathrm{i}\omega))}\mathbf{Q}^{-1}(\mathrm{i}\omega) + \mathbf{Q}^{-1}(\mathrm{i}\omega). \tag{29}$$

Equation (10) can be rewritten as

$$E_{\text{c}}^{\text{RI-SOSEX}} = -\frac{1}{2} \int_{-\infty}^{\infty} \frac{\mathrm{d}\omega}{2\pi} \, \mathrm{Tr}\{\mathbf{W}(\mathrm{i}\omega)\mathbf{Y}\}. \tag{30}$$

Insertion of Eqs. (18) and (27) then yields

$$E_{\text{c}}^{\text{RI-SOSEX}} = \frac{1}{2} \int_{-\infty}^{\infty} \frac{\mathrm{d}\omega}{2\pi} \mathrm{Tr}\Big\{ \sum_{P,Q} M^P_{\underline{i},\nu'}(\mathrm{i}\omega)M^P_{\underline{j},\sigma'}(\mathrm{i}\omega)B^Q_{\underline{i},\sigma'}B^Q_{\underline{j},\nu'} \Big\}, \tag{31}$$

with the definition

$$\mathbf{M}(\mathrm{i}\omega) = (-\mathbf{W}(\mathrm{i}\omega))^{1/2}\mathbf{C}^{1/2}\tilde{\mathbf{M}}(\mathrm{i}\omega). \tag{32}$$

Note that we have absorbed the minus sign into the matrix root since $\mathbf{W}(\mathrm{i}\omega)$ is negative definite and this therefore allows for a real-valued, symmetric decomposition.

While Eq. (31) is our final RI-formulation, it is insightful to stress that whereas

$$\sum_Q B^Q_{\underline{i},\sigma'}B^Q_{\underline{j},\nu'} = K_{\underline{i}\nu',\underline{j}\sigma'} \tag{33}$$

is the RI-decomposition of the exchange-type electron repulsion integral, we introduce the RI-decomposition of the coupling-strength averaged screened Coulomb interaction $\overline{W}(\mathrm{i}\omega)$,

$$- \sum_P M^P_{\underline{i},\nu'}(i\omega)M^P_{\underline{j},\sigma'}(i\omega) = (\underline{i}\nu'(i\omega)|\overline{W}(i\omega)|\underline{j}\sigma'(i\omega)). \quad (34)$$

This can be easily seen by following the treatment of Secs. II B and II C again, starting from an alternative resummation of Eq. (3) given in Ref. 20,

$$E^{\text{SOSEX}}_c = -\frac{1}{2}\int_{-\infty}^{\infty}\frac{d\omega}{2\pi}\text{Tr}\Big\{(ia|\overline{W}(i\omega)|jb)(ib|ja)$$
$$\times \Pi_0(i\omega)_{ia,ia}\Pi_0(i\omega)_{jb,jb}\Big\}, \quad (35)$$

which results in

$$E^{\text{SOSEX}}_c = -\frac{1}{2}\int_{-\infty}^{\infty}\frac{d\omega}{2\pi}\text{Tr}\Big\{(\underline{i}\nu'(i\omega)|\overline{W}(i\omega)|\underline{j}\sigma'(i\omega))(\underline{i}\sigma'|\underline{j}\nu')\Big\}. \quad (36)$$

Here we note that not only the coupling-strength averaged screened Coulomb interaction but also the charge distributions $(\underline{i}\nu'(i\omega)|$ are frequency dependent. An RI-decomposition of the screened Coulomb interaction has been introduced in Ref. 51 and was applied to RPA-SOSEX using a numerical coupling-strength integration in Ref. 20. The approach presented in our work, Eqs. (31) and (29), can in contrast be evaluated directly from the already integrated $\mathbf{Q}(i\omega)$ and $\mathbf{B}$.

Equation (31) bears close resemblance to the exchange-type term of RI-CDD MP2, where an efficient evaluation technique has been proposed.[37] Due to the exchange type coupling of the local charge distributions, one can select a linear number of Coulomb ERIs [Eq. (33)] and coupling-strength averaged screened Coulomb ERIs [Eq. (34)], which contribute significantly to the final energy. These integrals are then calculated using the RI and directly summed up for the final energy according to Eq. (31).

To find this linear number of significant integrals, one needs to find efficient integral estimates to reduce the number of integrals that explicitly need to be evaluated. While in Ref. 37, QQR-type integral estimates were used, we presently use simple Schwarz estimates since the exchange coupling ensures linear scaling of the number of integrals with respect to the system size,

$$|(\underline{i}\sigma'|\underline{j}\nu')| \le (\underline{i}\sigma'|\underline{i}\sigma')^{1/2}(\underline{j}\nu'|\underline{j}\nu')^{1/2} = Q_{\underline{i}\sigma'}Q_{\underline{j}\nu'}, \quad (37)$$

$$|(\underline{i}\nu'(i\omega)|\overline{W}(i\omega)|\underline{j}\sigma'(i\omega))| \le (-(\underline{i}\nu'(i\omega)|\overline{W}(i\omega)|\underline{i}\nu'(i\omega)))^{1/2}$$
$$\times (-(\underline{j}\sigma'(i\omega)|\overline{W}(i\omega)|\underline{j}\sigma'(i\omega)))^{1/2}$$
$$=: Q_{\underline{i}\nu'}(i\omega)Q_{\underline{j}\sigma'}(i\omega), \quad (38)$$

and hence

$$|(\underline{i}\nu'(i\omega)|\overline{W}(i\omega)|\underline{j}\sigma'(i\omega))(\underline{i}\sigma'|\underline{j}\nu')|$$
$$\le Q_{\underline{i}\nu'}(i\omega)Q_{\underline{j}\sigma'}(i\omega)Q_{\underline{i}\sigma'}Q_{\underline{j}\nu'}. \quad (39)$$

This method not only allows for fine grained use of sparsity but also reduces the formal scaling by a factor of $N_{\text{Aux}}/N_{\text{Bas}}$, compared to the method in Sec. II C, to $\mathcal{O}(\mathcal{N}_{\text{Aux}}\mathcal{N}^2_{\text{occ}}\mathcal{N}^2_{\text{Bas}})$.

While all three-index quantities in Eq. (31) contain the matrix square root of the RI-matrix, $\mathbf{C}^{1/2}$, and therefore linear scaling of the number of significant elements in the $\mathbf{B}$ and $\mathbf{M}(i\omega)$ tensors is lost, it is still advisable to use a local metric, such as the overlap or attenuated Coulomb metric. This allows using sparsity in the formation of $\mathbf{B}$ and $\mathbf{M}(i\omega)$, by first forming $\tilde{\mathbf{B}}$ and $\tilde{\mathbf{M}}(i\omega)$ and then performing the contraction with the respective RI matrix. In the asymptotic limit, this should show quadratic scaling behavior since the local metric ensures a constant number of AO/Cholesky-indices for each auxiliary basis index.

For RPA-AXK, the only difference is that the $\mathbf{W}(i\omega)$ matrix is given as

$$\mathbf{W}(i\omega) = \mathbf{Q}^{-1}(i\omega)\log(\mathbf{1}-\mathbf{Q}(i\omega))\mathbf{Q}^{-1}(i\omega)$$
$$+\mathbf{Q}^{-1}(i\omega)(\mathbf{1}-\mathbf{Q}(i\omega))^{-1} \quad (40)$$

and we will refer to these methods as QQ-CDD-RI in Sec. IV.

III. COMPUTATIONAL DETAILS

We have implemented all methods including the canonical formulation and the canonical RI formulation in the FermiONs++[52,53] program package developed in our group. For the canonical RI formulation, we follow the idea given in the supplementary material of Ref. 29 which shows a $\mathcal{O}(\mathcal{N}^3_{\text{Aux}}\mathcal{N}^2_{\text{occ}})$ scaling behavior and makes optimal use of efficient linear algebra libraries. For the canonical RI formulation, we use the Coulomb RI-metric. Unless noted otherwise, we employ the attenuated Coulomb metric with $\omega = 0.1$ for all low scaling algorithms, as has been shown to be optimal for dRPA calculations.[7]

For the grids of the numerical frequency integration and the double-Laplace transform, we employ the minimax grids presented in Ref. 14. The rationale behind the fitting procedure given in Ref. 14 is easily extendable to the beyond RPA methods treated here. For RPA-SOSEX and RPA-eh-TDHF, the second-order approximation corresponds to the MP2 energy,[29] as compared to the direct (opposite spin) MP2 energy for dRPA. Since this only affects the integral tensors but leaves the integrand unchanged, the exact same procedure as for dRPA can be used. As discussed in the supplementary information of Ref. 18, RPA-SOSEX and RPA-AXK recover the same second-order contribution, which is why the grids are also suited for RPA-AXK.

We employ 15 grid points for the time and frequency grid in the general case. Where the integration interval is sufficiently small for 15 grid points not to yield any more accuracy in our double precision implementation, less grid points are automatically employed.

As a sparse algebra format, we use the blocked compressed sparse row (BCSR) format optimized for quantum chemical methods.[54,55] We employ a block size of 50 elements and a sparsity threshold of 10^{-7} unless noted otherwise. For the canonical algorithms, we of course always employ dense algebra. For the remaining algorithms, we will mention this explicitly in Sec. IV. The integral threshold ϑ for the AO-LinK formulation was set to 10^{-10}. The screening threshold for the QQ-CDD-RI method was set to 10^{-9}. The Schwarz estimates used for the QQ-CDD-RI formulation are calculated using the RI as in Ref. 37.

The exact procedure for pivoted CD of density matrices is detailed in, e.g., Refs. 7 and 37. For the generation of the pseu-dodensities, we employ a Fermi shift to enhance numerical stability as detailed in Ref. 56.

The evaluation of the RI-RPA-eh-TDHF correlation energy using Eq. (12) with given $\mathbf{Q}(i\omega)$ and $\mathbf{Y}(i\omega)$ poses some numerical challenges due to the need to explicitly calculate $\mathbf{Q}^{-1}(i\omega)$, as $\mathbf{Q}(i\omega)$ can turn out to be numerically close to a singular matrix. Therefore, we follow the idea presented in Ref. 40 and project all quantities on the space spanned by the eigenvectors of $\mathbf{Q}(i\omega)$, corresponding to non-zero eigenvalues (in this case absolute values larger than 10^{-14}). Furthermore, the argument in the logarithm is non-symmetric and therefore complex eigenvectors are possible. A numerically more stable version of Eq. (12) is work in progress.

All calculations use reference KS orbitals obtained from DFT calculations with the Perdew-Burke-Ernzerhof (PBE) functional.[57] We employ def2-SVP, def2-TZVP, and def2-QZVP basis sets[58,59] along with their corresponding RI basis sets.[60,61] Total energies are obtained by adding correlation energies to the Hartree-Fock energy evaluated with the KS-orbitals. All calculations employ the frozen core approximation.

IV. RESULTS AND DISCUSSION

Since the purpose of this work is to show the efficient yet accurate calculation of $\mathbf{Y}(i\omega)$, we present our results exemplarily using RPA-SOSEX correlation energies. We will start with showing the accuracy of our methods using the S22 test set,[62] before demonstrating the efficiency of our methods. We finish with an illustrative large scale application, by presenting RPA-SOSEX results for the L7 test set of large, dispersion dominated molecules.[63]

A. Convergence of the frequency quadrature and the double-Laplace transform

The convergence of the frequency quadrature and the double-Laplace transform has been shown nicely for dRPA correlation energies in a plane wave implementation.[14] Here we want to show briefly that minimax grids also allow for well-converged results for beyond RPA correlation energies with less than 20 grid points. Therefore, we calculated the RPA-SOSEX correlation energies for the methane monomer and dimer of the S22 test set[62] using the def2-TZVP and def2-QZVP basis sets, along with the corresponding RI basis set. As a reference, we use canonical RI-RPA-SOSEX results obtained with Clenshaw-Curtis quadrature with the RPA adjusted parameter optimization,[9] which has been shown to also work for closed-shell RPA-SOSEX.[29] For the reference calculations, we employ 500 grid points, which ensures well-converged results.

Table I shows that the minimax grids allow converging the absolute correlation energies to below 10^{-10} hartree with respect to the numerical frequency integration. When additionally using the corresponding grids for the double-Laplace transform of the non-interacting polarization propagator, the minimax grids allow converging the total energies to 10^{-10} hartree as well (Table II). Beyond 13 grid points, the interaction

energy fluctuates in the range of 10^{-6} kcal/mol, which is well beyond the accuracy of the methods under inspection. Based on these results, we have chosen 15 grid points in Secs. IV B–IV D.

B. Calculations on the S22 test set

To further examine the accuracy of all our presented methods, we have performed calculations on the entire S22 test set.[62] We have performed calculations using def2-SVP, def2-TZVP, and def2-QZVP basis sets along with their

TABLE I. Convergence of the numerical frequency integration using mini-max grids referenced against a well converged Clenshaw-Curtis quadrature with 500 grid points. All results are RI-RPA-SOSEX correlation energies of the methane monomer/dimer from the S22 test set.[62] The interaction energy is denoted as ΔE.

def2-TZVP			
No. pts.	Monomer (hartree)	Dimer (hartree)	ΔE (kcal/mol)
10	−0.201 615 930 3	−0.404 493 209 8	−0.304 712
13	−0.201 615 931 6	−0.404 493 214 3	−0.304 713
15	−0.201 615 931 6	−0.404 493 214 4	−0.304 713
18	−0.201 615 931 6	−0.404 493 214 4	−0.304 713
500	−0.201 615 931 6	−0.404 493 214 4	−0.304 713

def2-QZVP			
No. pts.	Monomer (hartree)	Dimer (hartree)	ΔE (kcal/mol)
10	−0.226 027 242 2	−0.453 494 471 6	−0.377 841
13	−0.226 027 338 4	−0.453 494 608 6	−0.377 806
15	−0.226 027 339 7	−0.453 494 612 4	−0.377 807
18	−0.226 027 339 9	−0.453 494 613 0	−0.377 807
500	−0.226 027 339 9	−0.453 494 613 0	−0.377 807

TABLE II. Convergence of the numerical frequency integration and double-Laplace transform of the non-interacting polarization propagator using mini-max grids referenced against a well converged Clenshaw-Curtis quadrature with 500 grid points. The reference results are RI-RPA-SOSEX correlation energies, while the convergence is tested using CDD-RI-RPA-SOSEX (Coulomb metric) correlation energies. All correlation energies are calculated for the methane monomer/dimer from the S22 test set.[62] The interaction energy is denoted as ΔE.

def2-TZVP			
No. pts.	Monomer (hartree)	Dimer (hartree)	ΔE (kcal/mol)
10	−0.201 615 914 1	−0.404 493 171 7	−0.304 708
13	−0.201 615 931 3	−0.404 493 213 8	−0.304 713
15	−0.201 615 931 6	−0.404 493 214 4	−0.304 713
18	−0.201 615 931 6	−0.404 493 214 4	−0.304 713
500	−0.201 615 931 6	−0.404 493 214 4	−0.304 713

def2-QZVP			
No. pts.	Monomer (hartree)	Dimer (hartree)	ΔE (kcal/mol)
10	−0.226 028 705 4	−0.453 497 574 2	−0.377 951
13	−0.226 027 299 6	−0.453 494 532 3	−0.377 806
15	−0.226 027 332 9	−0.453 494 596 5	−0.377 799
18	−0.226 027 339 6	−0.453 494 612 4	−0.377 807
500	−0.226 027 339 9	−0.453 494 613 0	−0.377 807

corresponding RI-basis sets. As a reference, we have performed calculations using both the canonical implementation and the RI-canonical implementation using the Coulomb metric.

The error introduced through the use of the RI within the S22 test set as compared to the canonical implementation is 0.014 and 0.009 kcal/mol in the mean absolute error (MAE) for the def2-SVP and def2-TZVP basis set, respectively, and is therefore negligible (Fig. 1). For the def2-QZVP results, we therefore employ the canonical RI implementation as a reference for our newly developed methods since the computational cost and memory requirements for the canonical implementation for the def2-QZVP basis set become unfeasible.

To examine the impact of the different approximations made here, we perform calculations using separately the numerical double-Laplace transform with the Coulomb RI-metric and calculations using the numerical double-Laplace transform with the attenuated Coulomb metric also employing sparse algebra. The results for the def2-SVP and def2-TZVP basis sets are shown in Fig. 1. The results for the def2-QZVP basis are shown in Fig. 2.

For all basis sets employed here, the error introduced through the double-Laplace transform is barely noticeable, as can be seen from the error bars for the CDD-RI and QQ-CDD-RI calculations, as compared to the plain RI error. The error introduced by changing from the Coulomb to the attenuated Coulomb metric shows a maximum of 0.004 kcal/mol for the
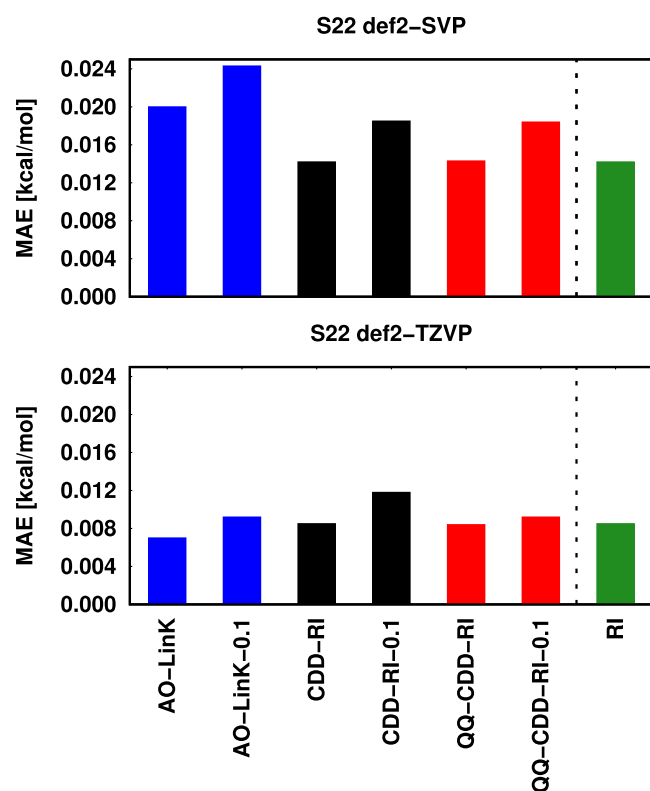

FIG. 1. Bar chart showing the mean absolute error of the RPA-SOSEX interaction energies of the S22 test set as compared to the canonical implementation using def2-SVP and def2-TZVP basis sets along with the corresponding RI-basis set. As RI-metric the Coulomb metric is employed unless the suffix 0.1 is appended, which implies use of the attenuated Coulomb metric with $\omega = 0.1$.
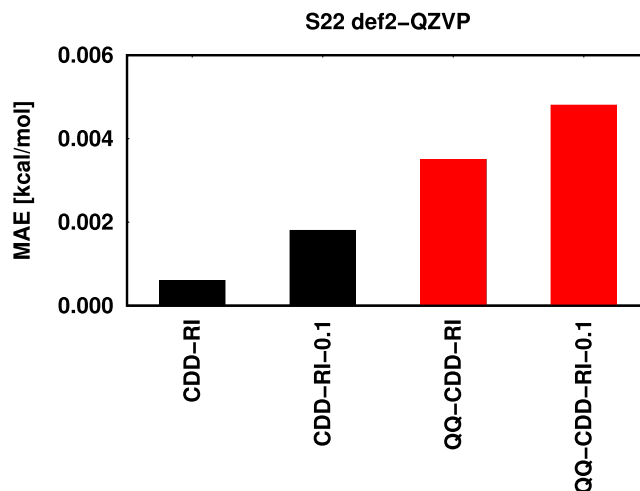

FIG. 2. Bar chart showing the mean absolute error of the RPA-SOSEX interaction energies of the S22 test set as compared to the RI-canonical implementation using the def2-QZVP basis set along with the corresponding RI-basis set. As RI-metric the Coulomb metric is employed unless the suffix 0.1 is appended, which implies use of the attenuated Coulomb metric with $\omega = 0.1$. For the QQ-CDD-RI, CDD-RI and CDD-RI-0.1 results we have employed dense algebra, while the QQ-CDD-RI-0.1 results were produced using sparse-algebra.

def2-SVP basis in the MAE as compared to the RI-canonical value and is therefore also negligible. For the QQ-CDD-RI formulation, the maximum deviation in the MAE as compared to the RI-canonical implementation is 0.004 kcal/mol, showing that the Schwarz screening does not introduce a relevant error. The maximum error caused by Schwarz screening and the use of the attenuated Coulomb metric combined is 0.005 kcal/mol for the def2-QZVP basis set. The use of sparse algebra with the thresholds given in Sec. III in conjunction with the def2-QZVP basis for the CDD-RI formulation leads to significantly higher errors for some individual systems and a total MAE of 0.3 kcal/mol. Employing dense algebra with the attenuated Coulomb metric as shown in Fig. 2 produces again a negligible deviation, as compared to the RI-canonical implementation. This problem is related to the atomic blocking used in BCSR, which would require larger block sizes and a tighter sparsity threshold for large basis sets.

For the AO-LinK method with the chosen thresholds, the deviation in the MAE shows a maximum of 0.020 kcal/mol (0.024 kcal/mol with the attenuated Coulomb metric) for the def2-SVP basis set. This additional error as compared to the CDD-RI variants could stem from the integral screening employed in the integral-direct computation. We omitted the computation of S22 interaction energies with the method formulated in a pure AO basis for the def2-QZVP basis set due to too high computational cost. The problem here stems from the aforementioned bad scaling of pure AO methods with respect to the basis set size due to the redundancy present in pure AO basis sets. This already shows one advantage of the two low scaling methods, which employ CDD to avoid this problem and show similar formal scaling as the RI-canonical implementation, while still being efficient for large molecular systems, as will be shown in Secs. IV C and IV D.

To put the above errors into perspective, the MAE of the canonical implementation using def2-SVP and def2-TZVP

basis sets is 0.85 kcal/mol and 0.35 kcal/mol, respectively, and 0.27 kcal/mol for the def2-QZVP basis using the RI-canonical implementation (all values referenced against the S22A revised results of Ref. 64). This shows that the errors introduced through our approximations are at least one order of magnitude smaller than the method error calculated with the reference implementation and therefore insignificant.

The mean absolute percentage error of 7.0% for the largest def2-QZVP basis set as compared to the S22A revised reference results[64] is in good agreement with the values of 9.5% and 10.5% reported for a plane wave[34] and numerical atomic orbital implementation[20] of RPA-SOSEX, respectively.

C. Efficiency and asymptotic scaling behavior

To show the efficiency and the low asymptotic scaling behavior of our presented methods for large systems with a nonvanishing HOMO-LUMO gap, we performed RPA-SOSEX correlation energy calculations for linear alkanes up to $C_{160}H_{322}$. As has been discussed, e.g., in Ref. 6, these systems serve as good and practical systems to determine the asymptotic scaling of a quantum chemical method. We have performed all calculations using the def2-SVP basis with the corresponding RI basis set. We compare the scaling of our method to the RI-canonical implementation. The calculations were performed using 12 threads on dual-processor Intel Xeon CPU E5-2620 machines with 64 GB of memory. All timings shown in this section correspond to the wall time needed to perform the beyond RPA correction. The time required for the calculation of $Q(i\omega)$ is excluded since we want to focus on the efficient calculation of the beyond RPA energy and $Q(i\omega)$ is part of the dRPA calculation. For the performance of the linear-scaling dRPA implementation, see Refs. 7 and 8. As a rough estimate about the comparative cost to form $Q(i\omega)$ vs. the cost to form $Y(i\omega)$, we consider the calculation of $C_{160}H_{322}$ for which the calculation of $Q(i\omega)$ is presently faster by a factor of about 70. This can be explained with the fact that the formal scaling of the linear scaling CDD-RI-dRPA algorithm with respect to the molecular size is smaller by one power, leading to a significantly smaller prefactor.

To calibrate the sparsity settings, i.e., thresholds and block sizes for our sparse algebra routines, we compare the results for $C_{40}H_{82}$ against the RI-canonical implementation. Using

FIG. 3. Timings for the calculations on a set of linear alkanes using the def2-SVP basis set with the corresponding RI basis set. The AO-LinK, CDD-RI, and QQ-CDD-RI methods employ the attenuated Coulomb metric with $\omega = 0.1$ along with sparse algebra. The point labelled with an asterisk was estimated conservatively based on the timing for a subset of the frequency points.

the thresholds and block sizes listed in Sec. III, this leads to an error of 57 and 42 μhartree for $C_{40}H_{82}$ in the absolute RPA-SOSEX correlation energy for the CDD-RI and QQ-CDD-RI formulation, respectively. For the AO-LinK method with the chosen thresholds, the deviation is 2.9 $m$hartree. While this deviation is significantly higher, one has to keep in mind that in this method the integral tensor corresponding to K is computed without the RI approximation, which means that the canonical RI calculation contains the additional RI error introduced through the RI decomposition of K.

The wall times shown in Fig. 3 for RPA-SOSEX calculations on a series of alkanes from $C_{10}H_{22}$ to $C_{160}H_{322}$ exemplify that all our presented methods significantly outperform the RI-canonical implementation for large, electronically sparse systems in terms of computational efficiency: The AO-LinK method shows a crossover to the RI-canonical method at $C_{60}H_{122}$, the CDD-RI method at $C_{40}H_{82}$, and the QQ-CDD-RI method already at $C_{20}H_{42}$. Extrapolating the wall-time for the RI-canonical method for the largest system ($C_{160}H_{322}$) assuming an $\mathcal{O}(\mathcal{N}^5)$ scaling behavior, the speed-up obtained with the AO-LinK method is 42×, with the CDD-RI method is 61×, and with the QQ-CDD-RI method is 183×.

TABLE III. Wall times and observed computational complexities for a set of linear alkanes using the def2-SVP basis set along with the corresponding RI basis set for the different methods presented and the RI canonical implementation. The computational complexities were calculated using the preceding calculation in the table. The number labelled with an asterisk was estimated conservatively based on the timing for a subset of the frequency points.

Atoms	AO-LinK		CDD-RI		QQ-CDD-RI		RI-canonical	
	Time (h)	Scaling	Time (h)	Scaling	Time (h)	Scaling	Time (h)	Scaling
62	12.8		1.7		0.6		0.9	
122	65.6	2.4	14.9	3.2	4.1	2.8	22.9	4.8
242	184.7	1.5	81.4	2.5	18.0	2.1	644.7*	4.9
362	362.4	1.7	183.4	2.0	50.6	2.6		
482	488.6	1.0	338.6	2.1	112.8	2.8		

The observed computational scaling behavior of our methods is examined in more detail in Table III. The RI-canonical implementation shows an $\mathcal{O}(\mathcal{N}^5)$ scaling behavior as expected. For the AO-LinK method, the observed scaling behavior in the limit of sparse molecules is linear; for the CDD-RI method, quadratic; and for the QQ-CDD-RI method, sub-cubic. To show that for the QQ-CDD-RI formulation we indeed only calculate a linear number of significant integrals, we have counted the number of calculated integrals during each of the calculations on the linear alkanes. The result is shown in Fig. 4. As can be seen clearly, the number of integrals shows early on perfect linear scaling.

D. Large scale calculations

In this section, we show that the methods based on CDDs also outperform the canonical-RI variant for larger than double-ζ basis sets. Furthermore, we apply the QQ-CDD-RI method to present RPA-SOSEX results for the L7 test set of large, dispersion dominated molecules[63] with up to triple-ζ basis sets.

First, to study the performance of our methods for larger basis sets, we have performed RPA-SOSEX correlation energy calculations on linear alkanes up to $C_{80}H_{162}$ with the canonical RI implementation and the CDD-RI and QQ-CDD-RI variant using the def2-TZVP basis set. All calculations were performed using 16 threads on a dual-processor Intel Xeon CPU E5-2667 machine. The results presented in Fig. 5 show that both the CDD-RI and the QQ-CDD-RI variant outperform the canonical implementation for large systems. The crossover to the canonical implementation occurs at $C_{60}H_{122}$ with the CDD-RI method and at $C_{40}H_{82}$ with the QQ-CDD-RI method. Furthermore, to show that the QQ-CDD-RI method is beneficial also for quadruple-ζ basis sets, we have performed a RPA-SOSEX correlation energy calculation on the $C_{40}H_{82}$ molecule with the def2-QZVP basis set and the corresponding RI-basis set. Here the calculation of the RPA-SOSEX correlation energy takes 104 h for the QQ-CDD-RI method, while the calculation using the RI-canonical implementation requires 408 h (extrapolated from 8 of the 15 frequency points).
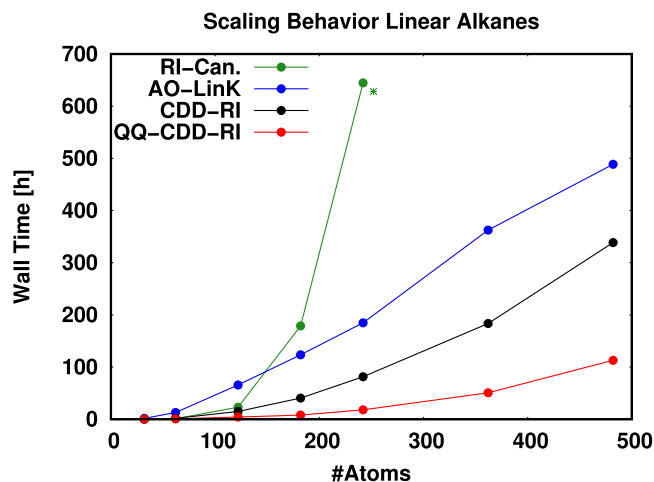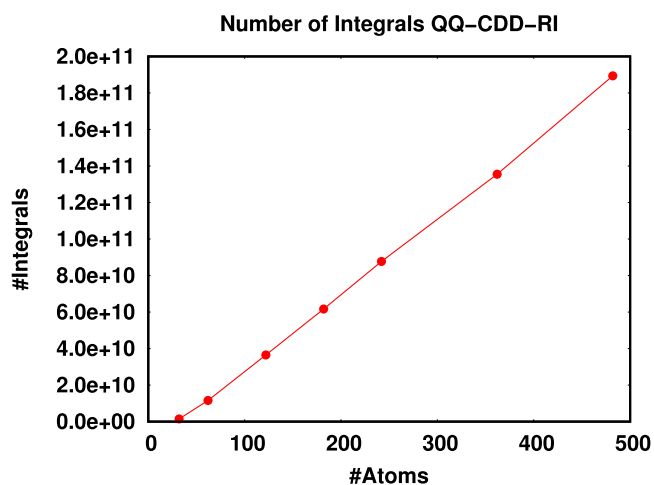
FIG. 5. Timings for the calculations on a set of linear alkanes using the def2-TZVP basis set with the corresponding RI basis set. The CDD-RI, and QQ-CDD-RI methods employ the attenuated Coulomb metric with $\omega = 0.1$ along with sparse algebra. Points labelled with an asterisk were estimated conservatively based on the timings for a subset of the frequency points.

This speed-up of a factor of 3.9 still compares well against the speed-ups obtained with triple-ζ (speed-up: 4.5) and double-ζ (speed-up: 5.6) basis sets obtained with the same method. These results show that also for larger than double-ζ basis sets significant speed-ups over the canonical implementation can be obtained with the CDD-RI and QQ-CDD-RI methods, supported by the dimensionality reduction of the AO basis set via Cholesky decomposition.

Finally, we present RPA-SOSEX benchmark results for the L7 test set[63] with def2-SVP and def2-TZVP basis sets along with their corresponding RI-basis sets. The results shown in Table IV exemplify two important aspects: The first aspect is that our QQ-CDD-RI variant can also treat large molecular systems without excessive sparsity in the electronic structure such as the circumcoronene$\cdots$guanine-cytosine base pair complex. The second aspect is that including exchange effects yields a significant accuracy gain over plain dRPA for the L7 test set, which can be seen when comparing the results to dRPA results presented in Ref. 7 obtained with the same basis set. The RPA-SOSEX results with double-ζ basis set already improve upon dRPA results with a triple-ζ basis set. The triple-ζ RPA-SOSEX results show a MAE to the reference results[63] of less than 1 kcal/mol, which is the desired chemical accuracy.

FIG. 4. Number of integrals calculated with the QQ-CDD-RI method for a set of linear alkanes using the def2-SVP basis set with the corresponding RI basis set. The attenuated Coulomb metric was employed with $\omega = 0.1$ along with sparse algebra.

TABLE IV. Benchmark results showing the root mean squared deviation (RMSD), mean absolute and mean signed error (MAE and MSE) for the L7 test set[63] of large, dispersion dominated systems as compared to the reference results. The CDD-dRPA values were taken from Ref. 7. The RPA-SOSEX values were calculated using the QQ-CDD-RI approach described in this work with the attenuated Coulomb metric ($\omega = 0.1$) along with sparse algebra.

	RMSD	MAE	MSE
dRPA (def2-TZVP)[7]	2.90	2.45	−2.08
RPA-SOSEX (def2-SVP)	2.44	1.94	−0.13
RPA-SOSEX (def2-TZVP)	1.19	0.81	0.11

V. CONCLUSION

We have introduced three methods that enable efficient beyond RPA calculations for large molecular systems up to 500 atoms, while the accuracy is under full numerical control. These developments significantly extend the applicability of beyond RPA methods by reducing the computational cost compared to the canonical formulation with and without RI. Next to the beyond RPA variants mentioned in the main text, our methods are obviously also applicable to the short-range RPA-SOSEX variant recently introduced by us.[65] For the present range of system sizes, we recommend the QQ-CDD-RI method for general use; since even though it shows the worst asymptotic scaling behavior of the newly presented methods, it is most efficient for a wide range of molecular sizes and shows very good scaling behavior with respect to basis set size. Furthermore, we have shown that the methods employing CDDs also allow for significant computational savings when larger than double-ζ basis sets are used, which ensures the applicability of these methods, since RPA correlation energies require rather large basis sets to obtain converged results.[66] To this end, range separated variants of RPA correlation energies[67–72] would be a valuable addition to our approach. These schemes reduce the basis set dependence significantly so that double-ζ results were shown to be sufficiently accurate already.[73]

ACKNOWLEDGMENTS

APPENDIX: DERIVATION FOR RI-RPA-AXK

To derive the RI-expression for RPA-AXK, we expand the logarithm and the inverse of $(\mathbf{1} - \mathbf{\Pi}_0(i\omega)\mathbf{V})$ appearing in Eq. (4) as a series

$$\mathrm{Tr}\Big\{\log\left(\mathbf{1} - \mathbf{\Pi}_0(i\omega)\mathbf{V}\right)\mathbf{V}^{-1}\mathbf{K}\Big\} = \mathrm{Tr}\Big\{-\sum_{n=1}^{\infty}\frac{(\mathbf{\Pi}_0(i\omega)\mathbf{V})^n\mathbf{V}^{-1}\mathbf{K}}{n}\Big\},$$
(A1)

$$\mathrm{Tr}\Big\{(\mathbf{1} - \mathbf{\Pi}_0(i\omega)\mathbf{V})^{-1}\mathbf{\Pi}_0(i\omega)\mathbf{K}\Big\}$$
$$= \mathrm{Tr}\Big\{\sum_{n=1}^{\infty}(\mathbf{\Pi}_0(i\omega)\mathbf{V})^{n-1}\mathbf{\Pi}_0(i\omega)\mathbf{K}\Big\}.$$
(A2)

For $n = 1$, the terms of the two series cancel. Inserting the RI for $\mathbf{V}$ and $\mathbf{K}$, one can introduce the definitions of $\mathbf{Q}(i\omega)$ and $\mathbf{Y}(i\omega)$ [see Eqs. (9) and (13)] using the cyclic invariance of the trace,

$$\mathrm{Tr}\Big\{\log\left(\mathbf{1} - \mathbf{\Pi}_0(i\omega)\mathbf{V}\right)\mathbf{V}^{-1}\mathbf{K} + (\mathbf{1} - \mathbf{\Pi}_0(i\omega)\mathbf{V})^{-1}\mathbf{\Pi}_0(i\omega)\mathbf{K}\Big\}$$
$$= \mathrm{Tr}\Big\{-\sum_{n=2}^{\infty}\frac{\mathbf{Q}(i\omega)^{(n-2)}\mathbf{Y}(i\omega)}{n} + \sum_{n=2}^{\infty}\mathbf{Q}(i\omega)^{(n-2)}\mathbf{Y}(i\omega)\Big\}.$$
(A3)

This can be brought to the closed form of Eq. (11), where again the first term of each sum cancels.

[1] H. Eshuis, J. E. Bates, and F. Furche, Theor. Chem. Acc. **131**, 1084 (2012).
[2] X. Ren, P. Rinke, C. Joas, and M. Scheffler, J. Mater. Sci. **47**, 7447 (2012).
[3] G. P. Chen, V. K. Voora, M. M. Agee, S. G. Balasubramani, and F. Furche, Annu. Rev. Phys. Chem. **68**, 421 (2017).
[4] F. Furche, Phys. Rev. B **64**, 195120 (2001).
[5] M. Kállay, J. Chem. Phys. **142**, 204105 (2015).
[6] H. F. Schurkus and C. Ochsenfeld, J. Chem. Phys. **144**, 031101 (2016).
[7] A. Luenser, H. F. Schurkus, and C. Ochsenfeld, J. Chem. Theory Comput. **13**, 1647 (2017).
[8] D. Graf, M. Beuerle, H. F. Schurkus, A. Luenser, G. Savasci, and C. Ochsenfeld, J. Chem. Theory Comput. **14**, 2505–2515 (2018).
[9] H. Eshuis, J. Yarkony, and F. Furche, J. Chem. Phys. **132**, 234114 (2010).
[10] N. Shenvi, H. van Aggelen, Y. Yang, and W. Yang, J. Chem. Phys. **141**, 024119 (2014).
[11] E. G. Hohenstein, R. M. Parrish, and T. J. Martínez, J. Chem. Phys. **137**, 044103 (2012).
[12] E. G. Hohenstein, R. M. Parrish, C. D. Sherrill, and T. J. Martínez, J. Chem. Phys. **137**, 221101 (2012).
[13] R. M. Parrish, E. G. Hohenstein, T. J. Martínez, and C. D. Sherrill, J. Chem. Phys. **137**, 224106 (2012).
[14] M. Kaltak, J. Klimeš, and G. Kresse, J. Chem. Theory Comput. **10**, 2498 (2014).
[15] J. Wilhelm, P. Seewald, M. Del Ben, and J. Hutter, J. Chem. Theory Comput. **12**, 5851 (2016).
[16] J. F. Dobson, J. Wang, B. P. Dinte, K. McLennan, and H. M. Le, Int. J. Quantum Chem. **101**, 579 (2005).
[17] J. F. Dobson and T. Gould, J. Phys. Condens. Matter **24**, 073201 (2012).
[18] J. E. Bates and F. Furche, J. Chem. Phys. **139**, 171103 (2013).
[19] J. Paier, X. Ren, P. Rinke, G. E. Scuseria, A. Grüneis, G. Kresse, and M. Scheffler, New J. Phys. **14**, 043002 (2012).
[20] X. Ren, P. Rinke, G. E. Scuseria, and M. Scheffler, Phys. Rev. B **88**, 035120 (2013).
[21] T. M. Henderson and G. E. Scuseria, Mol. Phys. **108**, 2511 (2010).
[22] G. E. Scuseria, T. M. Henderson, and D. C. Sorensen, J. Chem. Phys. **129**, 231101 (2008).
[23] D. Langreth and J. Perdew, Solid State Commun. **17**, 1425 (1975).
[24] D. C. Langreth and J. P. Perdew, Phys. Rev. B **15**, 2884 (1977).
[25] F. Furche, J. Chem. Phys. **129**, 114105 (2008).
[26] A. Grüneis, M. Marsman, J. Harl, L. Schimka, and G. Kresse, J. Chem. Phys. **131**, 154115 (2009).
[27] D. L. Freeman, Phys. Rev. B **15**, 5512 (1977).
[28] J. G. Ángyán, R.-F. Liu, J. Toulouse, and G. Jansen, J. Chem. Theory Comput. **7**, 3116 (2011).
[29] B. Mussard, D. Rocca, G. Jansen, and J. G. Ángyán, J. Chem. Theory Comput. **12**, 2191 (2016).
[30] A. Dixit, J. G. Ángyán, and D. Rocca, J. Chem. Phys. **145**, 104105 (2016).
[31] A. Heßelmann and A. Görling, Mol. Phys. **108**, 359 (2010).
[32] J. Erhard, P. Bleiziffer, and A. Görling, Phys. Rev. Lett. **117**, 143002 (2016).
[33] P. Bleiziffer, A. Heßelmann, and A. Görling, J. Chem. Phys. **136**, 134102 (2012).
[34] A. Dixit, J. Claudot, S. Lebègue, and D. Rocca, J. Chem. Theory Comput. **13**, 5432 (2017).
[35] J. E. Moussa, J. Chem. Phys. **140**, 014107 (2014).
[36] A. Heßelmann, J. Chem. Phys. **146**, 174110 (2017).
[37] S. A. Maurer, L. Clin, and C. Ochsenfeld, J. Chem. Phys. **140**, 224112 (2014).
[38] M. Feyereisen, G. Fitzgerald, and A. Komornicki, Chem. Phys. Lett. **208**, 359 (1993).
[39] H.-J. Werner, F. R. Manby, and P. J. Knowles, J. Chem. Phys. **118**, 8149 (2003).
[40] H. F. Schurkus, A. Luenser, and C. Ochsenfeld, J. Chem. Phys. **146**, 211106 (2017).
[41] Y. Jung, A. Sodt, P. M. W. Gill, and M. Head-Gordon, Proc. Natl. Acad. Sci. U. S. A. **102**, 6692 (2005).
[42] Y. Jung, Y. Shao, and M. Head-Gordon, J. Comput. Chem. **28**, 1953 (2007).
[43] S. Reine, E. Tellgren, A. Krapp, T. Kjærgaard, T. Helgaker, B. Jansik, S. Høst, and P. Salek, J. Chem. Phys. **129**, 104101 (2008).

[44]C. Ochsenfeld, C. A. White, and M. Head-Gordon, J. Chem. Phys. **109**, 1663 (1998).

[45]C. Ochsenfeld, Chem. Phys. Lett. **327**, 216 (2000).

[46]A. Luenser, J. Kussmann, and C. Ochsenfeld, J. Chem. Phys. **145**, 124103 (2016).

[47]H. Koch, A. S. de Merás, and T. B. Pedersen, J. Chem. Phys. **118**, 9481 (2003).

[48]J. Zienau, L. Clin, B. Doser, and C. Ochsenfeld, J. Chem. Phys. **130**, 204112 (2009).

[49]N. J. Higham, Wiley Interdiscip. Rev.: Comput. Mol. Sci. **1**, 251 (2009).

[50]H. Harbrecht, M. Peters, and R. Schneider, Appl. Numer. Math. **62**, 428 (2012).

[51]X. Ren, P. Rinke, V. Blum, J. Wieferink, A. Tkatchenko, A. Sanfilippo, K. Reuter, and M. Scheffler, New J. Phys. **14**, 053020 (2012).

[52]J. Kussmann and C. Ochsenfeld, J. Chem. Phys. **138**, 134114 (2013).

[53]J. Kussmann and C. Ochsenfeld, J. Chem. Theory Comput. **11**, 918 (2015).

[54]J. Kussmann and C. Ochsenfeld, J. Chem. Phys. **127**, 054103 (2007).

[55]F. G. Gustavson, ACM Trans. Math. Software **4**, 250 (1978).

[56]P. Y. Ayala and G. E. Scuseria, J. Chem. Phys. **110**, 3660 (1999).

[57]J. P. Perdew, K. Burke, and M. Ernzerhof, Phys. Rev. Lett. **77**, 3865 (1996).

[58]F. Weigend, F. Furche, and R. Ahlrichs, J. Chem. Phys. **119**, 12753 (2003).

[59]F. Weigend and R. Ahlrichs, Phys. Chem. Chem. Phys. **7**, 3297 (2005).

[60]F. Weigend, M. Haser, H. Patzelt, and R. Ahlrichs, Chem. Phys. Lett. **294**, 143 (1998).

[61]C. Hättig, Phys. Chem. Chem. Phys. **7**, 59 (2005).

[62]P. Jurecka, J. Sponer, J. Cerny, and P. Hobza, Phys. Chem. Chem. Phys. **8**, 1985 (2006).

[63]R. Sedlak, T. Janowski, M. Pitonak, J. Rezac, P. Pulay, and P. Hobza, J. Chem. Theory Comput. **9**, 3364 (2013).

[64]T. Takatani, E. G. Hohenstein, M. Malagoli, M. S. Marshall, and C. D. Sherrill, J. Chem. Phys. **132**, 144104 (2010).

[65]M. Beuerle and C. Ochsenfeld, J. Chem. Phys. **147**, 204107 (2017).

[66]H. Eshuis and F. Furche, J. Chem. Phys. **136**, 084105 (2012).

[67]J. Toulouse, I. C. Gerber, G. Jansen, A. Savin, and J. G. Ángyán, Phys. Rev. Lett. **102**, 096404 (2009).

[68]W. Zhu, J. Toulouse, A. Savin, and J. G. Ángyán, J. Chem. Phys. **132**, 244108 (2010).

[69]J. Toulouse, W. Zhu, J. G. Ángyán, and A. Savin, Phys. Rev. A **82**, 032502 (2010).

[70]B. G. Janesko, T. M. Henderson, and G. E. Scuseria, J. Chem. Phys. **130**, 081105 (2009).

[71]B. G. Janesko, T. M. Henderson, and G. E. Scuseria, J. Chem. Phys. **131**, 034110 (2009).

[72]R. M. Irelan, T. M. Henderson, and G. E. Scuseria, J. Chem. Phys. **135**, 094105 (2011).

[73]B. Mussard, P. Reinhardt, J. G. Ángyán, and J. Toulouse, J. Chem. Phys. **142**, 154123 (2015).

122

3.6 Efficient Reduced-Scaling Second-Order Møller–Plesset Perturbation Theory with Cholesky-Decomposed Densities and an Attenuated Coulomb Metric

M. Glasbrenner, D. Graf, C. Ochsenfeld

J. Chem. Theory Comput. **16**, 6856 (2020).

Abstract

We present a novel, highly efficient method for the computation of second-order Møller–Plesset perturbation theory (MP2) correlation energies, which uses the resolution of the identity (RI) approximation and local molecular orbitals obtained from a Cholesky decomposition of pseudodensity matrices (CDD), as in the RI-CDD-MP2 method developed previously in our group [Maurer, S. A.; Clin, L.; Ochsenfeld, C. *J. Chem. Phys.* **2014**, *140*, 224112]. In addition, we introduce an attenuated Coulomb metric and subsequently redesign the RI-CDD-MP2 method in order to exploit the resulting sparsity in the three-center integrals. Coulomb and exchange energy contributions are computed separately using specialized algorithms. A simple, yet effective integral screening protocol based on Schwarz estimates is used for the MP2 exchange energy. The Coulomb energy computation and the preceding transformations of the three-center integrals are accelerated using a modified version of the natural blocking approach [Jung, Y.; Head-Gordon, M. *Phys. Chem. Chem. Phys.* **2006**, *8*, 2831–2840]. Effective subquadratic scaling for a wide range of molecule sizes is demonstrated in test calculations in conjunction with a low prefactor. The method is shown to enable cost-efficient MP2 calculations on large molecular systems with several thousand basis functions.

Reprinted with permission from:

Efficient Reduced-Scaling Second-Order Møller−Plesset Perturbation Theory with Cholesky-Decomposed Densities and an Attenuated Coulomb Metric

Michael Glasbrenner, Daniel Graf, and Christian Ochsenfeld*

Read Online

ACCESS | Metrics & More | Article Recommendations | Supporting Information

ABSTRACT: We present a novel, highly efficient method for the computation of second-order Møller−Plesset perturbation theory (MP2) correlation energies, which uses the resolution of the identity (RI) approximation and local molecular orbitals obtained from a Cholesky decomposition of pseudodensity matrices (CDD), as in the RI-CDD-MP2 method developed previously in our group [Maurer, S. A.; Clin, L.; Ochsenfeld, C. *J. Chem. Phys.* **2014**, *140*, 224112]. In addition, we introduce an attenuated Coulomb metric and subsequently redesign the RI-CDD-MP2 method in order to exploit the resulting sparsity in the three-center integrals. Coulomb and exchange energy contributions are computed separately using specialized algorithms. A simple, yet effective integral screening protocol based on Schwarz estimates is used for the MP2 exchange energy. The Coulomb energy computation and the preceding transformations of the three-center integrals are accelerated using a modified version of the natural blocking approach [Jung, Y.; Head-Gordon, M. *Phys. Chem. Chem. Phys.* **2006**, *8*, 2831−2840]. Effective subquadratic scaling for a wide range of molecule sizes is demonstrated in test calculations in conjunction with a low prefactor. The method is shown to enable cost-efficient MP2 calculations on large molecular systems with several thousand basis functions.

1. INTRODUCTION

The accurate and efficient computation of electron correlation energies is one of the central challenges in *ab initio* electronic structure theory. Proper treatment of electron correlation is essential for a quantitative description of many chemical phenomena including dispersion, which is highly important in inter- and intramolecular interactions of many molecular systems. One of the most cost-efficient and commonly used wave function-based methods for computing correlation energies is second-order Møller−Plesset perturbation theory (MP2).[1] MP2 is significantly more accurate than Hartree−Fock, and because of its comparatively low N^5 scaling, it is computationally cheaper than other wave function methods such as Coupled Cluster (see, e.g., ref 2), which scale conventionally at least as N^6. Due to this good compromise between accuracy and computational cost, MP2 is one of the most widely used quantum chemistry methods.

In recent years, several variants of MP2 theory have been proposed. Empirical scaling of the same-spin and opposite-spin contributions to the MP2 energy in the spin-component-scaled MP2 (SCS-MP2)[3] has been shown to further increase the accuracy for energetics and molecular properties. The related scaled-opposite spin MP2 model (SOS-MP2)[4] leads to very efficient methods, since it allows to avoid the computationally challenging exchange contributions to the MP2 energy.

Furthermore, MP2 has also been combined with density functional theory (DFT)[5] in the context of double-hybrid functionals.[6] These functionals contain an MP2-like term and have been shown to provide excellent accuracy for many applications.[6−8]

Due to the widespread use of MP2 and its related methods, the development of efficient MP2 algorithms, which allow one to treat large molecules, is an important endeavor. The unfavorable fifth-order scaling of canonical MP2 severely limits its applicability to larger systems. Over the last decades, much work has been devoted to the development of more efficient MP2 methods with reduced scaling and prefactor (see, e.g., refs 9−39).

Many efficient MP2 methods employ decompositions of the electron repulsion integral (ERI) tensor. The most commonly used decomposition is the resolution of the identity (RI) approximation,[40] which decomposes the fourth-order ERI tensor into third- and second-order tensors using a set of
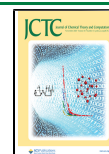
auxiliary basis functions. Although RI-MP2 has the same scaling as canonical MP2 with four-center integrals, the prefactor and the storage requirements are significantly reduced. Apart from RI, also Cholesky decomposition of the ERI tensor[21,30] and the pseudospectral approximation[12] have been applied to MP2. More recently, tensor hypercontraction has been introduced by Martínez and co-workers,[31,41] which allows one to reduce the formal scaling of MP2 to quartic.

In order to tackle the steep scaling of MP2 algorithms for larger systems, one can also exploit the locality of electron correlation. Pulay and Saebø pioneered the field of local correlation methods and introduced localized molecular orbitals (MOs) and the concept of correlation domains into MP2 theory.[9,10] Many local MP2 methods have been proposed since then,[13,14,16−20,22,35] including the divide-expand-consolidate (DEC) ansatz,[29,36] which employs iterative optimization of the orbital spaces. Recently, Neese and co-workers have employed local pair natural orbitals for MP2 and other correlation methods using the domain-based local pair natural orbital approach.[34,42,43]

Another path to reduced-scaling MP2 algorithms starts from a Laplace transformation of the orbital energy denominator appearing in canonical MP2, which was introduced by Almlöf and Häser.[11,44,45] Later, an atomic-orbital-based reformulation of Laplace-transformed MP2 (AO-MP2) was developed.[11,15] In combination with integral screening approaches, the scaling of AO-MP2 can be reduced to be asymptotically linear.[23,26,27,32] However, the prefactor of AO-MP2 is high, especially for large basis sets, leading to a late crossover with canonical MP2.

The efficiency of the AO-MP2 method is improved in the RI-CDD-MP2 method[28,33] by introducing the RI approximation and using local orbitals obtained from a Cholesky decomposition of the pseudodensity matrices (CDD). Both modifications lead to a significantly reduced prefactor compared to AO-MP2 and make RI-CDD-MP2 applicable to large molecules also with high-quality basis sets. RI-CDD-MP2 in its standard formulation scales asymptotically cubic.[33] Maurer et al.[33] also presented a second formulation, which employs the local density fitting approach from Werner et al.[22] and scales asymptotically linear. However, the prefactor of linear-scaling RI-CDD-MP2 is high, and speed-ups compared to the cubic scaling RI-CDD-MP2 formulation are only observed for very large systems.[33]

In this work, we aim to improve the RI-CDD-MP2 method by replacing the Coulomb metric used for the RI with an attenuated Coulomb metric.[46] Furthermore, we redesigned the RI-CDD-MP2 algorithm in order to optimally exploit the additional sparsity in the three-center integrals. In particular, we compute the Coulomb and exchange contributions to the MP2 energy separately using specialized algorithms for each contribution. For the exchange term, we present an efficient screening approach based on Schwarz estimates,[47] which is able to capture the exponential decay behavior of this contribution. The Coulomb contribution and the transformations of the three-center integrals from the AO basis to the basis of Cholesky-pseudo-MOs are accelerated with the natural blocking approach from Jung et al.[24,25] We also employ several upper bounds for the three-center integrals in order to reduce the number of elements in the naturally blocked integral tensors at an early stage during the transformations. In addition, an efficient transformation sequence for the three-center integrals is proposed, which involves an initial

transformation of the AO-three-center integrals with the Cholesky factor of the ground state density followed by a transformation from occupied Cholesky-MOs to occupied Cholesky-pseudo-MOs for every Laplace point. For the efficient computation of three-center integrals in the atomic orbital basis, a distance including screening based on the integral partition bounds from Thompson and Ochsenfeld[48] is used.

The new MP2 method is shown to scale subquadratically for sufficiently large and sparse systems and displays a small prefactor. Significant speed-ups compared to the RI-CDD-MP2 method are obtained for molecular systems of various sizes. The asymptotic scaling of the method is cubic; however, the cubic scaling steps have a small prefactor and are irrelevant for all molecules used in the present study, of which the largest system is a DNA strand with 16 AT base pairs, 1052 atoms, 11 230 basis functions, and 37 248 auxiliary functions. The new method therefore enables efficient MP2 and double-hybrid DFT calculations on large molecular systems.

2. THEORY

2.1. Review of AO-MP2 and RI-CDD-MP2. The MP2 energy of a closed-shell molecule can be obtained from the following expression:

$$E_{MP2} = -\sum_{ijab} \frac{(ia|jb)[2(ia|jb) - (ib|ja)]}{\epsilon_a + \epsilon_b - \epsilon_i - \epsilon_j} \qquad (1)$$

The indices $ijk...$ denote occupied MOs, and $abc...$ denote virtual MOs. ϵ values are the orbital energies. The denominator from eq 1 can be decoupled using a Laplace transformation.[44] In general, the Laplace transformation allows one to replace the fraction $\frac{1}{x}$ by an integral of an exponential function:

$$\frac{1}{x} = \int_0^\infty \exp(-xt)\,dt \approx \sum_\alpha \omega_\alpha \exp(-xt_\alpha) \qquad (2)$$

The integral from eq 2 can be approximated by numerical integration using quadrature points t_α and quadrature weights ω_α. In the case of the MP2 orbital energy denominator, only 5 to 8 Laplace points are usually sufficient to obtain errors on the order of a few μHartree.[44] The major benefit of applying the Laplace transformation to the MP2 energy denominator is the possibility to factorize the resulting exponential into product form:

$$E_{MP2} = -\sum_\alpha \omega_\alpha \sum_{ijab} e^{-t_\alpha \epsilon_a} e^{-t_\alpha \epsilon_b} e^{+t_\alpha \epsilon_i} e^{+t_\alpha \epsilon_j} (ia|jb)$$
$$\times [2(ia|jb) - (ib|ja)] \qquad (3)$$

Inserting the expansion of the MOs as a linear combination of atomic orbitals (LCAO) and subsequently summing over MO indices gives the energy expression of AO-MP2:[11]

$$E_{MP2}^{AO} = -\sum_\alpha \sum_{\mu\nu\lambda\sigma} \sum_{\mu'\nu'\lambda'\sigma'} \underline{P}_{\mu\mu'}^{(\alpha)} \overline{P}_{\nu\nu'}^{(\alpha)} \underline{P}_{\lambda\lambda'}^{(\alpha)} \overline{P}_{\sigma\sigma'}^{(\alpha)} (\mu\nu|\lambda\sigma)$$
$$\times [2(\mu'\nu'|\lambda'\sigma') - (\mu'\sigma'|\lambda'\nu')] \qquad (4)$$

where $\underline{\mathbf{P}}^{(\alpha)}$ and $\overline{\mathbf{P}}^{(\alpha)}$ denote the occupied and virtual pseudodensities, respectively. The pseudodensity matrices are defined as follows:

$$\underline{P}_{\mu\mu'}^{(\alpha)} = \sqrt[4]{\omega_\alpha} \sum_i C_{\mu i} e^{+\epsilon_i t_\alpha} C_{\mu' i} \tag{5}$$

$$\overline{P}_{\nu\nu'}^{(\alpha)} = \sqrt[4]{\omega_\alpha} \sum_a C_{\nu a} e^{-\epsilon_a t_\alpha} C_{\nu' a} \tag{6}$$

In the CDD-MP2 method,[28] the pseudodensity matrices are subjected to a Cholesky decomposition with complete pivoting:[49]

$$\underline{P}_{\mu\mu'}^{(\alpha)} = \sum_{\underline{i}} \underline{L}_{\mu\underline{i}}^{(\alpha)} \underline{L}_{\mu'\underline{i}}^{(\alpha)} \tag{7}$$

$$\overline{P}_{\nu\nu'}^{(\alpha)} = \sum_{\overline{a}} \overline{L}_{\nu\overline{a}}^{(\alpha)} \overline{L}_{\nu'\overline{a}}^{(\alpha)} \tag{8}$$

The obtained Cholesky factors are the expansion coefficients of occupied and virtual Cholesky-pseudo-MOs $\phi_{\underline{i}}^{(\alpha)}$ and $\phi_{\overline{a}}^{(\alpha)}$, respectively:

$$\phi_{\underline{i}}^{(\alpha)}(\mathbf{r}) = \sum_\mu \underline{L}_{\mu\underline{i}}^{(\alpha)} \chi_\mu(\mathbf{r}) \tag{9}$$

$$\phi_{\overline{a}}^{(\alpha)}(\mathbf{r}) = \sum_\nu \overline{L}_{\nu\overline{a}}^{(\alpha)} \chi_\nu(\mathbf{r}) \tag{10}$$

Inserting the Cholesky factors into eq 4 gives the energy expression for CDD-MP2:[33]

$$E_{\mathrm{MP2}}^{\mathrm{CDD}} = -\sum_\alpha \sum_{\underline{ij}\overline{ab}} (\underline{i}\overline{a}|\underline{j}\overline{b})^{(\alpha)} [2(\underline{i}\overline{a}|\underline{j}\overline{b})^{(\alpha)} - (\underline{i}\overline{b}|\underline{j}\overline{a})^{(\alpha)}] \tag{11}$$

where

$$(\underline{i}\overline{a}|\underline{j}\overline{b})^{(\alpha)} = \sum_{\mu\nu\lambda\sigma} \underline{L}_{\mu\underline{i}}^{(\alpha)} \overline{L}_{\nu\overline{a}}^{(\alpha)} \underline{L}_{\lambda\underline{j}}^{(\alpha)} \overline{L}_{\sigma\overline{b}}^{(\alpha)} (\mu\nu|\lambda\sigma) \tag{12}$$

In the RI-CDD-MP2 method,[33] the ERIs are in addition approximated by RI:[40]

$$(\underline{i}\overline{a}|\underline{j}\overline{b})^{(\alpha)} \approx \sum_{PQ} (\underline{i}\overline{a}|P)^{(\alpha)} [\mathbf{V}^{-1}]_{PQ} (Q|\underline{j}\overline{b})^{(\alpha)} \tag{13}$$

$$V_{PQ} = \iint \chi_P(\mathbf{r}_1) \frac{1}{r_{12}} \chi_Q(\mathbf{r}_2) \, d\mathbf{r}_1 d\mathbf{r}_2 \tag{14}$$

where the indices $PQ...$ denote auxiliary basis functions.

2.2. Calculation and Transformation of Three-Center Integrals.

In the new method presented in this work, RI with an erfc-attenuated Coulomb metric[25,46,50] is used for approximating the ERIs:

$$(\mu\nu|\lambda\sigma) \approx \sum_{PQ} (\mu\nu\vdots P) \tilde{C}_{PQ} (Q\vdots\lambda\sigma) \tag{15}$$

$$(\mu\nu\vdots P) = \iint \chi_\mu(\mathbf{r}_1) \chi_\nu(\mathbf{r}_1) \frac{\mathrm{erfc}(\omega r_{12})}{r_{12}} \chi_P(\mathbf{r}_2) \, d\mathbf{r}_1 d\mathbf{r}_2 \tag{16}$$

$$\tilde{C}_{PQ} = \sum_{RS} [\tilde{\mathbf{V}}^{-1}]_{PR} V_{RS} [\tilde{\mathbf{V}}^{-1}]_{SQ} \tag{17}$$

$$\tilde{V}_{PR} = \iint \chi_P(\mathbf{r}_1) \frac{\mathrm{erfc}(\omega r_{12})}{r_{12}} \chi_R(\mathbf{r}_2) \, d\mathbf{r}_1 d\mathbf{r}_2 \tag{18}$$

The erfc metric depends on the attenuation parameter ω and interpolates between the Coulomb metric and the overlap metric depending on the choice of ω. It was shown that the attenuated Coulomb metric with a value of 0.1 for ω provides comparable accuracy as the Coulomb metric without sacrificing useful sparsity in the three-center integrals.[51] Due to the central role of the local metric, we will in the following denote the new MP2 method as ω-RI-CDD-MP2. We want to stress that ω should not be viewed as an empirical parameter but as a threshold, because lowering ω allows one to systematically reduce the deviations from the Coulomb metric; an exact agreement with the Coulomb metric is obtained for ω equal to zero.

The computation of the three-center integrals from eq 16 would scale quadratically, if only the sparsity of $\mu\nu$-shell pairs is exploited. Due to the attenuation with the complementary error function, these integrals decay quickly with increasing bra-ket separation. We exploit this distance decay by using the rigorous distance-including screening based on integral partition bounds (IPB) from Thompson and Ochsenfeld;[48] by default, our implementation employs the approximate bound aIPB and neglects integrals below a threshold ϑ_{3c}. With aIPB screening, only an asymptotically linear-scaling number of three-center integrals in the AO basis needs to be computed.

The three-center integrals in the atomic orbital basis need to be transformed to the basis of Cholesky-pseudo-MOs for each Laplace point. This could be done by applying the transformations shown in eqs 19 and 20:

$$(\underline{i}\nu\vdots P)^{(\alpha)} = \sum_\mu \underline{L}_{\mu\underline{i}}^{(\alpha)} (\mu\nu\vdots P) \tag{19}$$

$$(\underline{i}\overline{a}\vdots P)^{(\alpha)} = \sum_\nu \overline{L}_{\nu\overline{a}}^{(\alpha)} (\underline{i}\nu\vdots P)^{(\alpha)} \tag{20}$$

A more efficient way to obtain the transformed integrals involves the Cholesky factors of the ground state density matrix $\mathbf{P}$:

$$P_{\mu\nu} = \sum_i L_{\mu i} L_{\nu i} \tag{21}$$

Using $\mathbf{L}$, the transformation from eq 19 can be replaced by a succession of two transformations:

$$(i\nu\vdots P) = \sum_\mu L_{\mu i} (\mu\nu\vdots P) \tag{22}$$

$$(\underline{i}\nu\vdots P)^{(\alpha)} = \sum_i T_{\underline{i}i}^{(\alpha)} (i\nu\vdots P) \tag{23}$$

The matrix $\mathbf{T}^{(\alpha)}$ employed in eq 23 transforms the occupied Cholesky-MOs to occupied Cholesky-pseudo-MOs. It can be derived by considering the following identity for the pseudodensity matrix $\underline{\mathbf{P}}^{(\alpha)}$:[52]

$$\underline{\mathbf{P}}^{(\alpha)} = \underline{\mathbf{P}}^{(\alpha)} \mathbf{SP} = \mathbf{PS}\underline{\mathbf{P}}^{(\alpha)} \mathbf{SP} \tag{24}$$

Equation 24 is closely related to the well-known idempotency condition for the density matrix:[53]

$$\mathbf{P} = \mathbf{PSP} = \mathbf{PSPSP} \tag{25}$$

After inserting the Cholesky factors of the occupied density matrix and the occupied pseudodensity matrix into eq 24, one can identify the sought transformation matrix as the product $\underline{\mathbf{L}}^{T(\alpha)} \mathbf{SL}$:

$$\underline{\mathbf{P}}^{(\alpha)} = \underline{\mathbf{L}}^{(\alpha)} \underline{\mathbf{L}}^{T(\alpha)} = \mathbf{L} \underbrace{\mathbf{L}^T \mathbf{S} \underline{\mathbf{L}}^{(\alpha)}}_{\mathbf{T}^{T(\alpha)}} \underbrace{\underline{\mathbf{L}}^{T(\alpha)} \mathbf{SL}}_{\mathbf{T}^{(\alpha)}} \mathbf{L}^T \tag{26}$$
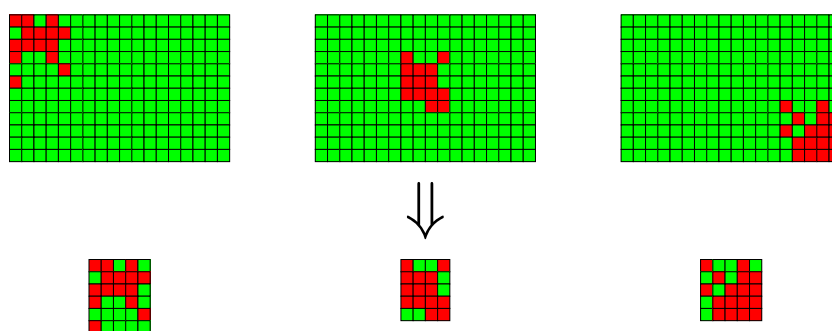
Figure 1. Illustration of the natural blocking format. A third-order tensor is stored as an array of matrices (top row). Red cells correspond to significant entries, while green cells correspond to insignificant entries. When natural blocking is applied, all columns and rows containing only insignificant entries are deleted (bottom row).

Thus, the elements of $\mathbf{T}^{(\alpha)}$ are given by

$$T_{\underline{i}\,\underline{i}}^{(\alpha)} = (\underline{\mathbf{L}}^{T(\alpha)}\mathbf{S}\mathbf{L})_{\underline{i}\,\underline{i}} \tag{27}$$

The advantage of the presented transformation sequence is that eq 23 requires only a sum over occupied MOs instead of a sum over AOs as in eq 19. Due to the smaller number of occupied MOs, eq 23 is thus less computationally costly to evaluate, especially for extended basis sets. The additional transformation shown in eq 22 is also less expensive than the transformation in eq 19, because it has to be carried out only once and not for every Laplace point.

In order to reduce the scaling of the integral transformations, we employ the natural blocking approach from Jung et al.,[24,25] which provides a sparse data format for the three-center integrals. In general, a third-order tensor is often represented as a one-dimensional array of matrices; we will in the following denote these matrices as "slices" of the tensor. The index that labels the one-dimensional matrix array will be called the "slow index". One way to exploit sparsity in a third-order tensor would be to use a block-sparse data format for each slice. In contrast, in the natural blocking approach, entire rows and columns of the slices are deleted if they contain only insignificant values below a given threshold.[24,25] This is illustrated in Figure 1. The threshold used for deleting rows and columns will be called the "natural blocking threshold" ϑ_{NB}. Following Jung et al.,[25] we employ a separate threshold $\vartheta_{\mathrm{NB}}^{iaP}$ for the fully transformed $(\underline{i}\,\overline{a}\vdots P)^{(\alpha)}$ integrals. The advantage of natural blocking is that each slice remains a single, relatively large matrix after deleting rows and columns; in a block-sparse approach, in contrast, the slice is divided up into a large number of small blocks. As the relative efficiency of common matrix multiplications implementations is in general higher for larger matrices, a smaller computational overhead in multiplications involving the slices can be obtained with natural blocking. In order to efficiently exploit sparsity in the natural blocking format, it is important that the third-order tensor has a suitable sparsity pattern. In particular, for each value of the slow index, only $O(1)$ rows and columns should be significant. For the three-center integrals with a local RI metric, this is fulfilled for both the atomic orbital basis and a basis of localized MOs, because all three indices couple only over short distances. In cases where the slices still have significant sparsity after row and column deletion, one might consider to also use a block-sparse matrix format for these slices; however, we have not exploited this so far.

As a specific example for the application of natural blocking, consider the $(P\vdots\mu\nu)$ integrals. If the integrals are ordered such that P is the slow index, each value of P is associated with an $N_{\mathrm{AO}} \times N_{\mathrm{AO}}$ slice, where N_{AO} denotes the number of AOs. In a large molecule, the $(P\vdots\mu\nu)$ integrals will only have significant values, if both χ_μ and χ_ν are spatially close to χ_P. Therefore, many elements of the $\mu\nu$ slice will be insignificant; in particular, many rows and columns will contain only negligible elements. By deleting these, the size of the slice can be reduced to $N_{\mathrm{AO}(P)} \times N_{\mathrm{AO}(P)}$, where $N_{\mathrm{AO}(P)}$ is the number of significant AOs for the given P. For bookkeeping purposes, it is important to store the indices of all significant rows (and columns) for a particular P in a list $\{\mu\}_P$. More precisely, the list $\{\mu\}_P$ can be build according to

$$\{\mu\}_P \equiv \{\mu | \max_\nu |(P\vdots\mu\nu)| > \vartheta_{\mathrm{NB}}\} \tag{28}$$

One situation, in which this list is needed, is the following transformation:

$$(P\vdots i\nu) = \sum_\mu L_{i\mu}(P\vdots\mu\nu) \tag{29}$$

This transformation is carried out with matrix multiplications of the $\mu\nu$ slices with the coefficient matrix $\mathbf{L}$. Before the multiplication of one particular $\mu\nu$ slice with the matrix $\mathbf{L}$ can be performed, all columns in $\mathbf{L}$, whose index μ is not in the list $\{\mu\}_P$, need to be deleted. This reduces the size of $\mathbf{L}$ to $N_{\mathrm{occ}} \times N_{\mathrm{AO}(P)}$. Due to the reduction of the dimensions of the involved matrices, the multiplication can be accelerated significantly. This illustrates how computational savings can be realized with natural blocking.

In an analogous manner to $\{\mu\}_P$, several other lists of significant orbital combinations are constructed and used during the integral transformations. An overview of them is shown in Table 1. The information about the significance of orbital pairs can also be used to create "inverted" lists; the list $\{\underline{i}\}_{\overline{a}}^{(\alpha)}$, e.g., can be obtained by "inversion" of $\{\overline{a}\}_{\underline{i}}^{(\alpha)}$. Furthermore, the letters used in our notation are interchangeable as long as they refer to the same type of orbital; the list $\{\overline{a}\}_{\underline{i}}^{(\alpha)}$, e.g., is the same as $\{\overline{b}\}_{\underline{i}}^{(\alpha)}$.

In contrast to Jung et al.,[24,25] we also employ several rigorous upper bounds for the three-center integrals. Using these, we can exploit sparsity at an earlier stage during the sequence of integral transformation. We also build sparse lists based on the integral bounds, for which we will use a slightly different notation with square brackets such as $[\overline{a}]_{\underline{i}}^{(\alpha)}$. For

Table 1. Overview of All Employed Lists of Significant Orbital Combinations, Which Are Used for Natural Blocking[a]

list of orbital pairs	integral tensor
$\{\overline{a}\}_{\underline{i}}^{(\alpha)}$	$(\underline{i}\,\overline{a}{:}P)^{(\alpha)}$
$\{i\}_P$	$(P{:}i\nu)$
$\{\nu\}_P$	$(P{:}\mu\nu)$
$\{\underline{i}\}_P^{(\alpha)}$	$(P{:}\underline{i}\,\overline{a})^{(\alpha)}$
$\{\overline{a}\}_P^{(\alpha)}$	$(P{:}\underline{i}\,\overline{a})^{(\alpha)}$

[a]The lists are generated by inspecting entries of the corresponding integral tensors shown in the right column in analogy to eq 28. The indices of the integral tensors are sorted such that the leftmost index is the "slow index".

computing the upper bounds, the matrices $\mathbf{M}$ and $\mathbf{N}$ defined in eqs 30 and 31 are needed:

$$M_{\mu\nu} = \max_P |(\mu\nu{:}P)| \tag{30}$$

$$N_{\mu P} = \max_\nu |(\mu\nu{:}P)| \tag{31}$$

The entries of $\mathbf{M}$ and $\mathbf{N}$ are accumulated during the computation of the three-center integrals in the AO basis. Using these matrices, upper bounds for the transformed integrals can be obtained by multiplication with the absolute value of the MO or pseudo-MO coefficients. One example is shown in eq 32:

$$|(i\nu{:}P)| \le N_{iP} = \sum_\mu |L_{\mu i}| N_{\mu P} \tag{32}$$

The values N_{iP} of the transformed $\mathbf{N}$ matrix can then be used to construct the list $[i]_P$:

$$[i]_P \equiv \{i | N_{iP} > \vartheta_{\mathrm{NB}}\} \tag{33}$$

All employed lists based on upper bounds are shown in Table 2.

Table 2. Lists of Significant Orbital Pairs, Which Are Generated by Using Upper Bounds for the Three-Center Integrals

list of orbital pairs	upper bound
$[i]_P$	$N_{iP} = \sum\limits_\mu |L_{\mu i}| N_{\mu P} \ge |(i\nu{:}P)|$
$[\underline{i}]_P^{(\alpha)}$	$N_{\underline{i}P} = \sum\limits_\mu |\underline{L}_{\mu\underline{i}}^{(\alpha)}| N_{\mu P} \ge |(\underline{i}\nu{:}P)^{(\alpha)}|$
$[\overline{a}]_P^{(\alpha)}$	$N_{\overline{a}P} = \sum\limits_\mu |\overline{L}_{\mu\overline{a}}^{(\alpha)}| N_{\mu P} \ge |(\overline{a}\nu{:}P)^{(\alpha)}|$
$[\overline{a}]_{\underline{i}}^{(\alpha)}$	$M_{\underline{i}\,\overline{a}} = \sum\limits_{\mu\nu} |\underline{L}_{\mu\underline{i}}^{(\alpha)}| M_{\mu\nu} |\overline{L}_{\nu\overline{a}}^{(\alpha)}| \ge |(\underline{i}\,\overline{a}{:}P)^{(\alpha)}|$

With the sparse lists from Tables 1 and 2, the integral transformations can be carried out with a linear-scaling computational effort. The full algorithm for the transformations is shown in Figure 2. During the transformations, the integrals are ordered such that the auxiliary index P is the slow index. This allows one to perform all transformations as multiplications of the slices and the coefficient matrices $\mathbf{L}$, $\mathbf{T}^{(\alpha)}$, and $\overline{\mathbf{L}}^{(\alpha)}$. After the transformations, the integrals are reordered such that $\underline{i}$ becomes the slow index; this ordering is more convenient for the computation of the energy.

```
for all P do
    build {ν}_P and [i]_P lists
    for all i ∈ [i]_P and ν ∈ {ν}_P do
        (P:iν) =  Σ   L_μi (P:μν)
               μ∈{μ}_P
    end for
    build {i}_P list
end for

for all α do
    build [i]_P^(α) and [a]_P^(α) lists
    for all P do
        for all i ∈ [i]_P^(α) and ν ∈ {ν}_P do
            (P:iν)^(α) =   Σ    T_ii^(α) (P:iν)
                       i∈{i}_P^(α)
        end for

        for all i ∈ [i]_P^(α) and a ∈ [a]_P^(α) do
            (P:ia)^(α) =   Σ    L_νa^(α) (P:iν)^(α)
                        ν∈{ν}_P
        end for
        build {i}_P^(α) and {a}_P^(α) lists
    end for
    reorder integrals: (P:ia)^(α) → (ia:P)^(α)
    build {a}_i^(α) list
    compute energy contribution (see Figures 3 and 4)
end for
```

Figure 2. Algorithm for the transformation of the three-center integrals. The leftmost index in the three-center integrals is the "slow index".

2.3. Computation of the MP2 Coulomb Energy. In contrast to the implementation of RI-CDD-MP2 of Maurer et al.,[33] our new implementation treats the Coulomb and exchange contributions to the MP2 energy separately using specialized algorithms. As we will show, this is particularly beneficial in combination with a local RI metric. A separate treatment of Coulomb and exchange contributions has already been proposed in related work by Beuerle et al.[54] for low-scaling beyond-RPA methods and by Helmich-Paris et al.[55] for relativistic RI-CDD-MP2; in both works, also, a local RI metric was employed.

For the Coulomb contribution

$$E_{\mathrm{MP2}}^{\mathrm{C}} = \sum_\alpha E_{\mathrm{MP2}}^{\mathrm{C},(\alpha)} = -2 \sum_\alpha \sum_{\underline{ij}\,\overline{ab}} (\underline{i}\,\overline{a}|\underline{j}\,\overline{b})^{(\alpha)} (\underline{i}\,\overline{a}|\underline{j}\,\overline{b})^{(\alpha)} \tag{34}$$

a matrix $\mathbf{Z}^{(\alpha)}$ is computed by contracting three-center integrals over the pseudo-MO indices:

$$Z_{PQ}^{(\alpha)} = \sum_{\underline{i}\,\overline{a}} (\underline{i}\,\overline{a}{:}P)^{(\alpha)} (\underline{i}\,\overline{a}{:}Q)^{(\alpha)} \tag{35}$$

Next, $\mathbf{Z}^{(\alpha)}$ is multiplied with the matrix $\tilde{\mathbf{C}}$ defined in eq 17:

$$D_{PQ}^{(\alpha)} = \sum_R Z_{PR}^{(\alpha)} \tilde{C}_{RQ} \tag{36}$$

From $\mathbf{D}^{(\alpha)}$, the contribution of the current Laplace point α to the MP2 Coulomb energy can be computed via the following equation:

$$E_{\mathrm{MP2}}^{\mathrm{C},(\alpha)} = -2 \sum_{PQ} D_{PQ}^{(\alpha)} D_{QP}^{(\alpha)} \tag{37}$$

The contraction in eq 35 has the highest formal scaling (N^4), which is nevertheless lower than the formal scaling of the MP2

exchange (N^5). The use of natural blocking allows one to exploit both the sparsity of the $\underline{i}\,\overline{a}$-charge densities and the sparsity resulting from the local metric as shown in the algorithm in Figure 3. Thus, eq 35 can be evaluated with

$\mathbf{Z}^{(\alpha)} = 0$

for all $\underline{i}$ **do**
    for all $P \in \{P\}_{\underline{i}}^{(\alpha)}$ and $Q \in \{Q\}_{\underline{i}}^{(\alpha)}$ **do**
        $Z_{PQ}^{(\alpha)} \mathrel{+}= \displaystyle\sum_{\overline{a} \in \{\overline{a}\}_{\underline{i}}^{(\alpha)}} (\underline{i}\,\overline{a} \mathbin{:} P)^{(\alpha)} (\underline{i}\,\overline{a} \mathbin{:} Q)^{(\alpha)}$
    end for
end for

for all P and Q **do**
    $D_{PQ}^{(\alpha)} = \displaystyle\sum_{R} Z_{PR}^{(\alpha)} \tilde{C}_{RQ}$
end for

$E_{\text{MP2}}^{\text{C},(\alpha)} = -2 \displaystyle\sum_{PQ} D_{PQ}^{(\alpha)} D_{QP}^{(\alpha)}$

Figure 3. Algorithm for the computation of the Coulomb contribution to the ω-RI-CDD-MP2 energy.

asymptotically linear scaling. Note that the presented algorithm would be suboptimal in combination with a Coulomb metric as used in the original RI-CDD-MP2 method, because the asymptotic scaling of eq 35 would be cubic with a relatively large prefactor.

The matrix multiplication in eq 36 scales cubically with small prefactor; note that the scaling could be reduced to quadratic by exploiting the sparsity of $\mathbf{Z}^{(\alpha)}$. Since $\mathbf{D}^{(\alpha)}$ is a dense matrix, eq 37 is a low-prefactor quadratic scaling step.

2.4. Computation of the MP2 Exchange Energy. The algorithm used to evaluate the exchange contribution to the ω-RI-CDD-MP2 energy is shown in Figure 4. In this algorithm, the exchange energy contributions from individual $\underline{ij}$ pairs are computed according to

$$E_{\text{MP2}}^{\text{X},(\alpha),\underline{ij}} = \sum_{\overline{a}\overline{b}} (\underline{i}\,\overline{a}|\underline{j}\,\overline{b})^{(\alpha)} (\underline{i}\,\overline{b}|\underline{j}\,\overline{a})^{(\alpha)} \tag{38}$$

and summed up to obtain the total exchange energy $E_{\text{MP2}}^{\text{X}}$:

$$E_{\text{MP2}}^{\text{X}} = \sum_{\alpha} E_{\text{MP2}}^{\text{X},(\alpha)} = \sum_{\alpha} \sum_{\underline{ij}} E_{\text{MP2}}^{\text{X},(\alpha),\underline{ij}} \tag{39}$$

For each $\underline{ij}$ pair, only a subset of virtual pseudo-MOs is included in the sum of eq 38. The significant virtual pseudo-MOs are selected by Schwarz screening. The Schwarz upper bound for an individual four-center integral is given by

$$|(\underline{i}\,\overline{a}|\underline{j}\,\overline{b})^{(\alpha)}| \leq Q_{\underline{i}\,\overline{a}}^{(\alpha)} Q_{\underline{j}\,\overline{b}}^{(\alpha)} \tag{40}$$

where the Schwarz factors are defined as follows:

$$Q_{\underline{i}\,\overline{a}}^{(\alpha)} = \sqrt{(\underline{i}\,\overline{a}|\underline{i}\,\overline{a})^{(\alpha)}} \tag{41}$$

The Schwarz factors are computed on the fly during the algorithm for the MP2 exchange (see Figure 4) using the RI approximation:

$$Q_{\underline{i}\,\overline{a}}^{(\alpha)} \approx \sqrt{\sum_{PQ} (\underline{i}\,\overline{a} \mathbin{:} P)^{(\alpha)} \tilde{C}_{PQ} (Q \mathbin{:} \underline{i}\,\overline{a})^{(\alpha)}} \tag{42}$$

The Schwarz estimates for the integral products appearing in the MP2 exchange are given by

for all $\underline{i}$ **do**
    for all $\overline{a} \in \{\overline{a}\}_{\underline{i}}^{(\alpha)}$ and $Q \in (Q)_{\underline{i}}^{(\alpha)}$ **do**
        $\tilde{B}_{\underline{i}\,\overline{a}}^{Q(\alpha)} = \displaystyle\sum_{P \in \{P\}_{\underline{i}}^{(\alpha)}} (\underline{i}\,\overline{a} \mathbin{:} P)^{(\alpha)} \tilde{C}_{PQ}$
    end for

    for all $\overline{a} \in \{\overline{a}\}_{\underline{i}}^{(\alpha)}$ and $\overline{b} \in \{\overline{b}\}_{\underline{i}}^{(\alpha)}$ **do**
        $(\underline{i}\,\overline{a}|\underline{i}\,\overline{b})^{(\alpha)} = \displaystyle\sum_{Q \in (Q)_{\underline{i}}^{(\alpha)} \cap \{Q\}_{\underline{i}}^{(\alpha)}} \tilde{B}_{\underline{i}\,\overline{a}}^{Q(\alpha)} (Q \mathbin{:} \underline{i}\,\overline{b})^{(\alpha)}$
    end for
    $E_{\text{MP2}}^{\text{X},(\alpha),\underline{ii}} = \displaystyle\sum_{\overline{a} \in \{\overline{a}\}_{\underline{i}}^{(\alpha)}} \sum_{\overline{b} \in \{\overline{b}\}_{\underline{i}}^{(\alpha)}} (\underline{i}\,\overline{a}|\underline{i}\,\overline{b})^{(\alpha)} (\underline{i}\,\overline{b}|\underline{i}\,\overline{a})^{(\alpha)}$

    for all $\overline{a} \in \{\overline{a}\}_{\underline{i}}^{(\alpha)}$ **do**
        $Q_{\underline{i}\,\overline{a}}^{(\alpha)} = \sqrt{(\underline{i}\,\overline{a}|\underline{i}\,\overline{a})^{(\alpha)}}$
    end for

    $\underline{ij}$-prescreening (see eqs 44 to 46)
    for all significant $\underline{j} < \underline{i}$ **do**
        $E_{\text{MP2}}^{\text{X},(\alpha),\underline{ij}} = 0$
        determine significant $\overline{a}$ and $\overline{b}$ by
            Schwarz screening (see eq 43)
        for all significant $\overline{a}$ and $\overline{b}$ **do**
            $(\underline{i}\,\overline{a}|\underline{j}\,\overline{b})^{(\alpha)} = \displaystyle\sum_{Q \in (Q)_{\underline{i}}^{(\alpha)} \cap \{Q\}_{\underline{j}}^{(\alpha)}} \tilde{B}_{\underline{i}\,\overline{a}}^{Q(\alpha)} (Q \mathbin{:} \underline{j}\,\overline{b})^{(\alpha)}$
            $E_{\text{MP2}}^{\text{X},(\alpha),\underline{ij}} \mathrel{+}= \displaystyle\sum_{\overline{a}\overline{b}} (\underline{i}\,\overline{a}|\underline{j}\,\overline{b})^{(\alpha)} (\underline{i}\,\overline{b}|\underline{j}\,\overline{a})^{(\alpha)}$
        end for
        $E_{\text{MP2}}^{\text{X},(\alpha),\underline{ji}} = E_{\text{MP2}}^{\text{X},(\alpha),\underline{ij}}$
    end for
    $E_{\text{MP2}}^{\text{X},(\alpha)} = \displaystyle\sum_{\underline{ij}} E_{\text{MP2}}^{\text{X},(\alpha),\underline{ij}}$
end for

Figure 4. Algorithm for the computation of the exchange energy contribution.

$$|(\underline{i}\,\overline{a}|\underline{j}\,\overline{b})^{(\alpha)}(\underline{i}\,\overline{b}|\underline{j}\,\overline{a})^{(\alpha)}| \leq Q_{\underline{i}\,\overline{a}}^{(\alpha)} Q_{\underline{j}\,\overline{b}}^{(\alpha)} Q_{\underline{i}\,\overline{b}}^{(\alpha)} Q_{\underline{j}\,\overline{a}}^{(\alpha)} \tag{43}$$

Due to the structure of the MP2 exchange, the right-hand side of eq 43 not only provides a rigorous upper bound to the exchange energy contribution but also captures correctly its exponential decay behavior. We therefore use the product of Schwarz factors from eq 43 to screen virtual pseudo-MOs for a given $\underline{ij}$ pair and to neglect integrals below a threshold denoted as $\vartheta_{\text{schwarz}}$. With this screening, only an asymptotically linear-scaling number of four-center integrals needs to be computed.

For a given $\underline{ij}$ pair, only the virtual pseudo-MOs in $\{\overline{a}\}_{\underline{j}}^{(\alpha)}$ are considered in the screening. In order to further reduce the screening overhead, significant $\underline{ij}$ pairs are selected in a prescreening procedure, which is also based on Schwarz estimates. The exchange energy contribution from an $\underline{ij}$ pair given by eq 38 can be rigorously bound by the expression on the right-hand side of the following equation:

$$|E_{\text{MP2}}^{\text{X},(\alpha),\underline{ij}}| \leq \sum_{\overline{a}\overline{b}} Q_{\underline{i}\,\overline{a}}^{(\alpha)} Q_{\underline{j}\,\overline{b}}^{(\alpha)} Q_{\underline{i}\,\overline{b}}^{(\alpha)} Q_{\underline{j}\,\overline{a}}^{(\alpha)} \tag{44}$$

This upper bound does in general not provide an accurate *quantitative* estimate of the $\underline{ij}$ pair energy, because all contributions on the right-hand side of eq 44 are positive in contrast to the right-hand side of eq 38, where positive and negative contributions to the sum can cancel. Nevertheless, it is useful as a *qualitative* measure for the importance of an $\underline{ij}$ pair.

Table 3. Mean Absolute Deviations (MAD), Maximum Absolute Deviations (MAX), and Root Mean Square Deviation (RMSD) Compared to Canonical RI-MP2 in ω-RI-CDD-MP2 Calculations on the L7 Test Set[64] with Different Values for the Attenuation Parameter ω[a]

	Δ_{abs}			Δ_{int}		
ω	MAD	RMSD	MAX	MAD	RMDS	MAX
0.50	1.48×10^{-0}	1.83×10^{-0}	3.83×10^{-0}	4.70×10^{-1}	6.59×10^{-1}	1.18×10^{-0}
0.20	2.70×10^{-1}	3.52×10^{-1}	8.19×10^{-1}	1.57×10^{-1}	2.18×10^{-1}	3.77×10^{-1}
0.10	4.06×10^{-2}	5.73×10^{-2}	1.49×10^{-1}	3.77×10^{-2}	5.09×10^{-2}	8.39×10^{-2}
0.05	4.95×10^{-3}	7.47×10^{-3}	2.04×10^{-2}	5.73×10^{-3}	7.56×10^{-3}	1.22×10^{-2}
0.01	3.54×10^{-5}	4.95×10^{-5}	1.41×10^{-4}	4.49×10^{-5}	4.82×10^{-5}	7.61×10^{-5}
0.00	9.23×10^{-7}	1.53×10^{-6}	4.52×10^{-6}	1.89×10^{-6}	2.79×10^{-6}	5.36×10^{-6}

[a]For the octadecane monomers and dimer, 7 Laplace points were used; 10 Laplace points were used for all other systems. All screening and natural blocking thresholds were set to zero. Δ_{abs} denotes the error in absolute energies of monomers and dimers; equivalent monomers were only considered once. Δ_{int} denotes the error in interaction energies. All values are given in kcal/mol. The remaining errors for $\omega = 0.00$ arise from the Laplace transformation.

The expression from eq 44 can be implemented very efficiently by first performing a matrix multiplication of the matrix of Schwarz integrals with its transpose:

$$A_{\underline{i}\underline{j}}^{(\alpha)} = \sum_{\bar{a} \in \{\bar{a}\}_{\underline{i}}^{(\alpha)}} Q_{\underline{i}\bar{a}}^{(\alpha)} Q_{\bar{a}\underline{j}}^{(\alpha)} \tag{45}$$

Then, the squares of the entries of $\mathbf{A}^{(\alpha)}$ can be used to screen $\underline{i}\underline{j}$ pairs:

$$|E_{\text{MP2}}^{\text{X},(\alpha),\underline{i}\underline{j}}| \leq A_{\underline{i}\underline{j}}^{(\alpha)2} \tag{46}$$

An $\underline{i}\underline{j}$ pair is neglected, if the right-hand side of eq 46 is smaller than a threshold denoted as ϑij.

For all $\underline{i}\underline{j}\bar{a}\bar{b}$ combinations that are significant according to the presented screening approach, four-center integrals are built in two steps. In the first step, a third-order tensor $\tilde{B}^{(\alpha)}$ is computed by transforming the auxiliary index of the three-center integrals with the matrix $\tilde{\mathbf{C}}$ defined in eq 17:

$$\tilde{B}_{\underline{i}\bar{a}}^{Q,(\alpha)} = \sum_P (\underline{i}\bar{a}{:}P)^{(\alpha)} \tilde{C}_{PQ} \tag{47}$$

In the second step, the $\tilde{B}^{(\alpha)}$ tensor is contracted with three-center integrals over the auxiliary index:

$$(\underline{i}\bar{a}|\underline{j}\bar{b})^{(\alpha)} = \sum_Q \tilde{B}_{\underline{i}\bar{a}}^{Q,(\alpha)} (Q{:}\underline{j}\bar{b})^{(\alpha)} \tag{48}$$

Even though the number of four-center integrals that needs to be formed scales linearly, both steps from eqs 47 and 48 would scale quadratically, if implemented naïvely. The reason for this is the quadratic scaling number of significant elements in the $\tilde{B}^{(\alpha)}$ tensor. This can be explained from eq 47, where the indices $\underline{i}$ and P are coupled only over short distances due to the erfc metric; $\underline{i}$ and Q, in contrast, couple over large distances, because the matrix $\tilde{\mathbf{C}}$ is densely populated. It turns out, however, that the index Q in eqs 47 and 48 can be restricted to a subset of the space of auxiliary functions. In order to realize this, consider the MP2 exchange energy expression with the RI plugged in:

$$E_{\text{MP2}}^{\text{X},(\alpha)} = \sum_{\underline{i}\bar{a}\underline{j}\bar{b}} \sum_{PQRS} (\underline{i}\bar{a}{:}P)^{(\alpha)} \tilde{C}_{PQ} (Q{:}\underline{j}\bar{b})^{(\alpha)} (\underline{i}\bar{b}{:}R)^{(\alpha)} \tilde{C}_{RS} \\ (S{:}\underline{j}\bar{a})^{(\alpha)} \tag{49}$$

The coupling of $\underline{i}$ to both $\bar{a}$ and $\bar{b}$ decays exponentially because of the appearing $\underline{i}\bar{a}$- and $\underline{i}\bar{b}$-charge densities. $\bar{a}$ and $\bar{b}$ also

appear next to the index $\underline{j}$ on the ket-side of the four-center integrals, where they are coupled to Q and S by the short-ranged erfc-function. By combining these couplings, one can restrict the space of auxiliary functions χ_Q and χ_S that need to be included for a given $\underline{i}$. For a particular $\underline{i}$, a list $(Q)_{\underline{i}}^{(\alpha)}$ is constructed from the union of auxiliary function indices Q in all lists $\{Q\}_{\bar{a}}^{(\alpha)}$ for all $\bar{a}$ in $\{\bar{a}\}_{\underline{i}}^{(\alpha)}$. For readers familiar with the sparse-map formalism of Pinski et al.,[34] it shall be mentioned that this would correspond to a "chaining operation" of the lists $\{\bar{a}\}_{\underline{i}}^{(\alpha)}$ and $\{Q\}_{\bar{a}}^{(\alpha)}$. With these restrictions for the index Q, eqs 47 and 48 can be evaluated with an asymptotically linear-scaling computational effort.

3. COMPUTATIONAL DETAILS

The described method was implemented in a development version of the quantum chemistry program FermiONs++.[56−58] Unless stated explicitly, the def2-SVP basis set[59] was used in combination with the corresponding auxiliary basis set.[60] Shell pairs with an overlap of less than 10^{-12} are omitted from the calculation. An integral screening threshold of 10^{-10} is used during the SCF. The DIIS method[61] is employed for accelerating SCF convergence. The SCF energy is converged to 10^{-7} and the norm of the commutator ($\mathbf{FPS-SPF}$), where $\mathbf{F}$ is the Fock matrix and $\mathbf{S}$ is the overlap matrix, to 10^{-6}. Unless mentioned explicitly, five Laplace quadrature points are used. The Laplace points are determined using a minimax algorithm as described in ref 62; the number of integration points is reduced automatically in our implementation if the fitting interval is small, and no improved accuracy can be obtained with more integration points. In the calculation of pseudodensity matrices, Fermi-shifting as proposed by Ayala and Scuseria is applied.[15] The pseudodensity matrices are orthogonalized prior to the pivoted Cholesky decomposition as described in ref 51; afterward, the orthogonalization is reverted. The frozen-core approximation is employed in all calculations. For comparison, calculations are carried out with the RI-CDD-MP2 method[33] in the standard formulation, which scales cubically in the asymptotic limit, and with the implementation of canonical RI-MP2 in FermiONs++. All timings were performed using 20 threads on dual-processor Intel Xeon CPU E5-2630 v4 @ 2.20 GHz machines with 256 GB RAM and a solid-state drive (SSD) with a capacity of 1.7 TB.

Table 4. Benchmark Calculations for the aIPB Screening Threshold (ϑ_{3c}) and the Schwarz Screening Threshold ($\vartheta_{schwarz}$)[a]

ϑ_{3c}				$\vartheta_{schwarz}$			
value	MAD	RMSD	MAX	value	MAD	RMSD	MAX
10^{-5}	3.58×10^{-1}	1.16×10^{-0}	3.85×10^{-0}	10^{-8}	1.08×10^{-0}	1.51×10^{-0}	3.28×10^{-0}
10^{-6}	1.18×10^{-4}	1.99×10^{-4}	4.73×10^{-4}	10^{-9}	8.62×10^{-2}	1.09×10^{-1}	2.51×10^{-1}
10^{-7}	1.18×10^{-5}	2.43×10^{-5}	7.29×10^{-5}	10^{-10}	6.68×10^{-3}	7.86×10^{-3}	1.61×10^{-2}
10^{-8}	1.36×10^{-6}	2.42×10^{-6}	6.58×10^{-6}	10^{-11}	5.29×10^{-4}	6.06×10^{-4}	1.01×10^{-3}

[a]Mean absolute deviations (MAD), maximum absolute deviations (MAX), and root mean square deviation (RMSD) on the test set from Table 7 are shown. The reference energies were computed using ω-RI-CDD-MP2 without integral screening and natural blocking. 7 Laplace points are used for $[S_8]_5$; 8 Laplace points were used in all other calculations. All values are given in kcal/mol.

4. RESULTS

4.1. Accuracy of the Introduced Approximations.
Among the used approximations, we first consider the Laplace transformation of the MP2 denominator. This approximation has been used extensively, and numerous benchmarks on its accuracy exist;[11,15,44,45,62,63] in most cases, 5−8 Laplace points are sufficient in order to reach μHartree accuracy. As the Laplace transformation for MP2 is a well-established approximation, we did not analyze it further.

Next, we focus on the error introduced by the erfc-attenuated Coulomb metric. The accuracy of this approximation has been studied in detail for SOS-MP2,[25] direct RPA,[51] and full MP2 on small molecules.[46] In order to analyze the influence of the local metric on the accuracy of full MP2 including exchange on larger systems, we compare calculations with ω-RI-CDD-MP2 to canonical RI-MP2 with the standard Coulomb metric. The calculations were performed on the L7 test set,[64] and the results are shown in Table 3. When ω approaches zero, the deviations from the values computed with the Coulomb metric quickly decrease for both absolute energies and interaction energies. For $\omega = 0.1$, mean absolute deviations well below 0.1 kcal/mol are obtained. This is in line with the findings reported by Luenser et al.,[51] who showed that a value of 0.1 enables highly accurate direct RPA calculations. We thus set ω to 0.1 in all ω-RI-CDD-MP2 calculations shown in the following.

The remaining parameters were determined by carrying out benchmark calculations on a set of 11 molecules from the integral screening test set from ref 65. The used molecules all have between 40 and 146 atoms; the average number of atoms amounts to 98. Only the parameter of interest was varied in these calculations, while the others were set to zero, in order to isolate the effect of each parameter. Correlation energies computed with ω-RI-CDD-MP2 without integral screening and without natural blocking are used as references, which excludes the Laplace transformation and the RI as potential sources of error. The influence of the employed integral screening thresholds on the accuracy is analyzed in Tables 4 and 5. For each screening, the accuracy can be improved systematically by lowering the threshold. Suitable values for accurate calculations on large molecules were determined to be 10^{-6} for the aIPB threshold, 10^{-9} for the Schwarz screening threshold, and 10^{-6} for the ij prescreening threshold, respectively, as they lead to mean errors below 0.1 kcal/mol.

In Table 6, the errors introduced by natural blocking are displayed. Thresholds of $\vartheta_{NB} = 10^{-6}$ and $\vartheta_{NB}^{iaP} = 5.0 \times 10^{-6}$ are sufficient to obtain mean errors below 0.1 kcal/mol and are thus employed in all calculations with def2-SVP basis shown in the following. The same set of values has also been used by Jung et al.[25] For ϑ_{NB}, a significant decrease in accuracy can be

Table 5. Benchmark Calculations for the Threshold for Prescreening ij pairs (ϑij)[a]

ϑij		
value	MAD	RMSD	MAX
---	---	---	---
10^{-4}	1.27×10^{-0}	1.33×10^{-0}	2.08×10^{-0}
10^{-5}	1.00×10^{-1}	1.08×10^{-1}	1.68×10^{-1}
10^{-6}	1.07×10^{-2}	1.13×10^{-2}	1.75×10^{-2}
10^{-7}	8.79×10^{-4}	9.46×10^{-4}	1.53×10^{-3}

[a]Mean absolute deviations (MAD), maximum absolute deviations (MAX), and root mean square deviation (RMSD) on the test set from Table 7 are shown. The reference energies were computed using ω-RI-CDD-MP2 without integral screening and natural blocking. 7 Laplace points are used for $[S_8]_5$; 8 Laplace points are used in all other calculations. All values are given in kcal/mol.

observed in Table 6 upon increasing the threshold from 10^{-6} to 10^{-5}; a similar effect occurs for ϑ_{3c} in Table 4. This is caused by relatively large errors for graphite$_{96}$ and CNT$_{80}$, which are both systems with strongly delocalized electronic structure and a high degree of symmetry. Due to the symmetry, a large number of integrals with nearly identical values are neglected if the thresholds are raised above a certain value. One thus has to apply care in choosing thresholds for systems of this kind.

The influence of the integral screening and natural blocking thresholds on the accuracy was also studied on the S22 test set,[66] and the corresponding data is shown in the Supporting Information. Due to the small size of the molecules in the S22 test set, only a few contributions are neglected by integral screening or natural blocking and the obtained errors are therefore significantly smaller than the errors obtained with the employed test set containing large molecules.

The combined influence of the determined thresholds is analyzed in Table 7. A mean error of 0.103 kcal/mol compared to canonical RI-MP2 is obtained, which indicates that the employed set of thresholds is suitable to obtain chemically accurate results also for larger molecular systems. Therefore, we use this particular set of thresholds for the timings with the def2-SVP basis set shown in Section 4.2. In Table 7, also, the errors obtained with RI-CDD-MP2 using the recommended thresholds from ref 33 are shown. The mean error obtained with RI-CDD-MP2 is more than twice as large. Thus, we conclude that the use of these settings in the timings shown in Section 4.2 does not introduce a biased advantage for ω-RI-CDD-MP2 in the comparison with RI-CDD-MP2. In Table 8, calculations with a set of suitable thresholds are shown that allow highly accurate computations with a def2-TZVP basis set.

4.2. Scaling Behavior and Efficiency.
Timings on linear n-alkanes are shown in Figure 5 and Table 9. The wall time required for the ω-RI-CDD-MP2 calculations is smaller than

Table 6. Benchmark Calculations for the Natural Blocking Thresholds ϑ_{NB} and ϑ_{NB}^{iaP} [a]

ϑ_{NB}				ϑ_{NB}^{iaP}			
value	MAD	RMSD	MAX	value	MAD	RMSD	MAX
1.0×10^{-5}	4.51×10^{-1}	1.09×10^{-0}	3.54×10^{-0}	1.0×10^{-5}	7.69×10^{-1}	2.12×10^{-0}	6.99×10^{-0}
1.0×10^{-6}	4.99×10^{-4}	1.02×10^{-3}	3.28×10^{-3}	5.0×10^{-6}	4.08×10^{-2}	9.55×10^{-2}	3.10×10^{-1}
1.0×10^{-7}	4.18×10^{-6}	1.00×10^{-5}	3.26×10^{-5}	1.0×10^{-6}	2.08×10^{-4}	2.86×10^{-4}	6.50×10^{-4}
				1.0×10^{-7}	5.70×10^{-6}	1.11×10^{-5}	3.02×10^{-5}

[a] Mean absolute deviations (MAD) and maximum absolute deviations (MAX) on the test set from Table 7 are shown. The reference energies were computed using ω-RI-CDD-MP2 without integral screening and natural blocking. 7 Laplace points are used for $[S_8]_5$; 8 Laplace points are used in all other calculations. All values are given in kcal/mol.

Table 7. Errors Compared to Canonical RI-MP2 with a Coulomb Metric in ω-RI-CDD-MP2 Calculations ($\Delta_{\omega\text{-RI-CDD}}$) and RI-CDD-MP2 Calculations ($\Delta_{\text{RI-CDD}}$) [a]

molecule	$\Delta_{\omega\text{-RI-CDD}}$	$\Delta_{\text{RI-CDD}}$
amylose$_4$	1.69×10^{-2}	9.89×10^{-2}
angiotensin	9.08×10^{-2}	2.39×10^{-1}
β-carotene	1.85×10^{-2}	5.69×10^{-2}
CNT$_{80}$	1.04×10^{-1}	3.56×10^{-1}
diamond$_{102}$	9.89×10^{-2}	1.30×10^{-1}
DNA$_2$	1.15×10^{-1}	2.20×10^{-1}
graphite$_{96}$	2.56×10^{-1}	2.36×10^{-1}
LiF$_{72}$	7.64×10^{-2}	1.28×10^{-1}
polyethyne$_{64}$	1.01×10^{-1}	5.22×10^{-2}
polyyne$_{64}$	1.25×10^{-1}	5.20×10^{-2}
$[S_8]_5$	1.33×10^{-1}	9.70×10^{-1}
MAD	1.03×10^{-1}	2.31×10^{-1}
MRD [%]	0.0019	0.0051

[a] All calculations employ a def2-SVP basis set. For ω-RI-CDD-MP2, the following thresholds are used: $\vartheta_{3c} = 10^{-6}$, $\vartheta_{schwarz} = 10^{-9}$, $\vartheta_{ij} = 10^{-6}$, $\vartheta_{NB} = 10^{-6}$, and $\vartheta_{NB}^{iaP} = 5 \times 10^{-6}$. For RI-CDD-MP2, a QQR screening threshold of 10^{-9} and a block-sparse linear algebra threshold of 10^{-6} are used. 7 Laplace points are used for $[S_8]_5$; 8 Laplace points are used in all other calculations. All values are given in kcal/mol. MAD and MRD denote mean absolute and mean relative deviation, respectively. The MRD values are given in percent of the total RI-MP2 correlation energy.

Table 8. Errors Compared to Canonical RI-MP2 with a Coulomb Metric in ω-RI-CDD-MP2 Calculations ($\Delta_{\omega\text{-RI-CDD}}$) and RI-CDD-MP2 Calculations ($\Delta_{\text{RI-CDD}}$) [a]

molecule	$\Delta_{\omega\text{-RI-CDD}}$	$\Delta_{\text{RI-CDD}}$
amylose$_4$	1.87×10^{-2}	2.22×10^{-2}
angiotensin	6.90×10^{-2}	7.08×10^{-2}
β-carotene	2.75×10^{-2}	2.07×10^{-2}
CNT$_{80}$	1.76×10^{-1}	7.53×10^{-2}
diamond$_{102}$	3.91×10^{-2}	3.55×10^{-2}
DNA$_2$	6.87×10^{-2}	7.84×10^{-2}
graphite$_{96}$	1.32×10^{-1}	4.58×10^{-2}
LiF$_{72}$	3.20×10^{-2}	5.01×10^{-3}
polyethyne$_{64}$	2.22×10^{-2}	1.71×10^{-2}
polyyne$_{64}$	1.55×10^{-1}	2.78×10^{-2}
$[S_8]_5$	1.09×10^{-2}	4.36×10^{-1}
MAD	6.83×10^{-2}	7.58×10^{-2}
MRD [%]	0.00098	0.00143

[a] The def2-TZVP basis set was used in all calculations. For ω-RI-CDD-MP2, the following thresholds are used: $\vartheta_{3c} = 10^{-7}$, $\vartheta_{schwarz} = 10^{-10}$, $\vartheta_{ij} = 10^{-6}$, $\vartheta_{NB} = 10^{-7}$, and $\vartheta_{NB}^{iaP} = 10^{-6}$. For RI-CDD-MP2, a QQR screening threshold of 10^{-10} and a block-sparse linear algebra threshold of 10^{-8} are used. 7 Laplace points are used for $[S_8]_5$; 8 Laplace points are used in all other calculations. All values are given in kcal/mol. MAD and MRD denote mean absolute and mean relative deviation, respectively. The MRD values are given in percent of the total RI-MP2 correlation energy.
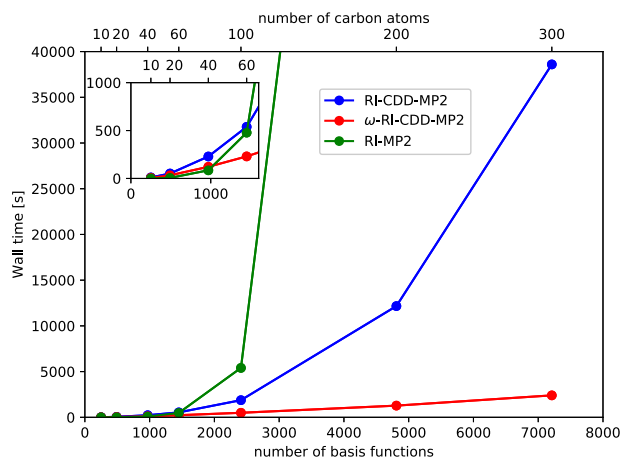
the wall time used for the RI-CDD-MP2 reference in all of these calculations, and the relative differences rise significantly for increasing chain lengths. This suggests that ω-RI-CDD-MP2 has both a lower prefactor and reduced effective scaling compared to RI-CDD-MP2. For comparison, timings with canonical RI-MP2 are shown. For the smallest alkanes, ω-RI-CDD-MP2 is slower than RI-MP2 because of the screening overhead and the required loop over Laplace points. Due to the lower scaling of ω-RI-CDD-MP2, the situation is reversed for large alkanes; the crossover occurs between 40 and 60 carbon atoms. The largest calculation was done on $C_{300}H_{602}$ with 7210 basis functions and required a compute time of 2400 s, which illustrates that the ω-RI-CDD-MP2 method exploits the available sparsity in an efficient manner. The scaling is analyzed in detail in Table 9. As shown, the effective scaling steadily decreases for alkanes with up to 200 carbon atoms, where the minimal scaling of 1.37 is reached. This shows that the scaling of the time-dominating steps has been reduced to be linear. Between a chain length of 200 and 300 carbon atoms, the effective scaling increases slightly to 1.56. This can be explained by the remaining asymptotically cubic and quadratic scaling steps. For some of these steps, the scaling could be reduced further; the computation of the pseudodensity matrices according to eqs 5 and 6, e.g., could be made to

Figure 5. Timings on linear n-alkanes with up to 300 carbon atoms. The ω-RI-CDD-MP2 method (red) is compared to RI-CDD-MP2 (blue) and canonical RI-MP2 (green). In all calculations, the def2-SVP basis set is employed in combination with the thresholds from Table 7. The inset shows the timings for the alkanes with up to 60 carbon atoms.

Table 9. Total Wall Times in Seconds and Scaling in Calculations for Linear n-Alkanes with the def2-SVP Basis Set and 5 Laplace Points[a]

#carbon atoms	#basisf.	wall time	scaling
10	250	7	
20	490	33	2.32
40	970	121	1.90
60	1450	230	1.59
100	2410	494	1.50
200	4810	1277	1.37
300	7210	2400	1.56

[a]The scaling exponents are computed relative to the calculation on the previous system.

be linear scaling by expressing the pseudodensities in terms of matrix exponentials[67] and using sparse linear algebra in their computation. Other steps such as the inversion of the matrix of two-center integrals in eq 18 or the matrix multiplications from eq 17 are intrinsically cubic scaling. Nevertheless, all steps with a scaling $>O(M)$ have a low prefactor and only become relevant for extremely large systems.

In Figure 6, the number of computed three- and four-center integrals is shown for the largest considered alkanes. The number of significant integrals that need to be computed scales close to linearly, which illustrates the effectiveness of the employed integral screening. Also, the number of significant ij pairs in the exchange contribution and the number of elements in the lists $(Q)_i$ show near linear scaling. The fact that the number of untransformed and transformed three-center integrals scales linearly allows one to also reduce the RAM and disk space requirements and the I/O overhead to linear.

Figure 7 shows calculations for linear n-alkanes with the def2-TZVP basis set. As for the def2-SVP basis set, significant speed-ups compared to RI-CDD-MP2 are observed with the new method. The effective scaling between the largest systems with 100 and 160 carbon atoms amounts to 1.46. This demonstrates that the ω-RI-CDD-MP2 method scales favorably with a small prefactor also for high-quality basis sets.

In order to illustrate the applicability of the new method to realistic systems such as large biomolecules, we also performed calculations on DNA strands. The corresponding timings are shown in Figure 8 and Table 10. Also for the DNA strands, significant speed-ups compared to RI-CDD-MP2 are obtained with the new ω-RI-CDD-MP2 method. The crossover between canonical RI-MP2 and ω-RI-CDD-MP2 occurs between AT_2 and AT_4. The largest ω-RI-CDD-MP2 calculation was
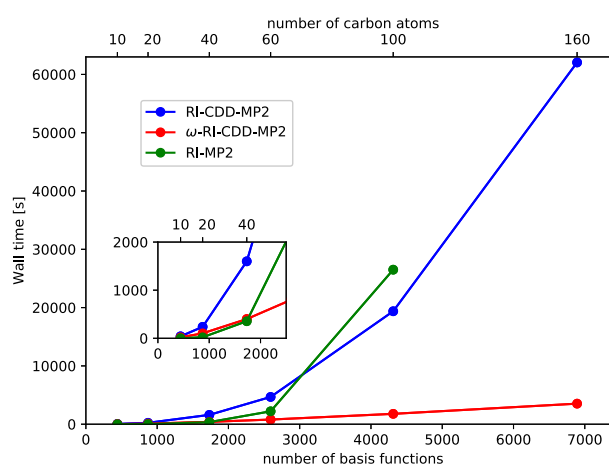

Figure 7. Timings on linear n-alkanes with up to 160 carbon atoms. The def2-TZVP basis set in combination with the thresholds from Table 8 was used in all calculations. The ω-RI-CDD-MP2 method (red) is compared to RI-CDD-MP2 (blue) and canonical RI-MP2 (green). The inset shows the timings for the alkanes with up to 40 carbon atoms.

performed on a DNA strand with 16 base pairs, 1052 atoms, 11 230 basis functions, and 37 248 auxiliary functions and required a computation time of 35.6 h on a single node (for the specifications, see Computational Details). This demonstrates that the ω-RI-CDD-MP2 method allows for efficient MP2 calculations for large biomolecular systems. Table 10 also shows how much individual steps contribute to the total wall time. For most systems, the computation of the exchange energy is the rate-limiting step, but also, the transformations of the three-center integrals require a significant fraction of the overall compute time. Note that the separate treatment of Coulomb and exchange contributions in the ω-RI-CDD-MP2 method allows for even more efficient SOS-MP2 calculations by simply omitting the exchange contributions. On the basis of the timings from Table 10, one can expect a ω-SOS-RI-CDD-MP2 method to be faster by roughly a factor of 2. The effective scaling for the DNA strands is also shown in Table 10. The effective scaling decreases for the larger DNA strands and reaches a value of 1.90 between AT_8 and AT_{16}. This demonstrates that subquadratic scaling can be achieved also for realistic systems.
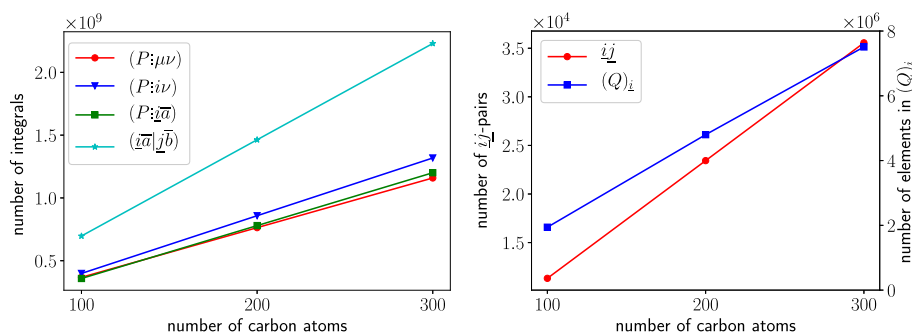

Figure 6. Left: Numbers of computed three-center and four-center integrals for linear alkanes with 100 to 300 carbon atoms. Right: The number of significant ij pairs from the ij prescreening and the number of elements in the lists $(Q)_i$ are shown. All values refer to the first Laplace point only.
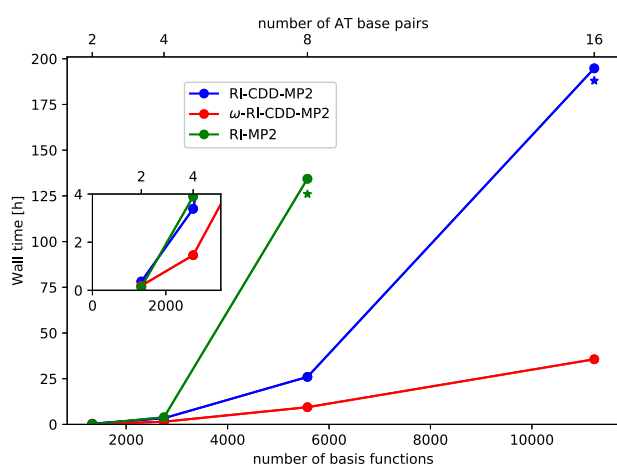
Figure 8. Timings on DNA strands with 2 to 16 adenine–thymine base pairs. The ω-RI-CDD-MP2 method (red) is compared to RI-CDD-MP2 (blue) and canonical RI-MP2 (green). The RI-CDD-MP2 calculation on AT_{16} could not be performed due to disk space limitations; the corresponding wall time marked with a blue star was extrapolated on the basis of the effective scaling between AT_4 and AT_8. The RI-MP2 calculation for AT_8 was extrapolated assuming an N^5 scaling. The inset shows the timings for AT_2 and AT_4.

Table 10. Total Wall Times and Wall Times of the Individual Computation Steps in Calculating Adenine–Thymine Base Pairs AT_n with the def2-SVP Basis Set and 5 Laplace Points[a]

	AT_2	AT_4	AT_8	AT_{16}
wall time	681	5252	33 851	128 274
$t_{exchange}$	298	2396	13 671	61 318
$t_{Coulomb}$	45	386	2094	7449
$t_{transform}$	259	2109	16 550	54 157
t_{3c}	70	303	1186	3315
scaling		2.82	2.63	1.90

[a]All timings are given in seconds. $t_{exchange}$ and $t_{Coulomb}$ denote the time used for the exchange and Coulomb contributions to the correlation energy, respectively. t_{3c} and $t_{transform}$ denote the wall time used for computing the AO three-center integrals and transforming them into the basis of Cholesky-pseudo-MOs, respectively. The scaling exponents are computed relative to the calculation on the previous system.

5. CONCLUSION

We presented a new method for the efficient computation of MP2 energies denoted as ω-RI-CDD-MP2. Local MOs obtained from a Cholesky decomposition of density and pseudodensity matrices and an erfc-attenuated Coulomb metric used for the RI approximation provide a high degree of sparsity in the occurring intermediates. This sparsity is exploited with efficient integral screening techniques and a sparse linear algebra approach called natural blocking. It was demonstrated in test calculations that the errors introduced by the used approximations can be systematically decreased by tightening the corresponding thresholds. Timings on alkane chains and DNA strands were performed with thresholds that allow one to obtain chemically accurate correlation energies also for large molecular systems. It was shown that the method displays effective subquadratic scaling behavior in conjunction with a small prefactor for sufficiently large and extended molecules. For both alkanes and DNA strands, significant

speed-ups compared to the RI-CDD-MP2 method are observed. The largest considered DNA system with 1052 atoms, 11 230 basis functions, and 37 248 auxiliary functions required a computation time of 35.6 h on a single node, which illustrates the potential of the method for applications to large biomolecular systems.

Further improvements might be possible by using iterative orbital localization techniques in order to increase the locality of Cholesky-MOs and Cholesky-pseudo-MOs. The applicability of the method might be extended by developing efficient parallelization schemes or by adapting the method to GPUs. The basis set error could be reduced by combining the method with explicitly correlated F12 approaches. Since the method relies only on integral screening and sparse linear algebra and not on any kind of domain approximation or fragmentation, no problems with discontinuities in the potential energy surfaces are to be expected, which makes the accurate and reliable computation of gradients possible. In future work, the development of analytical derivatives would therefore be desirable in order to allow for accurate and efficient computations of properties of large molecules.

■ ASSOCIATED CONTENT

ⓢ Supporting Information

The Supporting Information is available free of charge at https://pubs.acs.org/doi/10.1021/acs.jctc.0c00600.

Benchmark calculations on the S22 test set[66] (PDF)

■ AUTHOR INFORMATION

Corresponding Author

Christian Ochsenfeld − Chair of Theoretical Chemistry, Department of Chemistry, University of Munich (LMU), 81377 Munich, Germany; ⓞ orcid.org/0000-0002-4189-6558; Email: christian.ochsenfeld@uni-muenchen.de

Authors

Michael Glasbrenner − Chair of Theoretical Chemistry, Department of Chemistry, University of Munich (LMU), 81377 Munich, Germany

Daniel Graf − Chair of Theoretical Chemistry, Department of Chemistry, University of Munich (LMU), 81377 Munich, Germany

Complete contact information is available at:
https://pubs.acs.org/10.1021/acs.jctc.0c00600

Notes

The authors declare no competing financial interest.

■ ACKNOWLEDGMENTS

■ REFERENCES

(1) Møller, C.; Plesset, M. S. Note on an approximation treatment for many-electron systems. *Phys. Rev.* **1934**, *46*, 618.

(2) Cremer, D. Møller–Plesset perturbation theory: from small molecule methods to methods for thousands of atoms. *WIREs Comput. Mol. Sci.* **2011**, *1*, 509–530.

(3) Grimme, S. Improved second-order Møller–Plesset perturbation theory by separate scaling of parallel-and antiparallel-spin pair correlation energies. *J. Chem. Phys.* **2003**, *118*, 9095–9102.

(4) Jung, Y.; Lochan, R. C.; Dutoi, A. D.; Head-Gordon, M. Scaled opposite-spin second order Møller–Plesset correlation energy: an economical electronic structure method. *J. Chem. Phys.* **2004**, *121*, 9793–9802.

(5) Parr, R. G.; Yang, W. Density-functional theory of the electronic structure of molecules. *Annu. Rev. Phys. Chem.* **1995**, *46*, 701–728.

(6) Grimme, S. Semiempirical hybrid density functional with perturbative second-order correlation. *J. Chem. Phys.* **2006**, *124*, No. 034108.

(7) Goerigk, L.; Moellmann, J.; Grimme, S. Computation of accurate excitation energies for large organic molecules with double-hybrid density functionals. *Phys. Chem. Chem. Phys.* **2009**, *11*, 4611–4620.

(8) Goerigk, L.; Grimme, S. Double-hybrid density functionals. *WIREs Comput. Mol. Sci.* **2014**, *4*, 576–600.

(9) Pulay, P. Localizability of dynamic electron correlation. *Chem. Phys. Lett.* **1983**, *100*, 151–154.

(10) Pulay, P.; Saebø, S. Orbital-invariant formulation and second-order gradient evaluation in Møller–Plesset perturbation theory. *Theor. Chim. Acta* **1986**, *69*, 357–368.

(11) Häser, M. Møller–Plesset (MP2) perturbation theory for large molecules. *Theor. Chim. Acta* **1993**, *87*, 147–173.

(12) Martínez, T. J.; Carter, E. A. Pseudospectral Møller–Plesset perturbation theory through third order. *J. Chem. Phys.* **1994**, *100*, 3631–3638.

(13) Hampel, C.; Werner, H.-J. Local treatment of electron correlation in coupled cluster theory. *J. Chem. Phys.* **1996**, *104*, 6286–6297.

(14) Maslen, P.; Head-Gordon, M. Non-iterative local second order Møller–Plesset theory. *Chem. Phys. Lett.* **1998**, *283*, 102–108.

(15) Ayala, P. Y.; Scuseria, G. E. Linear scaling second-order Møller–Plesset theory in the atomic orbital basis for large molecular systems. *J. Chem. Phys.* **1999**, *110*, 3660–3671.

(16) Maslen, P. E.; Head-Gordon, M. Noniterative local second order Møller–Plesset theory: Convergence with local correlation space. *J. Chem. Phys.* **1998**, *109*, 7093–7099.

(17) Schütz, M.; Hetzer, G.; Werner, H.-J. Low-order scaling local electron correlation methods. I. Linear scaling local MP2. *J. Chem. Phys.* **1999**, *111*, 5691–5705.

(18) Lee, M. S.; Maslen, P. E.; Head-Gordon, M. Closely approximating second-order Møller–Plesset perturbation theory with a local triatomics in molecules model. *J. Chem. Phys.* **2000**, *112*, 3592–3601.

(19) Hetzer, G.; Schütz, M.; Stoll, H.; Werner, H.-J. Low-order scaling local correlation methods II: Splitting the Coulomb operator in linear scaling local second-order Møller–Plesset perturbation theory. *J. Chem. Phys.* **2000**, *113*, 9443–9455.

(20) Saebø, S.; Pulay, P. A low-scaling method for second order Møller–Plesset calculations. *J. Chem. Phys.* **2001**, *115*, 3975–3983.

(21) Koch, H.; Sánchez de Merás, A.; Pedersen, T. B. Reduced scaling in electronic structure calculations using Cholesky decompositions. *J. Chem. Phys.* **2003**, *118*, 9481–9484.

(22) Werner, H.-J.; Manby, F. R.; Knowles, P. J. Fast linear scaling second-order Møller–Plesset perturbation theory (MP2) using local and density fitting approximations. *J. Chem. Phys.* **2003**, *118*, 8149–8160.

(23) Lambrecht, D. S.; Doser, B.; Ochsenfeld, C. Rigorous integral screening for electron correlation methods. *J. Chem. Phys.* **2005**, *123*, 184102.

(24) Jung, Y.; Head-Gordon, M. A fast correlated electronic structure method for computing interaction energies of large van der Waals complexes applied to the fullerene-porphyrin dimer. *Phys. Chem. Chem. Phys.* **2006**, *8*, 2831–2840.

(25) Jung, Y.; Shao, Y.; Head-Gordon, M. Fast evaluation of scaled opposite spin second-order Møller–Plesset correlation energies using auxiliary basis expansions and exploiting sparsity. *J. Comput. Chem.* **2007**, *28*, 1953–1964.

(26) Doser, B.; Lambrecht, D. S.; Ochsenfeld, C. Tighter multipole-based integral estimates and parallel implementation of linear-scaling AO–MP2 theory. *Phys. Chem. Chem. Phys.* **2008**, *10*, 3335–3344.

(27) Doser, B.; Lambrecht, D. S.; Kussmann, J.; Ochsenfeld, C. Linear-scaling atomic orbital-based second-order Møller–Plesset perturbation theory by rigorous integral screening criteria. *J. Chem. Phys.* **2009**, *130*, No. 064107.

(28) Zienau, J.; Clin, L.; Doser, B.; Ochsenfeld, C. Cholesky-decomposed densities in Laplace-based second-order Møller–Plesset perturbation theory. *J. Chem. Phys.* **2009**, *130*, 204112.

(29) Kristensen, K.; Høyvik, I.-M.; Jansik, B.; Jørgensen, P.; Kjærgaard, T.; Reine, S.; Jakowski, J. MP2 energy and density for large molecular systems with internal error control using the Divide-Expand-Consolidate scheme. *Phys. Chem. Chem. Phys.* **2012**, *14*, 15706–15714.

(30) Boström, J.; Pitoňák, M.; Aquilante, F.; Neogrády, P.; Pedersen, T. B.; Lindh, R. Coupled cluster and Møller–Plesset perturbation theory calculations of noncovalent intermolecular interactions using density fitting with auxiliary basis sets from cholesky decompositions. *J. Chem. Theory Comput.* **2012**, *8*, 1921–1928.

(31) Hohenstein, E. G.; Parrish, R. M.; Martínez, T. J. Tensor hypercontraction density fitting. I. Quartic scaling second-and third-order Møller–Plesset perturbation theory. *J. Chem. Phys.* **2012**, *137*, No. 044103.

(32) Maurer, S. A.; Lambrecht, D. S.; Kussmann, J.; Ochsenfeld, C. Efficient distance-including integral screening in linear-scaling Møller–Plesset perturbation theory. *J. Chem. Phys.* **2013**, *138*, No. 014101.

(33) Maurer, S. A.; Clin, L.; Ochsenfeld, C. Cholesky-decomposed density MP2 with density fitting: Accurate MP2 and double-hybrid DFT energies for large systems. *J. Chem. Phys.* **2014**, *140*, 224112.

(34) Pinski, P.; Riplinger, C.; Valeev, E. F.; Neese, F. Sparse maps—A systematic infrastructure for reduced-scaling electronic structure methods. I. An efficient and simple linear scaling local MP2 method that uses an intermediate basis of pair natural orbitals. *J. Chem. Phys.* **2015**, *143*, No. 034108.

(35) Nagy, P. R.; Samu, G.; Kállay, M. An integral-direct linear-scaling second-order Møller–Plesset approach. *J. Chem. Theory Comput.* **2016**, *12*, 4897–4914.

(36) Baudin, P.; Ettenhuber, P.; Reine, S.; Kristensen, K.; Kjærgaard, T. Efficient linear-scaling second-order Møller–Plesset perturbation theory: The divide–expand–consolidate RI-MP2 model. *J. Chem. Phys.* **2016**, *144*, No. 054102.

(37) Pham, B. Q.; Gordon, M. S. Compressing the Four-Index Two-Electron Repulsion Integral Matrix using the Resolution-of-the-Identity Approximation Combined with the Rank Factorization Approximation. *J. Chem. Theory Comput.* **2019**, *15*, 2254–2264.

(38) Pham, B. Q.; Gordon, M. S. Hybrid distributed/shared memory model for the RI-MP2 method in the fragment molecular orbital framework. *J. Chem. Theory Comput.* **2019**, *15*, 5252–5258.

(39) Barca, G. M.; McKenzie, S. C.; Bloomfield, N. J.; Gilbert, A. T.; Gill, P. M. Q-MP2-OS: Møller–Plesset Correlation Energy by Quadrature. *J. Chem. Theory Comput.* **2020**, *16*, 1568–1577.

(40) Feyereisen, M.; Fitzgerald, G.; Komornicki, A. Use of approximate integrals in ab initio theory. An application in MP2 energy calculations. *Chem. Phys. Lett.* **1993**, *208*, 359–363.

(41) Parrish, R. M.; Hohenstein, E. G.; Martínez, T. J.; Sherrill, C. D. Tensor hypercontraction. II. Least-squares renormalization. *J. Chem. Phys.* **2012**, *137*, 224106.

(42) Riplinger, C.; Neese, F. An efficient and near linear scaling pair natural orbital based local coupled cluster method. *J. Chem. Phys.* **2013**, *138*, No. 034106.

(43) Riplinger, C.; Pinski, P.; Becker, U.; Valeev, E. F.; Neese, F. Sparse maps—A systematic infrastructure for reduced-scaling elec-

tronic structure methods. II. Linear scaling domain based pair natural orbital coupled cluster theory. *J. Chem. Phys.* **2016**, *144*, No. 024109.

(44) Almlöf, J. Elimination of energy denominators in Møller–Plesset perturbation theory by a Laplace transform approach. *Chem. Phys. Lett.* **1991**, *181*, 319–320.

(45) Häser, M.; Almlöf, J. Laplace transform techniques in Møller–Plesset perturbation theory. *J. Chem. Phys.* **1992**, *96*, 489–494.

(46) Jung, Y.; Sodt, A.; Gill, P. M.; Head-Gordon, M. Auxiliary basis expansions for large-scale electronic structure calculations. *Proc. Natl. Acad. Sci. U. S. A.* **2005**, *102*, 6692–6697.

(47) Häser, M.; Ahlrichs, R. Improvements on the direct SCF method. *J. Comput. Chem.* **1989**, *10*, 104–111.

(48) Thompson, T. H.; Ochsenfeld, C. Integral partition bounds for fast and effective screening of general one-, two-, and many-electron integrals. *J. Chem. Phys.* **2019**, *150*, No. 044101.

(49) Higham, N. J. Cholesky factorization. *Wiley Interdiscip. Rev. Comput. Stat.* **2009**, *1*, 251–254.

(50) Reine, S.; Tellgren, E.; Krapp, A.; Kjærgaard, T.; Helgaker, T.; Jansik, B.; Høst, S.; Salek, P. Variational and robust density fitting of four-center two-electron integrals in local metrics. *J. Chem. Phys.* **2008**, *129*, 104101.

(51) Luenser, A.; Schurkus, H. F.; Ochsenfeld, C. Vanishing-overhead linear-scaling random phase approximation by Cholesky decomposition and an attenuated Coulomb-metric. *J. Chem. Theory Comput.* **2017**, *13*, 1647–1655.

(52) Graf, D.; Beuerle, M.; Schurkus, H. F.; Luenser, A.; Savasci, G.; Ochsenfeld, C. Accurate and Efficient Parallel Implementation of an Effective Linear-Scaling Direct Random Phase Approximation Method. *J. Chem. Theory Comput.* **2018**, *14*, 2505–2515.

(53) McWeeny, R. Hartree-Fock theory with nonorthogonal basis functions. *Phys. Rev.* **1959**, *114*, 1528.

(54) Beuerle, M.; Graf, D.; Schurkus, H. F.; Ochsenfeld, C. Efficient calculation of beyond RPA correlation energies in the dielectric matrix formalism. *J. Chem. Phys.* **2018**, *148*, 204104.

(55) Helmich-Paris, B.; Repisky, M.; Visscher, L. Relativistic Cholesky-decomposed density matrix MP2. *Chem. Phys.* **2019**, *518*, 38–46.

(56) Kussmann, J.; Ochsenfeld, C. Pre-selective screening for matrix elements in linear-scaling exact exchange calculations. *J. Chem. Phys.* **2013**, *138*, 134114.

(57) Kussmann, J.; Ochsenfeld, C. Preselective screening for linear-scaling exact exchange-gradient calculations for graphics processing units and general strong-scaling massively parallel calculations. *J. Chem. Theory Comput.* **2015**, *11*, 918–922.

(58) Kussmann, J.; Ochsenfeld, C. Hybrid CPU/GPU integral engine for strong-scaling ab initio methods. *J. Chem. Theory Comput.* **2017**, *13*, 3153–3159.

(59) Weigend, F.; Ahlrichs, R. Balanced basis sets of split valence, triple zeta valence and quadruple zeta valence quality for H to Rn: Design and assessment of accuracy. *Phys. Chem. Chem. Phys.* **2005**, *7*, 3297–3305.

(60) Weigend, F.; Häser, M.; Patzelt, H.; Ahlrichs, R. RI-MP2: optimized auxiliary basis sets and demonstration of efficiency. *Chem. Phys. Lett.* **1998**, *294*, 143–152.

(61) Pulay, P. Convergence acceleration of iterative sequences. The case of SCF iteration. *Chem. Phys. Lett.* **1980**, *73*, 393–398.

(62) Kaltak, M.; Klimeš, J.; Kresse, G. Low scaling algorithms for the random phase approximation: Imaginary time and Laplace transformations. *J. Chem. Theory Comput.* **2014**, *10*, 2498–2507.

(63) Takatsuka, A.; Ten-No, S.; Hackbusch, W. Minimax approximation for the decomposition of energy denominators in Laplace-transformed Møller–Plesset perturbation theories. *J. Chem. Phys.* **2008**, *129*, No. 044112.

(64) Sedlak, R.; Janowski, T.; Pitoňák, M.; Řezáč, J.; Pulay, P.; Hobza, P. Accuracy of Quantum Chemical Methods for Large Noncovalent Complexes. *J. Chem. Theory Comput.* **2013**, *9*, 3364–3374.

(65) Maurer, S. A.; Lambrecht, D. S.; Flaig, D.; Ochsenfeld, C. Distance-dependent Schwarz-based integral estimates for two-electron integrals: Reliable tightness vs. rigorous upper bounds. *J. Chem. Phys.* **2012**, *136*, 144107.

(66) Jurečka, P.; Šponer, J.; Černỳ, J.; Hobza, P. Benchmark database of accurate (MP2 and CCSD (T) complete basis set limit) interaction energies of small model complexes, DNA base pairs, and amino acid pairs. *Phys. Chem. Chem. Phys.* **2006**, *8*, 1985–1993.

(67) Schweizer, S.; Doser, B.; Ochsenfeld, C. An atomic orbital-based reformulation of energy gradients in second-order Møller–Plesset perturbation theory. *J. Chem. Phys.* **2008**, *128*, 154101.

138

Supplementary Information for: Efficient Reduced-Scaling Second-Order Møller-Plesset Perturbation Theory with Cholesky-Decomposed Densities and an Attenuated Coulomb Metric

Michael Glasbrenner, Daniel Graf, and Christian Ochsenfeld

Chair of Theoretical Chemistry, Department of Chemistry, University of Munich (LMU), Butenandtstrasse 7, 81377 Munich, Germany

October 12, 2020

In Tab. 1, the results of benchmark calculations on the S22 test set are shown. Note that two different references are used. All calculations with ω-RI-CDD-MP2 employ RI with an attenuated Coulomb metric and an ω-value of 0.1 and furthermore employ a Laplace-transformation. The reference denoted as ω-RI-CDD-MP2$_{exact}$ also contains these two sources of error, but no additional approximations. The deviations from ω-RI-CDD-MP2$_{exact}$ thus show how large the errors due to integral screening and natural blocking are.

For all integral screening and natural blocking thresholds considered in Tab. 1, fast convergence towards the ω-RI-CDD-MP2$_{exact}$ reference is observed if the thresholds are lowered. The deviations from canonical RI-MP2, which are also shown in Tab. 1, are significantly larger and converge to a constant value upon lowering the thresholds. The remaining deviations are mostly caused by the use of an attenuated Coulomb metric instead of a standard Coulomb metric for the RI.

Table 1: Benchmark calculations on all monomers and dimers from the S22 test set for all ϑ-thresholds. Mean absolute viations (MAD) and maximum absolute deviations (MAX) are shown. The errors are computed either relative to canonical RI-MP2 or to ω-RI-CDD-MP2$_{\text{exact}}$, which refers to the ω-RI-CDD-MP2 method with Laplace transformation and attenuated Coulomb metric ($\omega = 0.1$) as the only approximations. 7 Laplace-points are used for $[S_8]_5$; 8 Laplace-points in all other calculations. The def2-SVP basis set is employed in all calculations. All values are given in kcal/mol.

threshold	value	Error vs. ω-RI-CDD-MP2$_{\text{exact}}$		Error vs. RI-MP2	
		MAD	MAX	MAD	MAX
ϑ_{3c}	10^{-5}	1.17×10^{-5}	5.22×10^{-5}	1.01×10^{-2}	2.59×10^{-2}
	10^{-6}	1.10×10^{-6}	6.84×10^{-6}	1.01×10^{-2}	2.58×10^{-2}
	10^{-7}	1.06×10^{-7}	6.28×10^{-7}	1.01×10^{-2}	2.58×10^{-2}
	10^{-8}	2.66×10^{-8}	4.39×10^{-7}	1.01×10^{-2}	2.58×10^{-2}
$\vartheta_{\text{schwarz}}$	10^{-8}	8.64×10^{-3}	7.22×10^{-2}	1.14×10^{-2}	5.54×10^{-2}
	10^{-9}	5.58×10^{-4}	5.00×10^{-3}	9.61×10^{-3}	2.57×10^{-2}
	10^{-10}	3.51×10^{-5}	3.58×10^{-4}	1.00×10^{-2}	2.58×10^{-2}
	10^{-11}	2.38×10^{-6}	2.09×10^{-5}	1.01×10^{-2}	2.58×10^{-2}
$\vartheta_{\underline{ij}}$	10^{-4}	7.75×10^{-2}	3.14×10^{-1}	6.78×10^{-2}	2.98×10^{-1}
	10^{-5}	7.46×10^{-3}	3.08×10^{-2}	6.14×10^{-3}	1.99×10^{-2}
	10^{-6}	6.16×10^{-4}	2.75×10^{-3}	9.54×10^{-3}	2.53×10^{-2}
	10^{-7}	6.03×10^{-5}	2.92×10^{-4}	1.00×10^{-2}	2.58×10^{-2}
ϑ_{NB}	10^{-4}	4.68×10^{-2}	5.75×10^{-1}	4.70×10^{-2}	5.66×10^{-1}
	10^{-5}	1.21×10^{-5}	3.30×10^{-4}	1.00×10^{-2}	2.58×10^{-2}
	10^{-6}	8.56×10^{-8}	1.82×10^{-6}	1.01×10^{-2}	2.58×10^{-2}
	10^{-7}	3.04×10^{-8}	6.90×10^{-7}	1.01×10^{-2}	2.58×10^{-2}
$\vartheta_{\text{NB}}^{iaP}$	10^{-4}	1.54×10^{-2}	5.72×10^{-1}	2.06×10^{-2}	5.63×10^{-1}
	10^{-5}	8.37×10^{-6}	2.88×10^{-4}	1.01×10^{-2}	2.58×10^{-2}
	10^{-6}	4.56×10^{-8}	1.07×10^{-6}	1.01×10^{-2}	2.58×10^{-2}
	10^{-7}	3.14×10^{-8}	4.39×10^{-7}	1.01×10^{-2}	2.58×10^{-2}

4

Conclusion

In this thesis, several contributions to the field of accurate and efficient electronic-structure methods — especially the increasingly popular and important ACFDT methods — were presented. The six most important bottlenecks of the promising random phase approximation, being the high computational cost, the high memory requirements, the missing variational optimization of the energy, the negative impact of a poor reference, the slow convergence with the basis-set size, and the self-correlation problem, were addressed subject to the constraint to obtain low- and linear-scaling electronic-structure methods.

By utilizing optimized integral and transformation schemes, the computational cost of the already efficient AO-RI-RPA method[50,51] was reduced further by a factor of four, while at the same time increasing its accuracy compared to canonical MO-RI-RPA by orders of magnitude. Additionally, a multi-node parallel algorithm was developed, which not only allows to evaluate RPA correlation energies in a fraction of the time of former theories, but also leads to a scalable decrease of the memory requirements by distributing them over multiple nodes. To decrease the memory requirements further, a new and elegant way of introducing local Cholesky orbitals was presented, enabling the transformation of the large third-order integral tensor at an early stage and thus decreasing the memory requirements by a factor of $N_{\text{basis}}/N_{\text{occ}}$ on a single compute node.

Furthermore, an efficient self-consistent minimization of the total RPA energy with respect to the one-particle density matrix in the atomic-orbital space was presented, which scales only with the second power of the system size. The method makes the total RPA energy stationary with respect to changes in the orbitals/density matrix and in addition eliminates the problems arising due to poor reference orbitals and orbital energies.

Besides that, a linear-scaling range-separated RPA method was put forward. Due to the high efficiency of the method, a detailed benchmark of range-separated RPA became possible. It was confirmed that range-separated RPA indeed shows faster convergence with the size of the basis set and reduces the well-known self-correlation error, since the critical short-range part of the electron-electron interaction is described by semi-local density functional theory. Additionally, it was demonstrated that the performance of range-separated RPA is more balanced over a broad range of chemical problems than that of standard post-KS RPA, making range-separated RPA an interesting candidate for future developments.

Moreover, a RPA-based generalized Kohn–Sham method was developed, which combines the above-mentioned advantages including local atomic/Cholesky orbitals, range-separation, and self-consistency. The method was shown to perform better than standard post-KS RPA, self-consistent RPA, and range-separated RPA on general main group thermochemistry, kinetics, and noncovalent interactions and even outperforms the popular G_0W_0 method in calculating ionization potentials and fundamental gaps.

Range-separation is one possible way to counteract the self-correlation inherent in the RPA correlation functional. However, a more rigorous way is to include the missing exchange-effects causing these problems. In the present work also contributions in this direction were made by combining the developments on standard RPA with newly developed integral estimates for screening purposes to put forward a low- and linear-scaling framework for RPA with exchange methods.

Finally, the tools to develop low-scaling RPA with exchange methods were transferred to MP2 and complemented with efficient linear-algebra routines, yielding a highly efficient and subquadratic-scaling MP2 method.

Overall, the field of electronic-structure theory was extended by several new methods and various broadly applicable tools to devise approaches, managing the difficult task of pairing accuracy with efficiency. In this way, the present work contributed to reaching one of the major goals in quantum chemistry: developing highly accurate and universally applicable electronic-structure methods with a tractable computational cost.

Bibliography

[1] E. Schrödinger, *Phys. Rev.* **1926**, *28*, 1049.

[2] M. Born, R. Oppenheimer, *Ann. Phys.* **1927**, *389*, 457.

[3] J. A. Pople, *Angew. Chem. Int. Ed.* **1999**, *38*, 1894.

[4] W. Kohn, L. J. Sham, *Phys. Rev.* **1965**, *140*, A1133.

[5] A. D. Becke, *J. Chem. Phys.* **2014**, *140*, 18A301.

[6] N. Mardirossian, M. Head-Gordon, *Mol. Phys.* **2017**, *115*, 2315.

[7] G. P. Chen, V. K. Voora, M. M. Agee, S. G. Balasubramani, F. Furche, *Annu. Rev. Phys. Chem.* **2017**, *68*, 421.

[8] J. P. Perdew, *Chem. Phys. Lett.* **1979**, *64*, 127.

[9] J. P. Perdew, A. Zunger, *Phys. Rev. B* **1981**, *23*, 5048.

[10] L. A. Cole, J. P. Perdew, *Phys. Rev. A* **1982**, *25*, 1265.

[11] C. Toher, A. Filippetti, S. Sanvito, K. Burke, *Phys. Rev. Lett.* **2005**, *95*, 146402.

[12] A. J. Cohen, P. Mori-Sánchez, W. Yang, *Science* **2008**, *321*, 792.

[13] Y. Zhang, W. Yang, *J. Chem. Phys.* **1998**, *109*, 2604.

[14] A. J. Cohen, P. Mori-Sánchez, W. Yang, *Chem. Rev.* **2012**, *112*, 289.

[15] P. Mori-Sánchez, A. J. Cohen, W. Yang, *Phys. Rev. Lett.* **2008**, *100*, 146401.

[16] P. Mori-Sánchez, A. J. Cohen, W. Yang, *J. Chem. Phys.* **2006**, *125*, 201102.

[17] T. M. Henderson, G. E. Scuseria, *Mol. Phys.* **2010**, *108*, 2511.

[18] J. M. Pérez-Jordá, A. D. Becke, *Chem. Phys. Lett.* **1995**, *233*, 134.

[19] D. Bohm, D. Pines, *Phys. Rev.* **1951**, *82*, 625.

[20] D. Pines, D. Bohm, *Phys. Rev.* **1952**, *85*, 338.

[21] D. Bohm, D. Pines, *Phys. Rev.* **1953**, *92*, 609.

[22] A. Heßelmann, *Top. Curr. Chem.* **2015**, *365*, 97.

[23]   M. Gell-Mann, K. A. Brueckner, *Phys. Rev.* **1957**, *106*, 364.

[24]   D. C. Langreth, J. P. Perdew, *Solid State Commun.* **1975**, *17*, 1425.

[25]   D. C. Langreth, J. P. Perdew, *Phys. Rev. B* **1977**, *15*, 2884.

[26]   H. B. Callen, T. A. Welton, *Phys. Rev.* **1951**, *83*, 34.

[27]   F. Furche, *Phys. Rev. B* **2001**, *64*, 195120.

[28]   M. Fuchs, X. Gonze, *Phys. Rev. B* **2002**, *65*, 235109.

[29]   Y. M. Niquet, M. Fuchs, X. Gonze, *Phys. Rev. A* **2003**, *68*, 032507.

[30]   M. Fuchs, Y. M. Niquet, X. Gonze, K. Burke, *J. Chem. Phys.* **2005**, *122*, 094116.

[31]   F. Furche, T. Van Voorhis, *J. Chem. Phys.* **2005**, *122*, 164106.

[32]   H. Eshuis, F. Furche, *J. Chem. Phys.* **2012**, *136*, 084105.

[33]   H. Eshuis, J. E. Bates, F. Furche, *Theor. Chem. Acc.* **2012**, *131*, 1084.

[34]   H. Eshuis, J. Yarkony, F. Furche, *J. Chem. Phys.* **2010**, *132*, 234114.

[35]   J. E. Bates, F. Furche, *J. Chem. Phys.* **2013**, *139*, 171103.

[36]   F. Furche, *J. Chem. Phys.* **2008**, *129*, 114105.

[37]   V. K. Voora, S. G. Balasubramani, F. Furche, *Phys. Rev. A* **2019**, *99*, 012518.

[38]   A. M. Burow, J. E. Bates, F. Furche, H. Eshuis, *J. Chem. Theory Comput.* **2014**, *10*, 180.

[39]   H. Eshuis, F. Furche, *J. Phys. Chem. Lett.* **2011**, *2*, 983.

[40]   A. Heßelmann, A. Görling, *Mol. Phys.* **2010**, *108*, 359.

[41]   A. Heßelmann, A. Görling, *Phys. Rev. Lett.* **2011**, *106*, 093001.

[42]   A. Heßelmann, A. Görling, *Mol. Phys.* **2011**, *109*, 2473.

[43]   J. Paier, X. Ren, P. Rinke, G. E. Scuseria, A. Grüneis, G. Kresse, M. Scheffler, *New J. Phys.* **2012**, *14*, 043002.

[44]   X. Ren, A. Tkatchenko, P. Rinke, M. Scheffler, *Phys. Rev. Lett.* **2011**, *106*, 153003.

[45]   P. Bleiziffer, A. Heßelmann, A. Görling, *J. Chem. Phys.* **2012**, *136*, 134102.

[46]   X. Ren, P. Rinke, C. Joas, M. Scheffler, *J. Mater. Sci.* **2012**, *47*, 7447.

[47]   G. E. Scuseria, T. M. Henderson, D. C. Sorensen, *J. Chem. Phys.* **2008**, *129*, 231101.

[48]   M. Beuerle, C. Ochsenfeld, *J. Chem. Phys.* **2017**, *147*, 204107.

[49]   M. Beuerle, C. Ochsenfeld, *J. Chem. Phys.* **2018**, *149*, 244111.

[50] H. F. Schurkus, C. Ochsenfeld, *J. Chem. Phys.* **2016**, *144*, 031101.

[51] A. Luenser, H. F. Schurkus, C. Ochsenfeld, *J. Chem. Theory Comput.* **2017**, *13*, 1647.

[52] P. Verma, R. J. Bartlett, *J. Chem. Phys.* **2012**, *136*, 044105.

[53] P. Bleiziffer, A. Heßelmann, A. Görling, *J. Chem. Phys.* **2013**, *139*, 084113.

[54] N. L. Nguyen, N. Colonna, S. de Gironcoli, *Phys. Rev. B* **2014**, *90*, 045138.

[55] M. Hellgren, F. Caruso, D. R. Rohr, X. Ren, A. Rubio, M. Scheffler, P. Rinke, *Phys. Rev. B* **2015**, *91*, 165110.

[56] Y. Jin, D. Zhang, Z. Chen, N. Q. Su, W. Yang, *J. Phys. Chem. Lett.* **2017**, *8*, 4746.

[57] J. P. Perdew, K. Schmidt in AIP Conf. Proc. *Vol. 577*, AIP, **2001**, pp. 1–20.

[58] E. Runge, E. K. U. Gross, *Phys. Rev. Lett.* **1984**, *52*, 997.

[59] J. F. Dobson in *Fundamentals of Time-Dependent Density Functional Theory*, (Eds.: M. Marques, N. Maitra, F. Nogueira, E. Gross, A. Rubio), Springer-Verlag, Berlin, **2012**, pp. 417–441.

[60] K. S. Singwi, M. P. Tosi, R. H. Land, A. Sjölander, *Phys. Rev.* **1968**, *176*, 589.

[61] S. Kurth, J. P. Perdew, *Phys. Rev. B* **1999**, *59*, 10461.

[62] P. Mori-Sánchez, A. J. Cohen, W. Yang, *Phys. Rev. A* **2012**, *85*, 042507.

[63] Z. Yan, J. P. Perdew, S. Kurth, *Phys. Rev. B* **2000**, *61*, 16430.

[64] J. Toulouse, I. C. Gerber, G. Jansen, A. Savin, J. G. Ángyán, *Phys. Rev. Lett.* **2009**, *102*, 096404.

[65] T. Kato, *Commun. Pure Appl. Math.* **1957**, *10*, 151.

[66] J. Toulouse, W. Zhu, A. Savin, G. Jansen, J. G. Ángyán, *J. Chem. Phys.* **2011**, *135*, 084119.

[67] B. Mussard, P. Reinhardt, J. G. Ángyán, J. Toulouse, *J. Chem. Phys.* **2015**, *142*, 154123.

[68] W. Zhu, J. Toulouse, A. Savin, J. G. Ángyán, *J. Chem. Phys.* **2010**, *132*, 244108.

[69] J. Toulouse, W. Zhu, J. G. Ángyán, A. Savin, *Phys. Rev. A* **2010**, *82*, 032502.

[70] J. G. Ángyán, R.-F. Liu, J. Toulouse, G. Jansen, *J. Chem. Theory Comput.* **2011**, *7*, 3116.

[71] E. Chermak, B. Mussard, J. G. Ángyán, P. Reinhardt, *Chem. Phys. Lett.* **2012**, *550*, 162.

[72] B. Mussard, P. G. Szalay, J. G. Ángyán, *J. Chem. Theory Comput.* **2014**, *10*, 1968.

[73] C. Kalai, B. Mussard, J. Toulouse, *J. Chem. Phys.* **2019**, *151*, 074102.

[74]   B. G. Janesko, T. M. Henderson, G. E. Scuseria, *J. Chem. Phys.* **2009**, *130*, 081105.

[75]   B. G. Janesko, T. M. Henderson, G. E. Scuseria, *J. Chem. Phys.* **2009**, *131*, 034110.

[76]   B. G. Janesko, G. E. Scuseria, *J. Chem. Phys.* **2009**, *131*, 154106.

[77]   J. Paier, B. G. Janesko, T. M. Henderson, G. E. Scuseria, A. Grüneis, G. Kresse, *J. Chem. Phys.* **2010**, *132*, 094103.

[78]   R. M. Irelan, T. M. Henderson, G. E. Scuseria, *J. Chem. Phys.* **2011**, *135*, 094105.

[79]   A. J. Garza, I. W. Bulik, A. G. S. Alencar, J. Sun, J. P. Perdew, G. E. Scuseria, *Mol. Phys.* **2016**, *114*, 997.

[80]   E. Goll, H. J. Werner, H. Stoll, T. Leininger, P. Gori-Giorgi, A. Savin, *Chem. Phys.* **2006**, *329*, 276.

[81]   J. Harl, G. Kresse, *Phys. Rev. B* **2008**, *77*, 045136.

[82]   A. Thierbach, D. Schmidtel, A. Görling, *J. Chem. Phys.* **2019**, *151*, 144117.

[83]   M. Modrzejewski, S. Yourdkhani, J. Klimeš, *J. Chem. Theory Comput.* **2020**, *16*, 427.

[84]   J. P. Perdew, K. Burke, M. Ernzerhof, *Phys. Rev. Lett.* **1997**, *78*, 1396.

[85]   J. P. Perdew, K. Burke, M. Ernzerhof, *Phys. Rev. Lett.* **1996**, *77*, 3865.

[86]   H. Jiang, E. Engel, *J. Chem. Phys.* **2007**, *127*, 184108.

[87]   A. Grüneis, M. Marsman, J. Harl, L. Schimka, G. Kresse, *J. Chem. Phys.* **2009**, *131*, 154115.

[88]   A. Heßelmann, *Phys. Rev. A* **2012**, *85*, 012517.

[89]   T. Gould, *J. Chem. Phys.* **2012**, *137*, 111101.

[90]   D. L. Freeman, *Phys. Rev. B* **1977**, *15*, 5512.

[91]   B. Mussard, D. Rocca, G. Jansen, J. G. Ángyán, *J. Chem. Theory Comput.* **2016**, *12*, 2191.

[92]   A. Dixit, J. G. Ángyán, D. Rocca, *J. Chem. Phys.* **2016**, *145*, 104105.

[93]   C. Møller, M. S. Plesset, *Phys. Rev.* **1934**, *46*, 618.

[94]   Y. Jung, M. Head-Gordon, *Phys. Chem. Chem. Phys.* **2006**, *8*, 2831.

[95]   W. Heisenberg, *Z. Phys.* **1926**, *38*, 411.

[96]   P. A. M. Dirac, *Proc. R. Soc. A* **1926**, *112*, 661.

[97]   W. Pauli, *Z. Phys.* **1925**, *31*, 373.

[98]   W. Pauli, *Z. Phys.* **1925**, *31*, 765.

[99]   J. C. Slater, *Phys. Rev.* **1929**, *34*, 1293.

[100] C. D. Sherrill, H. F. Schaefer III., *Adv. Quant. Chem.* **1999**, *34*, 143.

[101] P. Jordan, O. Klein, *Z. Phys.* **1927**, *45*, 751.

[102] P. Jordan, E. Wigner, *Z. Phys.* **1928**, *47*, 631.

[103] V. Fock, *Z. Phys.* **1932**, *75*, 622.

[104] A. L. Fetter, J. D. Walecka, *Quantum Theory of Many-Particle Systems*, McGraw-Hill, New York, **1971**.

[105] D. R. Hartree, *Math. Proc. Camb. Philos. Soc.* **1928**, *24*, 89.

[106] J. C. Slater, *Phys. Rev.* **1930**, *35*, 210.

[107] V. Fock, *Z. Phys.* **1930**, *61*, 126.

[108] A. Szabo, N. S. Ostlund, *Modern Quantum Chemistry*, Dover, Mineola, New York, **1996**.

[109] C. C. J. Roothaan, *Rev. Mod. Phys.* **1951**, *23*, 69.

[110] G. G. Hall, *Proc. R. Soc. A* **1951**, *205*, 541.

[111] P. Hohenberg, W. Kohn, *Phys. Rev.* **1964**, *136*, B864.

[112] K. Capelle, *Braz. J. Phys.* **2006**, *36*, 1318.

[113] E. Engel, R. M. Dreizler, *Density-Functional Theory: An Advanced Course*, Springer-Verlag Berlin Heidelberg, **2011**.

[114] R. P. Feynman, *Phys. Rev.* **1939**, *56*, 340.

[115] H. Lehmann, *Nuovo Cim.* **1954**, *11*, 342.

[116] E. K. U. Gross, N. T. Maitra in *Fundamentals of Time-Dependent Density Functional Theory*, (Eds.: M. A. Marques, N. T. Maitra, F. M. S. Nogueira, E. K. U. Gross, A. Rubio), Springer-Verlag, **2012**, pp. 53–99.

[117] A. J. Stone in *Non-Covalent Interactions in Quantum Chemistry and Physics*, (Eds.: A. Otero-de-la Roza, G. A. DiLabio), Elsevier, **2017**, pp. 3–26.

[118] M. Petersilka, U. J. Gossmann, E. K. U. Gross, *Phys. Rev. Lett.* **1996**, *76*, 1212.

[119] J. P. Perdew, *Int. J. Quantum Chem.* **1993**, *48*, 93.

[120] J. Linderberg, Y. Öhrn, *Propagators in Quantum Chemistry*, John Wiley & Sons, **2004**.

[121] E. E. Salpeter, H. A. Bethe, *Phys. Rev.* **1951**, *84*, 1232.

[122] A. D. McLachlan, M. A. Ball, *Rev. Mod. Phys.* **1964**, *36*, 844.

[123]   J. L. Whitten, *J. Chem. Phys.* **1973**, *58*, 4496.

[124]   E. J. Baerends, D. E. Ellis, P. Ros, *Chem. Phys.* **1973**, *2*, 41.

[125]   B. I. Dunlap, J. W. D. Connolly, J. R. Sabin, *J. Chem. Phys.* **1979**, *71*, 4993.

[126]   C. Van Alsenoy, *J. Comput. Chem.* **1988**, *9*, 620.

[127]   M. Feyereisen, G. Fitzgerald, A. Komornicki, *Chem. Phys. Lett.* **1993**, *208*, 359.

[128]   O. Vahtras, J. Almlöf, M. Feyereisen, *Chem. Phys. Lett.* **1993**, *213*, 514.

[129]   K. Eichkorn, O. Treutler, H. Öhm, M. Häser, R. Ahlrichs, *Chem. Phys. Lett.* **1995**, *240*, 283.

[130]   M. Sierka, A. Hogekamp, R. Ahlrichs, *J. Chem. Phys.* **2003**, *118*, 9136.

[131]   F. Weigend, A. Köhn, C. Hättig, *J. Chem. Phys.* **2002**, *116*, 3175.

[132]   F. Weigend, *Phys. Chem. Chem. Phys.* **2002**, *4*, 4285.

[133]   M. M. J. Grundei, A. M. Burow, *J. Chem. Theory Comput.* **2017**, *13*, 1159.

[134]   M. Kaltak, J. Klimeš, G. Kresse, *J. Chem. Theory Comput.* **2014**, *10*, 2498.